



The  
University  
Of  
Sheffield.

I-Tung Chan

*Department of Computer Science*

Supervisor

Dr. Paul Watton

A NOVEL  
FLUID-SOLID-GROWTH-TRANSPORT  
FRAMEWORK FOR MODELLING THE  
EVOLUTION OF ARTERIAL DISEASE:  
**Application to Aneurysms**

A thesis resubmitted for the degree of  
**PhD**

April 2019







**A thesis resubmitted for the degree of PhD.**

*A novel Fluid-Solid-Growth-Transport framework for modelling the evolution of arterial disease*

**By I-Tung Chan, Department of Computer Science.**

Submitted April 2019.

## **Abstract**

Arterial diseases affect more than 1 in 20 adults in the world. However, our current knowledge in the mechanisms of arterial disease formation and progression is incomplete and this creates enormous limitations to clinical diagnosis and treatment. The urgent need for a better understanding of arterial pathophysiology motivates different modelling approaches to explore the underlying mechanisms. This thesis focuses on the development of an *in silico* model which represents the mechanical arterial environment, the transport of chemical species, the biology of arterial wall, and the interaction between them. The concept of chemo-mechano-biology is crucial in this research: mechanical forces and chemical levels of the artery can trigger the cell signalling which in turn affect the biological behaviour of the arterial tissues, in both healthy and diseased states. We present a novel fluid-solid-growth-transport (FSGT) computational framework for modelling arterial disease evolution: it identifies and quantifies the influence of the arterial mechanical and chemical environments on the growth and remodelling (G&R) of vascular constituents, elastin and collagen.

For the development of the proposed computational framework, a conceptual thick-walled fibre-reinforced tube model is firstly introduced to represent a healthy vascular structure, in which the physiological stress distribution is determined by the inclusion of residual stress. Numerical analysis of arterial mechanical response is validated with analytical solutions. The oxygen concentration within the arterial wall is simulated by a diffusion-only analysis, and the oxygen level is altered due to the propagation of thrombus layer. To apply the G&R method in this conceptual model, a prescribed elastin degradation causes the radial enlargement and initiates subsequent collagen adaptation due to the altered mechanical and chemical environments. This workflow is then applied to a 2D axisymmetric fusiform model to demonstrate the spatial variation modelling behaviour of this computa-

tional framework. Lastly, a sophisticated FSGT framework is applied to a 3D patient-specific aneurysm geometry. Results from this *in silico* framework can provide insights into the underlying mechanisms of aneurysm evolution with the quantification of mechanical and chemical stimuli. Additionally, this simulation workflow is fully integrated into ANSYS engineering software which would allow its clinical translation by global healthcare technology industries for maximum clinical impact.

## **Statement of Originality**

I hereby declare that this submission is my own work and to the best of my knowledge it contains no materials previously published or written by another person, or substantial proportions of material which have been accepted for the award of any other degree or diploma at the University of Sheffield or any other educational institution, except where due acknowledgement is made in the thesis.

Any contribution made to the research by others, with whom I have worked at the University of Sheffield or elsewhere, is explicitly acknowledged in the thesis.

I also declare that the intellectual content of this thesis is the product of my own work, except to the extent that assistance from others in the project's design and conception or in style, presentation and linguistic expression is acknowledged.

I-TUNG CHAN

9 April 2019.



## Acknowledgements

I would like to express my gratitude to my supervisor, Dr. Paul Watton, for his guidance and support throughout my doctoral study in the University of Sheffield. Especially for an international student like me, he has been really helpful not only in academia research but also on daily life to help me get involved in this friendly environment. I would also like to sincerely thank Dr. Emilie Dickinson for sharing her research experience and providing valuable feedback of this thesis. Many thanks go to my colleagues Haoyu, Katia, Raj, Hamna, Shakti, Yuqian, and Giulia for creating a nice research community and supporting each other as a strong group. For my friends in Sheffield, Yuan, Kewei, Moran, and John, we have been supporting each other since the first day we met and we share lots of great memories in Sheffield. Finally, I would like to gratefully thank my family and my girlfriend Lai Hing. I could not make this far without your unconditional love and continuous support.

I would like to express my gratitude for the financial support provided by Department of Computer Science, University of Sheffield.



# Dissemination

## Conference Presentations and Posters

1. **Chan I.**, Dickinson E., Afaq H., Kampa R., Daly D., Gundiah N., Per-rault C. M. and Watton P. N. *A novel microfluidic perfusion biore-actor system for vascular tissue engineering: in vitro and in sil-ico modelling*, N8 HPC Network Event - Multiscale Computational Mechanics, Sheffield, UK, Oct 30th, 2015.
2. **Chan I.**, Dickinson E., Afaq H., Kampa R., Daly D., Gundiah N., Per-rault C. M. and Watton P. N. *A novel microfluidic perfusion biore-actor system for vascular tissue engineering: in vitro and in sil-ico modelling*, ANSYS Medical Devices Innovation Seminar, Leeds, UK, Nov 17th, 2015.
3. **Chan I.**, Dickinson E., Afaq H., Kampa R. and Watton P. N. *A novel Fluid-Solid-Growth-Transport framework with the application on bioreactor system*, BBSRC Multiscale Biology Meeting, Sheffield, UK, Dec 1th, 2015.
4. **Chan I.** and Watton P. N. *A novel Fluid-Solid-Growth-Transport framework for arterial growth and remodelling*, Summer School on Biomechanics of Soft Tissues, Graz University of Technology, Aus-tria, July 4th-8th, 2016.
5. Mei Y., **Chan I.**, Chen D. and Watton P. N. *A novel Fluid-Solid-Growth-Transport framework for modelling the evolution of in-tracranial aneurysm disease*, Proc. of 5th Int. Conference on Com-putational and Mathematical Biomedical Engineering, Vol 2: 1271-72., 2017.

# CONTENTS

---

<b>Contents</b>	<b>xii</b>
<b>List of Figures</b>	<b>xvi</b>
<b>List of Tables</b>	<b>xxi</b>
<b>Acronyms</b>	<b>xxii</b>
<b>1 Introduction</b>	<b>1</b>
1.1 Motivation . . . . .	1
1.2 Aneurysm disease . . . . .	2
1.3 Arterial structure in health and disease . . . . .	5
1.3.1 Architecture of the healthy arterial wall . . . . .	5
1.3.2 Aneurysm structure . . . . .	7
1.4 Arterial biomechanics and mechanobiology . . . . .	8
1.4.1 Biomechanics of the vessel wall . . . . .	8
1.4.2 Arterial Mechanobiology . . . . .	10
1.5 Adaptive responses to biochemical transport through the arterial wall	12
1.5.1 Motivation . . . . .	12
1.5.2 Mass transport within arterial wall . . . . .	13
1.5.3 Adaptive responses to hypoxic environments . . . . .	14
1.6 Review of the <i>in silico</i> modelling . . . . .	15
1.7 Overview of thesis . . . . .	21
<b>2 Structural model of arterial wall</b>	<b>25</b>
2.1 Arterial histology . . . . .	26
2.1.1 Intima . . . . .	26
2.1.2 Media . . . . .	27
2.1.3 Adventitia . . . . .	28
2.2 Residual stresses . . . . .	28

2.2.1	Significant effect of residual stresses within the vessel wall . . .	28
2.2.2	Opening angle method . . . . .	31
2.3	Mechanical behaviour: continuum mechanical framework . . . . .	34
2.3.1	Description of deformation . . . . .	34
2.3.2	Governing equation . . . . .	35
2.3.3	Specific form of strain energy function . . . . .	36
2.3.4	Hyperelastic stress response . . . . .	36
2.3.5	Geometric model of artery . . . . .	37
2.3.6	Constitutive model for the artery layers . . . . .	39
2.3.7	Arterial model as a two-layered thick-walled tube . . . . .	40
2.4	ANSYS implementation . . . . .	43
2.4.1	Finite element arterial model . . . . .	43
2.4.2	Sensitivity analysis of the number of elements . . . . .	49
2.4.3	Influence of opening angle on stress distribution . . . . .	51
2.4.4	Mechanical behaviour of the ANSYS model . . . . .	53
2.5	Discussion and concluding remarks . . . . .	61
<b>3</b>	<b>Advection-diffusion modelling of oxygen transport through the arterial wall</b>	<b>63</b>
3.1	Oxygen mass transport in arteries . . . . .	64
3.1.1	Oxygen transport in healthy arteries . . . . .	65
3.1.2	Oxygen transport in diseased arteries: thrombosed aneurysms	68
3.1.3	Potential influence of oxygen concentration on aneurysm evolution . . . . .	69
3.2	Model description for oxygen transport . . . . .	69
3.2.1	Artery geometry . . . . .	69
3.2.2	Oxygen transport properties . . . . .	70
3.2.3	Oxygen consumption rate . . . . .	71
3.3	Theory and Methodologies . . . . .	72
3.3.1	Steady-state oxygen diffusion through thrombus and wall . . .	72
3.3.2	Boundary conditions . . . . .	74
3.4	ANSYS implementation . . . . .	77
3.5	Sensitivity analysis of the number of elements . . . . .	81
3.6	Influence of thrombus thickness, oxygen consumption rate and diffusivity on oxygen transport . . . . .	82
3.6.1	Thrombus thickness effect . . . . .	82
3.6.2	Consumption rate effect . . . . .	84
3.6.3	Diffusivity effect . . . . .	85

3.7	Discussion and concluding remarks . . . . .	87
<b>4</b>	<b>A novel chemo-mechano-biological mathematical framework with the application on a 1D cylindrical model</b>	<b>91</b>
4.1	Overview of 1D SGT model . . . . .	92
4.2	Growth and Remodelling . . . . .	93
4.2.1	Elastin degradation . . . . .	94
4.2.2	Propagation of thrombus layer during aneurysm growth . . . .	95
4.2.3	Collagen adaption . . . . .	95
4.3	Illustrative cases of SGT . . . . .	99
4.4	Software implementations . . . . .	100
4.4.1	PERL . . . . .	100
4.4.2	MATLAB . . . . .	102
4.4.3	ANSYS . . . . .	102
4.5	Results . . . . .	102
4.5.1	Case 1: uniform elastin degradation across the arterial wall . .	102
4.5.2	Case 2: non-uniform elastin degradation across the arterial wall	110
4.6	Discussion . . . . .	117
4.7	Conclusion: the benchmark of the 1D model . . . . .	120
<b>5</b>	<b>Application on 2D SGT fusiform model</b>	<b>123</b>
5.1	2D SGT fusiform aneurysm . . . . .	123
5.1.1	Axisymmetric elastin degradation (Fusiform aneurysm) . . . .	124
5.1.2	Mesh projection between solid model and transport model . .	126
5.2	Results . . . . .	130
5.3	Discussion of fusiform model . . . . .	143
5.4	Conclusion . . . . .	145
<b>6</b>	<b>Application on 3D FSGT patient-specific aneurysm</b>	<b>147</b>
6.1	3D FSGT framework . . . . .	147
6.1.1	Overview of the FSGT . . . . .	148
6.1.2	Blood flow simulation . . . . .	151
6.1.3	Structural analysis . . . . .	151
6.1.4	Collagen adaption . . . . .	156
6.1.5	Elastin degradation link to low WSS . . . . .	158
6.2	3D patient-specific aneurysm with elastin degradation linked to WSS	159
6.2.1	Evolution of WSS and $m_E$ . . . . .	159
6.2.2	Evolution of oxygen concentration . . . . .	161
6.3	Two comparative cases with transport modelling on/off . . . . .	162

6.3.1	Model setup . . . . .	162
6.3.2	Results of the two comparative cases . . . . .	165
6.4	Discussion . . . . .	176
6.5	Conclusion . . . . .	178
<b>7</b>	<b>Conclusions and considerations for future development</b>	<b>179</b>
7.1	Summaries of the study . . . . .	179
7.2	Limitations of the proposed FSGT framework . . . . .	181
7.3	Potential improvements to the computational framework . . . . .	183
7.3.1	Multiscale modelling on EC morphology . . . . .	183
7.3.2	Volumetric change . . . . .	184
7.3.3	Reconstruction of healthy artery . . . . .	185
7.4	Concluding remarks . . . . .	187
	<b>References</b>	<b>189</b>
<b>A</b>	<b>Radial inflation of a cylindrical membrane model</b>	<b>199</b>
<b>B</b>	<b>Define the number of nodes and elements</b>	<b>201</b>
<b>C</b>	<b>Mathematical Stability of the G&amp;R framework</b>	<b>205</b>
<b>D</b>	<b>Modelling codes and scripts</b>	<b>213</b>

## LIST OF FIGURES

---

1.1	Two main types of intracranial aneurysms . . . . .	3
1.2	Options for treatment of saccular IAs . . . . .	4
1.3	Structure of the healthy arterial wall . . . . .	6
1.4	Structural comparison between the healthy arterial wall and aneurysm wall . . . . .	8
1.5	Activation of cellular signalling pathways in response to the extracellular mechanical triggers . . . . .	11
1.6	Fluid-Solid-Growth (FSG) framework for modelling the mechanobiology of vascular disease evolution. . . . .	17
2.1	Schematic of arterial wall layered structure . . . . .	27
2.2	Three different states of the artery: <i>in vivo</i> state, no-load state and zero-stress state . . . . .	30
2.3	Photos of coronary rings cut radially to reveal sectors with opening angles $\theta < 180^\circ$ (left) and $> 180^\circ$ (right) . . . . .	32
2.4	Diagram defining the opening angle . . . . .	32
2.5	Illustration of the corresponding positions of stress-free configuration and load-free configuration denoted by the opening angle $\varphi$ , reference radius $R_i$ , load-free radius $r_i$ , and a shift of central point $x_i$ . . . . .	33
2.6	Illustrative model for the description of deformation in continuum mechanics . . . . .	35
2.7	Arterial ring in the stress-free reference configuration, the load-free configuration and the current configuration . . . . .	38
2.8	The pressure-diameter relationship for the membrane model of the artery including the contribution from elastin and collagen . . . . .	43
2.9	Mesh of the arterial model . . . . .	47
2.10	Different opening angles for FE model and target position . . . . .	48
2.11	Comparison between the analytical and numerical solutions on the pressure-diameter relationship of the arterial model . . . . .	49

2.12	Influence of element number (elR) through the wall thickness on stress distribution . . . . .	50
2.13	Different opening angles for single layered vessel wall with only elastin constituent . . . . .	52
2.14	Different opening angles for two-layered vessel wall with collagen and elastin constituents . . . . .	53
2.15	The pressure-diameter curves for the FIB cases . . . . .	57
2.16	Influence of mechanical cases on stress distribution through the wall thickness . . . . .	58
2.17	Influence of blood pressure on stress distribution through the wall thickness . . . . .	60
3.1	Illustrative cylindrical model of a thrombosed artery for oxygen transport modelling . . . . .	70
3.2	Cross-section of arterial geometry; Parameters of geometrical, material and transport properties, and boundary conditions . . . . .	75
3.3	Radial profiles of oxygen concentration for Case 1 boundary condition (a fixed concentration ( $C_2=0.052 \text{ mol}/m^3$ ) outside adventitia) . . . . .	80
3.4	Radial profiles of oxygen concentration for Case 2 boundary condition (a free diffusion flux B.C. ( $DF=0$ ) outside adventitia) . . . . .	80
3.5	Influence of different thrombus thicknesses on normalised oxygen level inside arterial wall . . . . .	83
3.6	Influence of different oxygen consumption rates $Q_w$ in arterial wall on normalised oxygen concentration across the two-layered model; zero oxygen consumption in thrombus layer . . . . .	84
3.7	Influence of different diffusivities in thrombus layer $D_{th}$ on normalised oxygen concentration across the two-layered model . . . . .	85
3.8	Influence of different diffusivities in arterial wall $D_w$ on normalised oxygen concentration across the two-layered model . . . . .	86
4.1	Workflow of the 1D SGT framework . . . . .	92
4.2	Thrombus formation . . . . .	96
4.3	Illustration of the influence of $k_2$ change on pressure-diameter relationship of arterial model . . . . .	97
4.4	Iteration loop of the coupled G&R and oxygen transport model . . . . .	99
4.5	Prescribed elastin degradation over 10 years (Case 1) . . . . .	103
4.6	Influence of collagen growth rate $\beta$ on the evolution of aneurysm diameter . . . . .	103
4.7	Average oxygen concentration $\overline{C_w}$ at each times step during aneurysm growth and thrombus propagation (Case 1) . . . . .	105

4.8	Collagen growth rate $\beta$ changes over time (Case 1) . . . . .	105
4.9	Collagen parameter $k_2$ along the wall thickness changes during G&R in each time step (Case 1) . . . . .	106
4.10	Normalised mass density of collagen along the wall thickness changes during G&R in each time step (Case 1) . . . . .	106
4.11	Comparison of the $k_2$ evolution between the elements at the innermost layer, outermost layer, and the media-adventitia interface (Case 1) . . . . .	108
4.12	Comparison of the growth of normalised mass density of collagen between the elements at the innermost layer, outermost layer, and the media-adventitia interface (Case 1) . . . . .	108
4.13	Circumferential stress deviation $(\sigma(t) - \sigma_h)/\sigma_h$ at each time step and the comparison between the innermost layer, outermost layer, and the media-adventitia interface (Case 1) . . . . .	109
4.14	Different prescribed elastin degradation in the media and adventitia layers over 10 years (Case 2) . . . . .	111
4.15	Influence of the uniform and non-uniform elastin degradation on aneurysm diameter (Case 1 vs Case 2) . . . . .	112
4.16	The normalised oxygen concentration and collagen growth rate under non-uniform elastin degradation (Case 2) . . . . .	113
4.17	Collagen parameter $k_2$ along the wall thickness changes during G&R with non-uniform elastin degradation in each time step (Case 2) . . . . .	114
4.18	Normalised mass density of collagen along the wall thickness changes during G&R with non-uniform elastin degradation in each time step (Case 2) . . . . .	114
4.19	Comparison of the $k_2$ evolution between the elements at the innermost layer, outermost layer, and the media-adventitia interface (Case 2) . . . . .	115
4.20	Comparison of the growth of normalised mass density of collagen between the elements at the innermost layer, outermost layer, and the media-adventitia interface (Case 2) . . . . .	116
4.21	Circumferential stress deviation $(\sigma(t) - \sigma_h)/\sigma_h$ at each time step and the comparison between the innermost layer, outermost layer, and the media-adventitia interface (Case 2) . . . . .	116
5.1	Illustration of the axisymmetric fusiform aneurysm on the tube model . . . . .	125
5.2	Illustrative models with different degree of the localisation in elastin degradation ( $m_1$ ) . . . . .	125
5.3	Meshes for the mechanical model and transport model of the arterial wall . . . . .	127
5.4	Definition of nodes and paths along the radial direction . . . . .	129
5.5	Axisymmetric elastin degradation in the media layer . . . . .	132

5.6	Axisymmetric elastin degradation in the adventitia layer . . . . .	132
5.7	Axial cross-section of the fusiform model and the thrombus layer within .	133
5.8	Maximum diameter of the fusiform aneurysm at each time step . . . . .	133
5.9	Oxygen concentration in different layers along the axial direction during the aneurysm progression . . . . .	134
5.10	Collagen growth rate $\beta$ along the wall thickness over time at the centre of the fusiform model . . . . .	136
5.11	$k_2$ remodelling at the innermost layer over time of the fusiform model . .	136
5.12	$k_2$ remodelling at the outermost layer over time of the fusiform model . .	137
5.13	$k_2$ remodelling at the media-adventitia interface over time of the fusiform model . . . . .	137
5.14	Normalised collagen mass density at the innermost layer over time of the fusiform model . . . . .	140
5.15	Normalised collagen mass density at the outermost layer over time of the fusiform model . . . . .	140
5.16	Normalised collagen mass density at the media-adventitia interface over time of the fusiform model . . . . .	141
5.17	Influence of the opening angle on the $k_2$ remodelling in different layers .	142
6.1	Geometry of intracranial saccular aneurysm . . . . .	148
6.2	Workflow of the 3D FSGT framework . . . . .	149
6.3	Boundary conditions of human intracranial aneurysm . . . . .	150
6.4	CFD simulation of the 3D IA: WSS distribution . . . . .	150
6.5	The localised region and meshes of the 3D aneurysm model for structural analysis . . . . .	152
6.6	Distribution of constitutive modulus on the extracted aneurysm model .	152
6.7	Saddle surface with normal planes in directions of principal curvatures .	155
6.8	Distribution of principal curvatures on the surface of aneurysm geometry	155
6.9	Spatial evolution of WSS at the inner surface of the aneurysm geometry .	160
6.10	Spatial evolution of normalised mass density of elastin $m_E$ in the aneurysm geometry . . . . .	160
6.11	Comparison of oxygen concentration at the outer surface of the aneurysm at the initial and last time steps . . . . .	161
6.12	A sphere coordinate is placed at the aneurysm bulb to restrict the degra- dation of elastin and collagen within this region . . . . .	163
6.13	A thrombus layer is created at the bulb of aneurysm . . . . .	163
6.14	Comparison of aneurysm enlargements between Case 1 and Case 2 . . . .	166
6.15	Degradation of elastin and collagen . . . . .	167
6.16	Remodelling of first family of collagen fibres $I_4$ . . . . .	168

6.17	Remodelling of second family of collagen fibres $I_6$ . . . . .	169
6.18	Stretches of fibroblasts in the direction of collagen family $I_4$ and $I_6$ in Case 1 and Case 2 . . . . .	171
6.19	Oxygen distribution and corresponding growth parameter $\beta$ for Case 2 at the end state . . . . .	171
6.20	Corresponding mass density of collagen fibres $m_{C2}$ mediated from Fig- ure 6.18 . . . . .	172
6.21	Collective mass density of collagen fibres $m_C$ . . . . .	174
6.22	Effective stiffness of collagen fibres . . . . .	175
7.1	Reconstruction of the hypothetical healthy artery from the geometry of patient-specific IA . . . . .	186
B.1	Reference configuration with an opening angle $\varphi$ . . . . .	202
B.2	Labelling of nodes of one layer in a 3-D domain with $e_r = 8, e_z = 3$ . . . . .	202
B.3	Group the reference nodes (elR=8, elC=100, elZ=3) . . . . .	204
C.1	Comparison of different stress-mediated G&R approaches . . . . .	209
C.2	Comparison of different SEFs on G&R (remodelled based on total stress) .	210
C.3	Comparison of different SEFs on G&R (remodelled based on collagen fi- bre stress) . . . . .	211
C.4	Stress against stretch curves of the two different SEF forms right-shift with decreased $k_2$ values . . . . .	212

## LIST OF TABLES

---

2.1	Geometrical and material parameters for the arterial wall model . . . . .	41
2.2	Comparison of stress values at the innermost and outermost elements with different number of elements (elR) of the ANSYS arterial model . . .	51
2.3	Mechanical cases . . . . .	54
3.1	Experimental values of oxygen consumption rate in physiological models	72
3.2	Comparison of the numerical result generated by different number of el- ements in oxygen transport modelling . . . . .	81
4.1	Parameters used for modelling the aneurysm evolution on the 1D thick- walled model . . . . .	101
5.1	Parameters used for modelling the evolution of fusiform aneurysm . . . .	131
6.1	Material parameters for the 3D aneurysm model . . . . .	153



## ACRONYMS

---

AAA	Abdominal aortic aneurysm
CS	Cyclic stretch
CT	Computed tomography
CFD	Computational fluid dynamics
EC	Endothelial cell
ECM	Extra-cellular matrix
FEM	Finite element method
FSG	Fluid-Solid-Growth
FSGT	Fluid-Solid-Growth-Transport
G&R	Growth and Remodelling
IA	Intracranial aneurysm
ILT	intraluminal thrombus
LDL	low-density lipoprotein
OSI	Oscillatory shear index
SEF	Strain energy function
SGT	Solid-Growth-Transport
SMC	Smooth Muscle Cell
WSS	Wall shear stress



# INTRODUCTION

---

This chapter introduces the aneurysm disease, the need for modelling this disease, and the fundamentals for modelling aneurysm structure (Section 1.1, 1.2 and 1.3). Studies of arterial biomechanics and mechanobiology (Section 1.4) are essential for modelling the evolution of aneurysm. Existing aneurysm models are all based on these studies. Recent researches have been focused on the biochemical transport which is deemed to play a vital role in arterial diseases (Section 1.5), however, there were not many studies regarding to the evolution of aneurysm. Therefore, this research aims to couple the biomechanical and biochemical influences with the application of patient-specific aneurysms. Literature review of the development of computational models can guide us to construct the simulation process and identify what is needed for further improvements (Section 1.6). Summary of this thesis (Section 1.7) gives the general idea of each chapter and a step-by-step procedure to achieve the research goal.

---

## 1.1 MOTIVATION

The rupture of aneurysms, i.e. intracranial aneurysms (IAs), represents the leading cause of devastating, spontaneous subarachnoid hemorrhage in the world. According to statistics from NHS (National Health Service) in the UK, it could be as high as 1 in 20 people be affected by brain aneurysms each year in 2017. If aneurysms rupture, it could lead to severe strokes and disabilities and the fatal rate is high (80%) (Holzapfel et al. (2004); Etminan and Rinkel (2016)) However, there are only a minor portion ( $\leq 1\%$ ) of detected IAs rupture each year (Mandaltsi, 2016). The default

management for detected aneurysms is open surgery which also brings unnecessary risks and costs to remove the stabilised IAs. Therefore it is of great interest to develop diagnostic tools to predict aneurysm progression and identify between stabilised and risky aneurysms. The most challenging part would be the physiological mechanism of the initiation, growth and rupture of aneurysms, all of which still remain unclear. In engineering fields, many researchers attempt to use computational models to simulate the biological responses of arteries (Gasser et al. (2006); Humphrey and Taylor (2008); Watton and Ventikos (2009); Humphrey and Holzapfel (2012)). Growth and remodelling (G&R) of soft tissue such as arterial wall has been studied for several years but it still requires a more comprehensive representation of the complex cell/tissue mechanobiology.

Based on previous studies on vascular biology, this research will provide a computational framework to model the vascular mechanics, biochemical transport, cellular biology and the interaction among them. It aims to build a novel computational tool coupling the influence of mechanical and chemical environments on the progression of aneurysm. Hypotheses of vascular growth and remodelling (G&R) will be implemented in the computational framework that can be compared with available experimental data to improve current understanding of vascular mechanobiology. Furthermore, in order to be more widely accepted, this simulation workflow will be fully integrated into a commercial engineering software to allow for clinical translation by global healthcare technology industries and thus have meaningful impact.

## 1.2 ANEURYSM DISEASE

An aneurysm is a localised, blood-filled balloon-like bulge in the wall of blood vessel. Aneurysms can occur in any blood vessel with three of the most commonly observed aneurysms being classified in terms of location: cerebral/intracranial aneurysms (IAs), thoracic aorta aneurysms (TAAs) and abdominal aorta aneurysms (AAAs). Among these three types of aneurysms, IA and AAA are more frequently discussed in clinical research. Although there are differences between the types of aneurysms due to their positions in the arteries, they still share some common characteristics in the pathogenesis: elastin degradation and collagen adaptation (Humphrey and Taylor, 2008).

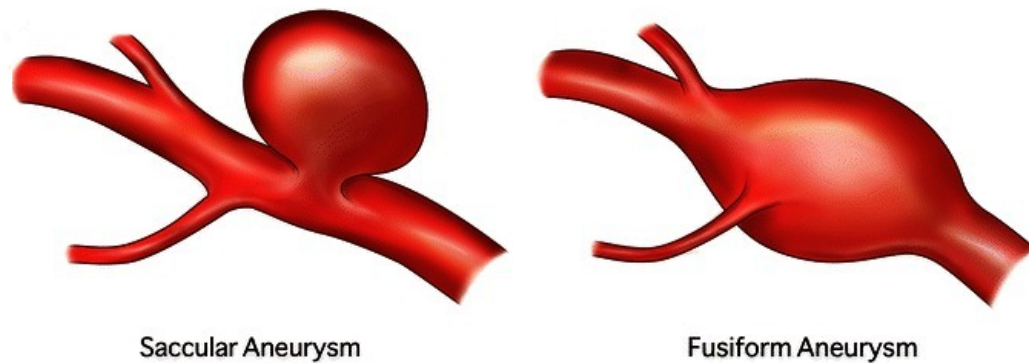


Figure 1.1: Two main types of intracranial aneurysms (image adapted from <https://www.quora.com/What-is-a-brain-aneurysm-and-why-is-it-deadly>).

Aneurysms can also be classified in terms of their general form and shape. Taking IAs for example, there are two main types of IAs in terms of form: saccular and fusiform, as illustrated in Figure 1.1. For saccular IAs (90% of IA cases (Lasheras, 2007)), they are in spherical shape with a neck connecting to the parent vessels, and often filled partially or fully by a thrombus. For fusiform IAs, they are elongated, spindle-shaped dilation of arteries, in which the localised circumference of the vessel is distended. Note that the shape of an aneurysm is not specifically related to certain diseases of arteries but it randomly appears. The precise aetiology of IA inception, development, and potential rupture is still unknown, yet it is assumed to be affected by multiple factors (Caranci et al., 2013). Smoking (Schievink, 1997), older age (Inagawa and Hirano, 1990), female (de Rooij et al., 2007), and hypertension (Tateshima et al., 2007) have been found to increase the risk on aneurysm formation and enlargement. Furthermore, the sites of IAs are generally located at bifurcations and sharp curvatures, especially occurring at the anterior region of the Circle of Willis, which is an anastomotic system of arteries that sits at the base of the brain (Brisman et al., 2006). However, most IAs remain asymptomatic which increases the difficulty for IA detection and prompt treatment before it is too late.

The detection and identification of IAs are generally conducted by modern imaging techniques: computed tomography (CT), magnetic resonance imaging (MRI), and intracranial angiography (Forsting and Wanke, 2008). For a detected IA, relevant treatments normally involve immediate intervention with endovascular or open surgery to stop the blood supply to the aneurysm (Brisman et al. (2006);

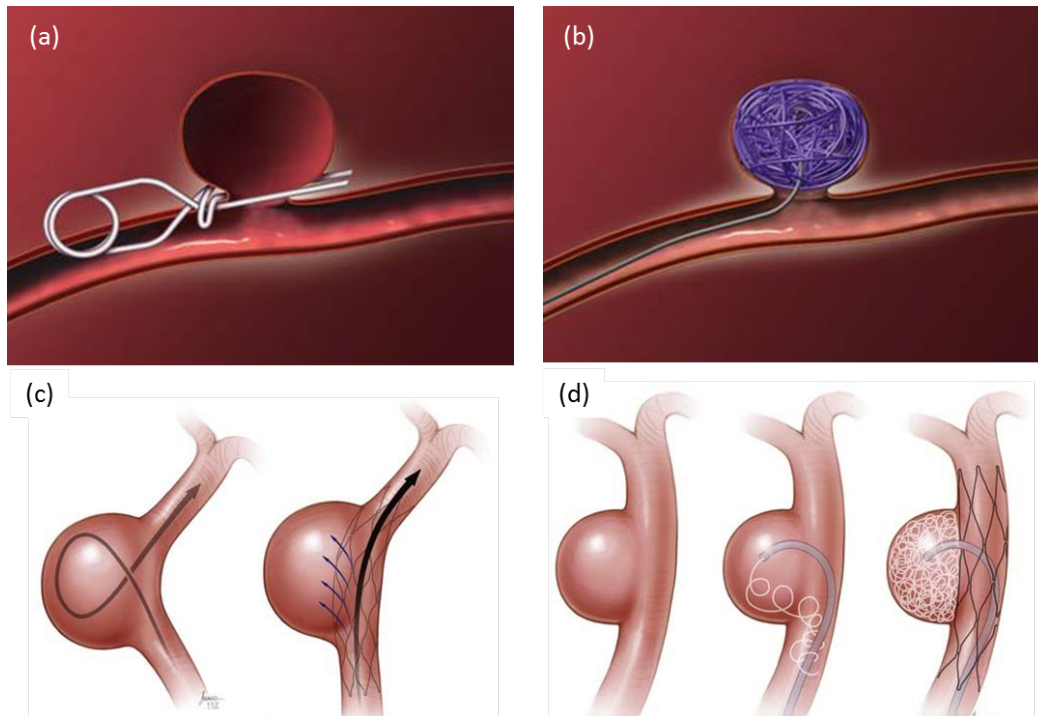


Figure 1.2: Options for treatment of saccular IAs: (a) clipping; (b) coiling; (c) flow diverting stent deployment; (d) combination of coil and stent deployment (images adapted from <http://web.behindthegray.net/articles.html/general/endovascular-coiling-r161/> and <https://neupsykey.com/endovascular-stenting-of-intracranial-aneurysms/>).

Wong et al. (2011)). Major treatments for detected IAs can be categorised in four options as illustrated in Figure 1.2. In Figure 1.2(a), clipping of the aneurysm from the neck by an MRI-compatible alloy is shown, which excludes the aneurysm from blood circulation in the brain (Brisman et al., 2006). Figure 1.2(b) shows an endovascular approach of coil embolisation, which uses a microcatheter to advance into the aneurysm and to place detachable coils to occlude the blood flow from filling the aneurysm (Alshekhlee et al., 2010). The above two methods have been applied to clinical cases for years, and studies have shown that the coiling approach is associated with higher survival rate and better cost-effectiveness compared to clipping (Van Rooij and Sluzewski (2006); Greving et al. (2009)). However, the decision of treatment still depends on aneurysm morphology, clinician's expertise, and patient's preference (Keedy, 2006). Figure 1.2(c) and Figure 1.2(d) demonstrate two stent-based approaches. Figure 1.2(c) shows the deployment of a flow diverting stent, which redirects the blood flow from the aneurysm sac, and allows tissue

overgrowth across the aneurysm neck (Pierot, 2011). In Figure 1.2(d), the stent is deployed as the scaffold to reinforce the coils to be delivered and placed in the aneurysm sac more stable and effectively (Akpek et al., 2005). These stent-based methods are suggested to be suitable for wide-necked and possibly fusiform IAs (Wong et al., 2011).

However, it is of note that approximately 80% of detected aneurysms do not rupture during a person's lifetime (Brisman et al., 2006). Current indicator for clinical decision of rupture risk still relies on statistical observations. For example, it is assumed that there is higher potential of rupture when IA is larger than 10mm (Wiebers et al., 2003). This is clearly insufficient for assessing the risk of rupture on this complex disease. Ideally, it is preferred not to treat aneurysms that are unlikely to rupture to avoid unnecessary risks from surgical interventions (6% morbidity, Park et al. (2005)) as well as expensive costs. Therefore, there is an urgent need for an improved aneurysm management by developing a standard method to differentiate the stable aneurysms from those likely to rupture, for both health and economic benefits.

### **1.3 ARTERIAL STRUCTURE IN HEALTH AND DISEASE**

To investigate the evolution of aneurysms, it is essential to understand the change of biological structure in healthy and diseased arteries. Experimental observations of the biological changes of aneurysms allow us to postulate important factors on aneurysm development and potential rupture. Therefore, the essential first step is to understand the biology of the healthy arterial wall, especially since the arterial tissue is a dynamic living entity, which can adjust itself to changing environments. This section will firstly introduce the arterial biology in healthy state and then provide experimental observations on the changes of arterial structure in IAs.

#### **1.3.1 Architecture of the healthy arterial wall**

It is of note that this section focuses on the biological perspective on arterial histology, while more details of the mechanical perspective on arterial structure will be presented in Section 2.1 to construct the vascular model in the computational framework. Figure 1.3 illustrates the structure of a healthy artery, which generally consists of three different layers: intima, media, and adventitia, from the lumen

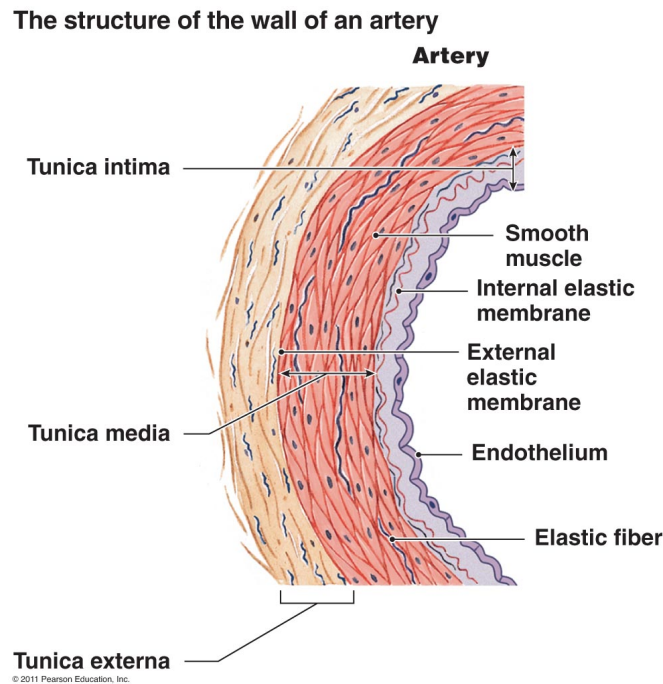


Figure 1.3: Structure of the healthy arterial wall which generally consists of: tunica intima, internal elastic membrane, tunica media, external elastic membrane, and tunical externa (image adapted from <http://www2.highlands.edu/academics/divisions/scipe/biology/faculty/harnden/2122/notes/cvbw.htm>).

towards the external surfaces respectively. Each layer has its own function and different cells embedded in.

The innermost layer is the tunica intima layer which normally consists of a monolayer of endothelial cells (ECs) and subendothelial connective tissue, and is supported by the internal elastic membrane. The ECs are directly in contact with the lumen area, and the alignment of ECs is influenced by the blood flow direction, whereby controls the passage of material between the vessel lumen and the arterial wall (Langille and Adamson, 1981). The ECs also regulate various biochemical pathways for maintaining vascular homeostasis such as the balance between vasodilators and vasoconstrictors, and the reaction to inflammation and angiogenesis in wound healing (Traub and Berk (1998); Eroschenko and Di Fiore (2013)).

The tunica media is the middle layer and generally the thickest among the three main layers. This middle layer generally consists of smooth muscle cells (SMCs), which are surrounded by the extracellular matrix (ECM). The ECM is comprised of various types of elastin, collagen fibres, and proteoglycans. The elastin and collagen

fibres are the load-bearing vascular constituents that contribute significantly to the mechanical strength of vessel wall (Shadwick, 1999). The main function of SMCs is to regulate the diameter of the artery and maintain ECM structure. SMCs contract or relax actively to change the vessel's diameter for maintaining vascular mechanical homeostasis in blood flow and redistributing the blood to areas where needed. Moreover, SMCs synthesise and secrete the elastin constituent to the ECM, which is deemed to have structural impact on aneurysm formation and enlargement (Kondo et al. (1998); Lee et al. (2001)).

The tunica externa layer (adventitia) is the outermost layer and mainly composed of fibroblast cells, collagen fibres, and ground substance. Fibroblasts regulate the production of collagen fibres, which help to maintain the structural integrity of vascular tissue. Hence the collagen synthesis is also deemed to play a key role during aneurysm evolution.

To summarise, the primary function of SMCs and fibroblasts within the vascular layers is to maintain the structure of the artery. The communication between ECs, SMCs, and fibroblasts also plays a critical role in the structural regulation in healthy and diseased arteries.

### 1.3.2 Aneurysm structure

Figure 1.4 illustrates the structural difference between healthy and diseased cerebral arteries. It is of note that the media layer and the SMCs are almost replaced by collagen fibres after the development of an IA. This histopathological characteristic is based on a general observation in cerebral aneurysm tissue (Zhang et al. (2003); Brisman et al. (2006)). The abnormal structure within the aneurysm wall shows a lack of elastic membrane and supporting tissue, and the elastin is sparsely distributed or completely lost (Finlay et al., 1998). The collagen turnover rate is deemed to be an important factor in the assessment of rupture risk, as collagen fibres become the main load bearer in the aneurysm structure (Mitchell and Jakubowski, 2000), e.g. newly formed aneurysms may have higher risk of rupture because new collagen is not attached to the ECM in time to compensate the loss of previous destroyed collagen.

Furthermore, Frösen et al. (2004) indicated that the identification of the histopathological profile of aneurysms would be the key for the assessment of po-

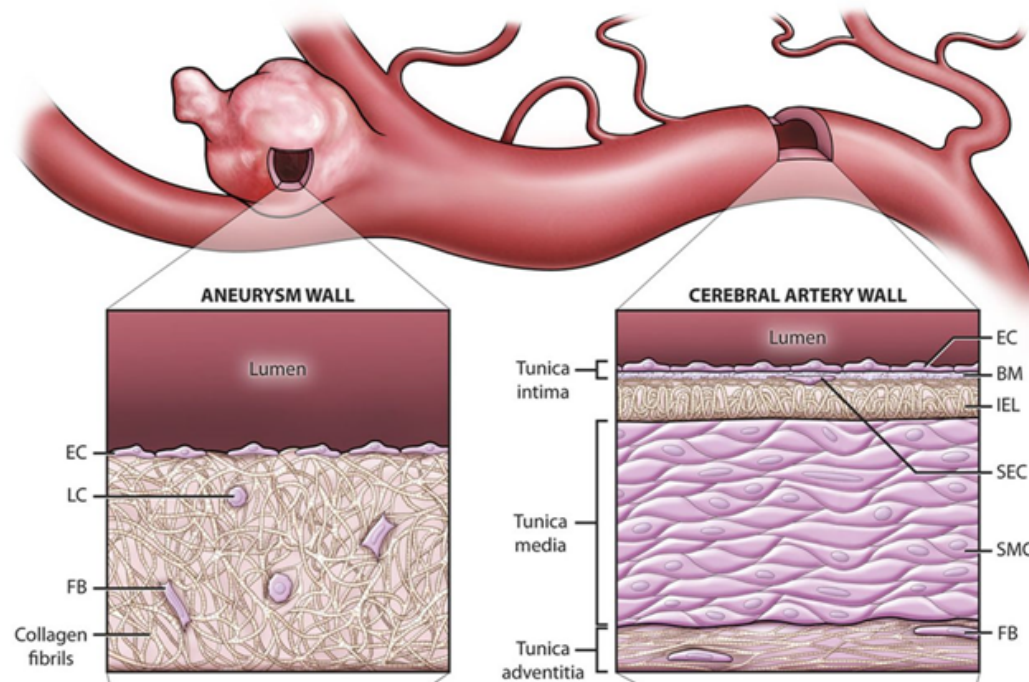


Figure 1.4: Structural comparison between the healthy arterial wall and aneurysm wall (image adapted from Etminan et al. (2014)).

tential rupture. Some aneurysm groups were still found with layers of SMCs and intact endothelial layer, while others showed a dispersed network of SMCs or a significant decrease in SMCs. However, aneurysm disease is generally associated with many other vascular pathologies, including intramural haemorrhage, immunodeficiency, and trauma (Krings et al., 2011), thus it is also crucial to identify important biological features with the bio-complexity for the development of aneurysms.

## 1.4 ARTERIAL BIOMECHANICS AND MECHANOBIOLOGY

This section introduces the biomechanical characteristics of arterial tissue and the interaction between vascular biology and mechanics, which need to be considered when modelling the evolution of aneurysms.

### 1.4.1 Biomechanics of the vessel wall

Arteries have very unique and different mechanical properties compared to common solid materials such as steel. This is mainly due to the fact that vessels are dynamic and living tissues consist of vascular constituents and vascular cells, which

continuously deposit and degrade during life time. Therefore, from a mechanical perspective, vascular structure can be considered as a fibre-reinforced composite material, which would react to local conditions and changes over time. The specific mechanical properties of the arterial wall can be categorised as follows:

- **Nonlinearity**

The nonlinear mechanical response of an artery is the consequence of the composite contribution from different types of load-bearing constituents. At lower strain, the elastin constituents are the main load bearer and govern the mechanical response in a linear manner. The collagen fibres are initially crimped and not bearing the load at lower strain. While at higher strain, the collagen fibres are stretched and begin to bear the major load, which present an exponential stiffening effect (Shadwick, 1999).

- **Anisotropy**

The mechanical behaviour of vessel wall is commonly deemed to be anisotropic with respect to the axial and circumferential directions with experimental evidence on both humans and animals. From a modelling perspective, this anisotropic behaviour is characterised by the orientations of the collagen fibres for the resistance to stretch at high pressures in different directions (Holzapfel et al., 2000).

- **Residual stress**

Experiments on arterial tissue ((Chuong and Fung, 1986); Fung and Liu (1992)) have shown that when an unloaded artery is cut transversally it contracts along the axial direction, which proves the existence of an internal stress field in the physiological state. Also, when the cut is made longitudinally in an arterial ring, it opens releasing circumferential stresses. These experimental observations imply the existence of residual stresses within the arterial wall, and the load-free state of an artery is not in a zero-stress state.

- **Heterogeneity**

The heterogeneity of an artery is due to the specific layered mechanical properties within the vessel wall. The media and adventitia layers are the primary load-bearing components, while each layer has individual material modulus of elastin and collagen (Holzapfel et al., 2000). The media is normally stiffer

than the adventitia at lower strain with greater elastin modulus. While at higher strain, both layers respond similarly with more collagen fibres being stretched and contributed to the mechanical equilibrium (Sommer, 2008). It is of note that the material properties of vascular constituents vary in different types of arteries, and also adapt to the changes of physiological conditions such as intense exercise, age, and disease.

- **Incompressibility**

For a healthy artery, it is a common assumption that the arterial material is incompressible due to the high water content within the wall (70% ~ 80%) (Sommer, 2008).

- **Viscoelasticity**

The arterial tissue exhibits elastic and a certain level of viscous characteristic when undergoing deformation. This is demonstrated by experiments on arterial creep and stress relaxation, as well as hysteresis in arteries under cyclic loads (Gasser et al., 2006).

- **Active mechanical response**

The elastin and collagen constituents provide the passive mechanical responses of the vascular structure. Additionally, SMCs would actively contract or relax to change the diameter of vessel in order to maintain the vascular homeostasis of local blood pressure.

Overall, the mechanical behaviour of arteries generally show the characteristics of nonlinearity, anisotropy, heterogeneity, and incompressibility in a spatial layered-specific manner. These characteristics are essential to be included when modelling the arterial structure, in both healthy and diseased states.

### 1.4.2 Arterial Mechanobiology

Mechanobiology is the study of the effects of physical cues such as applied forces on cell behaviour. In arteries, growth and remodelling (G&R) involve activation of intramural cells by chemical and mechanical stimuli such as blood pressure and shear stress, leading to deposition and degradation of tissue components (Humphrey, 2008). G&R processes are invoked by developmental, physiological (maintenance and ageing), pathological phenomena (disease and injury) and even environmental

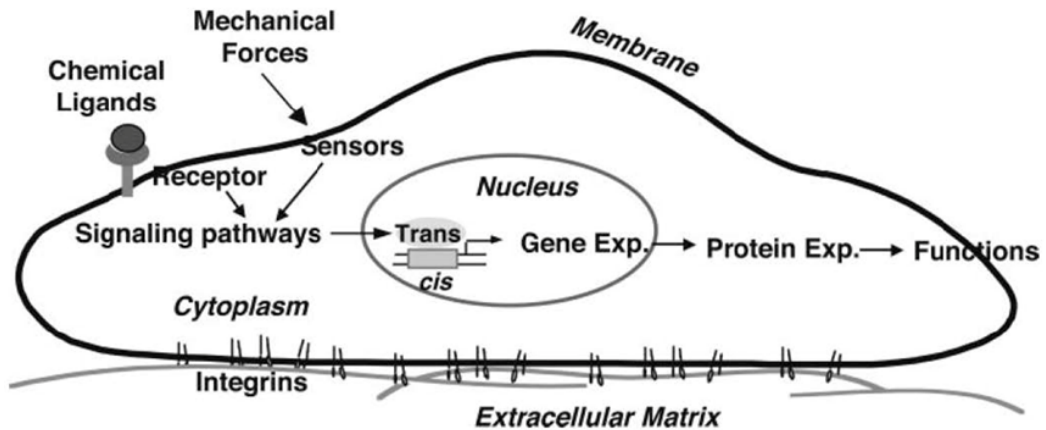


Figure 1.5: Activation of cellular signalling pathways in response to the extracellular mechanical triggers (image adapted from Chien (2007)).

adaptations. Many of the aforementioned processes are associated with alterations in arterial loads, suggesting the involvement of mechanical homeostasis. Hence, it is important to investigate the mechanobiology in both healthy condition and aneurysm disease, not only for a better understanding of the aetiology of the disease but also for establishing more accurate and reliable diagnostic criteria.

The arterial wall is a highly dynamic tissue with remarkable capabilities such that through genetic and biochemical processes, its properties can adjust to maintain or restore vascular homeostasis (Robertson and Watton, 2013). Cells in these tissues play a major role in the G&R processes (Humphrey et al., 2015). Mechanical stimuli can be transduced from ECM to cells via receptors, which then activate cellular signalling pathways essential for homeostasis regulation. Such process is termed mechanotransduction (Figure 1.5). Since haemodynamic and biological stimuli interrupt with the local arterial homeostasis as well as the arterial remodelling needed for the restoration of homeostasis (Humphrey, 2009), the failure to maintain or restore mechanical homeostasis may potentially contribute to progression of aneurysm.

ECs are important in vascular physiology and pathophysiology (Nerem, 1993). Just like many other types of cells, ECs are surrounded by a complex mechanical loading environment. The endothelium forms the inner lining of the arterial wall and is directly exposed to blood flow, hence experiencing direct influences from hemodynamic forces. Cyclic strain due to vessel wall distension, and shear stress

resulting from frictional forces caused by blood flow, i.e. wall shear stress (WSS), are pivotal mechanical forces that influence the structure and functions of EC (Wang and Thampatty, 2006). Differential EC responses to WSS have been demonstrated, such that WSS of different magnitudes, directions, and even spatial and temporal gradients, can alter the EC form and functions (Hoffman et al. (2011); Meng et al. (2011)). Interestingly, studies have suggested the effect of the direction of WSS and cyclic stretch on EC morphology. Alterations in morphology in turn influence the EC permeability (Cummins et al., 2007). Disturbed flow could produce an inflammatory effect on the arterial wall, in which the altered permeability of EC allows greater penetration of macromolecules (Chiu and Chien (2011); Chien (2007)). Notably, alterations in molecular homeostasis have been linked to aneurysm disease (Kassam et al., 2004). On the other hand, SMCs are mainly influenced by cyclic stretch resulting from pulsatile changes in blood pressure (Haga et al. (2007); Li and Xu (2007)). Adventitial fibroblasts are surrounded by ECM and are more prone to strains during the cardiac cycle (Wang and Thampatty, 2006). Structural protein collagen is the most abundant component of ECM. It is also one of the many components of ECM produced by fibroblasts. There are indications that WSS heterogeneities might have a local effect on collagen production (Rodriguez-Feo et al., 2005).

## **1.5 ADAPTIVE RESPONSES TO BIOCHEMICAL TRANSPORT THROUGH THE ARTERIAL WALL**

### **1.5.1 Motivation**

Most G&R models of aneurysms have focused either on the mechanical clues or the haemodynamics within the lesion (Humphrey and Taylor (2008); Wilson et al. (2013)). However, very few studies look into the biochemical influence on the evolution of aneurysms (Holland (2012); Virag et al. (2015); Aparício et al. (2016)). Due to the chemo-mechano-biological complexity of an aneurysm, it is essential to consider multi-factorial and multi-physical factors when modelling the aneurysm evolution. Therefore, the goal of this research is to develop the first computational framework to predict the aneurysm evolution by quantifying the interrelationship of biomechanical responses and biochemical transport on arterial tissues. This integrated G&R model has the promise to improve our understanding of the underlying mechanisms of aneurysm growth, to encourage the design of experiments on vas-

cular tissues, and to advance the prediction of aneurysm enlargement and risk of rupture.

Most studies related to biochemical transport in arteries have been focused on atherosclerosis, where the continuing accumulation of LDL and the adaptive SMCs proliferation create a plaque which leads to the chronic stenosis of the lumen (Guyton and Klemp, 1989). Consequently, modelling the mass transport of corresponding molecules has become the leading trend of the study. The density of LDL (Wada and Karino (1999); Ueda et al. (2004); Sun et al. (2007)) and oxygen (Back (1976); Moore and Ethier (1997); Qiu et al. (2000); Kaazempur-Mofrad et al. (2005)) in the arteries are deemed to play key roles in the formation of atherosclerosis. These studies suggest and provide the fundamental of solute transport modelling in arterial diseases, as the arterial constituents are highly regulated by the local level of biochemical substances. Motivated by the transport modelling of atherosclerosis and the review of AAA growth (Wilson et al., 2013), the idea of combining the effect of chemical transport with previously proposed G&R models of the evolving mechanical behaviour of aneurysm wall is studied in this thesis.

### **1.5.2 Mass transport within arterial wall**

Tarbell (2003) reviewed and analysed mass transport in arteries and the localisation of atherosclerosis. Four mechanisms of mass transport (blood phase controlled hypoxia, leaky endothelial junctions, transient intercellular junction remodelling, and convective clearance of the subendothelial intima and media) are critical for evaluating the localisation of atherosclerosis. Endothelial permeability is controlled by the first three mechanisms such that transport of larger molecules, e.g. LDL, is highly regulated, while transport of smaller molecules, e.g. oxygen, is relatively more permeable through ECs.

The development of computational modelling of mass transport began with a fluid-wall modelling applied on an axisymmetric geometry to determine the LDL accumulation (Wada and Karino (1999); Ueda et al. (2004); Sun et al. (2007)). Further studies focused on the application of clinical geometry for the evaluation of EC permeability (Malek et al. (1999); Himburg et al. (2004)) and the comparison between the modelling results and the *in vivo* data for the location of atherosclerosis (Díaz-Zuccarini et al. (2014); Di Tomaso et al. (2015)). For the application of transport modelling on aneurysms, Sun et al. (2009) presented a computational analysis

of oxygen transport in a patient-specific model of AAA with intraluminal thrombus. Intraluminal thrombus which is found in 75% of all AAAs has been shown to substantially attenuate oxygen transport from lumen to aneurysm wall, resulting in further degeneration of aneurysm. A blood-thrombus-wall model was developed to demonstrate the profound influence of the presence of thrombus on oxygen concentration in the wall. Result shows that oxygen supply is reduced by 80% from lumen to the wall if thrombus thickness is greater than 5mm. Promising results from these studies suggest the potential to improve the therapeutic strategies for arterial diseases. Additionally, mass transport modelling is important in medical application. An example is drug delivery. Transport modelling has recently can be utilised in the design of drug-eluting stent to prevent restenosis after stent placement (Pontrelli and de Monte, 2007).

### 1.5.3 Adaptive responses to hypoxic environments

The influence of oxygen availability on the adaptive response of arterial tissue is set up as the example of biochemical influence for the development of the computational framework throughout this thesis. This section introduces an unfavourable environment, hypoxia, which significantly affects the functionality of arterial cells and tissues, and motivates the consideration of oxygen effects during aneurysm evolution. The blood flow circulation transports nutrients and oxygen to cells and tissues in the body and takes away metabolic products by a diffusion-based exchange mechanism. In the cardiovascular system, oxygen plays an important role as arterial cells are particularly sensitive to fluctuations in oxygen availability and have a corresponding mechanism to restore the normoxic condition. If the hypoxic condition continues, this could result in cell dysfunction or ultimately death.

All physiological mechanisms require aerobic and metabolic reactions for generating energy to function. Under an intermittent hypoxic condition, cells will adjust the metabolic respiration in order to achieve oxygen conformance, which is a decrease in oxygen consumption within cells. In other words, the demand for cellular energy is downgraded to a minimum requirement as an adaptive response to the hypoxic condition (Rissanen et al., 2006). More importantly, low oxygen levels have a significant effect on cell functionality. An experimental observation (Ray et al., 2008) found that when the rat aortic SMCs are continuously exposed to a low oxygen environment, the rates of SMC proliferation and apoptosis increase. Also,

hypoxia would affect SMC functionality in collagen synthesis. Pietilä and Jaakkola (1984) observed that rabbit aortic SMCs would decrease their collagen synthesis rate to approximately 50% in the hypoxia compared to the control group in normoxia. Furthermore, the production of collagen by fibroblasts was downregulated after 48 hours exposure to low oxygen level (0-2%) (Steinbrech et al., 1999).

Therefore, the hypoxic condition could lead to cell dysfunction, excessive SMCs apoptosis, and reduction in collagen deposition, which could have the potential to influence vascular adaptation on aneurysm evolution. Vorp et al. (2001) suggested that intraluminal thrombus within an AAA would possibly attenuate oxygen diffusion to the arterial wall causing localised hypoxia or wall weakening. This thesis would address this hypothesis that the presence of thrombus layer leads to cellular hypoxia and diminishes the wall strength, which may further result in wall weakening and increased potential for rupture.

## 1.6 REVIEW OF THE *in silico* MODELLING

Experimental models (*in vivo*, *in vitro*) on vascular tissues have provided valuable information on arterial physiology and pathophysiological mechanobiology, however, the underlying mechanisms are still poorly understood. To represent and quantify the local mechanical responses of the arterial wall, mathematical and computational (*in silico*) models are a useful tool. With the representation of mechanical responses, further applications of the computational models involve simulations of the adaptation and evolution in vascular structure and cell functionality, and the inception and growth of arterial diseases. In this thesis, we focus on the development of computational modelling on the progression of aneurysms. Therefore, it is important to investigate what has been achieved with *in silico* approaches in aneurysm evolution.

A mathematical approach to describe the biomechanical instability in aneurysm rupture with nonlinear elastic analysis was proposed by (Akkas, 1990). For mechanical modelling purposes, the strain energy function (SEF) term was implemented in a 1D model to illustrate the mechanical behaviour of the arterial wall. The mathematical analysis was validated with experimental data of axisymmetrically inflated biomembranes for measuring mechanical strains under various pressures (Hsu et al., 1995). This approach was then updated by using finite element

methods (FEM) to study the local properties for the anisotropic characteristic of arterial tissue (Seshaiyer et al., 2001). Both analytical (Humphrey and Kyriacou (1996); Haslach and Humphrey (2004)) and numerical (Shah and Humphrey, 1999) methods were applied to investigate the dynamic stability of aneurysm enlargement with spherical models. For realistic applications on clinical aneurysms, a methodology of nonlinear, anisotropic, and static structural analysis was developed in order to achieve a more accurate estimation of wall stress in the 3D geometry of saccular IAs, and to study the potential role of wall stress in aneurysm rupture (Ma et al., 2007). Furthermore, the concept of regional variation in remodelling of material parameters of an aneurysm was proposed by the hypothesis that collagen remodels in an attempt to restore its local stress field to a homeostatic value (Ryan and Humphrey, 1999).

Watton et al. (2004) developed the first mathematical framework to model aneurysm evolution with the application of AAA, in which the evolution of vascular microstructure and composition is simulated under the assumption that new collagen fibres are deposited to the ECM with an attachment stretch. This framework has also been applied to model the evolution of IAs (Watton and Ventikos (2009); (Watton et al., 2009b)), and extended to couple the G&R in response to local haemodynamic stimuli (Watton et al., 2009a) to form a fluid-solid-growth (FSG) computational framework as illustrated in Figure 1.6. This FSG framework was integrated into physiological aneurysm geometries, and the G&R approach was further linked to the cyclic stretch (CS) stimuli (Aparicio et al. (2014); Selimovic et al. (2014)), the volumetric changes (Eriksson et al., 2014), and the transmural variation through arterial wall thickness (Grytsan et al., 2015).

In soft tissue modelling, Humphrey and Rajagopal (2002) proposed a constrained mixture theory for G&R under the basis that new constituents are likely to be deposited with a level of "deposition stress". A subsequent study was conducted by a 2D model for the adaptation of collagen constituents with different evolving properties and configurations to represent the aneurysm growth (Gleason Jr and Humphrey, 2005). This mathematical G&R algorithm has been further implemented in theoretical models: the enlargement of idealised fusiform IAs (Baek et al., 2006), cerebral vasospasm (Baek et al., 2007), and arterial adaptation of altered blood flow and pressure (Valentín and Humphrey, 2009). A multilayered wall model (Karšaj and Humphrey, 2012) was proposed to suggest other important met-

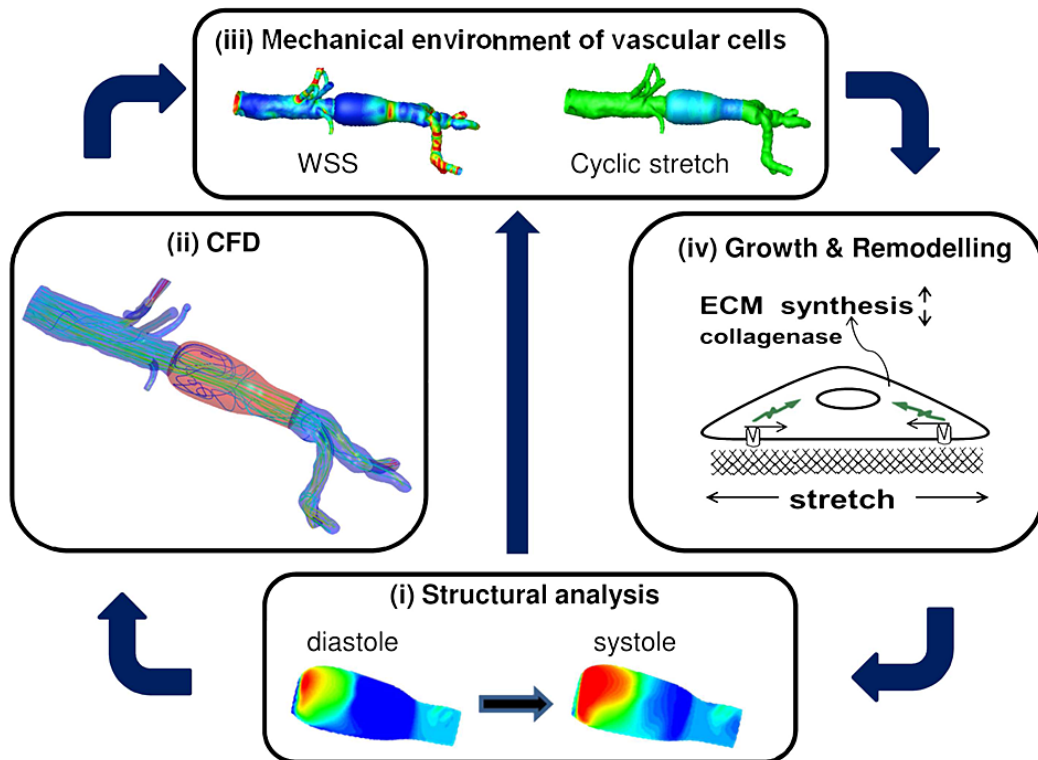


Figure 1.6: Fluid-Solid-Growth (FSG) framework for modelling the mechanobiology of vascular disease evolution (image adapted from Aparicio et al. (2014)): Modelling cycle– (i) structural analysis solves systolic/diastolic deformation fields; (ii) AAA geometry is integrated into a larger physiological domain. The volume domain is automatically meshed with ANSYS ICEM; physiological boundary conditions are applied; flow solved with ANSYS CFX. (iii) CFD/structural analyses export spatial distributions of the mechanical stimuli; (iv) G&R algorithms simulate cells responding to mechanical stimuli. The constitutive model of the tissue evolves. The cycle (i-iv) continues and as the tissue adapts an AAA evolves.

rics such as residual stress and transmural variation inside the arterial wall, which are fundamental to mechanical homeostasis and response to changes.

The G&R approaches mentioned above all focused on the mechanics of arterial wall and its relation to the G&R of vascular constituents. Recently, research has been focused on the biochemical influence and its interplay with mechanobiology on vascular diseases, especially on modelling the mass transport of biomolecules and its relation to cell behaviour and vascular tissue (Lambrechts et al. (2012); Bjork et al. (2012)). Wilson et al. (2013) reviewed the diffusion of biochemical transport in AAA binding to EC permeability. He suggested that the intraluminal thrombus inside AAA is biological active and the evolving mechanics of the wall highly depends

on biochemical effects of the adjacent thrombus. An extended study (Virag et al., 2015) presented a mathematical model to couple biomechanical and biochemical effects of intraluminal thrombus on the enlargement of AAAs, which supports the idea that ILT is biologically active (i.e. release of proteases). The G&R approach of this model adapts the constrained mixture method coupling with the effect of protease diffusion within the wall. Additionally, Virag et al. (2018) investigated parameter values under physiological range for the potential of different model predictions. The extended parameter study is useful to recognise the important features of AAA evolution and the key factors of the risk of rupture. Aparício et al. (2016) also proposed a mathematical model of arterial chemo-mechano-biology to describe the complex interplay between biomechanical and biochemical stimuli with the application of aneurysm growth. The collagen remodelling is based on Watton's stretch-mediated G&R method. While the collagen growth is represented by a biochemical pathway model, in which the fibroblast properties are regulated by the level of key biomolecule (TransformingGrowthFactor(TGF)- $\beta$ ). The mechanotransduction of TGF- $\beta$  is influenced by the deviation of mechanical stretch from homeostatic level. Results of this model demonstrate different modes of aneurysm growth. More importantly, the enlargement of aneurysm is stabilised with the increasing level of collagen promoting TGF- $\beta$ , which is consistent with the experimental observation.

These chemo-mechano-biological models mentioned above focused on the coupling between the mechanical responses and molecular level within the tissue, while EC permeability is an important aspect when modelling molecular transport from endothelium to the wall. Goodman et al. (2016) proposed a mathematical model to relate the WSS-dependent endothelium permeability, low-density lipoprotein (LDL) transport, and intimal thickening (hyperplasia) of arterial wall together. The main concept is that the hyperplasia occurs as a result of excess oxidised LDL, which then interrupts with blood flow, influencing the endothelial permeability through WSS. The model investigated the fluctuations of the lesion shape over time, and how this influenced WSS, influx rates of LDL as well as how sensitive these processes were to the oxidation parameters. Findings showed a downstream propagation of the lesion caused by high and low WSS, which lasted for a certain period of time after the disappearance of the hotspot, providing plenty of time for additional pro-atherogenic processes. For applications on patient-specific geometries, Alimohammadi et al. (2017) presented a mathematical model to understand atherosclerosis formation such that a multifactorial multiscale modelling approach

was employed to estimate the locations of vessel wall calcification and plaque formation. Remodelling of arteries occur during atherogenesis, leading to lipid accumulations (LDL cholesterol) known as plaques in the inner lining of arteries. Indications have demonstrated an association of the lipid accumulation with the site of endothelial mechanotransduction, a complex process involving biomechanical and biochemical processes. In view of this, the model provided by Alimohammadi et al. offered a comprehensive way to demonstrate an integrated framework explaining the interplay between mechanics and biology. Notably, a combined index called HOLMES was used to underscore locations with highly oscillatory, low-magnitude WSS, and results were in line with other findings (Alimohammadi et al., 2016) which suggested the detrimental effects of such WSS environment on the endothelium. The model also successfully identified the majority of both the plaque regions and plaque-absent regions obtained from computed tomography (CT) scan. Therefore, another key message delivered by this model is that instead of merely focusing on the mechanics or the biology, mathematical modelling which takes into account the biological multiscale, multifactorial processes and mechanisms, is a more effective way to simulate cardiovascular diseases.

A detailed review of arterial multiphysics is done by Marino et al. (2017a), where the importance of molecular transport phenomenon affecting the tissue inflammatory state and biological structure is emphasised. Marino et al. (2017b) then proposed a state-of-the-art chemo-mechano-biological framework which accounts for the remodelling of arterial tissue and the diffusion of molecules involved in cell-cell signalling pathways. This model utilises a simple axisymmetric geometry for analytical solutions to introduce the coupling framework. The biochemical transport within the arterial wall is defined as an advection-diffusion-reaction problem for each active molecule, i.e. matrix metalloproteinases (MMPs) and TGF- $\beta$ , which regulate ECM degradation and deposition. The remodelling mechanism is driven by the alteration of structural feature (arterial radius) and molecular concentration from the homeostatic state. Volume fraction of elastin and collagen, collagen fibre radius, and structural stiffness are remodelled based on this strategy. Despite the simplified geometry setting, this model addresses a case study which shows the effect of vascular remodelling induced by molecular transport and mechanical equilibrium. More importantly, the result is able to capture the arterial dilation as a consequence of change in biochemical environment, in which shows the potential to be applied on modelling aneurysm diseases.

To summarise, in the development of *in silico* aneurysm models, many efforts are focused on simulating the adaptation and composition of arterial structure during the evolution of vascular diseases. These models are used to elucidate vascular mechanobiology and to quantify mechanical factors on remodelling the vascular structure. Nonetheless, it is essential to point out current limitations of the existing aneurysm models to address the direction of further improvements. Major limitations of the state-of-the-art computational framework for modelling aneurysm evolution are listed as below:

- Most mathematical frameworks on modelling aneurysm structure utilised either conceptual geometries, membrane formulations or simplified axisymmetric motions. The limitation of a membrane model is that it assumes constant properties in each layer which is not true in real cases.
- Existing FSG methodologies focused on the mechanical responses on arterial tissues (e.g. wall stress, fibre stretch, and flow condition), while there is very few *in silico* models investigate the biochemical effect on aneurysm progression.
- There is no chemo-mechano-biological framework applied on a patient-specific aneurysm geometry. The state-of-the-art coupling framework developed for modelling aneurysm evolution utilised simple geometries for the demonstration of the G&R method.
- The evolution process of healthy-to-pathological state of aneurysm is difficult to obtain. In clinical cases, most aneurysms remains asymptomatic until the physical condition of the patient is severe or the final rupture. Therefore, although the FSG model provides a useful tool to understand the underlying mechanisms for the aneurysm development, it is inadequate to assist therapeutic schemes in clinical applications.

This thesis would target on these issues to establish an advanced computational framework specifically designated for modelling the aneurysm progression.

## 1.7 OVERVIEW OF THESIS

This section briefly introduces the main components (by chapters) to develop a novel chemo-mechano-biology computational framework, which takes into account the influence of local mechanical responses and chemical levels on aneurysm evolution. As mentioned in the previous section, most *in silico* models of aneurysms focused on the mechanical effect, thus the novelty of this research is to include the chemical effect, i.e. oxygen level, into the G&R approach and with the application on an anatomical aneurysm geometry. Furthermore, the whole workflow of the computational framework is fully integrated in the ANSYS engineering software, which enables the direct interplay and communication between the mechanical and chemical environments. The outline of each chapter is presented below:

- **Chapter 2:** A two-layered thick-walled fibre-reinforced tube structure is established to represent a healthy artery, which is based on the constitutive framework for arterial wall mechanics proposed by Holzapfel et al. (2000). The residual stress is included to represent the physiological stress distribution within the vessel wall, whereby the zero-stress, load-free, and loaded configurations of the arterial model are defined. The influence of residual stress on the mechanical response is characterised by the opening angle method (Fung and Chuong, 1983). This model is integrated into the ANSYS software and the result is validated with analytical solutions in pressure-diameter relationship. Different mechanical cases are conducted to investigate the influence of material parameters and blood pressures on the mechanical response within the arterial wall. In this thesis, the aneurysm development begins with the microstructural change of the healthy arterial model, and the G&R method is associated with the disturbance of the physiological stress level.
- **Chapter 3:** Oxygen concentration within the arterial wall is used as the example for modelling the chemical influence on aneurysm evolution for the proposed computational framework. Therefore, this chapter introduces the modelling of oxygen transport through a diseased (thrombosed) arterial model. The oxygen transport properties are based on the review of experimental observations in healthy and thrombosed arteries (Vorp et al., 2001). A diffusion-only analytical derivation is conducted to describe the oxygen concentration through the thrombus layer and arterial wall in a steady state analysis. The nu-

merical simulation of oxygen transport is implemented in the diffusion model in ANSYS and the numerical results are validated with the analytical solution. A further investigation of the influence of thrombus thicknesses and oxygen transport properties on oxygen distribution is conducted in the ANSYS numerical model.

- **Chapter 4:** This chapter presents a novel chemo-mechano-biological computational framework with the application on a simple 1D cylindrical model, which focuses on the solid-growth-transport (SGT) interaction in aneurysm evolution. The mechanical and chemical environments for the healthy vascular model are defined as the homeostatic conditions as the adaptive basis for vascular G&R. A prescribed elastin degradation along the axial direction initiates the radial enlargement of the model, and the thrombus propagates to deter the oxygen delivered to the arterial wall. The hypothetical G&R method is implemented to model the adaptive response of collagen constituents, in which the collagen parameters are remodelled according to the stress deviation from the homeostatic level and the collagen growth rate is affected by the local oxygen level. Results demonstrate the modelling behaviour of the SGT framework including localised responses through the arterial wall.
- **Chapter 5:** This chapter extends the SGT framework on a 2D axisymmetric fusiform model to emphasise the spatial variation of the G&R response. The fusiform aneurysm is formed by a prescribed axisymmetric elastin degradation in the axial direction of the arterial tube model. Due to the geometrical effect, the mechanical and chemical environments are characterised with spatial variation in both axial and radial directions.
- **Chapter 6:** This chapter demonstrates the FSGT framework with the application on a clinical aneurysm geometry. The G&R methodology is integrated from previous chapters with an update in the representation of cell/tissue interaction. A thrombus is generated on the aneurysm geometry in order to investigate its influence on oxygen transport and the associated effect on aneurysm progression. Illustrative results of the FSGT model present potential indices to examine the stability of the aneurysm.
- **Chapter 7:** The final chapter summarises the findings from previous chapters and discusses potential improvements to the computational framework

in order to have a more comprehensive tool for investigating the underlying mechanisms of arterial diseases.



## STRUCTURAL MODEL OF ARTERIAL WALL

---

This chapter presents the constitutive model of an arterial wall with the simulation of mechanical responses in a continuum mechanics base. A general description of arterial histology of vessel wall is provided in Section 2.1. Section 2.2 describes the essential findings of residual stresses existing in the vessel wall and emphasises its importance on the physiological homeostatic state of arteries. The opening angle method (Chuong and Fung, 1986) is introduced to quantify the amount of residual stresses within the vessel wall and demonstrated in the later sections. Following the introduction of arterial structure and its mechanical behaviour, the arterial model is constructed in Section 2.3 based on the mechanical properties of biological tissues treated from the continuum mechanical perspective. A specific strain energy function which describes the nonlinear and hyperelastic characteristics of mechanical responses in arterial layers is presented. Section 2.4 shows the implementation of the mathematical model presented in Section 2.3 to the numerical model developed in the ANSYS software. A thick-walled cylindrical model which takes into account the transmural variation through the wall thickness is built in the modelling framework. This thick-walled model is then applied with different opening angles to illustrate the influence of residual stresses on the circumferential stress along the radial position of arterial wall. A series of sensitivity analyses on geometrical mesh and mechanical behaviour for the ANSYS model is conducted. As a result, this computational framework provides a general platform which enables the representation of realistic distributions of mechanical forces in arteries.

---

**Objective:** the objective of this chapter is to model the mechanical responses of the arterial structure by the numerical implementation of ANSYS software. This vascular solid model will then be coupled in the proposed G&R framework to simulate the mechanical structure of the aneurysm wall in each time step during aneurysm

evolution. The change of mechanical stress responses within the aneurysm wall is the key for the G&R approach of the computational framework.

The whole modelling framework begins with building a healthy artery based on the mathematical description proposed by Holzapfel et al. (2000). The artery is modelled as a thick-walled, non-linearly elastic cylindrical tube consisting of multiple layers. Each layer is treated as a fibre-reinforced material with the fibres corresponding to the collagenous components. With a reliable constitutive model, we summarise the theoretical framework to be used as the background for the description of the arterial mechanics. It is of note that the artery is not stress-free in the absence of the applied loading. A load-free state including the residual stress is carried out by characterising an opening angle in the natural reference configuration. Different natural reference configurations of load bearing constituents need to be integrated and investigated for accurately estimating the pre-stress state which is essential to model the mechanical environment in the arterial wall.

## 2.1 ARTERIAL HISTOLOGY

Efficient constitutive descriptions of the arterial wall require a fundamental knowledge and understanding of their entire histology. Here, the focus will be on the microscopic structure of an elastic arterial wall composed of three layers: the intima, the media and the adventitia. The constituents of the arterial wall from a mechanical perspective are discussed here, and particular emphasis is placed on important factors that govern the mechanical behaviour of the material. An overview of the layered structure of an artery is shown in Figure 2.1.

### 2.1.1 Intima

The intima is the innermost layer of the artery. It consists of endothelial cells lining the arterial wall that rest on a thin basal membrane. In healthy young arteries, the intima is very thin and makes an insignificant contribution to the mechanical properties of the arterial wall (Holzapfel et al., 2004). However, it should be noted that the intima thickens and stiffens with age, so that the mechanical contribution may become significant over time (Lasheras, 2007).

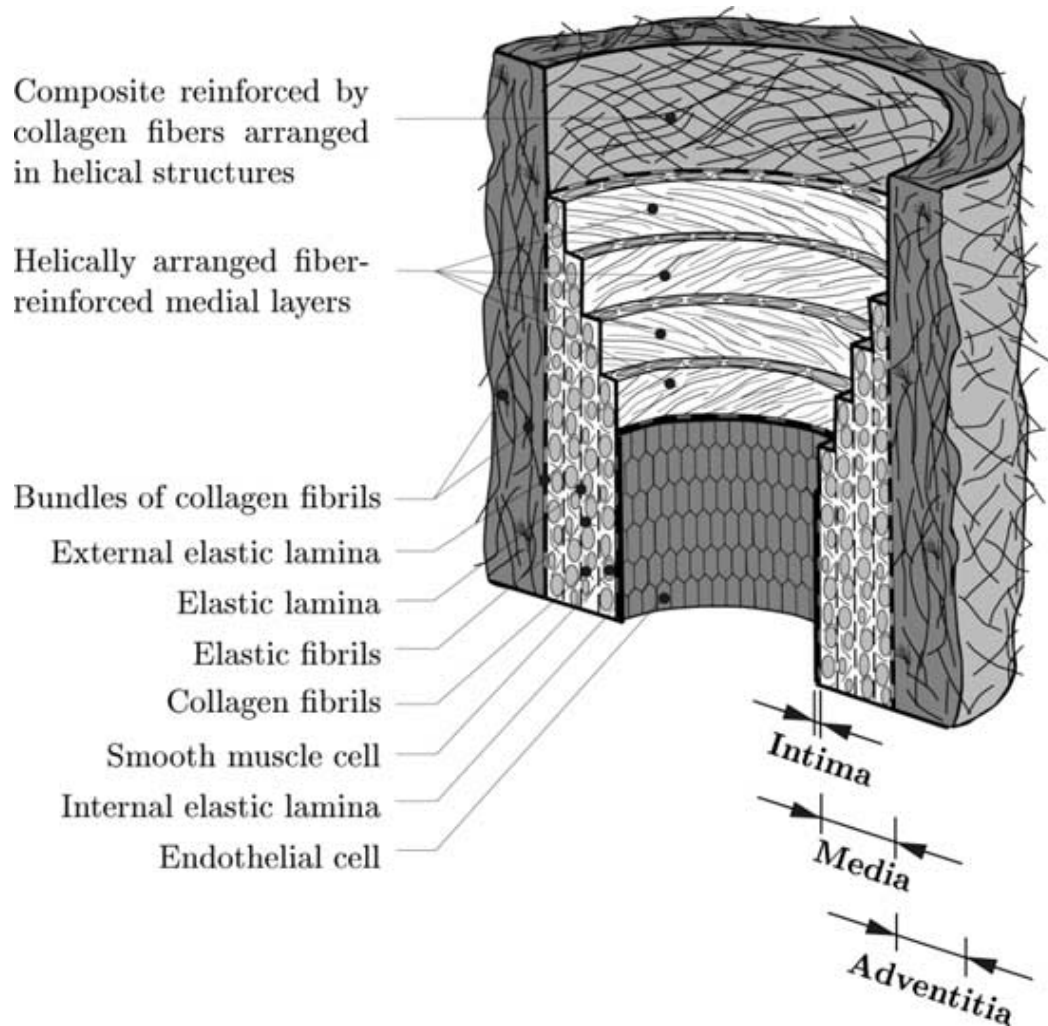


Figure 2.1: Schematic of arterial wall layered structure (adapted from Holzapfel et al. (2000).)

### 2.1.2 Media

The media is the middle layer of the artery and consists of a complex three dimensional network of smooth muscle cells, elastic connective tissues and various types of collagen. The media is separated from the intima and the adventitia by the internal elastic lamina and the external elastic lamina. The interconnection and the orientation of the elastic and collagen fibres, elastic laminae and smooth muscle cells together construct a continuous fibrous helix. The fibres are almost circumferential oriented in the helical structure of the media. This structural arrangement gives the media high strength, resilience and the ability to resist loads in both longitudinal and circumferential directions. The media is generally the thickest one of the three

layers and contributes significantly to the mechanical strength of the vessel.

### 2.1.3 Adventitia

Surrounding the media, the adventitia is the outermost layer of the artery and composed primarily of ground substance, elastin and collagen fibres. The thickness of the adventitia depends strongly on the type (elastic or muscular) and the physiological function of the blood vessel, for example, in cerebral blood vessels the adventitia is very thin (Brisman et al., 2006). Its mechanical function is to prevent over-distension of the blood vessel wall. The wavy collagen fibres are arranged in a helical structure and serve to reinforce the wall. Especially at higher levels of pressure the adventitia changes to a "jacket-like" tube to prevent the artery from over-stretch. This is due to the helical structure in the adventitia generally having a relatively greater pitch than in the media, so that the collagen fibres in the adventitia would reach their straightened lengths in advance to the collagen in the media.

In our vascular model, it is assumed that the mechanical response of the artery is due to the media and the adventitia; the intima is assumed to not contribute to the mechanical response.

## 2.2 RESIDUAL STRESSES

### 2.2.1 Significant effect of residual stresses within the vessel wall

With a general understanding of vascular structure, another critical aspect of blood vessel behaviour is residual stresses. Existing stresses within the solid structure under no-load state are called residual stresses. Early research on biomechanics (Fung and Chuong, 1983) assumed the arterial wall is in a zero-stress state without external loads, i.e. blood pressure. If the blood pressure is re-applied on the zero-stress solid arterial wall, it is expected that there would be higher circumferential stress concentrations at the inner wall that would gradually decrease towards the outer wall. Thus, there is transmural variation of the mechanical responses through the arterial wall.

Fung (1983) challenged the hypothesis that the vessel wall is in zero-stress state at its natural configuration by pointing out the importance of residual stresses affecting the stress distributions in living organs in working condition. In living or-

gans, the working function is highly dependent on the level of internal stress and strain. For example, the contraction of vascular smooth muscles in the vessel wall is stimulated by the instant response of stress and strain within the muscle cells. Moreover, the function of muscle cells would have influence on the metabolic activity, flow of oxygen and carbon dioxide through the wall, and thus are also related to the stress and strain values. If there are/were no residual stresses within living organs, the internal mechanical response would be solely determined by the external load resulting in a non-uniform cell functionality through the vessel wall. A stress concentration at the inner wall implies there is a higher demand of energy consumption which is not an optimal condition for the arterial structure. Hence, the introduction of residual stresses is important to model the physiological state of the vessel wall. Furthermore, for living tissues, cells proliferate and decay with a turnover rate: the connective tissues are continuously synthesised by age. Hence, if the living organs were not subjected to external loads, they could not maintain a zero stress state with the constant response of tissues over the years.

Chuong and Fung (1986) first showed the existence of circumferential residual stresses which reduce the transmural difference of stress and strain within the vascular wall. This is based on experiments whereby several cuts were made on rabbit's arteries and left ventricles resulting in the immediate opening of the structure. This phenomenon contradicts the hypothesis that the unloaded configuration of an artery is in the zero-stress state. Chuong and Fung then applied a mathematical approach to include the 'opened-up' characteristic into a vascular model, in which the results showed that the circumferential stress concentration is reduced. Almost simultaneously, Vaishnav and Vossoughi (1987) investigated similar results leading to the same conclusion. Fung and Liu (1992) then made further experimental examinations of residual stresses by cutting rabbit arteries into rings, and rings into sectors shown in Figure 2.2. The zero-stress state is characterised by the opening angle of each sector. By measuring and comparing the strain in experimental and computational models at the zero-stress state, unloaded state, and loaded state, results showed that even the opening angles vary with types and longitudinal positions of arteries, whereby the general function is to enhance the stress and strain to be uniformly distributed in normal loaded conditions (with homeostatic blood pressure). This is the first evidence that demonstrates the implication of residual stresses of arteries in the *in vivo* state.

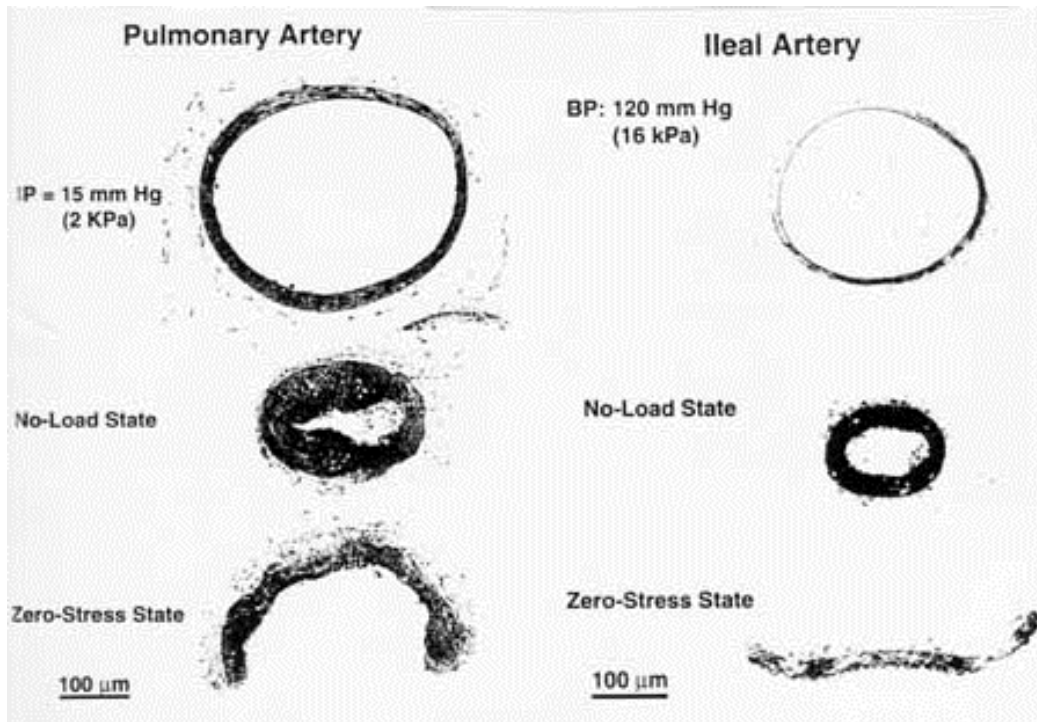


Figure 2.2: Three different states of the artery: *in vivo* state, no-load state and zero-stress state (adapted from Fung and Liu (1992) and modified by <http://www.umich.edu/~bme332/chap11bloodvessel/bme332bloodves.htm>).

For modelling purposes, it is vital to understand the zero-stress state (with an opening angle) as all the calculations of mechanical stress and strain are in reference to this initial state. In addition, according to the review of residual stresses in blood vessels (Fung, 1991), the change of stress has significant influence on the growth or resorption in tissue. Thus it is essential to include the residual stresses when modelling the mechanical response for the vessel wall. More importantly, this work aims to build up a computational framework to simulate the evolution of arterial diseases, which requires as a starting point, a model that can accurately represent the mechanical environment before applying a hypothetical G&R approach. Note that residual stresses may change over time during the growth of arteries, but this is beyond the scope of this thesis. The work presented herein focuses on modelling the homeostatic condition of arteries in the loaded state and the subsequent influence on the stress deviation from the homeostatic level. Further detail will be presented in Chapter 4.

To summarise, residual stresses are present in a large variety of biological tissues

and organs. They have a significant impact on the mechanical response of biological tissues to external loads. In the case of arterial tissue, when an artery is cut transversally it contracts along the axial direction, showing the existence of an auto-balanced internal axial stress field in the physiological state. Also, when the cut is made longitudinally in an arterial ring, it opens releasing circumferential stresses. Figure 2.2 adapted from Fung and Liu (1992) shows that different amounts of residual stress present in different rabbit arteries. Subsequent studies (Liu and Fung (1988); Han and Fung (1991); Taber and Humphrey (2001); Cardamone et al. (2009)) have demonstrated the importance of the introduction of residual stresses on arterial models to get an accurate calculation of the stress distribution throughout the arterial wall. The main effect of this stress field is to reduce the transmural gradient of circumferential stresses under physiological loads. Therefore, the inclusion of residual stress optimises the mechanical environment inside the vessel wall and provides a favourable and uniform condition for cell functionality throughout the domain.

### 2.2.2 Opening angle method

To apply residual stresses within an arterial model, Chuong and Fung (1986) suggested the opening angle of the vascular sample is the measurement to quantify the residual circumferential deformation of the vessel. This is a popular standard due to its simplicity. Especially we focus attention on the thick-walled cylindrical model which considers the transmural difference along the wall thickness, and so it is essential to employ residual stresses in order to have a realistic mechanical environment. In addition, the adaptive response of biological tissue is highly dependent on mechanical loads. As arteries react to the imposed loads, variations in the circumferential stress distribution through the wall play an important role in the adaptive processes. Applications with the influence of residual stresses on vascular mechanics is presented in Section 2.4.3.

The opening angle can be measured by image-analysis of physiological geometries. Figure 2.3 adapted from Guo et al. (2005) shows the opening angles measured in porcine coronary arterial trees. The vessels are carefully dissected and cut transversely into rings, then the radial cut is made to release the residual stresses. The image shows two segments from the arterial rings with the morphological measurement of opening angle  $\theta$ , which is defined by the two ends of open sector connecting

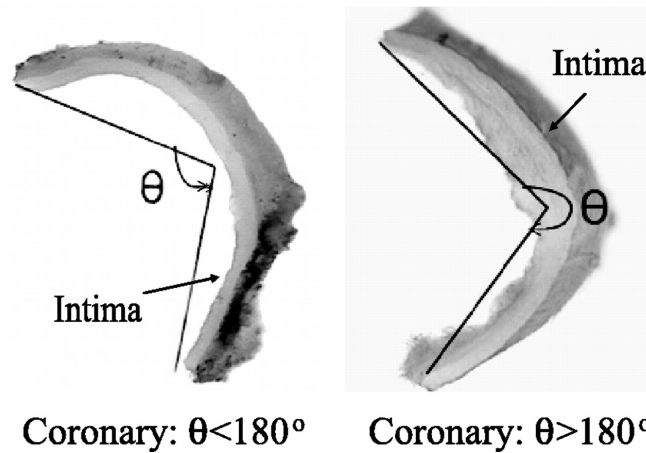


Figure 2.3: Photos of coronary rings cut radially to reveal sectors with opening angles  $\theta < 180^\circ$  (left) and  $\theta > 180^\circ$  (right) (adapted from Guo et al. (2005)).

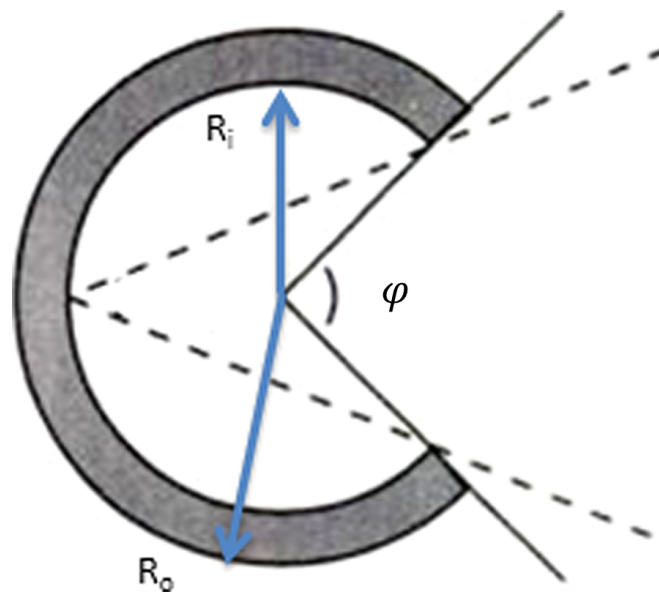


Figure 2.4: Diagram defining the opening angle (adapted from Avril et al. (2013)): The open sector is cut radially from the no-load configuration of arterial ring and assumed to be the stress-free undeformed configuration.  $\varphi$  is the opening angle determined from the central point of the open sector;  $R_i$  and  $R_o$  are the inner and outer radius of the zero-stress configuration.

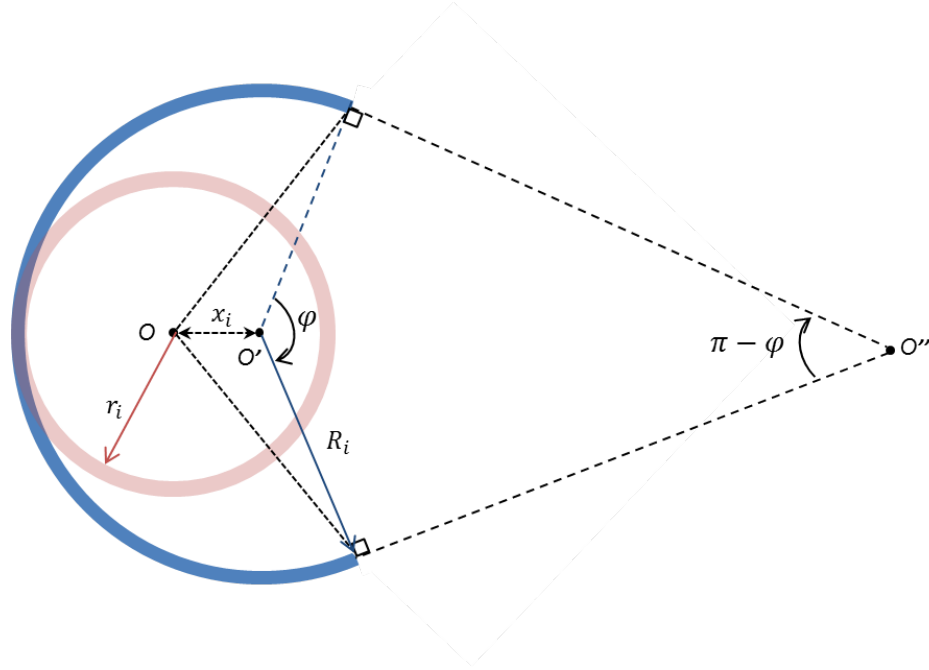


Figure 2.5: Illustration of the corresponding positions of stress-free configuration (blue) and load-free configuration (pink) denoted by the opening angle  $\varphi$ , reference radius  $R_i$ , load-free radius  $r_i$ , and a shift of central point  $x_i$ .

the midpoint of the inner wall. The opening angle could be less or greater than 180 degrees depending on the longitudinal position of the porcine arterial model. However, from a modelling perspective, the basic definition of opening angle as defined in Figure 2.4 is applied for a simple cylindrical model. The diagram depicts a stress free configuration where the opening angle is determined from the central point of the open sector connecting the two radii ends. Although the opening angle definitions are different between the experimental measurement and the cylindrical model, a correlation can be made for the implementation of an experimental opening angle on a computational model. Figure 2.5 shows a more detailed definition of opening angle for modelling purposes. The load-free configuration (pink circle) denotes the target model for the zero-stress configuration (blue arc). We first define the geometry of the target model, then apply an opening angle for constructing the geometry of an open sector in zero-stress state. Hence the known values are the target radius  $r_i$  and the opening angle  $\varphi$ , whilst the unknowns are the reference radius  $R_i$  and the curvature  $\kappa$  of the open sector. Since the circumferential lengths of the arterial rings in both configurations are meant to be the same:  $2\pi r_i = 2\pi R_i \left( \frac{2\pi - \varphi}{2\pi} \right)$ , the value of  $R_i$  is equal to  $r_i \left( \frac{2\pi}{2\pi - \varphi} \right)$  and the curvature of the open sector is  $\kappa = \frac{1}{R_i}$ .

In Figure 2.5, there is a shift ( $x_i = R_i - r_i$ ) of the central point between the load-free configuration ( $O$ ) and the stress-free configuration ( $O'$ ). The shift and the curvature are essential in order to calculate the nodal position of the arterial model for the open sector presented in Section 2.4 detailing the structural analysis. The open sector will gradually close up towards the load-free configuration to induce the residual stresses.

## 2.3 MECHANICAL BEHAVIOUR: CONTINUUM MECHANICAL FRAMEWORK

In this section, we follow Holzapfel's mathematical description of deformation definition and provide the general continuum description of the deformation to the material with hyperelastic stress response (Holzapfel et al., 2000). We also outline the basic tools from continuum mechanics: kinematics, deformation invariants, elasticity, strain energy and stress-deformation relations to model an arterial tube structure. As a basis for reporting the performance of the constitutive models, we consider the mechanical response of a thick-walled cylindrical tube model. Following the overview of the ingredients of continuum mechanics needed in soft tissue biomechanics and the phenomenological description of material properties, a two-layered thick-walled model is presented in Section 2.3.7.

### 2.3.1 Description of deformation

Here we provide descriptions of both the deformation of reference configuration and the deformed configuration shown in Figure 2.6. Let  $\Omega_0$  be a (stress-free) reference configuration of the continuous body of interest: we use the notation  $x : \Omega_0$  for the deformation, which transforms a typical material  $\mathbf{X} \in \Omega_0$  to a position  $\mathbf{x} = \chi(\mathbf{X}) \in \Omega$  in the deformed configuration, denoted  $\Omega$ . Further, let  $\mathbf{F}(\mathbf{X}) = \partial\chi(\mathbf{X})/\partial\mathbf{X}$  be the deformation gradient, and Jacobian determinant  $J(\mathbf{X}) = \det\mathbf{F} > 0$  be the local volume ratio. We base the kinematic formulation on a multiplicative split of deformation gradient

$$\mathbf{F} = (J^{1/3}\mathbf{I})\bar{\mathbf{F}} \quad (2.1)$$

where  $J^{1/3}\mathbf{I}$  is associated with volume-changing deformations and an isochoric deformation gradient  $\bar{\mathbf{F}}$  whereby  $\det(\bar{\mathbf{F}}) = 1$  is associated with volume-preserving deformations of the material.

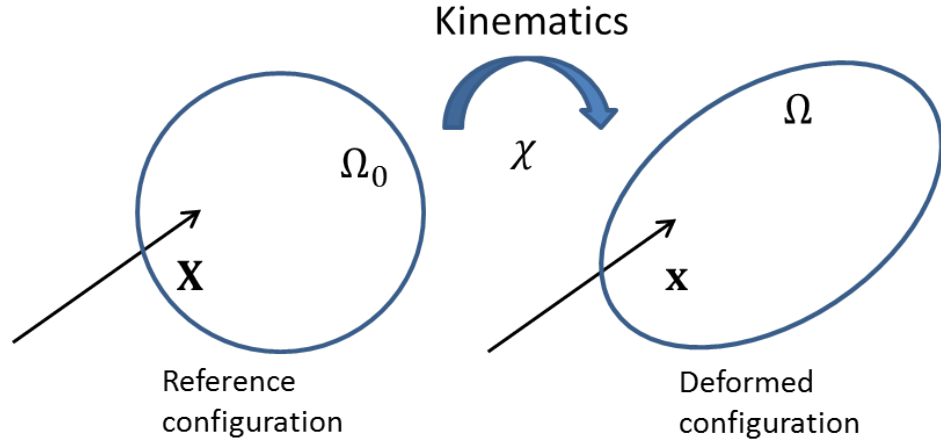


Figure 2.6: Illustrative model for the description of deformation in continuum mechanics.

We use the right and left Cauchy-Green tensors, denoted  $\mathbf{C}$  and  $\mathbf{b}$  respectively, and their modified counterparts, denoted  $\bar{\mathbf{C}}$  and  $\bar{\mathbf{b}}$  respectively, associated with  $\bar{\mathbf{F}}$ .

$$\text{Right } \mathbf{C} = \mathbf{F}^T \mathbf{F} = J^{2/3} \bar{\mathbf{C}}, \quad \bar{\mathbf{C}} = \bar{\mathbf{F}}^T \bar{\mathbf{F}} \quad (2.2)$$

$$\text{Left } \mathbf{b} = \mathbf{F} \mathbf{F}^T = J^{2/3} \bar{\mathbf{b}}, \quad \bar{\mathbf{b}} = \bar{\mathbf{F}} \bar{\mathbf{F}}^T \quad (2.3)$$

For polar decomposition, the deformation gradient can also be described as

$$\mathbf{F} = \mathbf{R} \mathbf{U} = \mathbf{V} \mathbf{R} \quad (2.4)$$

where  $\mathbf{R}$  is the rotation tensor,  $\mathbf{U}$  and  $\mathbf{V}$  are the positive definite symmetric tensors. Eigenvalues of  $\mathbf{U}$  and  $\mathbf{V}$  are the principal stretches  $\lambda_i > 0$  ( $i = 1, 2, 3$ ), and eigenvalues of  $\mathbf{b}$  and  $\mathbf{C}$  are  $\lambda_i^2$ . In addition, we introduce Green-Lagrange strain tensor  $\mathbf{E}$  and its associated modified strain tensor  $\bar{\mathbf{E}}$ .

$$\mathbf{E} = \frac{1}{2}(\mathbf{C} - \mathbf{I}) = J^{2/3} \bar{\mathbf{E}} + \frac{1}{2}(J^{2/3} - 1)\mathbf{I}, \quad \bar{\mathbf{E}} = \frac{1}{2}(\bar{\mathbf{C}} - \mathbf{I}) \quad (2.5)$$

where  $\mathbf{I}$  denotes the second-order unit tensor.

### 2.3.2 Governing equation

The equilibrium equation without any body forces is

$$\text{div}(\sigma) = 0 \quad (2.6)$$

where  $\text{div}(\cdot)$  denotes the material divergence of the spatial tensor field and  $\sigma$  is the Cauchy stress tensor which can be derived from strain energy functions defined in Sections 2.3.3 and 2.3.4.

### 2.3.3 Specific form of strain energy function

A strain energy function is now introduced, suitable for arterial tissue which consists of a volumetric and an isochoric term, i.e.

$$\Psi(\mathbf{E}, \mathbf{A}_1, \dots, \mathbf{A}_n) = U(J) + \bar{\Psi}(\bar{\mathbf{E}}, \mathbf{A}_1, \dots, \mathbf{A}_n) \quad (2.7)$$

where the function  $U$  is a purely volumetric contribution and  $\bar{\Psi}$  is a purely isochoric contribution to the free energy  $\Psi$ . We employ a set  $\{\mathbf{A}_1, \dots, \mathbf{A}_n\}$  of (second order) tensors to characterise the arterial structure with fibre reinforcements. The volumetric changes may be associated with increasing or decreasing in mass over a long time scale. However, on a short time scale, arterial tissues may be considered nearly incompressible. For an incompressible material ( $J = \det \mathbf{F} = 1$ ), the constraint is therefore  $J - 1 = 0$  to ensure incompressibility of a hyperelastic material that  $U(1) = 0$ .

However, when solving the problem numerically, the idea is that the material would not be perfectly incompressible, instead it would be slightly compressible. This leads to a penalty method for the volumetric strain energy  $U(J)$  by using a large value of bulk modulus to enforce incompressibility. More details about the penalty method can be found in section 8.3 of Holzapfel (2000), in which a simple form for  $U(J)$  often used in numerical computations can be adapted:

$$U(J) = \frac{\kappa}{2}(J - 1)^2 \quad (2.8)$$

where  $\kappa$  is the bulk modulus (penalty parameter) for the penalty function. The implementation of this penalty method for the computational framework is introduced in Section 2.4.1.

### 2.3.4 Hyperelastic stress response

In order to describe the hyperelastic stress response of arterial walls, we apply the chain rule of differential calculus on equation (2.7), the second Piola-Kirchhoff stress tensor  $S = \partial\Psi/\partial\mathbf{E}$  is given by

$$S = S_{vol} + \bar{S}, \quad \text{with} \quad S_{vol} = \frac{\partial U(J)}{\partial \mathbf{E}}, \quad \bar{S} = \frac{\partial \bar{\Psi}}{\partial \bar{\mathbf{E}}} \quad (2.9)$$

The standard results of the chain rules are required

$$\frac{\partial J}{\partial \mathbf{E}} = J\mathbf{C}^{-1} \quad \text{and} \quad \frac{\partial \bar{\mathbf{E}}}{\partial \mathbf{E}} = J^{-2/3} \left( \Lambda - \frac{1}{3} \bar{\mathbf{C}} \otimes \bar{\mathbf{C}}^{-1} \right) \quad (2.10)$$

From tensor analysis, where  $\Lambda$  denotes the fourth-order identity tensor which has the form  $(\Lambda)_{IJKL} = (\delta_{IK}\delta_{JL} + \delta_{IL}\delta_{JK})/2$ , and  $\delta_{IJ}$  being the Kronecker delta. With these results, equation (2.9) is substituted into (2.11) with the introduction of the hydrostatic pressure  $p = dU/dJ$ .

$$S = pJ\mathbf{C}^{-1} + J^{-2/3}\text{Dev}\left(\frac{\partial\bar{\Psi}}{\partial\bar{\mathbf{E}}}\right) \quad (2.11)$$

where the material deviatoric operator  $\text{Dev}(\cdot)$  is defined by

$$\text{Dev}(\cdot) = (\cdot) - \frac{1}{3}[(\cdot) : \bar{\mathbf{C}}]\bar{\mathbf{C}}^{-1} \quad (2.12)$$

A Piola transformation of equation (2.11) enables the Cauchy stress tensor  $\sigma = J^{-1}\mathbf{F}\mathbf{S}\mathbf{F}^T$  to be put in the decoupled form

$$\sigma = \sigma_{vol} + \bar{\sigma}, \quad \text{with} \quad \sigma_{vol} = p\mathbf{I}, \quad \bar{\sigma} = J^{-1}\text{dev}\left(\bar{\mathbf{F}}\frac{\partial\bar{\Psi}}{\partial\bar{\mathbf{E}}}\bar{\mathbf{F}}^T\right) \quad (2.13)$$

where the operator  $\text{dev}(\cdot)$  is defined by

$$\text{dev}(\cdot) = (\cdot) - \frac{1}{3}[(\cdot) : \mathbf{I}]\mathbf{I} \quad (2.14)$$

### 2.3.5 Geometric model of artery

We consider the artery as an incompressible thick-walled cylindrical tube subjected to axial stretch and internal pressure. In Figure 2.7, it is known that load-free configuration  $\Omega_{res}$  is exercised from the body and not subjected to any loads. Thus, when a cut is made longitudinally in an arterial ring, it opens releasing circumferential stresses and becomes stress-free reference configuration  $\Omega_0$ . Current configuration  $\Omega$  is the deformed geometry after applying the loads to the load-free configuration  $\Omega_{res}$  as depicted in Figure 2.7.

In terms of cylindrical polar coordinates  $(R, \Theta, Z)$ , the geometrical region  $\Omega_0$  of the tube is defined by

$$\begin{aligned} R_i &\leq R \leq R_o \\ 0 &\leq \Theta \leq (2\pi - \varphi) \\ 0 &\leq Z \leq L \end{aligned} \quad (2.15)$$

where  $R_i$ ,  $R_o$ ,  $\varphi$  and  $L$  denote the inner and outer radii, the opening angle and the length of the undeformed tube, respectively.

The deformation gradient  $\mathbf{F}$ , which takes  $\Omega_0$  into the current configuration  $\Omega$ , is the composition of the deformation  $\mathbf{F}_{close}$  and  $\mathbf{F}_{load}$ . As indicated in Figure 2.7,

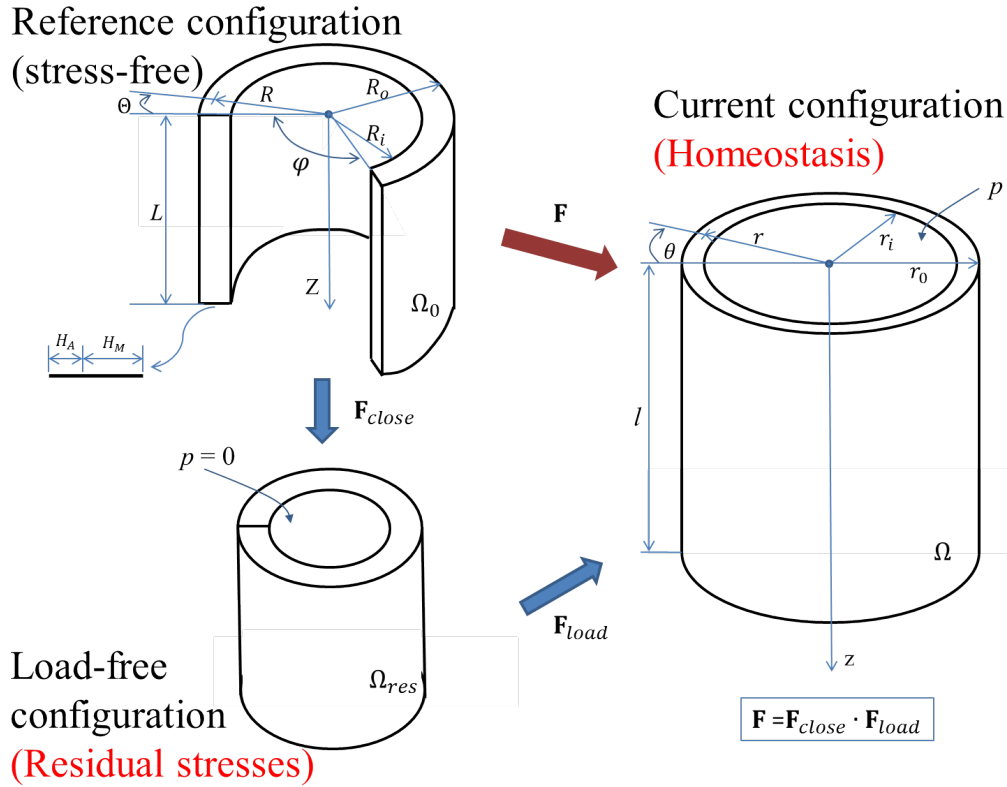


Figure 2.7: Arterial ring in the stress-free reference configuration, the load-free configuration and the current configuration.

$\mathbf{F}_{load}$  generates the load-free configuration  $\Omega_{res}$  associated with residual stresses, while  $\mathbf{F}_{load}$  is associated with physiological loads such as axial elongation and internal pressure that leads to the final configuration  $\Omega$ . In terms of cylindrical polar coordinates  $(r, \theta, z)$ , the geometry of the deformed configuration  $\Omega$  is given by

$$\begin{aligned} r_i &\leq r \leq r_o \\ 0 &\leq \theta \leq 2\pi \\ 0 &\leq z \leq l \end{aligned} \quad (2.16)$$

where  $r_i$ ,  $r_o$  and  $l$  denote the inner and outer radii, and the length of the deformed tube, respectively. The deformation gradient  $\mathbf{F}$ , which is taken to be isochoric, can be written in the form:

$$\mathbf{F} = r\mathbf{e}_r + z\mathbf{e}_z \quad (2.17)$$

with reference to the basis vectors  $\{\mathbf{e}_r, \mathbf{e}_\theta, \mathbf{e}_z\}$  associated with the cylindrical polar

coordinates  $(r, \theta, z)$ , where

$$\begin{aligned} r &= \sqrt{\frac{R^2 - R_i^2}{k\lambda_z} + r_i^2} \\ \theta &= k\Theta \\ z &= \lambda_z Z \end{aligned} \quad (2.18)$$

$\lambda_z$  is the axial stretch, the parameter  $k = 2\pi/(2\pi - \varphi)$  is a convenient measure of the opening angle of the reference configuration.

### 2.3.6 Constitutive model for the artery layers

In this section we propose a potential model of the artery as a fibre-reinforced composite. The material parameters involved may be associated with the histological structure of arterial walls such as fibre orientation. This model is based on the theory of the mechanics of composite material and contains the symmetries of a cylindrically orthotropic material.

The thick-walled model of the artery is considered as a composite reinforced by two families of collagen fibres which are arranged in symmetrical spirals. We assume each layer with similar mechanical characteristics and use the same form of strain-energy function, but a different set of material parameters.

We consider an incompressible material in our model and the strain energy function  $\bar{\Psi}$  consists of an isotropic term  $\bar{\Psi}_{iso}$  and an anisotropic term  $\bar{\Psi}_{aniso}$ . The  $\bar{\Psi}_{iso}$  term is associated with the mechanical response of elastin constituents which we assume to be isotropic. The anisotropic response is characterised by the orientation of the collagen fibres for the resistance to stretch at high pressures. Hence, the two-term potential is written as

$$\bar{\Psi} = \bar{\Psi}_{iso}(\bar{I}_1) + \bar{\Psi}_{aniso}(\bar{I}_{4,i}) \quad (2.19)$$

where the deformation invariants  $\bar{I}_1$  and  $\bar{I}_{4,i}$  are associated with deformation measure  $\bar{\mathbf{C}}$  and collagen structure  $\mathbf{A}_i$ ,  $\{i = 1, 2\}$  for two directions of collagen fibres.

$$\bar{I}_1 = \bar{\mathbf{C}} : \mathbf{I} = \text{tr}(\bar{\mathbf{C}}), \quad \bar{I}_{4,i} = \bar{\mathbf{C}} : \mathbf{A}_i \quad (2.20)$$

Note that the invariant  $\bar{I}_{4,i}$  is the square of the stretches in the direction of vector  $\mathbf{a}_{0i}$ ,  $\{i = 1, 2\}$ . We include structure tensors with the formulation in Sections 2.3.3 and 2.3.4, and the set  $\{\mathbf{A}\}$  of collagen structure is defined as the tensor products  $\mathbf{A}_i = \mathbf{a}_{0i} \otimes \mathbf{a}_{0i}$ . The anisotropy then only arises through the invariant  $\bar{I}_{4,i}$  which is sufficient to capture the typical features of arterial response.

Finally, the strain-energy functions  $\bar{\Psi}_{iso}$  and  $\bar{\Psi}_{aniso}$  must be particularised to fit the material parameters in order to observe the arterial response. For the elastin, we use a modified Neo-Hookean model to determine isotropic response in each layer, i.e.

$$\bar{\Psi}_{iso} = \frac{k_e}{2} (\bar{I}_1 - 3) \quad (2.21)$$

where  $k_e > 0$  is a stress-like material parameter of elastin modulus.

For the collagen, an exponential function form is used to describe the energy stored in the collagen fibres, so as to capture the strong stiffening effect that occurs at high pressures. The constants  $k_1$  and  $k_2$  are associated with the anisotropic contribution of collagen to the overall response.

$$\bar{\Psi}_{aniso} = \frac{k_1}{2k_2} \left\{ \exp \left[ k_2 (\bar{I}_{4,i} - 1)^2 \right] - 1 \right\} \quad (2.22)$$

where  $k_1 > 0$  is a stress-like material parameter and  $k_2 > 0$  is a dimensionless parameter. An appropriate choice of  $k_1$  and  $k_2$  enables to highlight the behaviour of collagen fibres in the high pressure domain.

All the equations above are for determining an expression of stress. By substituting (2.13) into the particularised strain-energy functions (2.21) and (2.22), we obtain the isochoric stress  $\bar{\sigma}$  to the Cauchy stress tensor,

$$\bar{\sigma} = k_e \text{dev}(\bar{\mathbf{b}}) + 2 \frac{\partial \bar{\Psi}_{aniso}}{\partial \bar{I}_{4,i}} \text{dev}(a_{0i} \otimes a_{0i}) \quad (2.23)$$

where  $a_i = \bar{\mathbf{F}} a_{0i}$  is the Eulerian counterpart of  $a_{0i}$ .

### 2.3.7 Arterial model as a two-layered thick-walled tube

In order to report the performance of the proposed constitutive model, we apply the model to a two-layered thick-walled tube structure. For this case the intima layer of the artery is not of mechanical interest, and we therefore focus on modelling the two remaining layers: media and adventitia.

The isochoric term of the strain-energy function for the two-layered problem is given by:

$$\Psi^j = m_E^j \bar{\Psi}_{iso}^j + m_C^j \bar{\Psi}_{aniso}^j \quad (2.24)$$

Where  $j = \{M, A\}$  relates to the layers:  $M$  for media and  $A$  for adventitia;  $m_E^j, m_C^j$  are the normalised mass densities of the elastin and collagen respectively. The initial

<i>Parameter</i>	<i>Symbol</i>	<i>Value</i>
<b>Initial geometry</b>		
Load-free radius	$r_0$	2 (mm)
Axial length	$L_{ref}$	20 (mm)
<b>Applied boundary conditions</b>		
Internal pressure on arterial wall	$p$	125 (mmHg)
Axial pre-stretch	$\lambda_z$	1.3
Radial pre-stretch	$\lambda_\theta$	1
<b>Fibre orientation</b>		
Media	$\alpha_M$	30°
Adventitia	$\alpha_A$	60°
<b>Wall thickness</b>		
Total	$H$	0.375 (mm)
Media	$H_M$	$\frac{3}{4}H$
Adventitia	$H_A$	$\frac{1}{4}H$
<b>Elastin modulus</b>		
Media	$k_e^M$	143.2 (kPa)
Adventitia	$k_e^A$	$0.1k_e^M$
<b>Collagen modulus</b>		
Media	$k_1^M$	3.84 (kPa)
	$k_2^M$	40
Adventitia	$k_1^A$	0.96 (kPa)
	$k_2^A$	40

Table 2.1: Geometrical and material parameters for the arterial wall model (Based on Watton et al. (2004), Watton et al. (2009a) and Grytsan et al. (2015))

values of normalised densities are equal to 1, i.e.  $m_E^j = 1$ ,  $m_C^j = 1$ . However, the values could increase or decrease to simulate growth/decay of individual constituents. Particularised forms of the strain-energy function for each layer can be written as

$$\Psi^M = m_E^M \frac{k_e^M}{2} (\bar{I}_1 - 3) + m_C^M \frac{k_1^M}{2k_2^M} \left\{ \exp \left[ k_2^M (\bar{I}_{4,i}^M - 1)^2 \right] - 1 \right\}, \quad \text{in media} \quad (2.25)$$

$$\Psi^A = m_E^A \frac{k_e^A}{2} (\bar{I}_1 - 3) + m_C^A \frac{k_1^A}{2k_2^A} \left\{ \exp \left[ k_2^A (\bar{I}_{4,i}^A - 1)^2 \right] - 1 \right\}, \quad \text{in adventitia} \quad (2.26)$$

This model uses 6 material parameters,  $k_e^M$ ,  $k_1^M$ ,  $k_2^M$  for the media and  $k_e^A$ ,  $k_1^A$ ,  $k_2^A$  for the adventitia. The constants  $k_e^M$  and  $k_e^A$  are associated with the elastin constituents, which describe the isotropic response of the tissue. The constants  $k_1^M$ ,  $k_2^M$  and  $k_1^A$ ,  $k_2^A$  are associated with the anisotropic contribution of collagen to the

overall response. The material parameters are constants and do not depend on the geometry, opening angle or fibre orientation.

The deformation invariant  $\bar{I}_{4,i}^j$ ,  $j = \{M, A\}$  associated with the media and the adventitia are defined by  $\bar{I}_{4,i}^j = \bar{\mathbf{C}} : \mathbf{A}_{i,j}$ ; ( $i = \{1, 2\}$ ,  $j = \{M, A\}$ ). The tensors  $\mathbf{A}_{i,j}$  characterising the collagen structure of the media and adventitia are given by

$$\mathbf{A}_{1,j} = a_{01,j} \otimes a_{01,j}, \quad \mathbf{A}_{2,j} = a_{02,j} \otimes a_{02,j}; \quad j = \{M, A\}. \quad (2.27)$$

whereby the components of the direction vectors have in matrix notation:

$$a_{01,j} = \begin{bmatrix} 0 \\ \cos(\alpha_j) \\ \sin(\alpha_j) \end{bmatrix}, \quad a_{02,j} = \begin{bmatrix} 0 \\ \cos(\alpha_j) \\ -\sin(\alpha_j) \end{bmatrix}, \quad j = \{M, A\} \quad (2.28)$$

and  $\alpha_j$  are the angles between the collagen fibres and the circumferential direction in the media and adventitia. Because of the wavy structure of collagen, it is regarded as being unable to support compressive stresses. We therefore assume the fibres are active in extension and inactive in compression so as to satisfy the condition:  $\bar{I}_{4,i}^j > 1$  in the strain-energy function. If  $\bar{I}_{4,i}^j$  is less or equal to 1, the response of the artery is purely isotropic.

Figure 2.8 demonstrates the pressure-diameter relationship derived from a membrane arterial model proposed by Watton et al. (2004). Although this membrane model simplified the transmural difference along radial direction, it still can give us a sense of the mechanical response of the artery. Note that the residual stress is not included in this membrane model and the normalised mass densities of elastin and collagen ( $m_E, m_C$ ) in each layer are all equal to 1 for homeostatic condition. The artery is subjected to blood pressure  $p$ , axial stretch  $\lambda_z$  and radial stretch  $\lambda_\theta$  with undeformed radius  $r_0$ . The force equilibrium based on membrane approximation can be written as

$$p = \frac{1}{r_0 \lambda_z} \left\{ (H_M k_e^M + H_A k_e^A) \left( 1 - \frac{1}{\lambda_z^2 \lambda_\theta^4} \right) + \sum_{j=M,A} 2H_j k_1^j (I_4^j - 1) \exp \left[ k_2^j (I_4^j - 1)^2 \right] \cos^2 \alpha_j \right\} \quad (2.29)$$

where  $H_j$  is the thickness of each layer and the invariant  $I_4^j = \lambda_z^2 \sin^2(\alpha_j) + \lambda_\theta^2 \cos^2(\alpha_j)$ ,  $\{j = M, A\}$  for media and adventitia, respectively. Geometrical and material parameters are listed in Table 2.1. A more detailed derivation of the simplified model can be found in Appendix A. The resulting pressure-diameter relationship

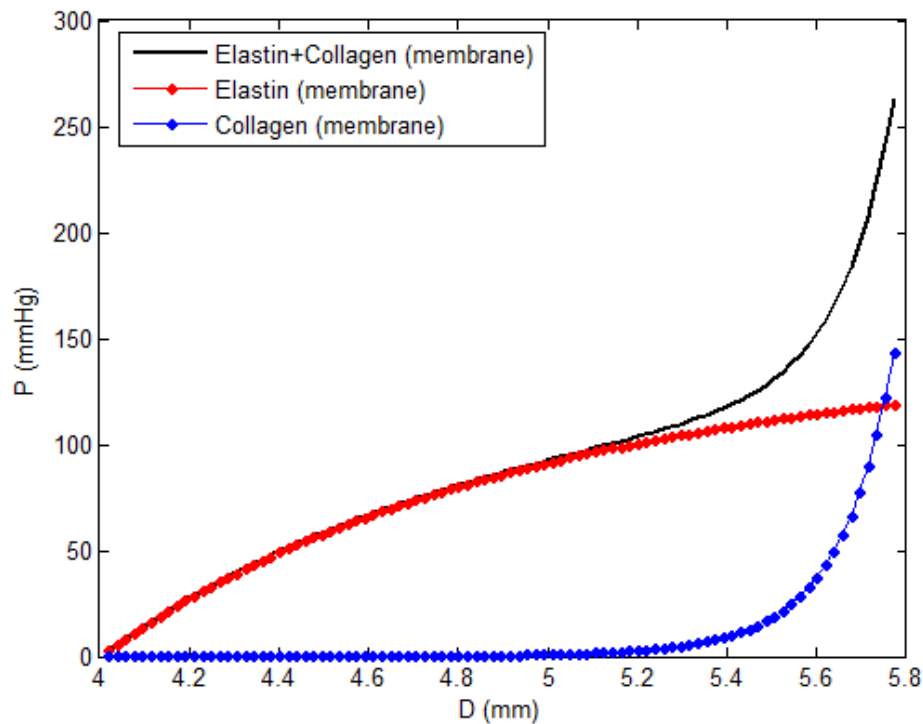


Figure 2.8: The pressure-diameter relationship for the membrane model of the artery including the contribution from elastin and collagen (Note: residual stress is not included (zero opening angle)).

shows that the exponential form of the strain-energy function in collagen is characterised that the collagen fibres bear more loads at high strains. The mechanical response of the artery at higher strains is governed chiefly by the collagenous constituents that are anisotropic, while at lower strains it is governed by the elastin that responds isotropically.

## 2.4 ANSYS IMPLEMENTATION

### 2.4.1 Finite element arterial model

The previous section demonstrates the analytical method on solving a simple membrane model on arterial mechanical response with a pressure-diameter relationship. For solving a more complex or arbitrary geometry, the analytical method is not applicable. Therefore, a numerical approach is introduced here for further development on modelling the arterial structure and the iterative simulation on arte-

rial G&R presented in Chapter 4. The numerical model is solved based on the finite element method (FEM) in the engineering software ANSYS Mechanical 16.1 version on the basis of solid mechanics. The FEM method firstly subdivides the whole domain into discrete number of elements (meshes) and assigns material parameters in each element. To solve the problem, the solving equations are represented in matrices by nodal degrees of freedoms within elements, material stiffness, boundary conditions, and loads. The known values yields the approximated unknown values by solving the simple equation in these finite elements. The solution of the original system is then assembled by the solutions from elements.

Based on the model description in the last section, the mechanical behaviour of the arterial wall is highly nonlinear and anisotropic hyperelastic. For the structural analysis in ANSYS, a built-in exponential-function-based strain energy potential (equation (2.30)) is available to describe the SEF presented in Section 2.3.7:

$$W = \sum_{i=1}^3 a_i (\bar{I}_1 - 3)^i + \sum_{j=1}^3 b_j (\bar{I}_2 - 3)^j + \frac{c_1}{2c_2} \left\{ \exp \left[ c_2 (\bar{I}_4 - 1)^2 \right] - 1 \right\} + \frac{e_1}{2e_2} \left\{ \exp \left[ e_2 (\bar{I}_6 - 1)^2 \right] - 1 \right\} \quad (2.30)$$

where  $W$  denotes the strain energy potential;  $(a_i, b_j, c_1, c_2, e_1, e_2)$  are the material constants;  $(\bar{I}_1, \bar{I}_2, \bar{I}_4, \bar{I}_6)$  are the deformation invariants. This built-in SEF is categorised for modelling anisotropic hyperelasticity of elastomers with reinforcements, and suitable for biomaterials such as arteries.

To implement this exponential anisotropic strain energy potential to the discrete elements within the model, an input file is needed for applying the material parameters for each element. In ANSYS, the **TB,AHYPER** command is for defining material modulus, material direction, and volumetric part for anisotropic hyperelasticity specifications (AHYPER). The input formats of the corresponding parameters for each element in ANSYS modelling are described as follows:

```
TB,AHYPER,,,EXPO
TBDATA,1,a1,a2,a3,b1,b2,b3
TBDATA,7,c1,c2,e1,e2
```

- The **EXPO** command is specific designated for the SEF in equation (2.30). The corresponding material modulus of elastin ( $k_e$ ) and collagen ( $k_1, k_2$ ) can be translated from equation (2.25) and (2.26) to (2.30) that  $(a_1 = \frac{k_e}{2}; c_1 = k_1; c_2 = k_2)$ . The rest of the parameters  $(b_j, e_1, e_2)$  in (2.30) are set to 0 to fit in the arterial model.

```
TB,AHYPER,,,AVEC
TBDATA,,A1,A2,A3
```

```
TB,AHYPER,,,BVEC
TBDATA,,B1,B2,B3
```

- The **AVEC**, **BVEC** commands define the material direction constants. For the arterial model, each command represents the orientation of one family of collagen fibres in relevant to the angle  $\alpha_j$  for both layers  $j = \{M, A\}$  in (2.28). Collagen fibres in both layers are assumed to be oriented in a double helical pitch ( $\pm\alpha_j$ ). Therefore, Constants sets of [A1,A2,A3] and [B1,B2,B3] denote the unit vector of the angles  $+\alpha_j$  and  $-\alpha_j$  respectively in both layers. The unit vector is calculated in the (x,y,z) direction of the global system based on the angle  $\alpha_j$  to the circumferential direction in each element corresponding to the global coordinate.

```
TB,AHYPER,,,PVOL
TBDATA,,d
```

- The command **PVOL** defines the volumetric potential. The volumetric strain energy is given by:  $U(J) = \frac{1}{d}(J - 1)^2$ , where  $d$  is the incompressible parameter and the bulk modulus  $\kappa$  equates to  $\frac{2}{d}$  corresponding to the penalty function (2.8). As the bulk modulus  $\kappa$  is considered to exceed the material modulus for insignificant volumetric response,  $\kappa$  is chosen to be 3 orders of magnitude higher than  $k_e$  in numerical models (Holzapfel and Gasser, 2007). Hence,  $d$  is given by  $\frac{2}{\kappa}$  (1/MPa) to enforce incompressibility in each element.

Next, to implement the constitutive model in elements, we specify the element type to be SOLID185 which is used for 3D modelling of solid structures and available for the implementation of **EXPO** strain energy potential. The element of SOLID185 is defined by eight nodes (hexahedral element) having three degrees of freedom at each node: translations of x,y,z directions. This element type has hyperelasticity, large deflection, and large strain capabilities suitable for modelling the extensive elasticity of the vessel wall. It also has mixed formulation capability for simulating deformations of fully incompressible hyperelastic materials to prevent shear and volumetric locking. The sparse direct solver (default solver in ANSYS) is applied for solving the nonlinear properties of the arterial model.

To apply boundary conditions and specific positions on vascular G&R, full control of the element location and order is needed. Therefore, the mesh of the model is not automatically generated by ANSYS with a random element order but rather defined by a sequential numbering of nodes of the elements which correspond to positions for the purpose of full control. With the brick shape of the SOLID185 element, it is easy to organise the element order to be inserted in the simple tube arterial model. A detailed description on the assignment of the nodal number and element order can be found in Appendix B.

An illustrative example of the mesh set-up is shown in Figure 2.9, in which there are 8 elements along the radial direction, 60 element along the circumferential direction, and 30 elements along the axial direction. As the focus of this work is to investigate the transmural variation inside the vessel wall, a mesh sensitivity analysis was carried out for the numerical model, the results of which are discussed in Section 2.4.2. With 8 elements through the wall thickness, the inner 6 elements denote the media layer whilst the outer 2 elements denote the adventitia layer based on the layer description in Table 2.1. The model is constructed in an open sector to include the residual stresses by closing it to the target tube model. By calculating the curvature and the corresponding positions to the target tube model, the nodal positions of elements for the open sector can be defined.

As demonstrated in Figure 2.7, the open sector is the reference configuration in zero-stress state, while the closed sector with residual stresses is the load-free configuration, then the inner blood pressure and axial stretch are applied for the current (loaded) configuration. Figure 2.10 shows the reference configurations with three different opening angles ( $0^\circ$ ,  $60^\circ$ ,  $180^\circ$ ) for the ANSYS model. The boundary conditions are defined differently in the reference configuration and the load-free configuration. For the reference configuration with an opening angle, the nodes in the middle point of the opening sector are fixed as demonstrated in Figure 2.10. From the fixed plane, nodes on both sides of the sector are moving gradually towards the target positions to close the opening sector in order to generate residual stresses. For the unloaded configuration, we release the boundary restraints of the fixed plane and apply symmetric boundary conditions with the closed tube. For the loaded configuration, one end of the tube model is fixed in the axial direction and the deformation of one-third the length of the model ( $\lambda_z = 1.3$ ) is applied at the other end to force axial stretch (Monson et al., 2003), while the normal systolic

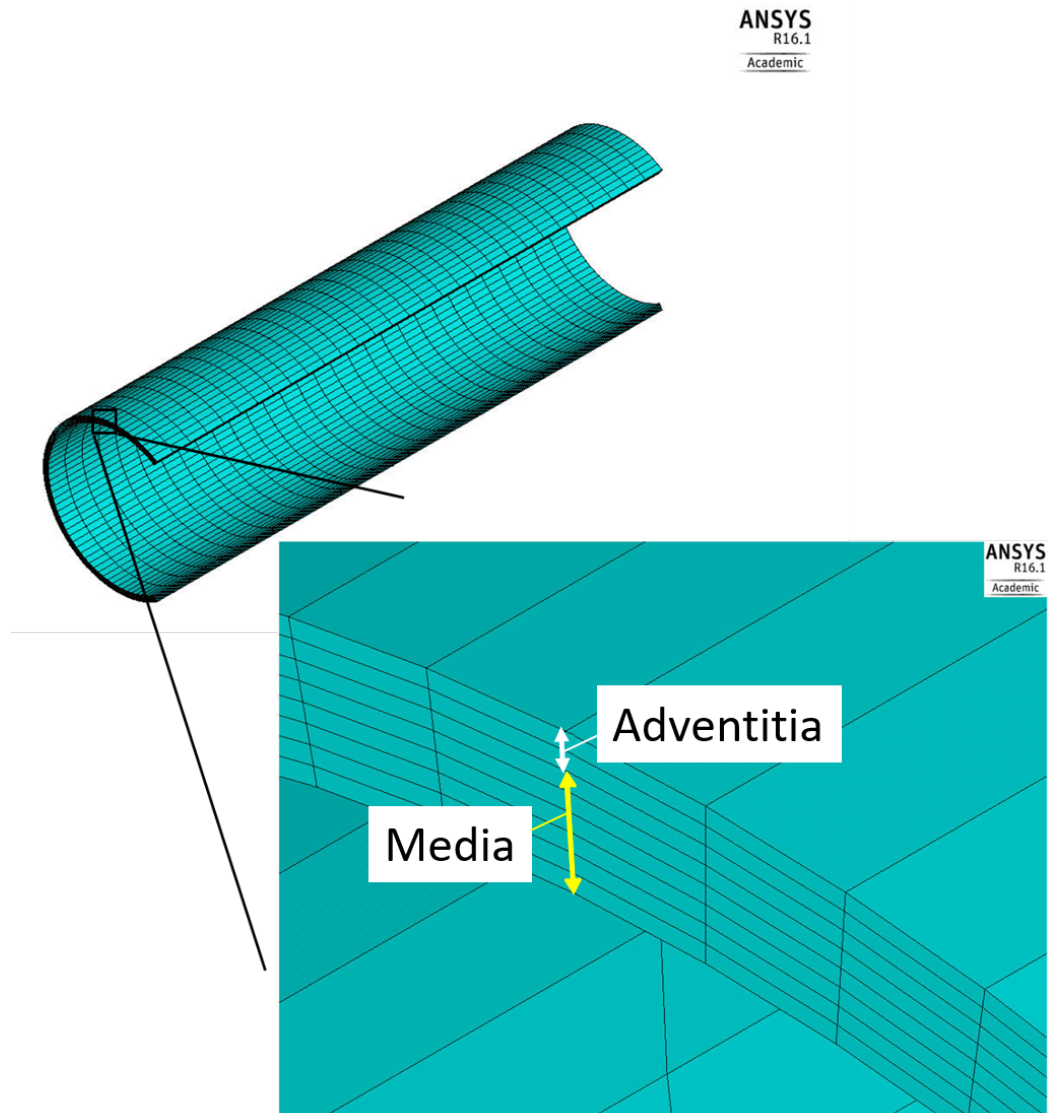


Figure 2.9: Mesh of the arterial model: The whole geometry of the mesh is built in the reference configuration (open sector) in a zero-stress state. The mesh of the model consists of 60 elements along the circumferential direction ( $eIC=60$ ), 8 elements along the wall thickness ( $eIR=8$ ) and 30 elements in the axial direction ( $eIZ=30$ ). Hence the total number of elements is 14400. According to the layer description in Table 2.1,  $3/4$  of the thickness towards the inner surface is the media layer;  $1/4$  of the thickness towards the outer surface is the adventitia layer. Hence 6 elements along the radial direction from inner surface is the medial element, whilst 2 elements along the radial direction from outer surface is the adventitia elements according to the setting ( $eIR=8$ ) in ANSYS.

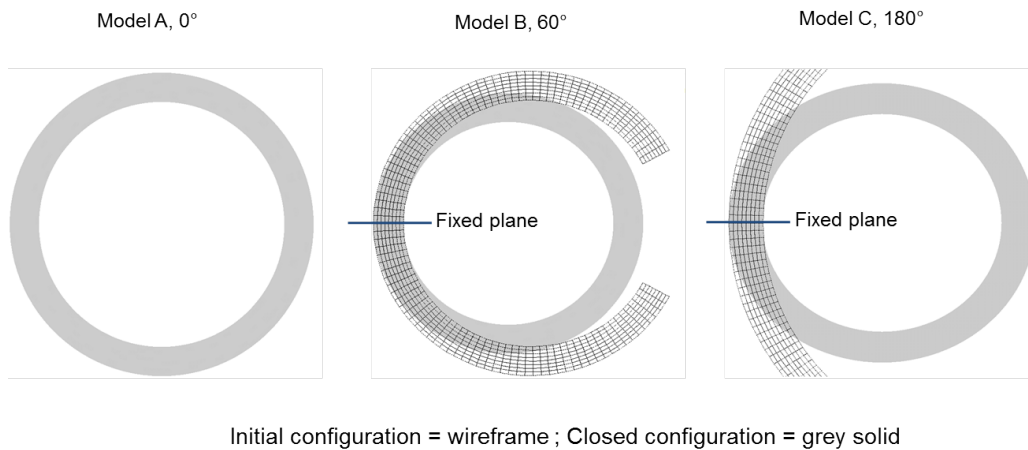


Figure 2.10: Different opening angles for FE model and target position.

blood pressure ( $p = 125 \text{ mmHg} = 16.67 \text{ kPa}$ ) is applied at the inner surfaces. The balance condition of the current configuration is defined as the homeostatic state. Mechanical responses such as stress and strain can be exported as element-based data for further use on the hypothetical G&R approach. Once there is disturbance of the mechanical environment, the original values of mechanical responses in each element can be set to the standard in order to restore the homeostatic condition. Applications of the element-based G&R will be presented in Chapter 4 and Chapter 5.

Note that the simulation in ANSYS is executed in batch mode by reading in a series of input files containing the nodal position, element order, material parameters, boundary conditions, and solving steps. These input files are written in MATLAB on the basis of Fortran language which is the only computational language recognised by ANSYS. The batch mode processing allows an automated modelling starting from the reference configuration to the current configuration without manual intervention which can highly increase the efficiency of the whole computational framework. In general, ANSYS reads in the input files generated from the MATLAB editor to simulate the mechanical environment of the arterial model and export the data. For the iterative G&R process, ANSYS keeps resolving equilibrium with updated material parameters to restore homeostatic values. This adaptive process is also included in the batch mode with a loop structure generating more time steps for G&R. More details of the G&R workflow will be presented in Section 4.1.

Figure 2.11 shows the results from the ANSYS implementation of the arterial

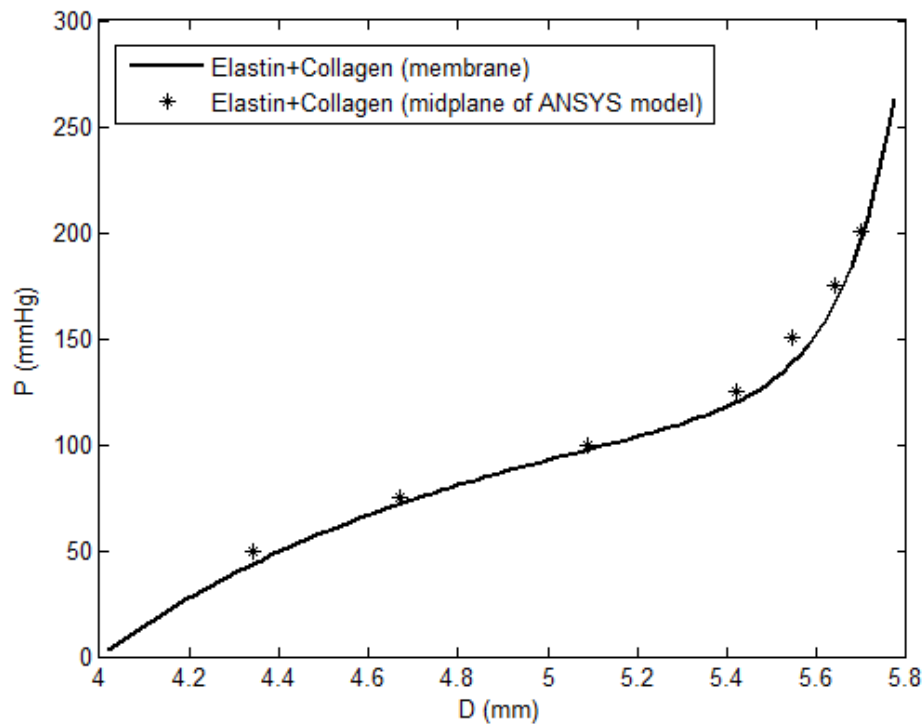


Figure 2.11: Comparison between the analytical and numerical solutions on the pressure-diameter relationship of the arterial model.

model described in Figure 2.8. We apply the same parameters in the ANSYS thick-walled model to have a validation of the numerical method and to compare the results with the analytical solution of the membrane model. The radial deformation in the mid-plane of the ANSYS model is compared with the responding diameter of the membrane model under the same internal pressure. It shows that the results from the ANSYS model are in good agreement with the results of the membrane model, and the ANSYS model is slightly stiffer on preventing dilation of the artery under the same pressure. Overall the ANSYS numerical model shows the ability to duplicate the analytical model and the potential for further extension in a 3D domain.

### 2.4.2 Sensitivity analysis of the number of elements

As we emphasise the transmural variation of the thick-walled model, the efficiency and sufficiency to present the different mechanical responses through the radial position are important for our simulation. Illustrated in Figure 2.12 is the circumferential stress distribution in the normalised radial position simulated with differ-

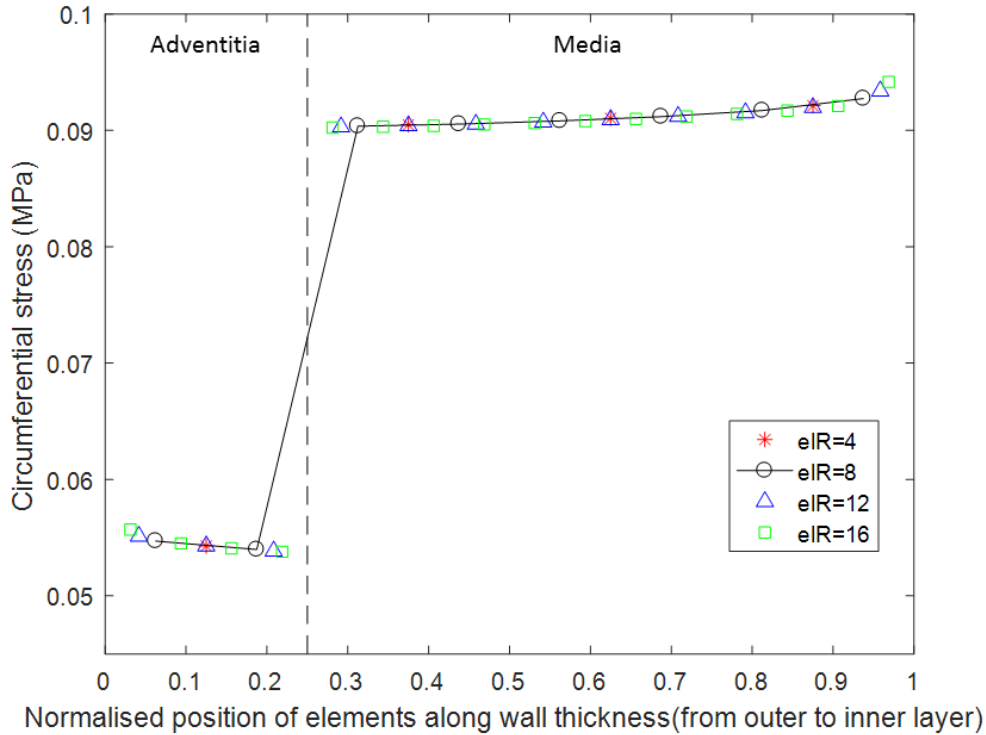


Figure 2.12: Influence of element number (eIR) through the wall thickness on stress distribution ( $p=125$  mmHg;  $\lambda_z = 1.3$ ; opening angle =  $60^\circ$ ).

ent number of element in radial direction (eIR) of the ANSYS model. Note that the stress output from ANSYS is the true Cauchy stresses in the global coordinate system which are computed from second Piola-Kirchhoff stresses as described in Section 2.3.4. The geometrical and material parameters are based on Table 2.1 with a given opening angle of  $60^\circ$ . A greater number of elements in the radial direction indicates more data points through the wall thickness, which can increase the accuracy of the approximated value in each element. Additionally, the number of elements (eIR) should be a multiple of 4 to well represent the fraction of layers:  $(1/4)H$  is adventitia;  $(3/4)H$  is media,  $H$  is the total wall thickness.

Figure 2.12 shows that the overall stress distribution varies very little within the layers. However, compared to the elements within the layers, the circumferential stresses in the innermost and outermost elements show a more obvious difference between eIR results. Therefore, we compare stress values at the innermost element and the outermost element between different eIR numbers to examine the accuracy and efficiency of the computational model. Comparisons of stress values, as well as

eIR	Innermost stress (kPa)	Error (%)	Outermost stress (kPa)	Error (%)
4	90.514	-3.87	54.018	-3.02
8	92.734	-1.51	54.706	-1.78
12	93.388	-0.82	55.121	-1.03
16	94.161	0	55.698	0

Table 2.2: Comparison of stress values at the innermost and outermost elements with different number of elements (eIR) of the ANSYS arterial model.

error percentages are listed in Table 2.2. Results from the greatest number of element eIR=16 is deemed as the standard to investigate the accuracy. From Table 2.2, as it is expected eIR=4 has the lowest accuracy with more than 3% deviation from eIR=16. Although the error percentage is already low for the eIR=4 case, while for eIR=8 and eIR=12, the deviation is less than 2% in both innermost and outermost elements giving a better performance. Moreover, eIR=4 implies only one element representing the adventitia layer without transmural difference, while eIR $\geq$ 8 provides at least two elements to describe the radial difference within this thin layer. In addition, eIR=8 saves more than 60% in computational time when compared to eIR=16. As we will model the evolution of an aneurysm, each time step requires another structural analysis for the G&R process, which will significantly increase the computational time. Hence to achieve a balance between computational cost and result sufficiency, we choose eIR=8 to obtain the adequate information from the numerical model to develop the whole computational framework for aneurysm modelling.

### 2.4.3 Influence of opening angle on stress distribution

According to the description of residual stresses in Section 2.2, the circumferential stresses are uniformly distributed through the wall thickness as an optimised balance condition in the biological perspective. For the implementation within ANSYS, if we apply physiological loads in the thick-walled model excluding the residual stresses, the stresses vary along the radial position with a higher stress concentration at the inner layer. Therefore, the opening angle method is applied to include residual stresses in order to adjust the stress distribution to the biological homeostatic condition.

In order to demonstrate the influence of residual stresses, we compare the cir-

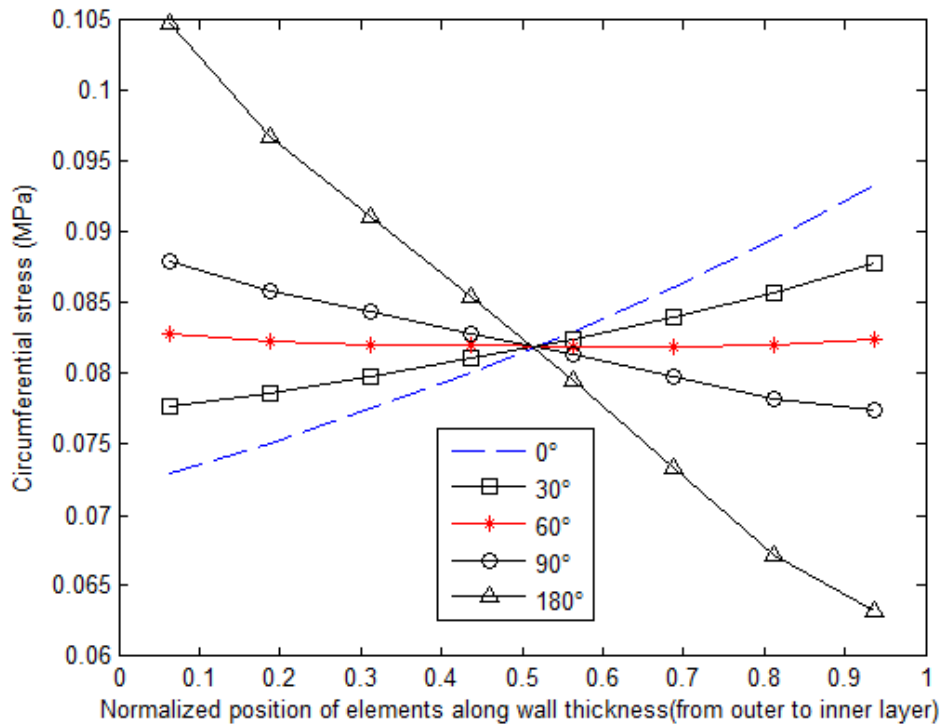


Figure 2.13: Different opening angles for single layered vessel wall with only elastin constituent.

cumferential stresses along the radial direction for different opening angles. The whole model reaches a mechanical equilibrium after applying the internal pressure ( $p = 125$  mmHg) inside the arterial wall and the axial stretch ( $\lambda_Z = 1.3$ ) in the axial direction. In Figure 2.13, the arterial structure is a simplified single-layered artery with only elastin constituents for which the elastin modulus is 0.1 MPa. As 0 degree opening angle indicates there is no residual stress, the stresses have the minimum value at the outermost layer and increase almost linearly to the innermost point which satisfies the force equilibrium. The residual stresses can be adjusted by the opening angle, and it is shown that for 60 degree the vessel wall has relatively uniform stress distributions with the interference of residual stresses. On the other hand, 180° is an extreme case of applying excessive residual stresses which leads to opposite stress distributions in the case of 0°. Despite the simplicity of the arterial structure, this single-layered elastin-only model provides an initial idea of the influence of the opening angle method.

Next, the opening angle is applied to the two-layered arterial model consisting of

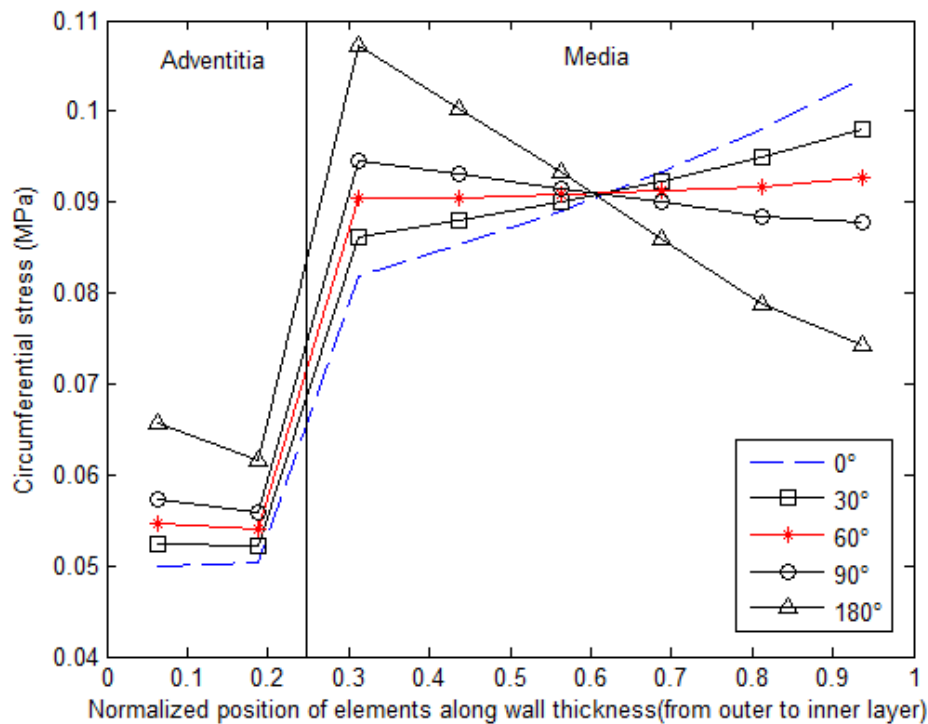


Figure 2.14: Different opening angles for two-layered vessel wall with collagen and elastin constituents.

both elastin and collagen constituents. The constitutive parameters of elastin and collagen in each layer are also based on Table 2.1. Note that the elastin modulus of the media is 10 times the value of the adventitia. Figure 2.14 shows the same effect within the different layers: the stress distribution for a  $60^\circ$  opening angle has a greater uniform state than other opening angles. Thus,  $60^\circ$  is the most effective opening angle to reduce the transmural variation of circumferential stresses through the wall thickness of the two-layered arterial model. The opening angle may vary for different arterial structures, nonetheless for the rest of our simulation of this specific two layered model we will apply a  $60^\circ$  angle.

#### 2.4.4 Mechanical behaviour of the ANSYS model

Previous sections give a general example of modelling the gross mechanical responses of a specific two-layered arterial model in the homeostatic state. However, it is of note that there is a high diversity between the studies on the mechanical properties of layers inside vessel wall. Before modelling the evolution of aneurysm

<b>Parameter \ Case</b>	MECH 1	MECH 2	MECH 3	MECH 4
<b>Elastin</b>				
$k_e^M / k_e^A$	10/1	1/1	1/10	2.13/1
$k_e^M$ (kPa)	143.2	91.4	14.32	99.3
$k_e^A$ (kPa)	14.32	91.4	143.2	46.6
<b>Collagen</b>				
$k_1^M / k_1^A$	4/1	1/1	1/4	6.04/1
$k_1^M$ (kPa)	3.84	2.02	2.1	1.74
$k_1^A$ (kPa)	0.96	2.02	8.4	0.29
$k_2^M / k_2^A$	1/1	1/1	1/1	1/5.83
$k_2^M$	40	40	40	47.6
$k_2^A$	40	40	40	277.7

Table 2.3: Mechanical cases

structure, it is essential to investigate the influence of mechanical properties, fibre orientations, and blood pressure on the mechanical behaviour of the homeostatic arterial model.

#### 2.4.4.1 Modelling cases

It is important to accurately model the mechanical response of individual layers of the vessel wall as the basis to predict the adaptive response during arterial diseases. However, due to the inconsistent picture of mechanical properties of arterial layers, different types of distinct layer properties must be examined in the ANSYS model to demonstrate different types of mechanical behaviours for potential development and application. To achieve this aim, we follow up the numerical study proposed by Schmid et al. (2013) and select 8 modelling cases of the arterial wall which have almost identical pressure-diameter relationships divided by 2 groups but with different layer-specific mechanical properties. We construct the 8 different modelling cases by using the combination of 4 cases of elastic mechanical properties (MECH) and 2 cases of fibre alignments (FIB). The geometrical setting for the reference configuration is the same in all cases.

##### **Mechanical cases: MECH**

As mentioned previously, there is a huge diversity in the investigation of the mechanical properties within the media and adventitia layers. Even with the same type

and the same location of arteries, the elastic modulus could differ remarkably. A common assumption is that the media is stiffer than the adventitia at lower strain, while at higher strain the adventitia becomes stiffer and acts as the protective sheath (Humphrey and Na (2002); Holzapfel et al. (2004); Holzapfel and Gasser (2007)). Some experimental observations have found that the media is 10 times stiffer than the adventitia over the whole strain domain (Pandit et al., 2005), while some found that the media is actually weaker than the adventitia (Holzapfel et al., 2005). Since the experimental results did not give a clear and consistent conclusion on layer-specific mechanical responses, 4 mechanical cases to simulate the mechanical behaviour of the media (M) and the adventitia (A) were created in our ANSYS model. Details of the material parameters for the 4 mechanical cases are listed in Table 2.3.

- (1) MECH 1:  $M > A$ , this is the reference case based on Table 2.1 which is the example model we will apply to the G&R simulation. Note that the material parameters of the media are up to 10 times greater than those of adventitia.
- (2) MECH 2:  $M = A$ , all material parameters in the media layer and the adventitia layer are identical as an intermediate case to be compared with other cases.
- (3) MECH 3:  $M < A$ , an opposite case to MECH 1 as the elastin modulus of the adventitia is 10 times greater than that of the media, while the ratio of collagen modulus  $k_1$  between the layers is also exchanged from MECH 1. This case is motivated by the experimental observation made by Holzapfel et al. (2005).
- (4) MECH 4:  $M \nearrow A$ , the media bears the major load at lower strain, while at higher strain, the adventitia "kicks in" earlier as the protective sheath with greater  $k_2$  value and bears the major load (Holzapfel et al. (2004); Holzapfel and Gasser (2007)).

#### **Fibre cases: FIB**

There are substantial differences in fibre orientations for different types of arteries (Canham (1989); Holzapfel et al. (2000); Rowe et al. (2003)). We include 2 general fibre cases to simulate the effect of fibre orientation to the layer-specific and overall mechanical responses:

- (1) FIB 1:  $\alpha_M = 30^\circ$  and  $\alpha_A = 60^\circ$ , the reference case of fibre orientations in Table 2.1 based on the studies in rabbit carotid arteries by Watton et al. (2004) and Schmid et al. (2010).
- (2) FIB 2:  $\alpha_M = 0^\circ$  and  $\alpha_A = 40^\circ$ , the comparative case is given by the studies of human arteries by Rowe et al. (2003) and Holzapfel (2006).

Figure 2.15 shows the pressure-diameter relationships of different modelling cases. In Figure 2.15(a), as the set of MECH 1 and FIB 1 is the target model, the estimations of material parameters for other MECH cases are adjusted to fit the MECH 1 pressure-diameter curve. Consequently, the curves of different MECH cases between the normal systolic and diastolic blood pressure (125/80 mmHg) are almost identical, but the variations between curves increase at higher pressures. Figure 2.15(b) shows the pressure-diameter curves for the FIB 2 case. The variations between MECH cases are slightly greater than the FIB 1 case but generally identical in the range of normal blood pressures. Note that the collagen fibres "kick in" earlier with smaller fibre orientations as the curve is steeper due to the influence of the exponential term of collagen in SEF.

Figure 2.16 demonstrates the influence of modelling cases on stress distribution through the media and adventitia under a blood pressure of 125 mmHg. In Figure 2.16(a), MECH 1 is the example model; it was previously shown in Section 2.3.7 that the media is bearing the major load from the lower strain. For MECH 2, the stress distribution is nearly uniform over the whole radius, which is not surprising as the material parameters in the media and the adventitia are the same except for fibre orientations. For MECH 3, the dominant layer becomes the adventitia as the ratios of material parameters are swapped from MECH 1. For MECH 4, although the elastic moduli of elastin and collagen in media are still greater than those in the adventitia, the greater  $k_2^A$  value allows the collagen in the adventitia to "kick in" earlier as the main load-bearer. If we compare cases (a) and (b) in Figure 2.16, FIB 2 decreases the transmural variation between layers for MECH 1 and MECH 4, but increases it for MECH 2 and MECH 3 in comparison to FIB 1. Overall, the role of the adventitia becomes more important when applying the loading condition of the FIB 2 case.

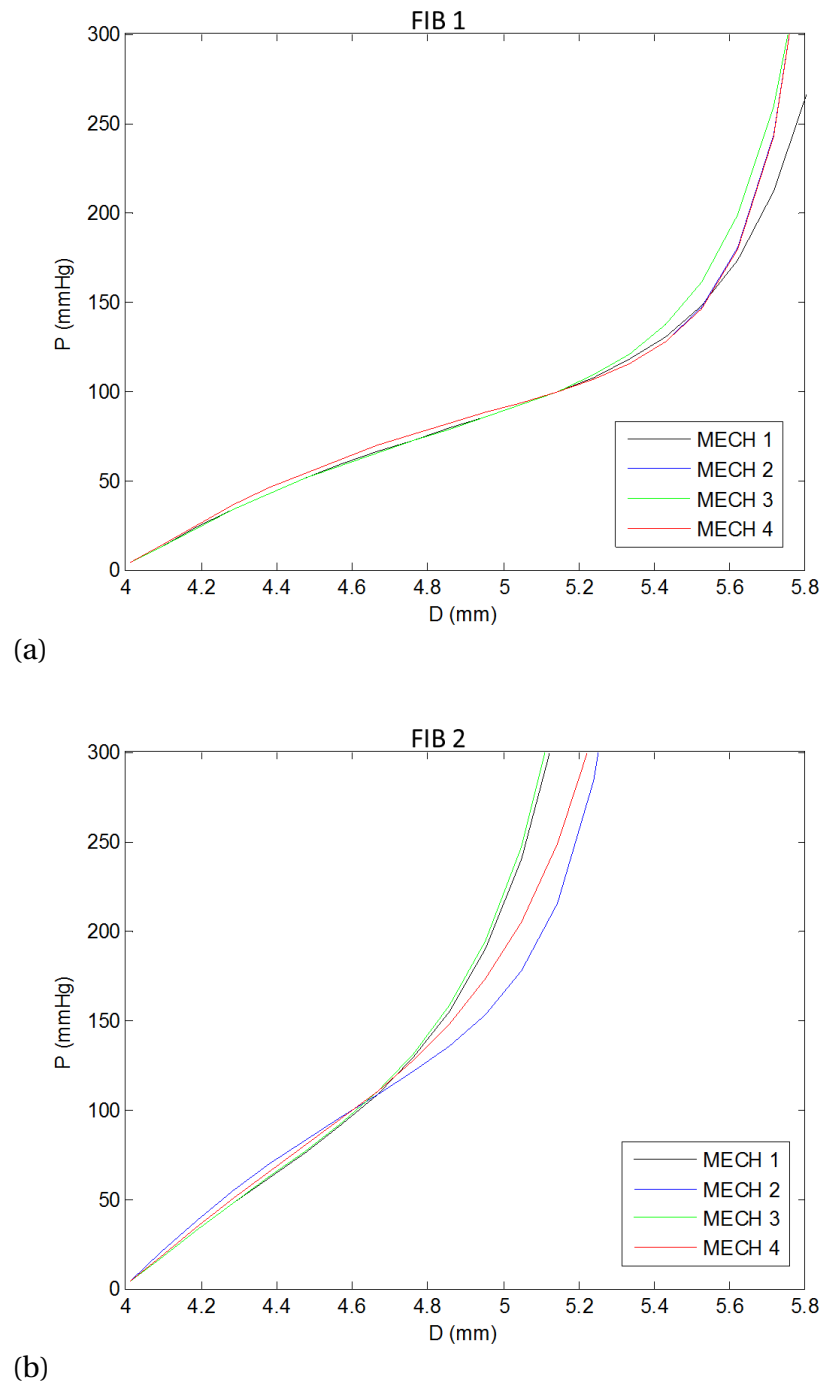


Figure 2.15: The pressure-diameter curves for the FIB cases: (a) FIB 1:  $\alpha_M = 30^\circ$ ;  $\alpha_A = 60^\circ$ ; (b) FIB 2:  $\alpha_M = 0^\circ$ ;  $\alpha_A = 40^\circ$  (shown under pressures between 0~300 mmHg).

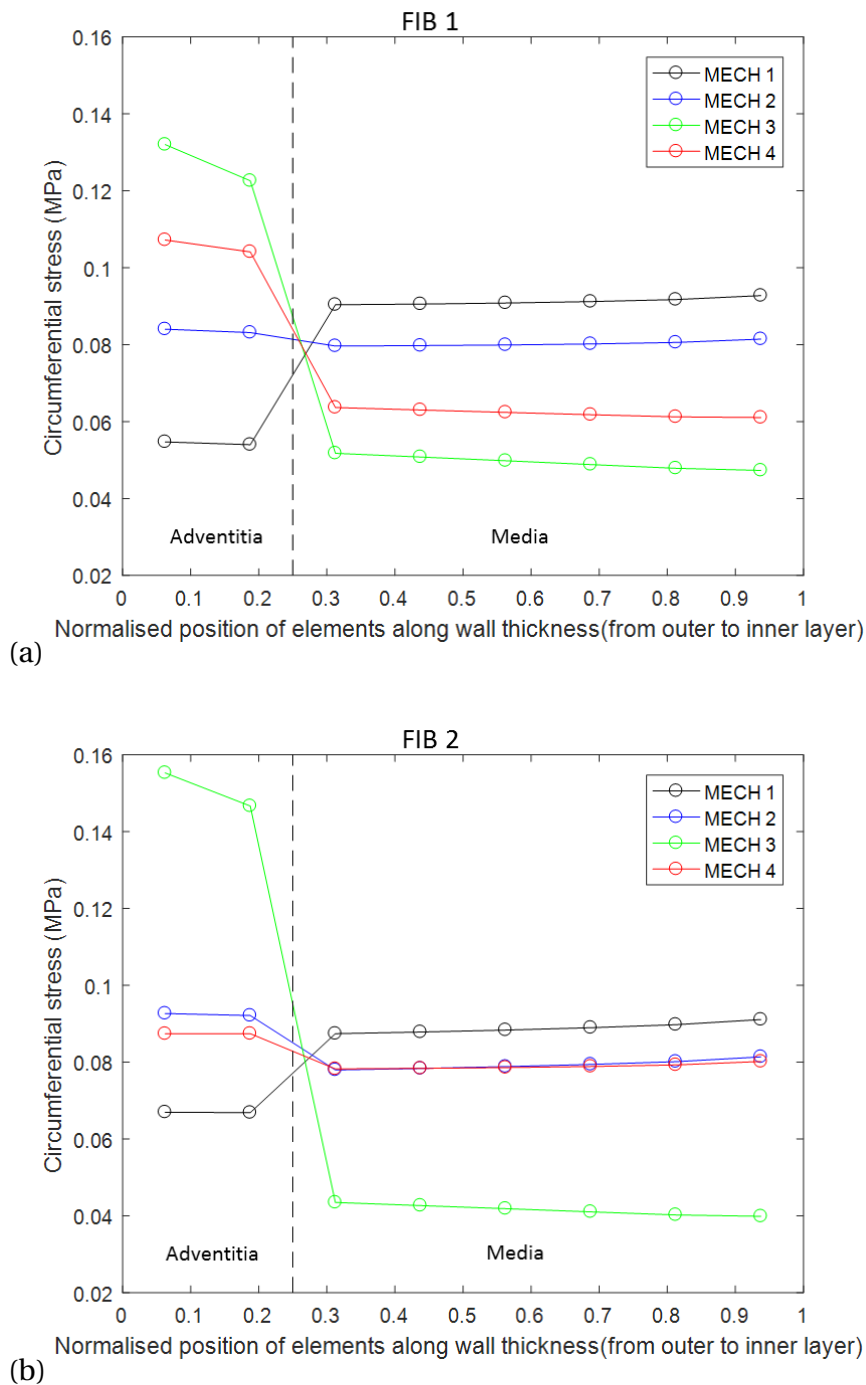


Figure 2.16: Influence of mechanical cases on stress distribution through the wall thickness: (a) FIB 1:  $\alpha_M = 30^\circ$ ;  $\alpha_A = 60^\circ$ ; (b) FIB 2:  $\alpha_M = 0^\circ$ ;  $\alpha_A = 40^\circ$  (shown under pressure of 125 mmHg).

#### 2.4.4.2 Influence of blood pressure

The normal systolic and diastolic blood pressures are in the range of 120-140 (mmHg) and 70-90 (mmHg) respectively. In our current development of the modelling framework, a systolic pressure of 125 (mmHg) is selected to be the normal blood pressure. However, under abnormal conditions, the blood pressure could rise up to extremely high levels of 480 (mmHg) (Haykowsky et al., 1996). Sudden stressful events such as weight lifting, heavy work, and blowing your nose could also lead to hypertension. In addition, according to experimental observations (Isaksen et al., 2008), the sites of aneurysm rupture are usually corresponding to areas with high wall tension. On the other hand, low blood pressure, also known as hypotension, is when the blood pressure is abnormally low. Although hypotension is assumed to be less harmful to the human body, it still indicates a restricted supply of blood flow to the brain and vital organs. Therefore, it is of great interest to model the effect of blood pressure on mechanical stress in the vessel wall for further development of modelling the mechanical behaviour of vascular diseases.

Figure 2.17 (a) shows the stress distribution through the wall thickness under higher and lower blood pressures of the two-layered example model in the case of MECH 1 and FIB 1 whereby the media is defined as being stiffer than the adventitia. With higher pressures (250 and 480 mmHg), the stress concentration is at the inner layer, and the overall stress level increases significantly in the media layer. For the normal diastolic pressure (80 mmHg) and the low blood pressure (40 mmHg), both the stress levels and the stress variation decrease through the layers. Especially for the 40 mmHg case: stresses in the adventitia layer are greater than in the media layer as the residual stresses have more impact on the stress distribution. In general, stresses in the adventitia layer are stable during the blood pressure change, while the media layer reacts more actively to the change due to the greater stiffness. To represent different types of layer-specific mechanical behaviour, Figure 2.17 (b) shows the stress distribution when the adventitia is set as the stiffer layer (MECH 3 and FIB 1). The variation between the layers is low when the blood pressure is lower. At the range of normal blood pressures (125/80 mmHg), the adventitia bears most of the load. Even at the higher pressure, the adventitia is still the dominant layer. However, when the blood pressure reaches an extreme value of 480 (mmHg), stress concentration in the media also increases significantly at the inner layer. Results from these models could indicate the weakest point inside the individual layer, which could be

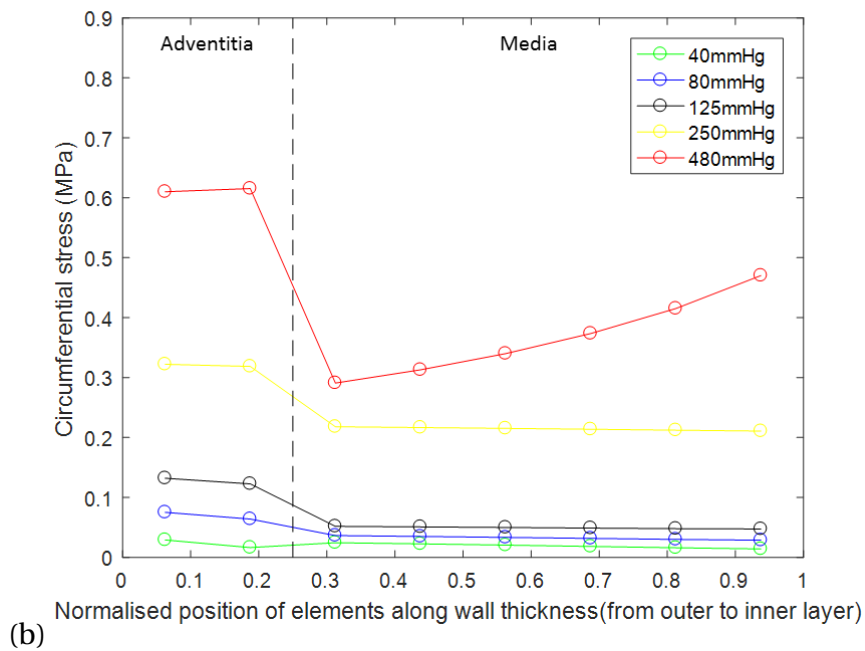
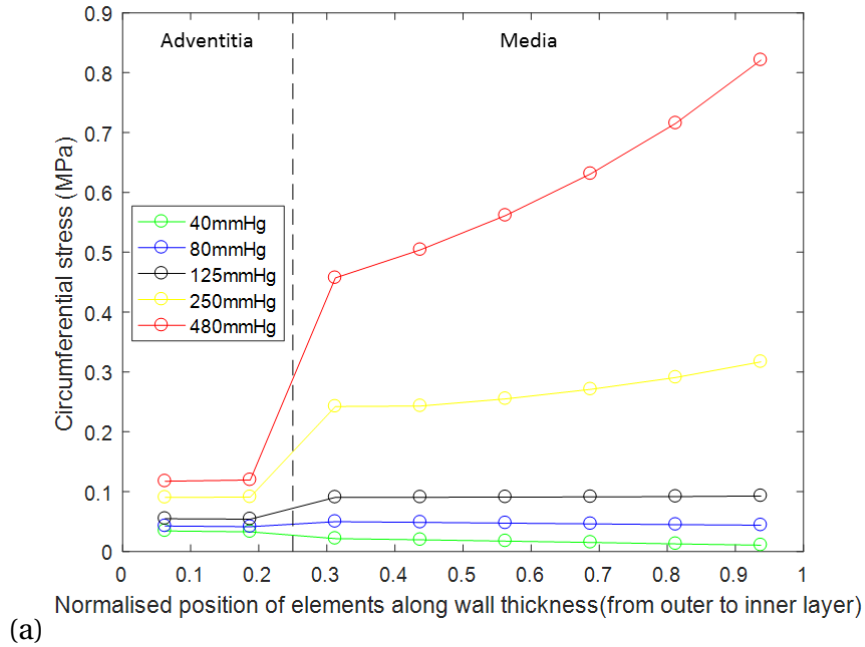


Figure 2.17: Influence of blood pressure on stress distribution through the wall thickness: (a) MECH 1 and FIB 1; (b) MECH 3 and FIB 1.

interpreted as the location at which wall stress exceeds the wall strength and could therefore lead to potential rupture under different physiological circumstances.

## 2.5 DISCUSSION AND CONCLUDING REMARKS

This chapter presents the implementation of the arterial structure into the ANSYS computational model. A simple tube-like, thick-walled model is used as an example for modelling a healthy artery. The mechanical responses are solved numerically based on the SEF proposed by Holzapfel et al. (2000), which are matched by the **EXPO** function of anisotropic-hyperelastic material in ANSYS. Moreover, a critical feature of the *in vivo* state of the vessel wall, the residual stress, is introduced into the numerical model. By rightly defining the zero-stress state, load-free state, and loaded state of arteries, the cylindrical thick-walled model can induce the residual stresses within the vessel wall by sealing an opening angle from the reference configuration. The ANSYS model investigates the influence of the opening angle on the circumferential stress distribution through the wall thickness. Comparison between the results of different opening angles helps to optimise a uniformly distributed stress field inside this specific cylindrical model. The purpose of this optimisation is to mimic the favourable physiological mechanical environment for the vessel wall in normal conditions (homeostatic state). Furthermore, different types of mechanical behaviours for the layer-specific responses are also demonstrated by the ANSYS model.

This whole framework for modelling the arterial structure is executed in the ANSYS engineering software in an automated manner, and the parameters can be updated with any available experimental data by updating the input files generated within the MATLAB editor. The advantage of this computational framework is to systematically simulate the mechanical environment of this arterial example whilst simultaneously validating any boundary changes on physiological loads. Hence the interaction between the *in vivo*, *in vitro*, and *in silico* models can enhance our understanding of vascular biomechanics. In addition, biological tissues tend to stay in a homeostatic stress/strain range. If the values of stress/strain inside tissues are beyond the range of homeostasis, this will lead to an adaptive procedure to regulate the tissue structure. This computational framework provides a basis for an updating potential in order to model the disturbance of the mechanical environment and subsequently the G&R process of constituents (e.g. elastin and collagen) within the

tissues. Application to the modelling of aneurysm evolution will be discussed in Chapter 4 and Chapter 5.

## ADVECTION-DIFFUSION MODELLING OF OXYGEN TRANSPORT THROUGH THE ARTERIAL WALL

---

This chapter presents a preliminary study of oxygen transport modelling in a cylindrical vascular model with the presence of thrombus. It is assumed that the thrombus layer increases the resistance of the oxygen delivery from the lumen-thrombus interface resulting in the disturbance of the oxygen homeostasis within the arterial wall. Section 3.1 gives a general motivation for adding the influence of oxygen transport on modelling arterial diseases. In Section 3.2, a description of the conceptual two-layered (thrombus and wall) model is provided with the review of physiological values on transport properties. In Section 3.3, the diffusion-only analytical derivation is presented to describe the oxygen concentration across the thrombus and arterial wall in the steady state. In Section 3.4, numerical results from the implementation of transport modelling in ANSYS are compared with the analytical solution, which show a good agreement between the two approaches. Thus the ANSYS implementation of oxygen transport is ready to be incorporated in the computational framework on modelling the evolution of aneurysms in Chapter 4 and 5. Parametric simulations involving the influence of thrombus thickness, cellular respiration rate and diffusivity within the wall on oxygen distributions are demonstrated in Section 3.5.

---

**Objective:** the objective of this chapter is to model the distribution of oxygen concentration through the aneurysm wall by the numerical implementation of ANSYS software. This model will then be coupled in the proposed G&R framework to simulate the alteration of oxygen transport within the thrombosed aneurysm wall in

each time step during the aneurysm evolution. The change of oxygen level within the wall would have influence on the collagen synthesis thus affect the aneurysm structure.

### 3.1 OXYGEN MASS TRANSPORT IN ARTERIES

Transport of blood-borne materials by the artery is not only delivering materials to surrounding tissues but also essential to maintain the arterial wall physiology. Disturbance of the transport of such materials may lead to the pathogenesis of vascular diseases. One major study among the transport of blood-borne materials is that of oxygen delivery, since it is important for cellular metabolic activity. Most studies on oxygen transport are associated to the progression of atherosclerosis as arterial wall hypoxia has been suggested as one important factor to its formation (Crawford and Blankenhorn (1991); Kojda and Harrison (1999); Harrison et al. (2003); Kaneto et al. (2010)). However, the limited research into the influence of oxygen variations on vascular aneurysms (Vorp et al., 1996) motivates our work to investigate their correlation based on atherosclerosis studies.

Although the atherosclerotic formation is not fully understood, it generally occurs at bifurcations and locations in response to haemodynamic WSS (Irace et al. (2004); Cunningham and Gotlieb (2005)). Himburg et al. (2004) proposed a leading hypothesis that the observed locations of low WSS related to wall hypoxia, which could lead to increased endothelium permeability and allow the accumulation of fat molecules into the vessel wall, and hence resulting in the progression of atherosclerosis. Consequently, this hypothesis has led to the development of mass transport modelling of various molecules in arteries, such as low-density lipoprotein (LDL) (Wada and Karino (1999); Ueda et al. (2004); Sun et al. (2007)) and oxygen (Back (1976); Moore and Ethier (1997); Qiu et al. (2000); Kaazempur-Mofrad et al. (2005)), which are deemed to play key roles on vascular pathophysiology.

As the focus here is the oxygen transport in arteries, analysis is normally complicated by two parts, blood-side and wall-side:

**Blood-side:** Oxygen is carried in the blood by free dissolved oxygen in the plasma and oxygen bound to hemoglobin (Hb) within red blood cells, where high percentage of oxygen (98.5%) in the blood is transported by the Hb. The binding of oxygen to Hb is highly nonlinear due to the nonlinear dependence of Hb-oxygen

saturation on plasma oxygen partial pressure (Moore and Ethier, 1997). As the oxygen partial pressure increases, the Hb-oxygen saturation also increases. In addition, carbon dioxide level, blood pH, body temperature, and diseases could also affect the carrying capacity and delivery of oxygen in the blood. From the modelling perspective, both the axial and radial profiles of oxygen concentrations in the blood can be solved by the convection-diffusion equations at the lumen/wall interface.

**Wall-side:** Oxygen transport within the arterial wall is solved by steady state diffusion modelling for the radial direction through the wall thickness. Each layer in the wall may have different oxygen diffusivity and consumption terms due to various cells embedded in. The diffusive flux is deemed to be continuous at each interface and boundary.

Moore and Ethier (1997) concluded that oxygen transport is primarily determined by wall-side effects, by means of the oxygen consumption by wall tissue and the resistance of oxygen diffusion through the wall. Hence, for the development of our computational framework for modelling aneurysm disease, we emphasise the wall-side effect of arteries and investigate the influence of oxygen diffusion and consumption parameters as they may change during aneurysm evolution. Furthermore, the G&R framework would focus on the solid model for the illustrative purpose of linking oxygen concentration to aneurysm evolution in later chapters. Flow-side effects on oxygen transport can be simulated as a boundary condition of concentration at the interface of lumen/endothelium or lumen/thrombus.

The following sections investigate the mass transport of molecules by modelling the oxygen transport within the arterial wall, in healthy and thrombosed arteries. The comparison between analytical and numerical approaches will be discussed in Section 3.4.

### 3.1.1 Oxygen transport in healthy arteries

#### 3.1.1.1 Pioneering analytical models

The pioneering analytical model of oxygen mass transport in 2D axisymmetric large arteries is proposed by Back (1975). The model focused on analytically solving blood flow domain by Navier-Stokes flow equations for the oxygen mass transport boundary at the lumen/wall interface. The transmural transport of oxygen across the arterial wall was not taken into account. An improvement of the model was made

by Back (1976) to include a single layer wall for transport modelling. The continuous diffusion flux boundary condition is applied at the lumen/wall interface for connecting the effects on both phases, blood flow and arterial wall. An oxygen consumption term in the wall was introduced to represent the utilisation of oxygen by the cells. Therefore, an analytical model solving for oxygen transport across both the blood-side and the wall-side was developed. Results demonstrated that flow pulsatility had a minor effect on the oxygen concentration near the lumen/wall interface hence we only conduct steady state results for the simulation. Additionally, oxygen distribution is highly affected by the endothelial permeability and cellular respiration in the wall which emphasise the importance of including the wall-side mass transport in the modelling (Schneiderman and Goldstick (1978); Schneiderman et al. (1982)). It is of note that the wall-side is the dominant term of oxygen mass transport modelling.

Furthermore, Buerk and Goldstick (1982) carried out an *in vivo* experiment of a dog thoracic aorta whereby measured transmural oxygen partial pressure profiles which were compared to analytical diffusion calculations across the wall. Curve fitting of experimental data to analytical solutions led to the speculation that vascular transport properties (diffusion coefficient and consumption rate) are spatially varied through the vascular layers (intima, media, and adventitia).

### 3.1.1.2 Computational modelling of oxygen transport

Advancements in computational models using the finite element approach have led to the emergence of numerical transport modelling of 3D patient geometric arteries (Rappitsch et al., 1997). A major focus of the numerical model is on linking the haemodynamics, i.e. wall shear stress (WSS), to the endothelial permeability (Qiu et al. (2000); Tarbell (2003); Tada and Tarbell (2006)), especially at the bifurcation and marked curvature in the arteries. It is believed that the WSS has great influence on the endothelial transport barrier for the permeability of large molecule such as LDL (Tarbell, 1993). However, for gases such as oxygen, the permeation is very high through the endothelium (Liu et al., 1994). Therefore, the consideration of endothelial permeability of oxygen may be too restrictive. Nonetheless, the flow condition is still in a strong correlation with the oxygen diffusion. A 2D stenosis model (Rappitsch and Perktold, 1996) demonstrated an oxygen reduction at downstream of a stenosis which may limit the oxygen transport in both the fluid-side and wall-side. In addition, Ma et al. (1997) computed the influence of low WSS on the spatial vari-

ation of oxygen levels within the lumen by simulating a CFD model of a carotid bifurcation.

Moore and Ethier (1997) carried out a two-side simulation on a 2D axisymmetric stenosed artery:

- For the fluid-side, the convection and diffusion of oxygen is solved within the lumen. As mentioned previously, the nonlinear saturation of Hb-oxygen is considered.
- For the wall-side, the transport of oxygen is determined by the diffusive flux and the oxygen consumption rate by the cells. Both terms remain constant across the wall in this model.

The two-phase model was then compared with a fluid-phase only model with a constant boundary condition at the lumen/wall interface. Comparison between the two models suggested that the resistance of the oxygen transport in the wall-side is much greater than the resistance in the flow-side. The local oxygen level is mainly controlled by the oxygen demand from the wall-side due to the prescribed oxygen consumption term. Moreover, the variation of wall thickness has great effects on the transmural oxygen distribution across the wall, but has no effect at the boundary of lumen/wall interface. This work highlighted the importance of taking into account the wall-side effect on oxygen transport.

On the other hand, numerous numerical studies have focused on 3D arterial models to investigate the influence of geometric effect on fluid-side oxygen transport (Qiu et al. (2000); Kaazempur-Mofrad and Ethier (2001); Tada and Tarbell (2006); Coppola and Caro (2008)). Although these models provided significant evidence that the blood flow patterns have a great impact on the oxygen transport, the lack of wall-side effect (especially the oxygen consumption term) cannot fully represent the oxygen concentration in a physiological domain of arteries. Tada (2010) then conducted a coupled fluid-wall model in a 3D idealised geometry of carotid bifurcation from the fluid-side only model (Tada and Tarbell, 2006). Comparison between these two models revealed that the fluid-side effect is dominated by the wall-side consumption term, while the wall-side oxygen transport is also limited by the blood flow condition.

### **3.1.2 Oxygen transport in diseased arteries: thrombosed aneurysms**

Wolf et al. (1994) carried out a series of clinical observations on 80 AAAs in the time period of 8 years. They compared the geometry of AAAs and the thrombus volume within (commonly observed in AAA ~75% (Harter et al., 1982)): a significant correlation was found between thrombus development and aneurysm evolution. Based on this observation, Vorp et al. (1996) proposed an initial hypothesis that the thrombus layer increases the resistance of oxygen diffusion from the lumen to the arterial wall resulting in the aggressive weakening of the aneurysm wall. This hypothesis was then applied to an idealised axisymmetric AAA model to investigate the effect of thrombus thickness on oxygen distribution (Vorp et al., 1998). The AAA model was simulated for steady state diffusion of oxygen with a constant oxygen level at the lumen/thrombus boundary, while the thrombus layer is a homogeneous layer in diffusivity, and a continuous diffusion flux at the thrombus/wall interface is driven by the consumption rate in the wall. Although this model has simplified boundary conditions, it still demonstrated that the thrombus thickness has great influence on the oxygen level at the thrombus/wall interface, and consecutive effect in the wall. Boundary conditions of the transport modelling presented in this chapter is primary based on this study.

Sun et al. (2009) conducted a numerical study of a coupled fluid-wall model on a patient-specific geometry of a thrombosed AAA. The CT scan only provided the geometries of lumen and thrombus, thus a uniform thickness of arterial wall is artificially created on the thrombus to model the wall-side effect. Flow through the thrombus is deemed negligible, thus the thrombus layer is modelled as another solid wall layer. Results shown that there is insignificant spatial variation of oxygen concentration at the lumen/thrombus interface. However, the thickness of thrombus layer appears to be a strong factor on the impedance of oxygen transport to the arterial wall. If the thrombus thickness is greater than 5 mm, the oxygen supply can be reduced by 80% from the lumen to the thrombus/wall interface.

### 3.1.3 Potential influence of oxygen concentration on aneurysm evolution

The goal of this research is to extend current Fluid-Solid-Growth (FSG) framework with diffusion modelling to investigate the oxygen transport and its link to aneurysm evolution. Existing G&R frameworks focus on the influence of mechanical stimuli acting on the vascular structure. Very few studies concentrate on the influence of chemical transport during the evolution of arterial diseases. Thus, we develop a computational framework to link the disturbance of the chemical environment (i.e. oxygen concentration) on cellular functionality, and consequently on the G&R of the vascular structure. Holland (2012) studied the effect of thrombus on the delivery of oxygen to an arterial wall and the consecutive influence on the G&R of collagenous constituents therein. Based on this study, we propose a computational G&R model integrated into ANSYS to include the influence of biochemical transport, and to build up a computational platform for modelling aneurysm evolution. More details on quantifying the influence of oxygen concentration on G&R within the aneurysm models are described and illustrated in Chapter 4 and Chapter 5.

## 3.2 MODEL DESCRIPTION FOR OXYGEN TRANSPORT

### 3.2.1 Artery geometry

The simple tube model consists of two layers: (i) a thrombus layer of constant thickness through the length of the model (ii) a homogeneous arterial wall as shown in Figure 3.1. Note that the arterial wall is described as a two-layered constitutive model (with media and adventitia) in Chapter 2, yet in this conceptual tube model, the diffusion property within the arterial wall is assumed to be homogeneous. The geometric attribute is taken from the anterior communicating artery where 30% of IAs are observed (Brisman et al., 2006). The physiological dimensions of the arterial tube model are the approximated numbers obtained from Moore et al. (2006) demonstrated in Figure 3.1. A "healthy" artery is defined when there is no thrombus formation to interfere with the oxygen transport to the endothelium of the artery. Here we implement a thrombus layer with the same thickness as the arterial wall to model the "diseased" artery. Further comparison of the influence between different thrombus thicknesses on oxygen transport will be presented in Section 3.6.1.

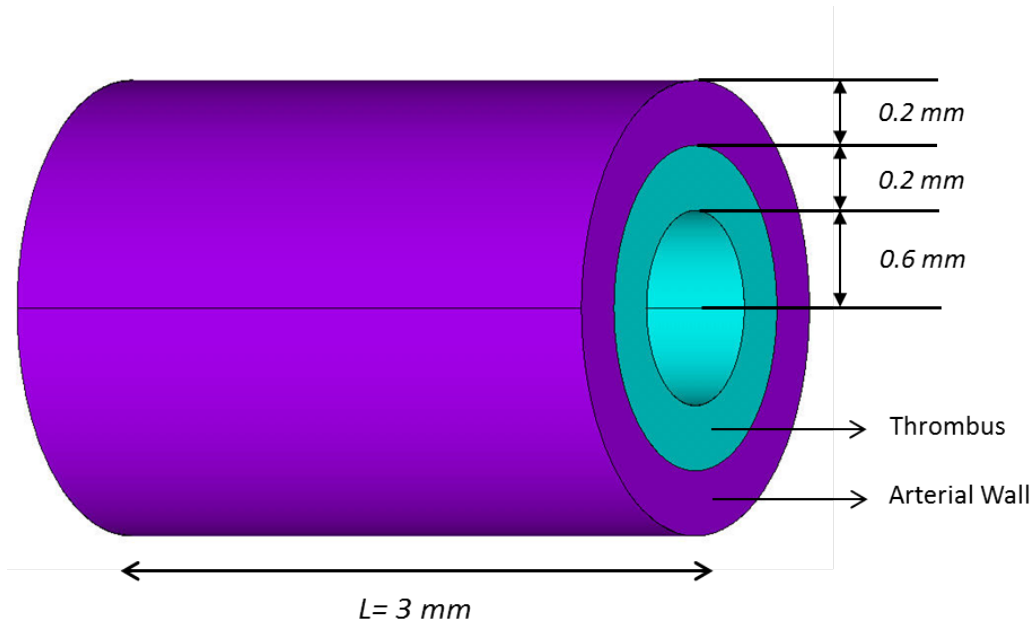


Figure 3.1: Illustrative cylindrical model of a thrombosed artery for oxygen transport modelling.

### 3.2.2 Oxygen transport properties

The oxygen diffusion properties of the artery are adapted from Moore and Ethier (1997), who proposed a 2D fluid-mass transfer model within the arterial lumen and wall. We focus on the solid part (wall and thrombus) of oxygen diffusion to be implemented in the G&R framework on arterial constituents.

#### **Arterial wall**

The oxygen through the arterial wall is firstly in contact with the endothelium. As the endothelial permeability to oxygen is very high (Tarbell and Qui, 2000), we assume the oxygen molecules are 100% passing through the first interface of the arterial structure. According to experimental measurements from Back (1976) and Tedgui and Lever (1984), the filtration velocities through the wall are in the range of  $1 \times 10^{-2}$  to  $1 \times 10^{-3}$ (mm/s). A simple evaluation made by Moore and Ethier (1997) showed that the diffusivity can be represented as the following equation:

$$D_w = V_D \times H_w \quad (3.1)$$

where  $D_w$  is the diffusivity of wall;  $V_D$  is the filtration velocity;  $H_w$  is the wall thickness. The diffusivity  $D_w$  is defined as a rate of diffusion, in this case, it repre-

sents the driving force of oxygen distributing within the wall. Higher diffusivity results in faster spread through the wall domain. For the particular values of  $V_D = 5 \times 10^{-3}$  (mm/s) and  $H_w = 0.2$  (mm), the diffusivity  $D_w$  equates to  $1 \times 10^{-3}$  ( $mm^2/s$ ) or  $1 \times 10^{-9}$  ( $m^2/s$ ). Additionally, based on the experimental measurement from Schneiderman and Goldstick (1978), the diffusivity coefficient of oxygen in the arterial wall is  $0.9 \times 10^{-9}$  ( $m^2/s$ ), which matches the mathematical approximation from equation (3.1).

### ***Thrombus***

Research (Adolph et al., 1997) shows that the thrombus layer is more permeable than the arterial wall. Further correlations between the structural properties in the thrombus and the clot permeability are revealed by Diamond (1999). According to the experimental data from Murray (1971), the diffusivity coefficient of oxygen in the thrombus layer is  $2.4 \times 10^{-9}$  ( $m^2/s$ ) which is two or three times greater than the diffusivity in the arterial wall.

## **3.2.3 Oxygen consumption rate**

### ***Arterial wall***

The metabolic activity of oxygen is primarily conducted by the SMCs in the media layer and the fibroblasts in the adventitia layer. The oxygen consumption rates, based on experimental measurements in physiological models, are summarised in Table 3.1. It can be seen that the respiration rates differ by species and type of artery. This may be due to the cellular wall composition inside the artery. One important finding (Buerk and Goldstick, 1982) is that the consumption rate varies along the radial direction through the arterial wall. More importantly, a slightly greater consumption amount is observed in the media layer due to the SMCs embedded within which require a greater level of energy to maintain cellular functionality. However, in this preliminary study of oxygen transport, we model the arterial wall as a homogeneous layer with a constant consumption rate. The variations in consumption rates will not be demonstrated but the overall distribution of oxygen across the arterial wall is shown. For modelling purposes, in order to choose one specific parameter for the respiration rate of the arterial wall, we take into account the value from the human aorta  $Q_w = 9.3 \times 10^{-4}$  ( $mol/m^3/s$ ) in Table 3.1. As this value is very close to the consumption rate  $Q_w = 1 \times 10^{-3}$  ( $mol/m^3/s$ ) for a pig carotid artery, for the para-

<i>Artery</i>	<i>Consumption rate</i> (mol/ $m^3$ /s)	<i>Reference</i>
Human aorta	$9.3 \times 10^{-4}$	Kirk et al. (1954)
Rabbit aorta	$1.6 \times 10^{-4}$	Whereat (1961)
Dog femoral artery	$5.8 \times 10^{-3}$	Crawford et al. (1983)
Pig carotid artery SMCs	$2.8 \times 10^{-4}$	Barron et al. (1996)
Pig carotid artery SMCs	$1.0 \times 10^{-3}$	Pittman and Duling (1973)
Pig carotid artery SMCs	$1.8 \times 10^{-4}$	Krisanda and Paul (1984)

Table 3.1: Experimental values of oxygen consumption rate in physiological models

metric study conducted in Section 3.6.2 to analyse the influence of consumption rates, it is more convenient to use an integer value. Thus the oxygen consumption rate in the wall,  $Q_w = 1 \times 10^{-3}$ (mol/ $m^3$ /s), is implemented in the conceptual tube model and further studies in Chapter 4 and 5.

### **Thrombus**

Cells embedded in the thrombus layer are mostly circulating cells such as T-cells and macrophages such that the respiration rate is relatively low according to experimental observations (Adolph et al., 1997). Therefore, we assume the amount of oxygen consumed in the thrombus is negligible. In terms of transport modelling, the oxygen consumption rate in thrombus  $Q_{th}$  is set to be 0.

## **3.3 THEORY AND METHODOLOGIES**

### **3.3.1 Steady-state oxygen diffusion through thrombus and wall**

The oxygen distribution is deemed to be a steady state diffusion-only transport through the thrombus and arterial wall. Theoretical solution of diffusion is governed by Fick's law (Bird et al., 2015):

$$\{J\} = -[D]\nabla C \tag{3.2}$$

It is also governed by the mass balance equation:

$$\nabla\{J\} + \frac{\partial C}{\partial t} = Q \quad (3.3)$$

where  $\{J\}$ =diffusion flux;  $[D]$ =diffusivity matrix;  $C$ =concentration of substance;  $Q$ =diffusion substance generation rate;  $\nabla$  is the gradient operator. Note that  $Q$  is a negative value as we define it as consuming the oxygen. For the steady state diffusion equation, only the stabilised condition is considered and independent of time. Thus the oxygen transport equation for a cylindrical model of radius  $r$  can be written as:

$$D \frac{\partial}{\partial r} \left( r \frac{\partial C}{\partial r} \right) = -rQ \quad (3.4)$$

### 3.3.1.1 Oxygen through the thrombus

It is suggested that very little amount of oxygen is consumed within the thrombus layer, so that the governing equation from (3.4) can be modified as:

$$D_{th} \frac{\partial}{\partial r} \left( r \frac{\partial C_{th}}{\partial r} \right) = 0 \quad (3.5)$$

where the  $C_{th}$  and  $D_{th}$  are the concentration and diffusivity for the thrombus layer respectively. The mathematical representation of concentration in thrombus can be yielded from (3.5):

$$C_{th}(r) = A_1 \ln r + B_1 \quad (3.6)$$

where  $A_1$  and  $B_1$  are real parameters which can be determined by the boundary conditions.

### 3.3.1.2 Oxygen through the wall

The arterial wall consumes the oxygen with a consumption rate  $Q_w$  by cells, so that the governing equation from (3.4) can be modified as:

$$D_w \frac{\partial}{\partial r} \left( r \frac{\partial C_w}{\partial r} \right) = -rQ_w \quad (3.7)$$

where the  $C_w$  and  $D_w$  are the concentration and diffusivity for the arterial wall respectively. The concentration of oxygen through the wall corresponds to the radial direction which satisfies the following equation:

$$C_w(r) = -\frac{r^2 Q_w}{4D_w} + A_2 \ln r + B_2 \quad (3.8)$$

where  $A_2$  and  $B_2$  are real parameters which can be determined by the boundary conditions.

### 3.3.2 Boundary conditions

Two types of boundary conditions for the derivation of oxygen transport are presented here:

- Case 1: fixed concentrations at the inner and outer surface
  - (a) Fixed concentrations at the inner and outer surfaces of the artery;
  - (b) Continuous concentration at the interface of two layers;
  - (c) Continuous diffusion flux at the interface of two layers.
- Case 2: free diffusion flux at the outer surface
  - (a) Known concentration at the inner surface only;
  - (b) Continuous concentration at the interface of two layers;
  - (c) Continuous diffusion flux at the interface of two layers;
  - (d) Free diffusion flux at the outer surface.

Both cases are applied for mathematical representation to depict the oxygen distribution across the two-layered model. Case 1 is for modelling the stabilised condition when concentrations are known inside and outside the artery. Case 2 is for modelling the steady state when only the oxygen concentration inside the fluid is known initially. The cross-section of the tube model and the geometrical indices are shown in Figure 3.2.

#### 3.3.2.1 Fixed concentrations at the inner and outer surfaces

This section shows Case 1 boundary condition with known concentrations at the inner and outer surfaces, and derivative analytical solutions for the concentration through the two layers. Taking into account the concentrations at the lumen/thrombus ( $r = r_{th}$ ) and adventitia ( $r = r_a$ ) boundaries imply the following equations:

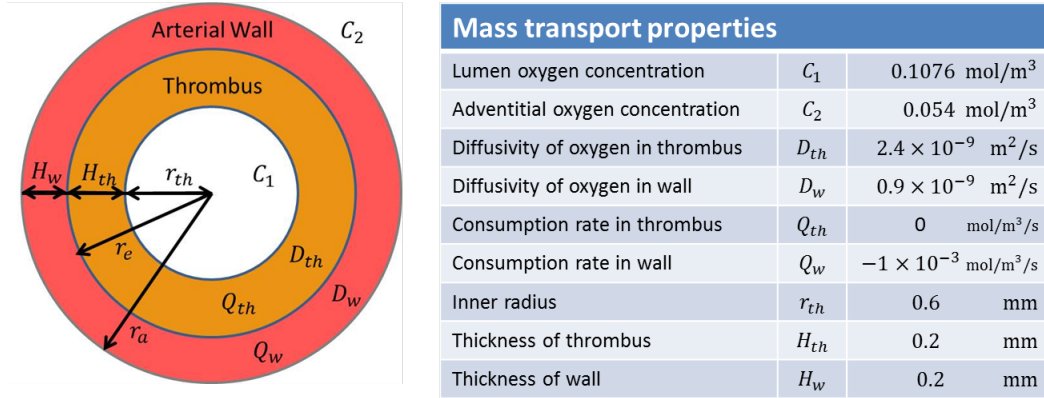


Figure 3.2: Cross-section of arterial geometry (left); Parameters of geometrical, material and transport properties, and boundary conditions (right).

$$C_{th}(r_{th}) = C_1 \quad C_1 = A_1 \ln r_{th} + B_1 \quad (3.9)$$

$$C_w(r_a) = C_2 \quad C_2 = -\frac{r_a^2 Q_w}{4D_w} + A_2 \ln r_a + B_2 \quad (3.10)$$

where  $C_1$  and  $C_2$  indicate the oxygen concentration at the lumen/thrombus interface and the outermost layer respectively.

At the thrombus/wall interface ( $r = r_e$ ), continuous concentration yields the equation (3.11) and continuous diffusion flux yields equation (3.12).

$$C_{th}(r_e) = C_w(r_e) \quad A_1 \ln r_e + B_1 = -\frac{r_e^2 Q_w}{4D_w} + A_2 \ln r_e + B_2 \quad (3.11)$$

$$J_1|_{r=r_e} = J_2|_{r=r_e} \quad D_{th} r_e \left( \frac{A_1}{r_e} \right) = D_w r_e \left( -\frac{r_e Q_w}{2D_w} + \frac{A_2}{r_e} \right) \quad (3.12)$$

$C_1$  and  $C_2$  are known constants of the concentrations at the boundaries which leave four unknowns:  $A_1$ ,  $A_2$ ,  $B_1$ ,  $B_2$  defined in the consecutive boundary equations (3.9), (3.10), (3.11), and (3.12). By rearranging and solving the above boundary equations, the unknown parameters can be expressed with  $C_1$  and  $C_2$  as follows:

$$A_2 = \frac{(C_2 - C_1) - \frac{Q_w}{4D_w} (r_e^2 - r_a^2) - \frac{D_w}{D_{th}} \left( \frac{r_e^2 Q_w}{2D_w} \right) \ln \frac{r_{th}}{r_e}}{\ln \frac{r_a}{r_e} - \frac{D_w}{D_{th}} \ln \frac{r_{th}}{r_e}} \quad (3.13)$$

$$A_1 = \frac{D_w}{D_{th}} \left( -\frac{r_e^2 Q_w}{2D_w} + A_2 \right) \quad (3.14)$$

Hence  $A_1$  and  $A_2$  can be replaced in (3.9) and (3.10) to define  $B_1$  and  $B_2$ :

$$B_1 = C_1 - A_1 \ln r_{th} \quad (3.15)$$

$$B_2 = C_2 - A_2 \ln r_a + \frac{r_a^2 Q_w}{4D_w} \quad (3.16)$$

Substituting the above parameters back to equation (3.6) and (3.8) yields the analytical solution of oxygen diffusion in radial position across the thrombus and arterial wall for Case 1 boundary conditions.

### 3.3.2.2 Free diffusion flux at the outer surface

This section derives the analytical solutions for Case 2 boundary conditions: only the oxygen concentration inside the fluid is known initially. Taking into account the concentration at the lumen/thrombus interface ( $r = r_{th}$ ) and free diffusion flux at the outer surface of adventitia ( $r = r_a$ ) imply the following equations:

$$C_{th}(r_{th}) = C_1 \quad C_1 = A_1 \ln r_{th} + B_1 \quad (3.17)$$

$$J_2|_{r=r_a} = 0 \quad -D_w r_a \left( -\frac{r_a Q_w}{2D_w} + \frac{A_2}{r_a} \right) = 0 \quad (3.18)$$

At the thrombus/wall interface ( $r = r_e$ ), continuous concentration yields the equation (3.19) and continuous diffusion flux yields equation (3.20).

$$C_{th}(r_e) = C_w(r_e) \quad A_1 \ln r_e + B_1 = -\frac{r_e^2 Q_w}{4D_w} + A_2 \ln r_e + B_2 \quad (3.19)$$

$$J_1|_{r=r_e} = J_2|_{r=r_e} \quad D_{th} r_e \left( \frac{A_1}{r_e} \right) = D_w r_e \left( -\frac{r_e Q_w}{2D_w} + \frac{A_2}{r_e} \right) \quad (3.20)$$

Free diffusion flux in equation (3.18) automatically generates  $A_2$  value:

$$A_2 = \frac{r_a^2 Q_w}{2D_w} \quad (3.21)$$

then substituting  $A_2$  into equation (3.20) yields  $A_1$ :

$$A_1 = \frac{Q_w}{2D_{th}} (r_a^2 - r_e^2) \quad (3.22)$$

Hence  $B_1$  and  $B_2$  can be defined with the given values of  $A_1$  and  $A_2$  in (3.22) and (3.21)

$$B_1 = C_1 - A_1 \ln r_{th} \quad (3.23)$$

$$B_2 = A_1 \ln r_e + B_1 + \frac{r_e^2 Q_w}{4D_w} - A_2 \ln r_e \quad (3.24)$$

Substituting the above parameters back to equation (3.6) and (3.8) yields the analytical solution of oxygen diffusion in radial position across the thrombus and arterial wall for Case 2 boundary conditions.

### 3.4 ANSYS IMPLEMENTATION

This section demonstrates the implementation of diffusion fundamentals in ANSYS diffusion modelling. It basically follows the theoretical derivations in Section 3.3. Substituting (3.2) and (3.3) produces the second Fick's law:

$$\frac{\partial C}{\partial t} = [D] \nabla^2 C + Q \quad (3.25)$$

where  $\nabla^2$  is the Laplacian operator. As this work solves for steady-state diffusion modelling, the applicable boundary conditions and loads are: (1) specific concentration; (2) specific diffusion flux acting on a surface; (3) diffusion substance generation rate  $Q$ . The concentration is determined over the finite element as follows:

$$C = \{N\}^T \{C_e\} \quad (3.26)$$

where  $\{N\}$  is element shape function;  $\{C_e\}$  is nodal concentration vector. The finite element approximation is generated by substituting (3.26) in (3.25):

$$[C^d] \{\dot{C}_e\} + [K^d] \{C_e\} = \{R_e^{flx}\} + \{R_e^Q\} \quad (3.27)$$

where  $[C^d] = \int_V \{N\} \{N\}^T dV$  is an element diffusion damping matrix;  $[K^d] = \int_V (\nabla \{N\}^T)^T [D] (\nabla \{N\}^T) dV$  is an element diffusion conductivity matrix;  $\{R_e^{flx}\} = \int_S \{Q_s\} \{N\}^T dS$  is an element diffusion flux vector;  $\{R_e^Q\} = \int_V \{Q\} \{N\}^T dV$  is an element diffusion substance generation load vector.

The matrix equation (3.27) is solved for the nodal concentration vector  $\{C_e\}$ , then the diffusion gradient  $\{g\}$  and the diffusion flux  $\{J\}$  are evaluated in nodal matrix as follows:

$$\{g\} = \nabla C \quad (3.28)$$

$$\{J\} = -[D] \{g\} \quad (3.29)$$

thus the nodal solutions of  $C$ ,  $\{g\}$ , and  $\{J\}$  are computed using the finite element method.

Note that the element type for the finite element model is SOLID240 which is a 3-D, 10-node tetrahedral element with only one degree of freedom, concentration (CONC), at each node. This element is applicable to the steady-state and transient diffusion analyses where this work focuses on steady-state solutions. The volume mesh is generated automatically in conformity with element size. The solution output associated with the element is primarily in the form of nodal concentration according to the nodal position within the element.

To start the ANSYS modelling, in addition to the input of material properties, the input of boundary conditions are given by the following:

- Nodal loads are defined with the **D** command in CONC;
- Surface loads are defined with the **SF** command in diffusion flux (DF);
- Body loads are defined with the **BFE** command in the diffusing substance generation (DGEN) to represent the consumption rate of each element.

Numerical solution of oxygen transport is generated from the ANSYS implementation mentioned above. Computational codes for transport modelling can be found in Listing D.3 of Appendix D. Initial setup involves creating the simple geometry of cylindrical model with defined diffusivities  $D$  and consumption rates  $Q$  in each layer. For both analytical and numerical simulations, we apply the same constitutive model and boundary conditions. All geometrical, material and transport properties, and boundary conditions are summarised in Figure 3.2. Diffusion simulation of the two-layered cylindrical model needs to satisfy the two boundary conditions described in the last section. Results of analytical and numerical solutions in two boundary conditions are compared as follows:

#### **Case 1 boundary condition**

The result of Case 1 boundary condition is shown in Figure 3.3. The oxygen concentrations are fixed at the lumen area and outside the artery as  $C_1 = 0.1076(\text{mol}/\text{m}^3)$  and  $C_2 = 0.054(\text{mol}/\text{m}^3)$  in Figure 3.2 respectively. The fixed value of lumen oxygen concentration  $C_1$  is taken from the observation of a flow-mass oxygen transport model proposed by Holland (2012) that the oxygen concentration in

contact with the inner surface (lumen/wall or lumen/thrombus) is stabilised of that set based on the transport properties stated in Figure 3.2. The given concentration at the outer surface  $C_2$  is an anticipation for approximately half of the oxygen supply is consumed by the arterial wall. The thrombus is considered not to be consuming oxygen and with higher diffusivity. The arterial wall is homogeneous when diffusion modelling, with an oxygen consumption rate  $Q_w$ . Figure 3.3 shows the comparison between the analytical and numerical results, which shows a good agreement between the two modelling approaches. Oxygen concentration within the thrombus layer decreases linearly from inner surface to the thrombus/wall interface with a zero respiration rate. At the interface, the concentration drops approximately 45 % from the deviation between the fixed concentrations  $C_1$  and  $C_2$ . Oxygen concentration within the arterial wall reduces in an exponential curve from the interface and stabilises towards the given concentration ( $C_2$ ) at the outer surface.

#### Case 2 boundary condition

The result of case 2 boundary condition is shown in Figure 3.4, which also shows a good agreement between the analytical and numerical solutions. Only the inner surface is fixed with the concentration  $C_1$ . A free diffusion flux ( $DF=0$ ) at the outer surface is given to determine the concentration when the transport model reaches a steady state. The concentration at the outer surface achieves a constant value  $0.0619(mol/m^3)$  under this boundary condition. The overall oxygen distributions for boundary conditions in Case 1 and Case 2 are identical. Additionally, the values of the fixed concentration  $C_2$  in Case 1 and the stabilised concentration in Case 2 are with minor variation (less than 9% to  $C_1$ ). This indicates that  $C_2$  is a feasible prediction of the concentration at the outer surface.

Under both boundary conditions, the numerical method is validated to represent the analytical solutions with this simple 1D model. Thus, the transport modelling in ANSYS is ready to be implemented to the computational framework for simulating the chemical environment and its effect on aneurysm progression which will be presented in Chapter 4.

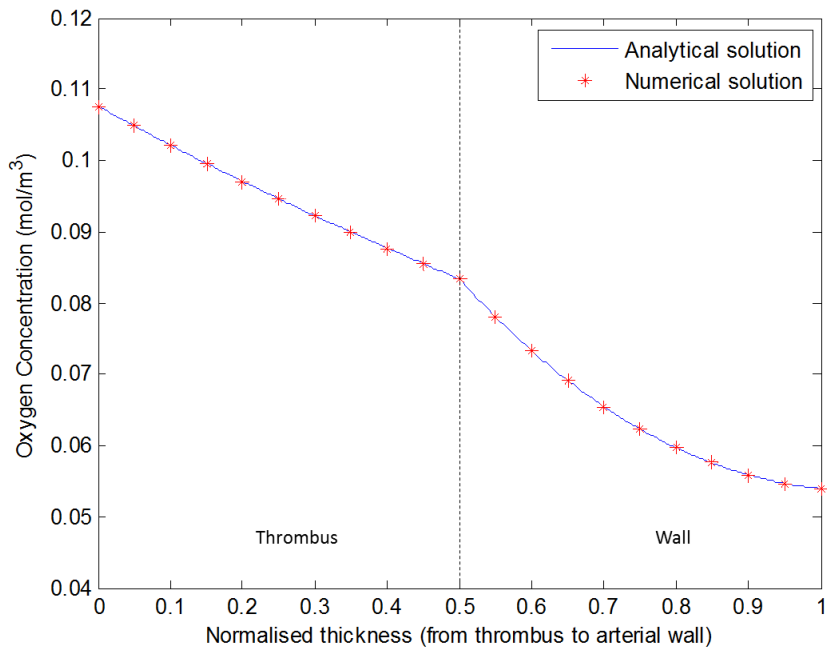


Figure 3.3: Radial profiles of oxygen concentration for Case 1 boundary condition (a fixed concentration ( $C_2=0.052 \text{ mol/m}^3$ ) outside adventitia).

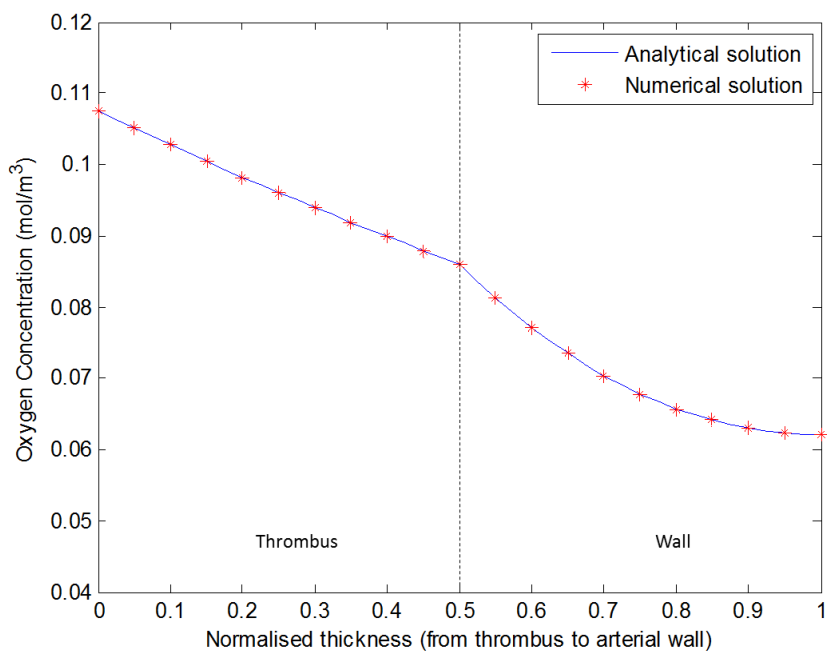


Figure 3.4: Radial profiles of oxygen concentration for Case 2 boundary condition (a free diffusion flux B.C. ( $DF=0$ ) outside adventitia).

Smart Size	Number of meshes	Average error (%) to analytical solution
1	8329	0
3	6819	0
6	4915	0.06
9	2603	0.5

Table 3.2: Comparison of the numerical result generated by different number of elements in oxygen transport modelling.

### 3.5 SENSITIVITY ANALYSIS OF THE NUMBER OF ELEMENTS

For the oxygen transport modelling in ANSYS, a sensitivity analysis of the number of elements is also conducted to examine whether the number of meshes is adequate to represent the analytical solution. In ANSYS, mesh control is defined by the smart size from 1 to 10, where smaller number indicates fine mesh and larger number denotes coarse mesh. The mesh generation in ANSYS is based on the geometric shape. For this simple 1D tube model, the mesh is symmetric along the axial direction. We compare results of smart size equal to 1, 3, 6, and 9 for the sensitivity analysis with the application of case 2 in previous section. Note that the result of case 2 is with the setting of smart size equal to 6, which gives a very consistent result with the analytical solution. In order to compare the data from each smart size, a path is depicted from the inner surface of thrombus to the outer surface of the arterial wall. There are 10 corresponding points along the path to be interpolated as the concentration data. The comparative result of different number of elements is presented in Table 3.2 with the quantification of error percentage. The error percentage of each smart size is the average number of the variation from each 10 points to its analytical solution. For smart size 1 and 3, there is no variation to the analytical solution; for smart size 6 and 9, the error percentage is extremely low. Overall, it shows a great consistency in each smart size due to the simplicity of the 1D model.

### 3.6 INFLUENCE OF THROMBUS THICKNESS, OXYGEN CONSUMPTION RATE AND DIFFUSIVITY ON OXYGEN TRANSPORT

The following results are solved with ANSYS modelling for Case 2 boundary condition with a free diffusion flux at the outer surface. The oxygen transport models reach steady state following perturbations to thrombus layer thickness, respiration rate, and diffusion coefficients. The concentrations at the outer surface ( $C_2$ ) are influenced by these changes in geometric and material properties. This section illustrates and investigates in detail the radial profiles of oxygen distribution through the layers due to these changes. The main purpose is to understand the essential factors of oxygen transport, and possibly mimic the changing environment of oxygen levels with propagating thrombus and cellular adaptive response during aneurysm evolution.

#### 3.6.1 Thrombus thickness effect

Figure 3.5 compares the oxygen transport through different thrombus thicknesses. Material parameters for thrombus and arterial wall remain the same as in Figure 3.2, while the thrombus is propagating towards the centre line of lumen. Figure 3.5(a) shows a healthy artery without thrombus layer. The oxygen concentration is reduced to 79% at the outer surface across the only layer (arterial wall). The balance condition of the healthy artery is defined as the homeostatic state in oxygen transport.

Figure 3.5(b) is the original geometrical configuration for the two-layered model in Figure 3.2. The thrombus layer has the same thickness (0.2mm) as the arterial wall. The reduced amount of oxygen is approximately 20% in both thrombus and wall layers. There is only 80% of oxygen passing through the thrombus/wall interface, hence the oxygen level at the outer surface drops to 59%.

Figure 3.5(c) doubles the thickness of the thrombus in Figure 3.5(b). The oxygen level within the thrombus goes down more rapidly compared to plot(b). At the thrombus/wall interface, the oxygen concentration is down to 51%, while the wall still depletes around 21% of oxygen. Thus, only 30% of oxygen is left at the outer surface when having reached steady state for the thrombus thickness  $H_{th} = 0.4\text{mm}$ .

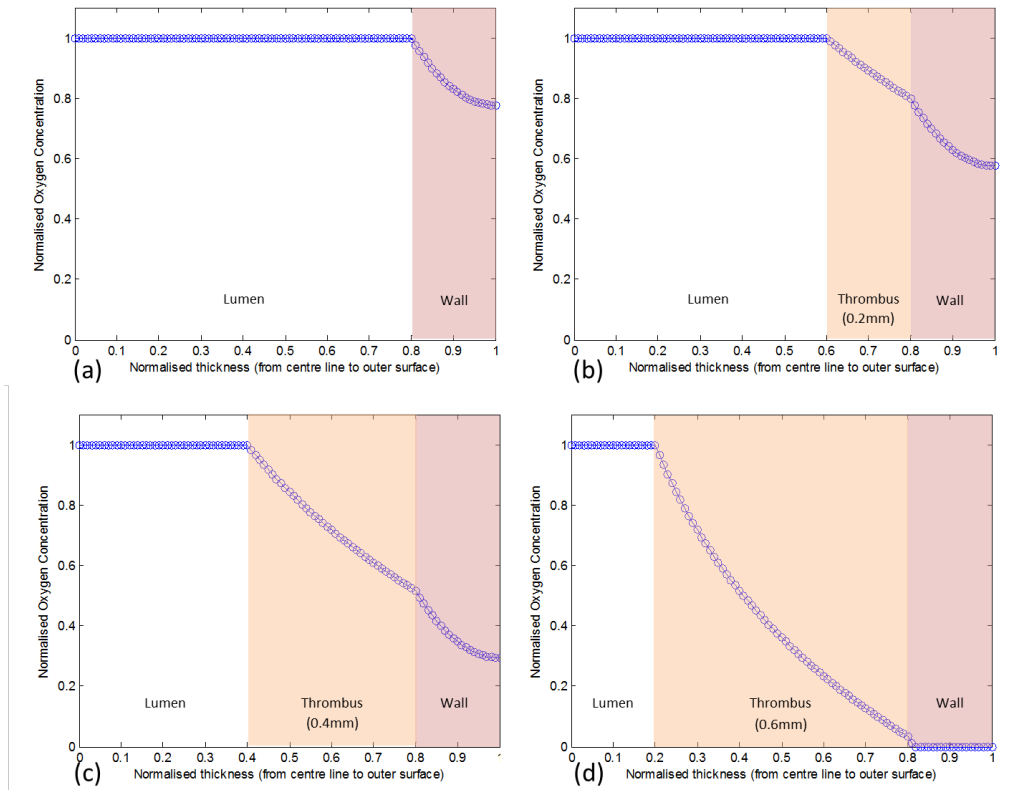


Figure 3.5: Influence of different thrombus thicknesses on normalised oxygen level inside arterial wall: (a) no thrombus (healthy artery); (b)  $H_{th}=0.2\text{mm}$ ; (c)  $H_{th}=0.4\text{mm}$ ; (d)  $H_{th}=0.6\text{mm}$ .

Figure 3.5(d) triples the thickness of the thrombus in Figure 3.5(b). It can be seen that the thrombus increases the resistance of oxygen passing through this domain significantly. Only a very little portion (3%) of oxygen penetrates through the thrombus/wall interface. Inside the arterial wall, there is basically a hypoxic environment with a thick thrombus layer ( $H_{th}=0.6\text{mm}$ ).

Overall, the arterial wall with a fixed thickness ( $H_w=0.2\text{mm}$ ) consumes a constant amount of oxygen ( $\sim 20\%$ ) regardless of the thickness of thrombus layer. The slope of oxygen distribution curve increases across the radial positions as the thrombus thickens. With a thicker thrombus layer, there is an obvious reduction in the transmural oxygen level and an extreme condition whereby a zero oxygen level could be reached within the wall.

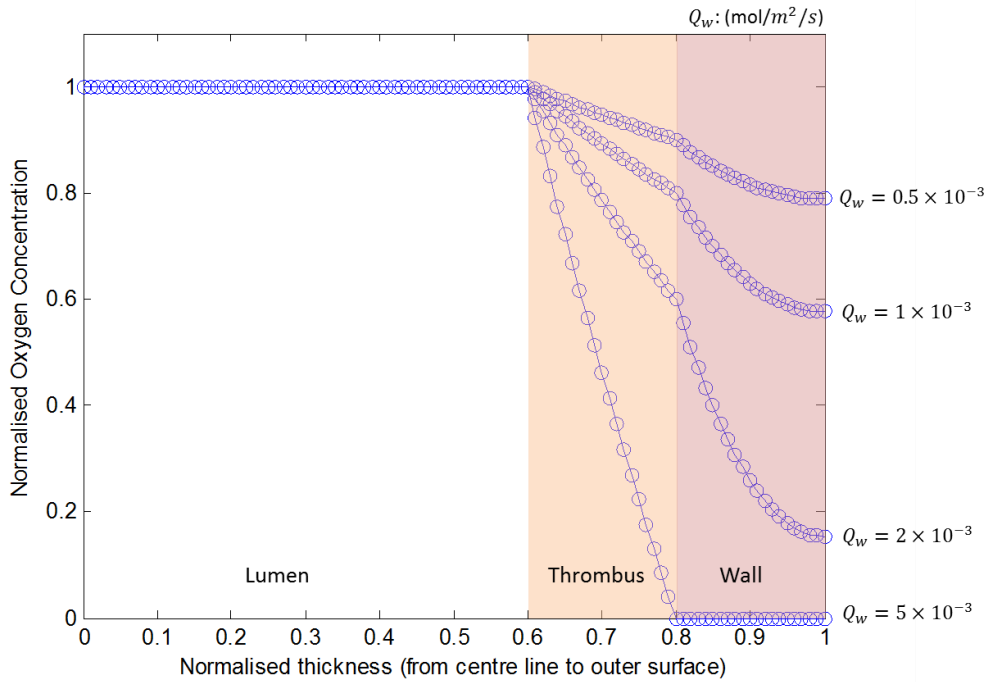


Figure 3.6: Influence of different oxygen consumption rates  $Q_w$  in arterial wall on normalised oxygen concentration across the two-layered model; zero oxygen consumption in thrombus layer.

### 3.6.2 Consumption rate effect

Figure 3.6 shows the influence of oxygen consumption rate to the oxygen transport through the two-layered model which is based on the model described in Figure 3.2. The only changing parameter is  $Q_w : (mol/m^2/s)$ . While  $Q_w = 1 \times 10^{-3}$  is the default consumption rate given by the brief summary in Section 3.2.3, we compare this default value with the two other consumption rates, which are 2 times smaller ( $Q_w = 0.5 \times 10^{-3}$ ) or greater ( $Q_w = 2 \times 10^{-3}$ ) than the original set-up. With a smaller consumption rate in the wall ( $Q_w = 0.5 \times 10^{-3}$ ), the oxygen is allowed to diffuse slowly throughout the domain and stabilised at 80% at the outer surface. Only a very little amount of oxygen is required by this low respiration rate in the wall ( $\sim 10\%$ ), hence the oxygen level stays high in both the thrombus and the wall. Note that with the consumption rate reduced to half ( $Q_w$  changes from  $1 \times 10^{-3}$  to  $0.5 \times 10^{-3}$ ), the consuming amount of oxygen inside the wall is decreased from 20% to 10% which is proportional to the degree of  $Q_w$  change. Whilst with a greater consumption rate in the wall ( $Q_w = 2 \times 10^{-3}$ ), the oxygen level instantly drops to 16% at the outer sur-

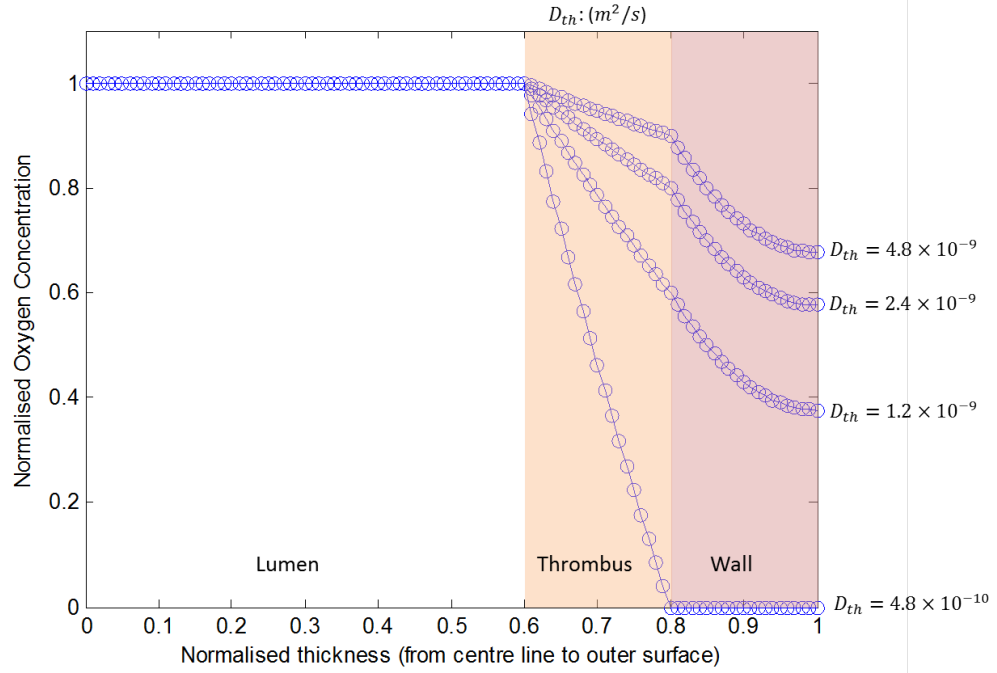


Figure 3.7: Influence of different diffusivities in thrombus layer  $D_{th}$  on normalised oxygen concentration across the two-layered model.

face and the amount of oxygen consumed by the wall is more than 40%. Although there is still remaining oxygen inside the arterial wall, the average oxygen concentration is reduced to approximately only 35% to maintain the tissue functionality. In addition, we model a lower bound of consumption rate which is 5 times greater than the default value ( $Q_w = 5 \times 10^{-3}$ ) for the zero oxygen condition (hypoxia) inside the arterial wall. There is not enough oxygen content to be consumed by the arterial wall resulting in a hypoxic environment with the presence of 0.2(mm) thickness thrombus.

### 3.6.3 Diffusivity effect

Figure 3.7 illustrates the influence of diffusivity within the thrombus ( $D_{th}:m^2/s$ ) on oxygen transport. We compare the prescribed value of  $D_{th} = 2.4 \times 10^{-9}$  in Figure 3.2 with the other two values  $4.8 \times 10^{-9}$  and  $1.2 \times 10^{-9}$ , which are 2 times greater or smaller than the default value. Different values of  $D_{th}$  allows different amounts of oxygen to pass through the thrombus layer in a certain time step. With a greater diffusivity of  $D_{th} = 4.8 \times 10^{-9}$ , it renders a lower resistance of oxygen transport through

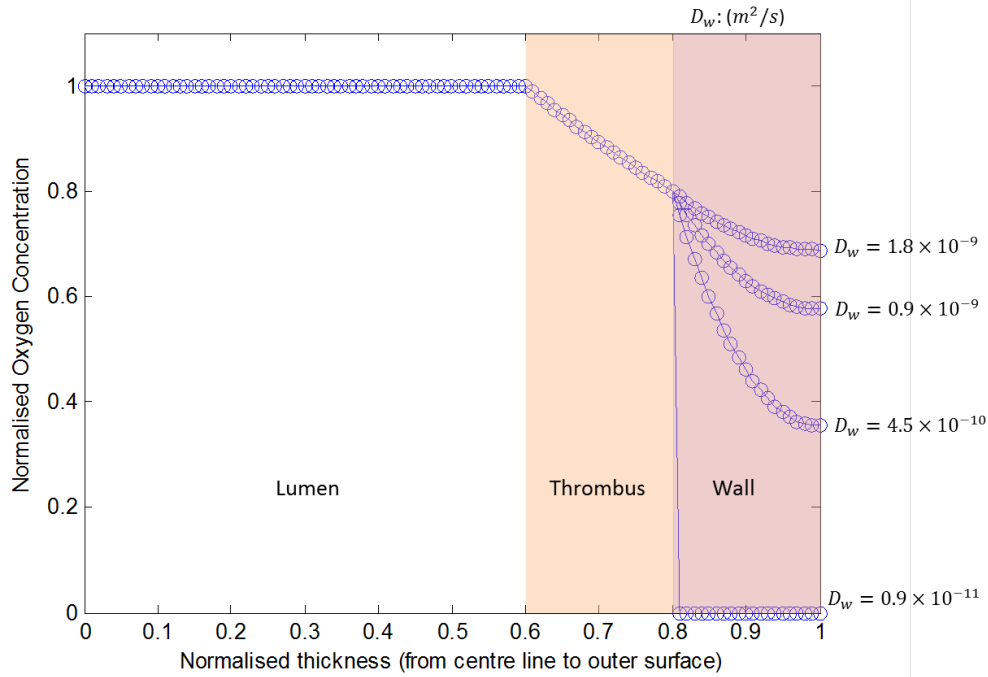


Figure 3.8: Influence of different diffusivities in arterial wall  $D_w$  on normalised oxygen concentration across the two-layered model.

the thrombus and the oxygen level at the thrombus/wall interface remains high at 91%. Whilst with a smaller diffusivity of  $D_{th} = 1.2 \times 10^{-9}$ , it increases the impedance of oxygen transport within the thrombus layer and the oxygen level is reduced to 59% at the interface which allows less amount of oxygen diffusing into the wall compared to the other two cases. Overall, even with different oxygen levels entering from the thrombus/wall interface to the wall, the oxygen consumption amount in the wall still stays around 20% in each case. Also we examine the lower bound of  $D_{th}$  for generating the zero oxygen environment inside the wall. When  $D_{th}$  is one order of magnitude smaller than the default value ( $D_{th} = 4.8 \times 10^{-10}$ ), the thrombus layer perfectly obstructs any oxygen transport to the wall with this low diffusivity.

Figure 3.8 illustrates the influence of diffusivity in arterial wall ( $D_w: m^2/s$ ) on oxygen transport. Again, we conduct a parametric study of  $D_w$  in comparison to the prescribed value  $D_w = 0.9 \times 10^{-9}$ , with the two other values  $1.8 \times 10^{-9}$  and  $4.5 \times 10^{-10}$  which are also 2 times greater or smaller than the default one. The concentration at the thrombus/wall interface remains constant (79%) among the 3 cases irrespective of the difference in  $D_w$ . A greater  $D_w$  ( $1.8 \times 10^{-9}$ ) allows a greater amount of

oxygen to penetrate through the wall at one time point. When reaching the steady state, there is a rich enough average oxygen content within the wall (76%) for the metabolic activity. For a lower  $D_w$  ( $4.5 \times 10^{-10}$ ), it increases the resistance of oxygen diffusing through the wall and the average oxygen concentration in the wall drops to 54%. A zero oxygen condition inside the wall happens when  $D_w$  equates to  $0.9 \times 10^{-11}$  which is 2 orders of magnitude smaller than the default value resulting in a sudden drop of oxygen level from 79% to 0% at the interface. The deficiency of oxygen transport leads to a hypoxic environment and there is not enough oxygen to meet the requirement needed for the metabolic activity inside the wall.

To summarise, this section investigates the influence of an individual parameter on the overall oxygen concentration. For a living tissue, this dynamic structure may adjust itself to overcome the hypoxic condition to maintain its function, which leads to the G&R hypothesis presented in Chapter 4.

### 3.7 DISCUSSION AND CONCLUDING REMARKS

This chapter introduces a preliminary study on the implementation of oxygen transport through a thrombosed artery in ANSYS modelling. Physiological values of diffusion properties and consumption rates are given based on experimental observations. We utilise the experimental data and apply it to a 1D model to demonstrate oxygen diffusion modelling. Comparison between the results from analytical and numerical methods of the 1D model shows a very good agreement of the solutions. However this simplified 1D model only considers the uniform thickness of thrombus and transmural oxygen distribution throughout the domain. To apply the diffusion modelling on 3D clinical cases, the ANSYS numerical approach is essential to take into account the spatial variation of oxygen distribution in an aneurysm with a more complex geometric shape. Thickness of the arterial wall and the thrombus may vary within the aneurysm structure resulting in the spatial difference in oxygen levels. The goal of implementing ANSYS on a 3D model is to be able to simulate the variation in concentration throughout the domain representing the artery using the finite element method. More work is required for simulating diffusion in 3D models, nonetheless, the validation of a 1D model shows the potential for further development of oxygen transport modelling in ANSYS. The mechanical model of an artery described in Chapter 2 and the diffusion model presented here are both simulated by ANSYS. Hence these can both be integrated into the computational

frameworks proposed in Chapter 4 and Chapter 5 for modelling the mechanical and chemical environments with a conceptual model of an aneurysm. Consequently the aneurysm modelling platform is built on the basis of engineering software ANSYS to achieve industrial translation in order to be widely used or updated by other researchers.

The parametric studies conducted in this chapter demonstrate that the thrombus thickness ( $H_{th}$ ), oxygen consumption rate ( $Q_w$ ), and diffusion coefficients ( $D_w$ ,  $D_{th}$ ) have evident influences on the transport of oxygen through the layers. The greater the thrombus thickness, the greater the resistance of oxygen delivery to the thrombus/wall interface. Conversely, the greater the diffusivity in the thrombus and the wall, the lower the obstruction of oxygen penetrating through the layers. For the oxygen consumption rate demonstrated in Figure 3.6, a low respiration rate ( $Q_w = 0.5 \times 10^{-3} \text{ mol/m}^2/\text{s}$ ) of the wall allows the high distribution of oxygen through the wall regardless of the presence of the thrombus, yet there is not enough oxygen delivered to satisfy the higher cellular demands in the wall imposed by a greater consumption rate ( $Q_w = 5 \times 10^{-3} \text{ mol/m}^2/\text{s}$ ).

In clinical application to aneurysms, the thrombus formation may thicken overtime to impede the oxygen transport to the wall, whilst the respiration rate and diffusivity of the wall may differ overtime due to cellular composition and decomposition during aneurysm progression. The parameters examined by the 1D model provide a general idea of oxygen transport through the layers in different conditions. To model the evolution of aneurysms, these parameters may be updated due to constitutive G&R. The arterial wall is a highly dynamic tissue which is in response to the changing environmental conditions. For perturbations such as a hypoxic condition, the adaptive response of artery is an attempt to restore the healthy/homeostatic state to maintain cellular functionality (Rissanen et al., 2006). A hypothetical method on linking the cellular functionality and the oxygen level will be discussed in the simulation of aneurysm evolution presented in Chapter 4 and Chapter 5.

Overall, this simplified model cannot fully interpret the accurate physiological oxygen concentration within the artery. Yet this is the initial step of framework development for the implementation into the coupled fluid-solid-growth-transport (FSGT) model of a 3D aneurysm geometry. Without specific statement as to whether the thrombus induced hypoxic condition leads to cell death in the perspective of vascular biology, results presented in this chapter still demonstrate the ability to

simulate the impact of propagating thrombus and cellular respiration rate on the impairment of oxygen transport to the arterial wall by the means of computational diffusion analysis.



**A NOVEL  
CHEMO-MECHANO-BIOLOGICAL  
MATHEMATICAL FRAMEWORK WITH THE  
APPLICATION ON A 1D CYLINDRICAL  
MODEL**

---

Present herein is the coupled solid-growth-transport (SGT) framework on a simple 1D cylindrical vascular model. The concept of chemo-mechano-biology is crucial in this research: mechanical forces on the artery can trigger the chemical signals which in turn affect the biological behaviour of the arterial tissue, in health and disease. We focus on the development of an *in silico* model which represents the mechanical arterial environment due to blood pressure, the transport of chemical species within the wall, the biology of arterial wall, and the interaction between them. The model enables the representation of realistic distributions of mechanical forces and chemical concentrations and their link to aneurysm evolution. Additionally, this simulation workflow is fully integrated into the ANSYS engineering software which would allow its clinical translation by global healthcare technology industries for maximum clinical impact.

---

**Objective:** the objective of this chapter is to bring together the vascular solid model and the oxygen transport model from previous chapters, along with the proposed G&R method to form the computational framework for modelling the evolution of aneurysms. All the numerical processes of this framework are integrated

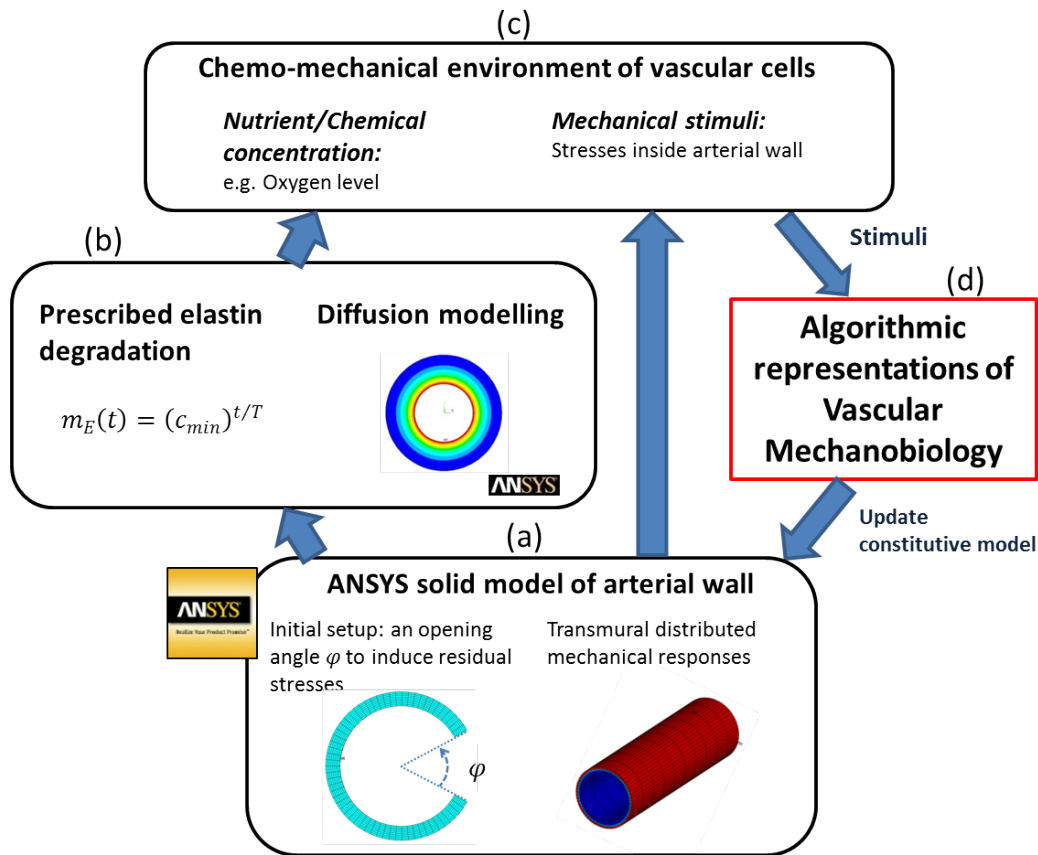


Figure 4.1: Workflow of the 1D SGT framework: (a) structural model of arterial wall; (b) prescribed elastin degradation and transport simulations; (c) results from mechanical and transport simulations provide inputs to the G&R algorithms; (d) chemical and mechanical stimuli are inputs to growth and remodelling algorithms which update the constitutive model of the tissue.

in the ANSYS software to achieve computational communication between the solid and transport models. A simple 1D model is demonstrated in this chapter to explore the computational behaviour of this G&R framework.

## 4.1 OVERVIEW OF 1D SGT MODEL

This novel mechanistic model of arterial/aneurysm tissue mechanobiology is formed by the coupling of a Solid-Growth framework and advection-diffusion simulation. It is to identify and quantify the influence of mechanical and chemical stimuli to the G&R of vascular constituents. The mechanical stimuli are the disturbance of physiological state such as the change of stresses within the arterial wall. The

chemical stimuli are the distribution or concentration of nutrients inside the arterial wall affected by the adaptive response of vascular constituents. Figure 4.1 gives a general idea of the interaction between solid, diffusion and growth of aneurysm evolution modelled by the novel SGT framework with the application of a simple 1D model. The structural model of the arterial wall is introduced in Chapter 2: a thick-walled model is implemented to consider the transmural difference through the wall thickness; the opening angle method is induced to include the residual stresses so as to represent a realistic physiological condition inside arterial wall. The mechanical environment is simulated in ANSYS: mechanical APDL for the arterial wall responses. The chemical environment is modelled by the transport simulation presented in Chapter 3. Here the local oxygen level is presented as the illustrative case of chemical stimuli in the SGT framework.

The aneurysm formation is initiated by a prescribed elastin degradation to create an imbalanced condition inside the arterial wall. Vascular cells sense the alteration and respond to it with a G&R process to adapt this structural change and restore the homeostatic condition of the vascular structure. A stress-mediated G&R method is brought out in Section 4.2.3 to put into practice the SGT workflow.

## 4.2 GROWTH AND REMODELLING

The screening is very costly and it requires intensive patient monitoring protocol to follow the growth of the vascular diseases. Therefore, a G&R which can accurately predict the patient-specific growth rate of the artery is desirable and needed. Previous research (Watton et al. (2004); Baek et al. (2006); Watton and Hill (2009); Watton et al. (2009a)) has produced a membrane model to simulate AAAs and IAs evolution from the healthy artery. However, the membrane model neglects the transmural variation along the radial direction of the vessel wall and it still requires a more sophisticated model to have a more detailed understanding inside the arterial elements. The constitutive models need to be improved to enable a G&R formulation to be implemented. Thus, we consider a thick-walled G&R framework of the artery structure which takes into account the transmural difference inside the vessel wall. The G&R framework is generally applied to vascular diseases with the deposition and degradation of constituents, but here we focus on updating the nature of material parameters. We do not have many details of how the vessels restore homeostasis from external changes, so we update the material parameter from a mechanical

point of view to simulate the process of remodelling in order to maintain homeostatic condition.

For implementation of the G&R in the ANSYS computational framework, we first recall the SEF presented in Chapter 2:

$$\Psi^j = m_E^j \bar{\Psi}_{iso}^j + m_C^j \bar{\Psi}_{aniso}^j \quad (4.1)$$

where  $j = \{M, A\}$  are relating to the layers,  $M$  for media and  $A$  for adventitia;  $m_E^j, m_C^j$  are the normalised mass densities of the elastin and collagen respectively. The initial values of normalised densities are equal to 1 which can be increased or decreased to represent the growth and decay of the vascular constituents.

Current knowledge on the pathophysiology of aneurysm growth is still limited. We present the G&R computational framework in order to compete with experimental observations and hypotheses. Previous studies focus on modelling the effect of mechanical forces on aneurysm tissues. The novelty of the G&R approach presented here is to couple the influence of mechanical and chemical environments on vascular constituents. At this stage, we attempt to use a simple 1D model to explain the hypothetical concept of the computational framework and hopefully to have available experimental data in the future. Subsections below describe the initiation of an aneurysm and the subsequent G&R responses of the artery.

### 4.2.1 Elastin degradation

The enlargement of an aneurysm is accompanied by the loss of elastin. The half-life of elastin is normally in 50 years but may intensify during aneurysm development. To date, the particular mechanism that leads to the degradation of elastin in aneurysms is not well understood. However, clinical observations (He and Roach (1994); Shimizu et al. (2006)) provide valuable information stating that the elastin constituents slowly degrade during the evolution of an aneurysm and sometimes there is complete loss. In the SGT 1D model, we prescribed an elastin degradation to create structural change of the artery and the G&R process will response to this structural change. The degrading function proposed by Watton et al. (2004) is applied in this model to describe the process of elastin loss:

$$m_E(t) = (c_{min})^{\frac{t}{T}} \quad (4.2)$$

$c_{min}$  is the minimum value of mass density of elastin;  $T$  is the total time period and  $t$  is the time step to the total time  $T$ . Normalised mass density of elastin  $m_E$  drops

towards  $c_{min}$  in an exponential curve over time. The prescribed elastin degradation induces the enlargement of the aneurysm. The loss of elastin weakens the structure of the arterial wall and dilates the arterial radius when under the same blood pressure.

### 4.2.2 Propagation of thrombus layer during aneurysm growth

In the SGT model for thrombosed aneurysms, we make an assumption that the thrombus layer deposits following the geometric change of the artery so as to retain the blood flow domain. The lumen diameter is fixed during the evolution of IAs. This is a reasonable assumption as the scale of an IA is very small so that the ratio between wall thickness and radii can be neglected. However, for AAAs, the aorta diameter is much greater than IA's and the ratio of wall thickness and radii would have great impact on thrombus formation and oxygen transport.

For the simple 1D model, the thrombus layer fills in the gap between the inner surface of arterial wall and the lumen volume as illustrated in Figure 4.2. Therefore, the thickness of the thrombus layer can be written in the deviation of radius change during the enlargement of the aneurysm:

$$H_{th} = R - R_L \quad (4.3)$$

where  $H_{th}$  is the thrombus thickness;  $R$  is the current inner radius of the vascular model;  $R_L$  is the inner radius at homeostatic condition. In addition, without changing the blood flow condition, the influence of an evolving thrombus layer on oxygen transport would be solely examined. Steady state oxygen diffusion modelling through two layers, thrombus and wall, is implemented in each iteration of the G&R model. The oxygen concentration inside the wall is exported and associated with the growth rate of collagenous constituents. As described in Chapter 3, the thickness of the thrombus layer has great influence on the substance diffusing through the wall. The fixed lumen area and the enlarging aneurysm formulate the growing of thrombus thickness. Thus, the alteration of oxygen level inside the wall is foreseen during the G&R process.

### 4.2.3 Collagen adaption

During the aneurysm development, along with the weakening wall, the collagen fibres are assumed to adapt and compensate the loss of elastin. Different approaches

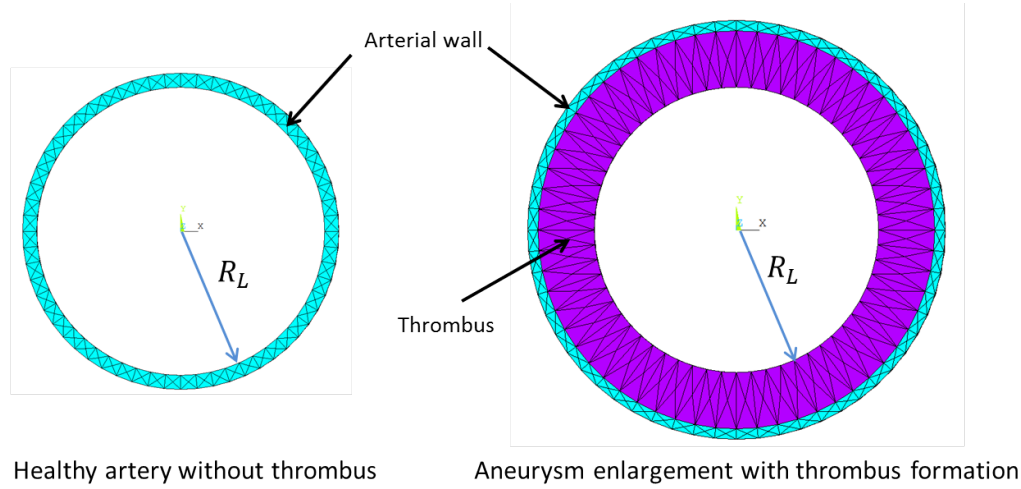


Figure 4.2: Thrombus formation: the healthy artery without thrombus layer is shown on the left, and the inner surface of wall is in contact with the lumen at the radius position  $R = R_L$ ; on the right, the thrombus fills in the gap between the lumen and the expanding arterial wall, while the inner surface of thrombus is in contact with the lumen at the fixed radius  $R_L$ .

((Watton et al., 2004), (Baek et al., 2006)) were proposed on collagen G&R with a strain or stress based method to restore the mechanical homeostatic state. As we focus and emphasise the physiological stress distribution within the arterial wall as presented in Chapter 2, the hypothetical stress-mediated G&R model is implemented for the development of the SGT framework. The novelty is the collagen growth method coupling with the oxygen transport modelling. In Section 4.2.3.1, the collagen parameters are remodelled based on the deviation of stresses to reduce the stresses on collagen. In Section 4.2.3.2, the mass density of collagen is regulated by the variation of oxygen concentration due to the presence of the thrombus layer.

#### 4.2.3.1 Stress-mediated G&R method

The purpose of the G&R model is to update the constitutive model to adapt the changing mechanical environment in the artery, i.e. remodel the collagen parameter inside the vessel wall during the evolution of aneurysm. To be more specific, we update the collagen parameter  $k_2$  in each element according to the stress distribution. As illustrated in Figure 4.3, by decreasing the collagen parameter  $k_2$ , the exponential curve of the strain energy function is shifting to the right and the stresses in the collagen fibres would be reduced for a given pressure without changing the reference configuration and the material modulus  $k_e$  and  $k_1$  of the constituents.

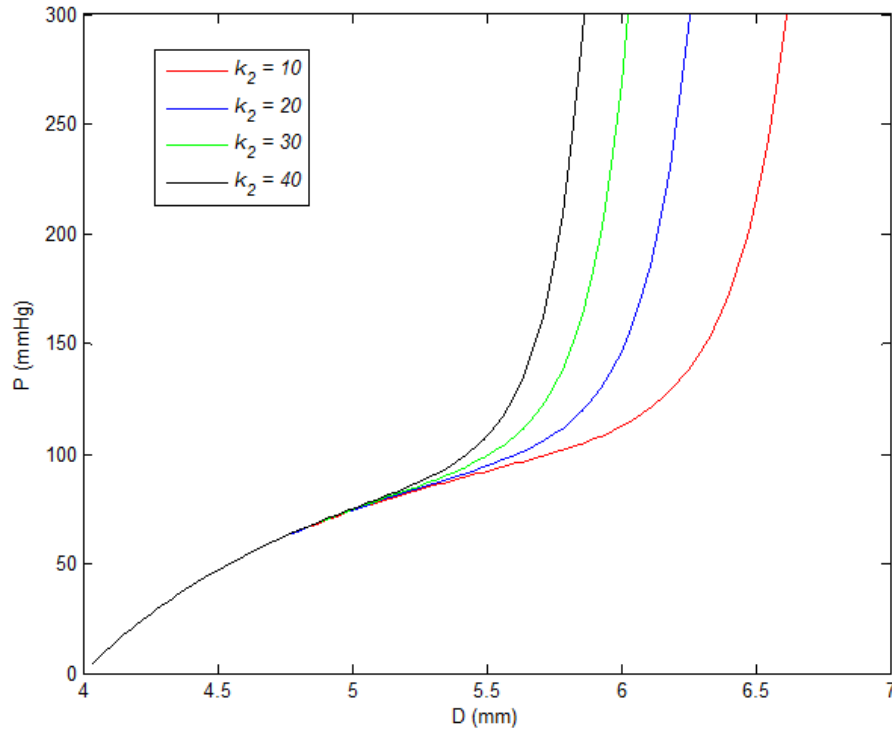


Figure 4.3: Illustration of the influence of  $k_2$  change on pressure-diameter relationship of arterial model.

We first have the homeostatic stresses from a balance condition set as the standard towards which the stress is remodelled back to. Then the elastin degradation is triggered as the initiation to alter the stress distribution of the artery. The remodelling of  $k_2$  is on the basis of the deviation of circumferential stresses from current and homeostatic values described below:

$$\frac{\partial k_2}{\partial t} = -\gamma \left( \frac{\sigma(t) - \sigma_h}{\sigma_h} \right) k_2 \quad (4.4)$$

$$k_2(t + \delta t) = k_2(t) + \frac{\partial k_2}{\partial t} \delta t \quad (4.5)$$

where  $\sigma(t)$  is the current stress field;  $\sigma_h$  is the stress field at homeostatic condition which is defined as the balance condition under physiological loading;  $\gamma$  is the growth parameter. Time step  $t = 0$  implies  $\sigma(t = 0) = \sigma_h$  and  $k_2(t = 0)$  is the initial value of  $k_2$  defined in each element. Time increment  $\delta t$  is equal to 1 to give one increment of a year and denote one cycle of G&R in the simulation. The purpose of the remodelling process is to maintain the stability of the internal environment

of arteries in response to the structural changes (elastin degradation). The stresses are supposed to be downgraded to homeostasis in order to maintain the stress level inside the arterial wall. However, the stress-strain relationship of the constitutive model is right-shifting due to  $k_2$  decreasing, so the aneurysm diameter is actually increasing.

At this stage we only update one individual parameter  $k_2$  in each material element to investigate the influence to this framework. A stability analysis of this remodelling approach is conducted in Appendix C.

#### 4.2.3.2 Collagen growth: Influence of oxygen level on fibroblast functionality

Steinbrech et al. (1999) investigated the functionality of fibroblast cells in a hypoxic environment. Experimental observation found that the collagen synthesis was downgraded after 2 days exposure to low oxygen level (0-2%). Based on these findings, the collagen growth rate  $\beta$  is linked to the local oxygen level and implemented in the SGT model. Holland (2012) proposed a mathematical model to depict and quantify the oxygen influence on collagen in the current time step  $t$  by suggesting that the average oxygen concentration  $\overline{C_w}(t)$  throughout arterial wall is linked with growth rate  $\beta(t)$  of collagen according to

$$\beta(t) = \beta_0 + (\beta_{min} - \beta_0) \left( \frac{(\overline{C_w}(t)) - (\overline{C_w})_0}{(\overline{C_w})_{min} - (\overline{C_w})_0} \right) \quad (4.6)$$

where  $\beta_0$  is the initial growth rate;  $\beta_{min}$  is the minimum growth rate;  $(\overline{C_w})_0$  is the initial oxygen concentration;  $(\overline{C_w})_{min}$  represents the least oxygen level required by the artery. The mass density of collagen  $m_C$  is updated with the stress-mediated G&R and modified growth rate  $\beta$  for each iteration of the SGT framework:

$$\frac{\partial m_C}{\partial t} = -\beta(t) \left( \frac{\sigma(t) - \sigma_h}{\sigma_h} \right) m_C \quad (4.7)$$

$$m_C(t + \delta t) = m_C(t) + \frac{\partial m_C}{\partial t} \delta t \quad (4.8)$$

Thus, collagen growth is regulated by deviations in both the stress levels and oxygen levels.

Overall, the adaptive response of collagen in the SGT framework is simulated by the  $k_2$  remodelling and the collagen growth in response to oxygen levels. Material

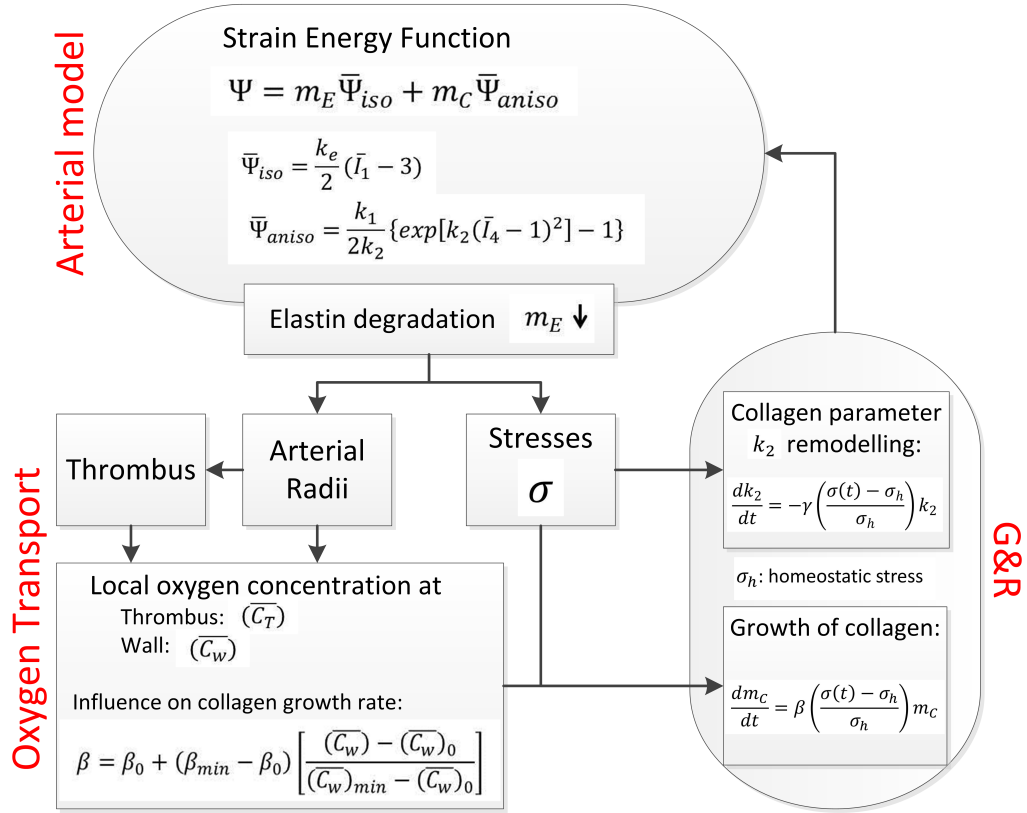


Figure 4.4: Iteration loop of the coupled G&R and oxygen transport model.

parameters and boundary conditions are provided in Section 4.3 and 4.5 to show illustrative examples to give a complete picture of the *in silico* modelling of aneurysm development.

### 4.3 ILLUSTRATIVE CASES OF SGT

The components of aneurysm G&R are thoroughly described in Section 4.2. Figure 4.4 interprets the whole workflow and the relationship between the models. Arterial structural model is presented in Chapter 2. Normalised mass density of elastin  $m_E$  and collagen  $m_C$ , constitutive parameters  $k_e$ ,  $k_1$ ,  $k_2$  in SEF define the overall mechanical responses. The initiation of an aneurysm is stimulated by the loss of elastin and its continuous degradation. A prescribed elastin degradation forces the arterial model to reach a new mechanical equilibrium which leads to two changes: arterial deformation and stresses inside the wall. The thrombus layer fills in the interval between the enlarging arterial radii and the fixed blood flow spaces. As a result, oxygen

transport inside the vascular wall is disturbed by the presence of the thrombus layer. The descending oxygen concentration from the baseline level affects the collagen synthesis on the growth rate  $\beta$ . For the G&R process, the collagen parameter  $k_2$  is remodelled based on the deviation of stresses from homeostatic condition. The remodelling parameter  $\gamma$  is set up to be a constant here. The growth of the normalised mass density of collagen is regulated by a growth rate  $\beta$  and deviations in stress. Growth rate  $\beta$  is not a constant and controlled by the oxygen transport through the wall. Therefore, the collagen growth is influenced by both the mechanical stimuli (stresses) and the chemical stimuli (oxygen concentration). The updated constitutive variables ( $k_2$ ,  $m_C$ ) consequently trigger another step on structural modelling to achieve mechanical equilibrium. The arterial geometry and stresses inside the wall are then revised resulting in the next G&R process. This iterative loop structure forms the 1D SGT framework. Table 4.1 provides the details of the setup of material parameters and boundary conditions for a simple G&R model. The result of this illustrative case of the coupled SGT numerical model is shown in the Section 4.5.

## 4.4 SOFTWARE IMPLEMENTATIONS

This section briefly introduces the required software to be implemented in the framework for the iterative G&R modelling on aneurysm evolution. Simulations are performed on a desktop PC with processor: Intel(R) Core(TM) i5-2320 CPU @ 3.00GHz 3.00GHz with 4 GB RAM and 64-bit Operation system, which takes an average of 40 minutes to complete one iteration.

### 4.4.1 PERL

A custom-written routine was developed using PERL programming language to enable communication between external programs. We utilise the PERL script as the central control to call MATLAB and ANSYS to execute at certain step for structural analysis and diffusion modelling. Driven by the altered environment, the PERL script is executing a loop structure to call a MATLAB script for remodelling the material parameters. The loop structure will run the number of iterative steps we enter in the PERL script.

<i>Parameter</i>	<i>Symbol</i>	<i>Value</i>
<b>Initial geometry</b>		
Opening angle in reference configuration	$\varphi$	60°
Target radius in load-free configuration	$r$	2 (mm)
Circumferential curvature in reference configuration	$\kappa$	$\frac{5}{12}$
Radius in reference configuration	$R$	$\frac{1}{\kappa}$
Axial length	$L_{ref}$	20 (mm)
<b>Applied boundary conditions</b>		
Internal pressure on arterial wall	$p$	125 (mmHg)
Axial pre-stretch	$\lambda_z$	1.3
<b>Fibre orientation</b>		
Media	$\alpha_M$	30°
Adventitia	$\alpha_A$	60°
<b>Wall thickness</b>		
Total	$H$	0.375 (mm)
Media	$H_M$	$\frac{3}{4}H$
Adventitia	$H_A$	$\frac{1}{4}H$
<b>Elastin modulus</b>		
Media	$k_e^M$	143.2 (kPa)
Adventitia	$k_e^A$	$0.1k_e^M$
<b>Collagen modulus</b>		
Media	$k_1^M$	3.84 (kPa)
	$k_2^M$	40
Adventitia	$k_1^A$	0.96 (kPa)
	$k_2^A$	40
<b>Oxygen transport boundary condition</b>		
Lumen oxygen concentration	$C_1$	0.1076(mol/m <sup>3</sup> )
<b>Oxygen diffusivity</b>		
Arterial wall	$D_w$	$0.9 \times 10^{-9}(m^2/s)$
Thrombus	$D_{th}$	$2.4 \times 10^{-9}(m^2/s)$
<b>Oxygen consumption rate</b>		
Arterial wall	$Q_w$	$1 \times 10^{-3}(mol/m^2/s)$
Thrombus	$Q_{th}$	0
<b>G&amp;R parameters</b>		
Remodelling parameter of collagen	$\gamma$	0.5
Initial collagen growth rate	$\beta_0$	1
Minimum collagen growth rate	$\beta_{min}$	0.1
Minimum average oxygen concentration in the wall	$(\overline{C_w})_{min}$	$0.1(\overline{C_w})_0$

Table 4.1: Parameters used for modelling the aneurysm evolution on the 1D thick-walled model.

### 4.4.2 MATLAB

The main task of using MATLAB2016 program is to generate input files for ANSYS to build the structure of the artery, and to update the solving step for each iteration. The main MATLAB script defines a structural mesh within the model which is demonstrated in Appendix B. This main script also generates the constitutive files of elastin and collagen to be modified by a secondary MATLAB script with the result files from ANSYS after each iteration. The secondary MATLAB script reads in the solution files from ANSYS and deletes irrelevant descriptions to save only the data of mechanical stress and oxygen concentration for the G&R purpose.

### 4.4.3 ANSYS

We use ANSYS Mechanical 16.1 to model the artery on the basis of solid mechanics and diffusion modelling as presented in Chapter 2 and Chapter 3 respectively.

## 4.5 RESULTS

Figure 4.4 shows the iterative cycle of the computational framework where each parameter is highly dependent on each other: i.e. the thickness of thrombus is dependent on the evolving inner radius of the wall; oxygen level inside the wall  $\overline{C_w}$  is controlled by the thrombus thickness, and further on the growth rate  $\beta$ ; the change of normalised mass density of collagen  $m_C$  is linked to  $\beta$  and stress  $\sigma$ ; the remodelling of collagen parameter  $k_2$  is fully dominated by stress  $\sigma$ . A new set of  $m_C$  and  $k_2$  updates the inner radius of the wall. Therefore, the results should be presented in a linear manner to demonstrate the consequential relationship from one variable to the next. This is starting with the elastin degradation to force the vascular diameter changes. Following the diameter changes and the presence of thrombus, the results of the oxygen level in the wall  $\overline{C_w}$  and the growth rate  $\beta$  are shown. Lastly, the growth of collagen  $m_C$  and the remodelling of  $k_2$  are calculated and turned into the change of diameter, thus completing the cycle.

### 4.5.1 Case 1: uniform elastin degradation across the arterial wall

The results of an illustrative, simple cylindrical model applied with the SGT are shown below. Figure 4.5 shows a time-dependent, prescribed elastin degradation in an exponential curve mentioned in Section 4.2.1. The time scale for the modelling

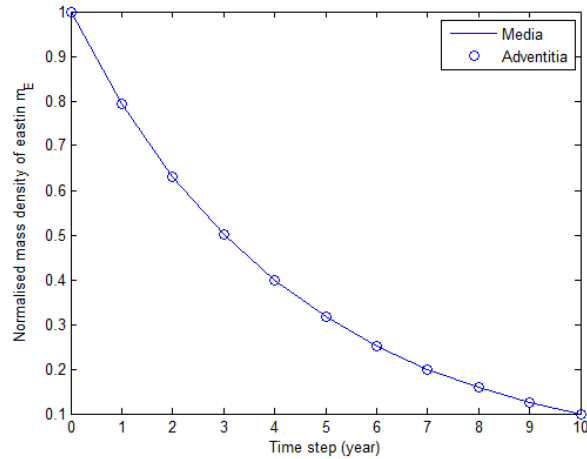


Figure 4.5: Prescribed elastin degradation over 10 years (Case 1).

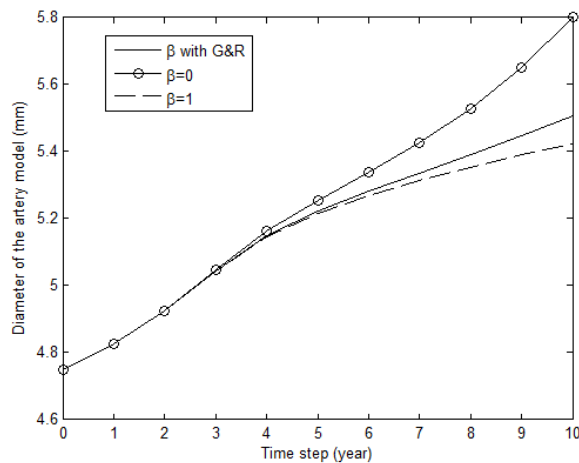


Figure 4.6: Influence of collagen growth rate  $\beta$  on the evolution of aneurysm diameter: ( $\beta = 0$ ) the diameter increases more due to the loss of elastin; ( $\beta = 1$ ) the diameter increases the least with more collagen growth; ( $\beta$  with G&R) is the mediated case from the previous two.

purpose of aneurysm evolution is set to be 10 years. The elastin degradation is uniform in both axial and radial directions of the tube model and  $m_E$  keeps decreasing towards the minimum value 0.1 at the end of the modelling time ( $T = 10$  years). The diameter of the artery is enlarging over time due to the loss of elastin in each time step. In Figure 4.6, the solid line shows the radial expansion of the cylindrical model with a dynamic collagen growth rate  $\beta$  confined by the G&R approach, where the evolution of  $\beta$  is plotted in Figure 4.8. The diameter goes up quickly at the first few time steps ( $t = 0 \sim 4$  years) and inclines to be steady at the end. To understand the influence of collagen growth on arterial diameter, two other cases are also depicted here: with a fixed growth rate ( $\beta = 1$ ), there are more collagen growth to compensate the loss of elastin, thus the enlargement of the model is stabilising faster than the G&R model; if there is no growth on collagen ( $\beta = 0$ ), the enlargement of the model continues without stabilisation compared to the other two. Following results shown stay with the approach of  $\beta$  with G&R. The increasing diameter comes along with the deposition of the thrombus layer and its thickness is directly proportional to the diameter. Oxygen concentration inside the vascular model is altered due to the presence of thrombus. The thicker the thrombus is, the lower the oxygen level inside the wall. In Figure 4.7, the presence of the thrombus layer ( $t = 1$  year) displays an obvious reduction on normalised oxygen value  $\overline{C_w}$  from its original condition ( $t = 0$ ). Due to the growing of thrombus layer, oxygen level  $\overline{C_w}$  is gradually decreasing to the last time step ( $t = 10$  years). The collagen growth rate  $\beta$  is affected and sharply correlated by the oxygen concentration through the wall  $\overline{C_w}$  as formulated in equation (4.6). To this point, the plotting curves for the remodelling of growth rate  $\beta$  shown in Figure 4.8 and the reducing oxygen level  $\overline{C_w}$  shown in Figure 4.7 are identical.

For the oxygen transport modelling, the wall and the thrombus are represented individually as homogeneous layers. For the 1D SGT framework, it is assumed that fibroblasts sense the change of average oxygen level within the wall and the consequential synthesis of collagen responds uniformly through the whole vessel. Therefore, the growth rate  $\beta$  is calculated from the average oxygen concentration  $\overline{C_w}$  which disregards the spatial and transmural difference of the model. On the contrary, for the G&R of arterial constitutive structure, the transmural variation through the wall thickness is taken into account which is a great improvement from existing FSG membrane model. Figure 4.9 and Figure 4.10 depict the G&R of parameter  $k_2$  and the mass density of collagen, respectively, along the normalised radial direction

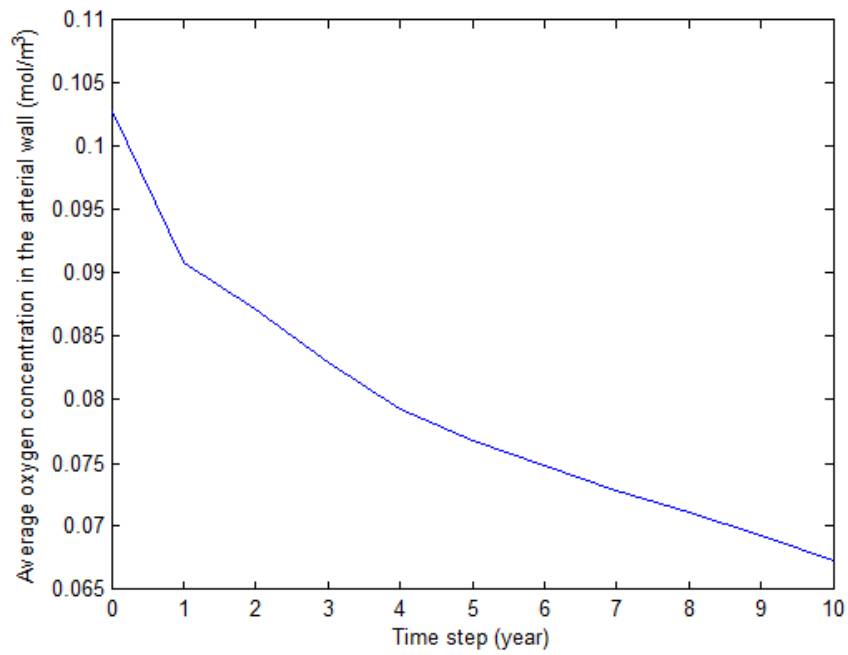


Figure 4.7: Average oxygen concentration  $\overline{C_w}$  at each times step during aneurysm growth and thrombus propagation (Case 1).

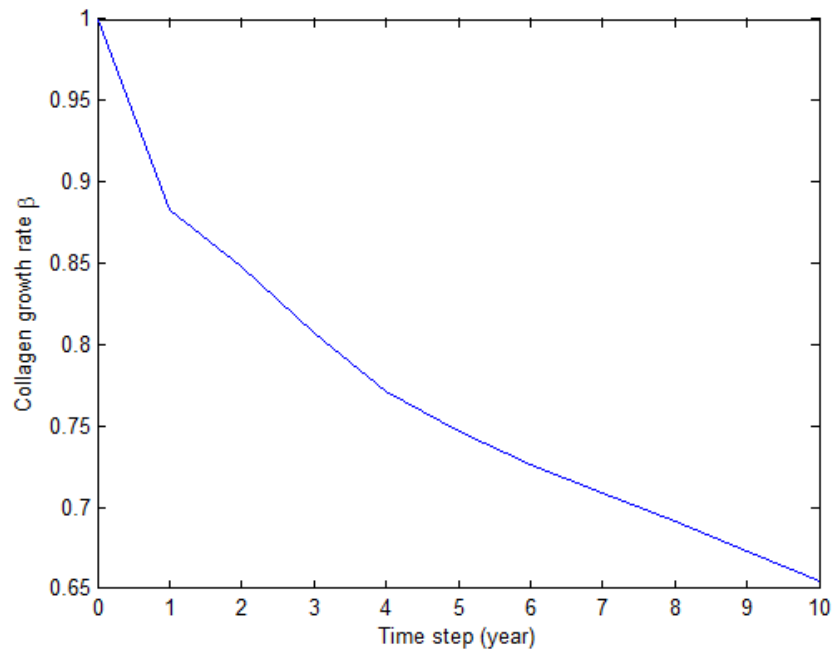


Figure 4.8: Collagen growth rate  $\beta$  changes over time (Case 1).

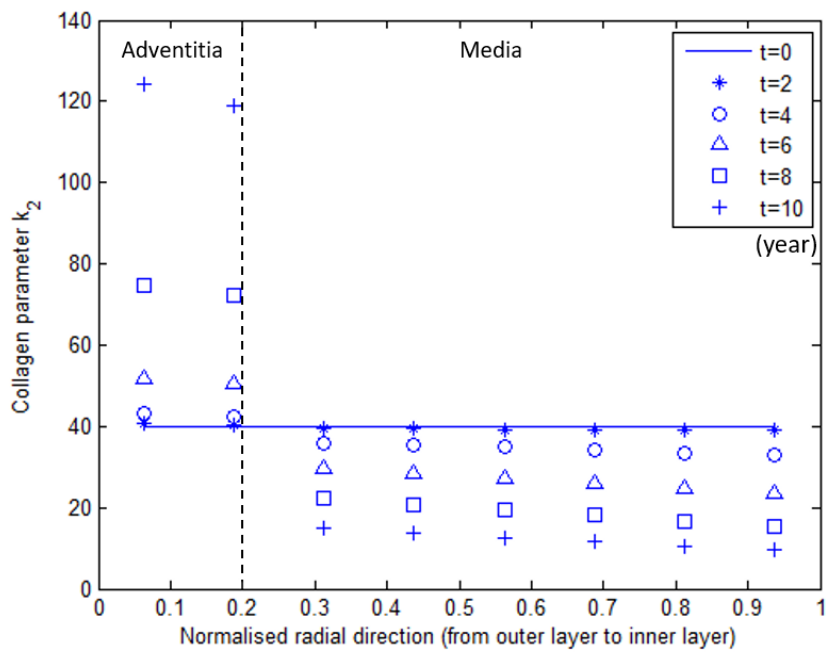


Figure 4.9: Collagen parameter  $k_2$  along the wall thickness changes during G&R in each time step (Case 1).

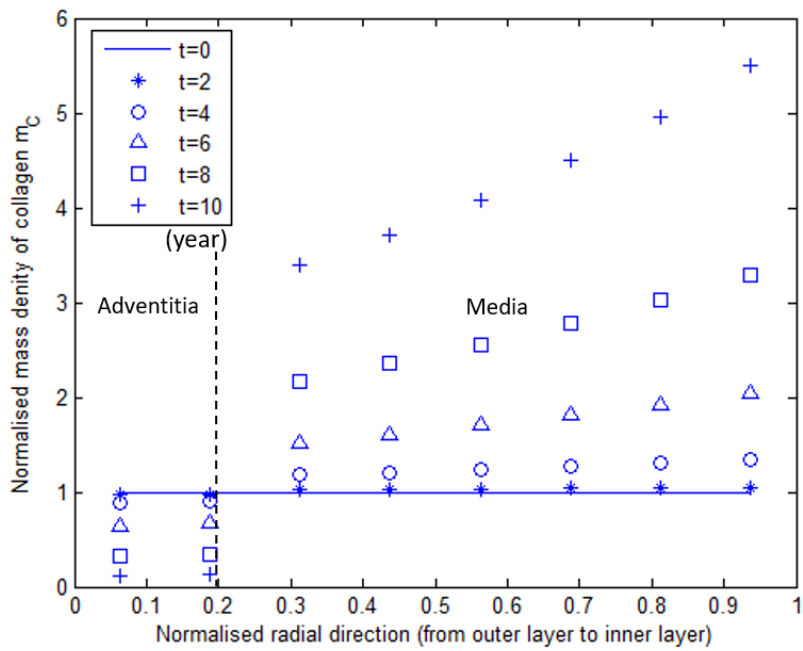


Figure 4.10: Normalised mass density of collagen along the wall thickness changes during G&R in each time step (Case 1).

at each time step.

In Figure 4.9, the material parameter  $k_2$  is solely controlled by the deviation of circumferential stresses as formulated in equation (4.4). The results show that the media and the adventitia layers are performing oppositely during the G&R. This is due to the difference in their natural structure: the adventitia is a weaker component of the model than the media. The media layer is the main load-bearing layer with stronger elastin and collagen constituents. The uniform elastin degradation forces the enlargement of the vascular diameter and the stress increasing in the media layer resulting in  $k_2$  decreasing. However,  $k_2$  values in the adventitia are increasing due to the descending stresses within. The degradation of the weaker elastin coefficient in the adventitia reduces the stress significantly that even the enlargement of the diameter cannot catch up the loss in mechanical equilibrium. The adhesion between media and adventitia inhibits further enlargement of the individual adventitia layer in reaction to the loss of elastin. As a result, stresses in the adventitia are actually going lower than the homeostatic values during G&R process. Based on equation (4.4), this leads to the increasing of  $k_2$  in the adventitia layer. Conversely, stresses in the media are going up leading to the decreasing of  $k_2$ . Note that the stress deviation does not vary that much due to the structural G&R resulting in geometric deformation to achieve a new force equilibrium. Nevertheless the accumulation of the G&R processes still demonstrates a significant update on the variables in Figure 4.9 and Figure 4.10.

In Figure 4.10, the normalised mass density of collagen  $m_C$  is controlled by the stress deviation and growth rate  $\beta$  as formulated in equation (4.7). The growth rate  $\beta$  in each time step is uniformly distributed throughout the model, providing a scale to regulate the collagen concentration. For the  $k_2$  remodelling, it is negative proportional to the stress deviation; for the growth of collagen mass density, on the contrary, it is positive proportional to the stress deviation. The collagen production is significantly increasing in the higher stress layer (media), especially at the innermost surface of the tube model which proliferates to 5.5 times from the original value. Yet, the normalised collagen mass density  $m_C$  is downregulated to almost zero in the lower stress layer (adventitia).

Figure 4.11 and Figure 4.12 emphasise the transmural variation through the wall thickness during the G&R of collagen parameter  $k_2$  and normalised mass density  $m_C$ , respectively. In Figure 4.11, it compares the  $k_2$  remodelling between the three

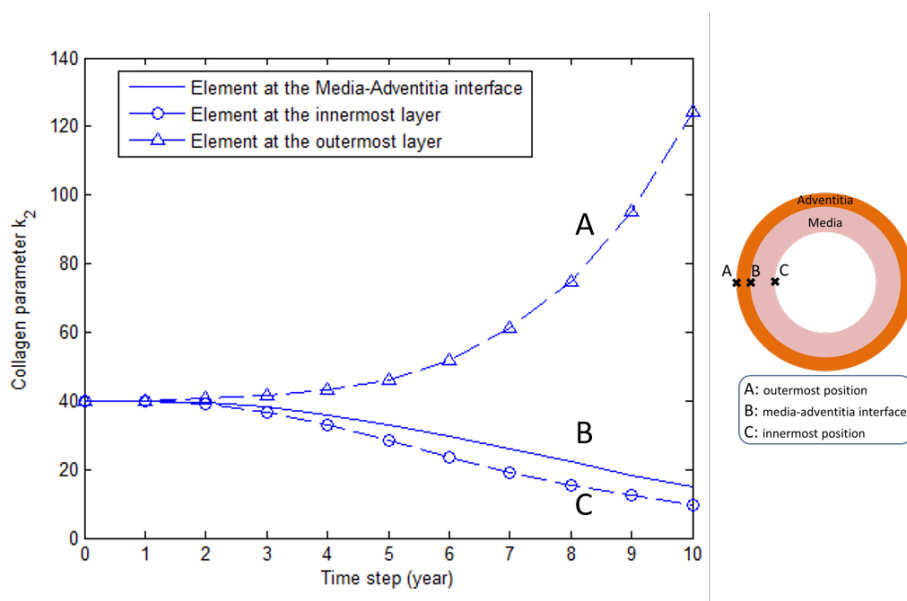


Figure 4.11: Comparison of the  $k_2$  evolution between the elements at the innermost layer, outermost layer, and the media-adventitia interface (Case 1).

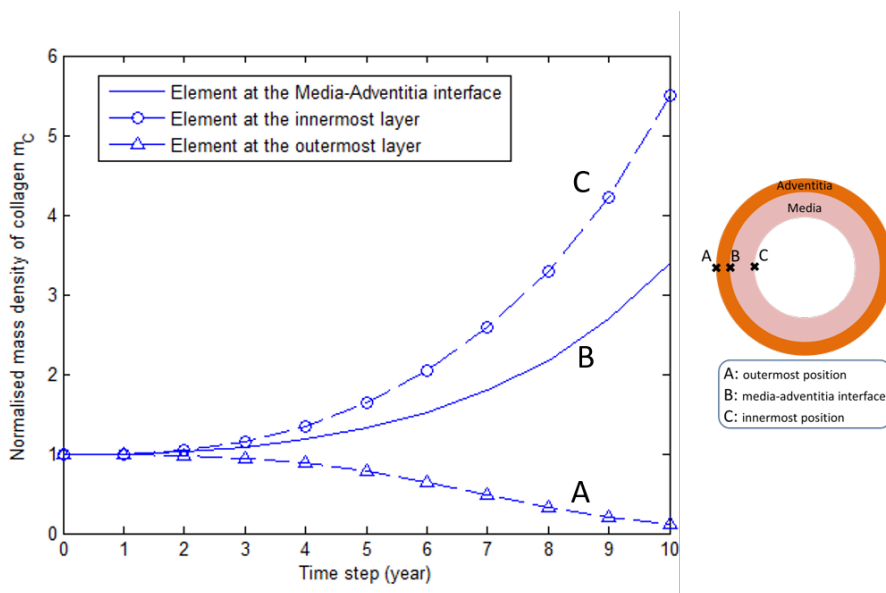


Figure 4.12: Comparison of the growth of normalised mass density of collagen between the elements at the innermost layer, outermost layer, and the media-adventitia interface (Case 1).

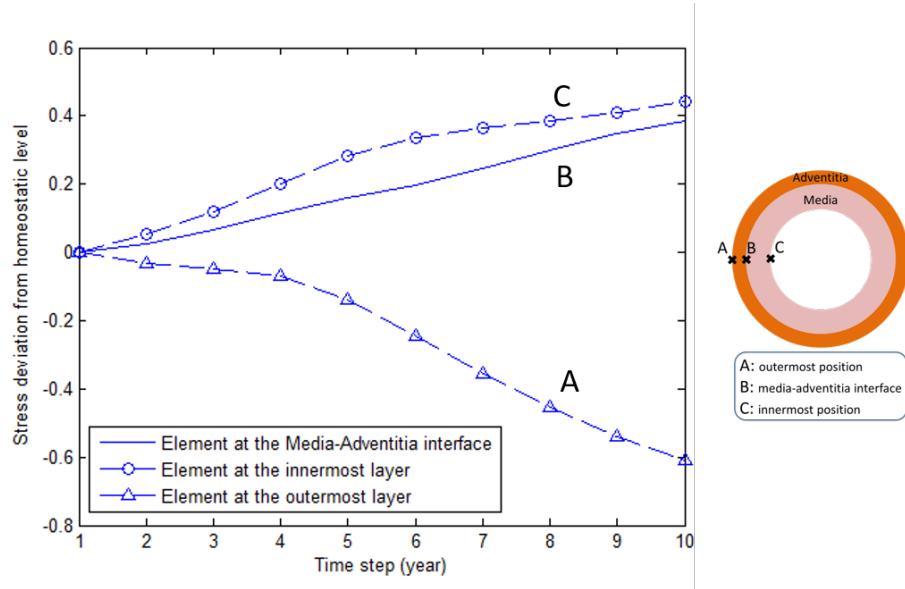


Figure 4.13: Circumferential stress deviation  $(\sigma(t) - \sigma_h)/\sigma_h$  at each time step and the comparison between the innermost layer, outermost layer, and the media-adventitia interface (Case 1).

different positions through the layers. The results show that in the innermost layer and the interface,  $k_2$  is continually decreasing after the initiation of elastin degradation; while in the outermost layer,  $k_2$  is continually increasing to more than three times of the original value at the last time step. Figure 4.12 shows the results of the G&R on the normalised collagen mass density  $m_C$ . For the innermost layer and media-adventitia interface, collagen keeps growing towards the end of time and the difference between the two layers increases without stabilisation. This implies that, even when the decreasing oxygen level downregulates the growth rate of collagen, the layers still demand more collagen production to maintain the strength of arterial structure, especially at the innermost layer. On the other hand, for the outermost layer, collagen keeps decreasing in response to the decreasing of stresses within.

Note that the G&R of  $k_2$  and  $m_C$  are all related to the stress deviation, but linked to different parameters. The  $k_2$  remodelling function (4.4) is multiplied by a constant parameter ( $\gamma = 0.5$ ); the growth function of collagen (4.7) is multiplied by a dynamic growth rate  $\beta$  associated with the average oxygen concentration. In Figure 4.8, the least value of  $\beta$  is approximately 0.65 which is still larger than the constant parameter ( $\gamma = 0.5$ ). Therefore, the curve for the accumulation of  $m_C$  is steeper than the curve for the decreasing  $k_2$ . Even though the stress deviation is stabilising

at the innermost layer and interface (Figure 4.13), the difference of collagen mass density is still growing due to the growth rate ( $\beta > 0.5$ ) multiplied with the value of collagen mass density in the previous time step in each layer.

Figure 4.13 displays the stress deviation at the three different positions across the wall during G&R. It provides more detail of the mechanical responses within the arterial model and the critical correlation to stimulate the G&R procedure in previous figures. When  $t = 0$  year, it represents the balance condition (homeostasis), thus the stress deviation is zero. From  $t = 1$  year, initiated by the elastin degradation, stress deviation goes up at the innermost layer and the interface, but goes down at the outermost layer. This implies that the collagen G&R cannot fully recover the homeostatic condition from the loss of elastin. From  $t = 6$  years, the deviation at the innermost layer begins to stabilise with the assistance from collagen G&R, while the deviation at the outermost layer increases more in a negative value. In addition, the difference in stress deviation between the innermost layer and the media-adventitia interface increases in the first few years, yet decreases from the middle to the end of simulation time. The transmural variation in stress in the media layer is reduced with collagen G&R as of  $t = 6$  years which is reflected in the stabilisation of aneurysm diameter shown in Figure 4.6.

#### 4.5.2 Case 2: non-uniform elastin degradation across the arterial wall

Results shown in Case 1 are based on the uniform elastin degradation in the media and adventitia layers, in which it shows a negative growth of collagen mass density in the adventitia. However, from histological observations, the adventitia layer should be acting as a protective sheath to restrict the radial expansion from the loss of elastin. During the aneurysm progression, the loads are transferred from the elastin to the collagen fibres due to the elastin degradation and the higher strain state. The collagen constituents are assumed to adapt the structural change for the loss of load bearing elastin, especially in the adventitia which has the majority of fibroblast cells. Furthermore, the media layer is the main load bearer at homeostasis due to greater elastin modulus as described in Table 4.1, while the portion of the overall mechanical response for elastin inside the adventitia is limited due to the lower elastin modulus. It was also shown that the mass density of elastin is lower in the media layer and higher in the adventitia from aneurysm examples (Sokolis et al.,

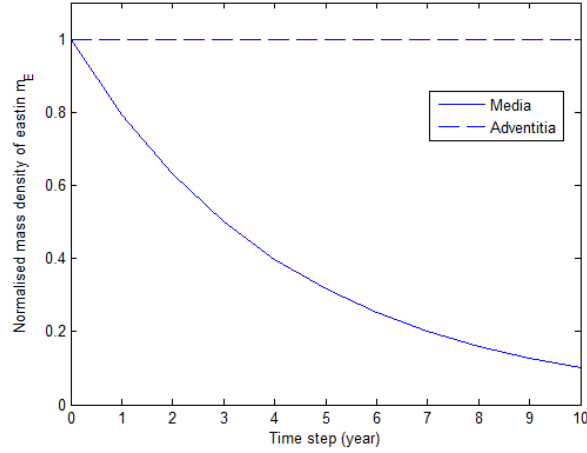


Figure 4.14: Different prescribed elastin degradation in the media and adventitia layers over 10 years (Case 2).

2012). Therefore, the elastin degradation mainly happens within the media layer. To achieve this point, the concentration of elastin in the media and adventitia is prescribed to downgrade to a different level of its original value. The model follows the setting:

$$c_{min}^M = 0.1; \quad c_{min}^A = 1 \quad (4.9)$$

where the minimum value of the normalised mass density of elastin in the media layer  $c_{min}^M$  is 0.1 and in the adventitia layer  $c_{min}^A$  is 1, which indicates no elastin loss in the adventitia. The exponential degradation of elastin in each layer is displayed in Figure 4.14.

The purpose of the non-uniform elastin degradation in the media and adventitia is to compute different G&R behaviour of the model, particularly on the regulation of the collagen adaptation in the adventitia layer. Figure 4.15 shows the results of the expanding diameter under uniform and non-uniform elastin degradation over time. It is prospective that the enlargement is reduced with no loss of elastin within the adventitia which demonstrates its function as a protective sheath. The thrombus thickness is thinner with the reduced expansion of aneurysm diameter. Therefore, in Figure 4.16, the corresponding normalised oxygen concentration  $\overline{C_w}$  and collagen growth rate  $\beta$  with non-uniform elastin degradation are greater than those with uniform degradation in Case 1 during G&R.

In Figure 4.17, the collagen parameter  $k_2$  in the adventitia is remodelled lower

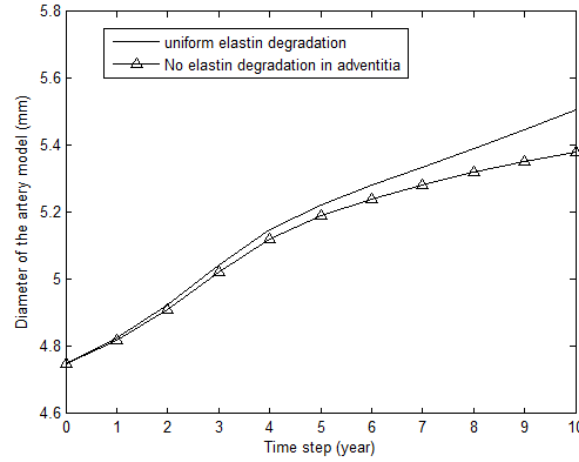
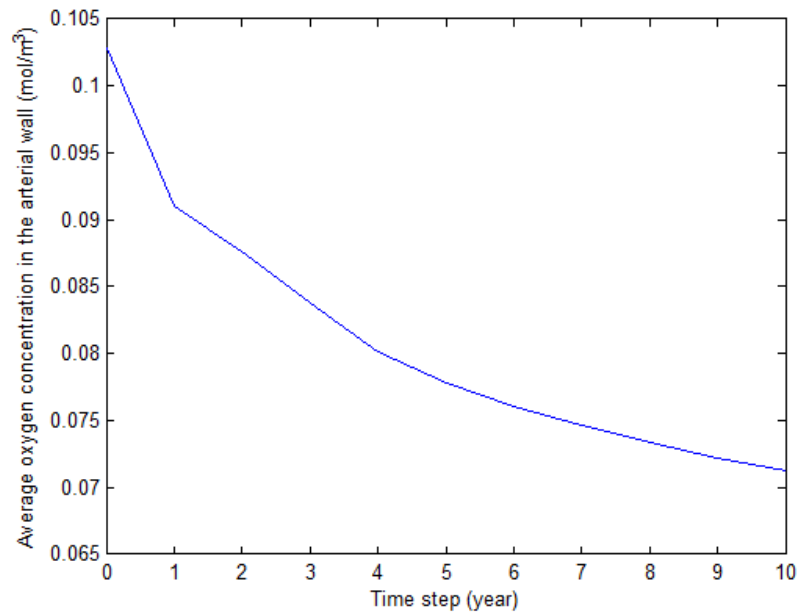
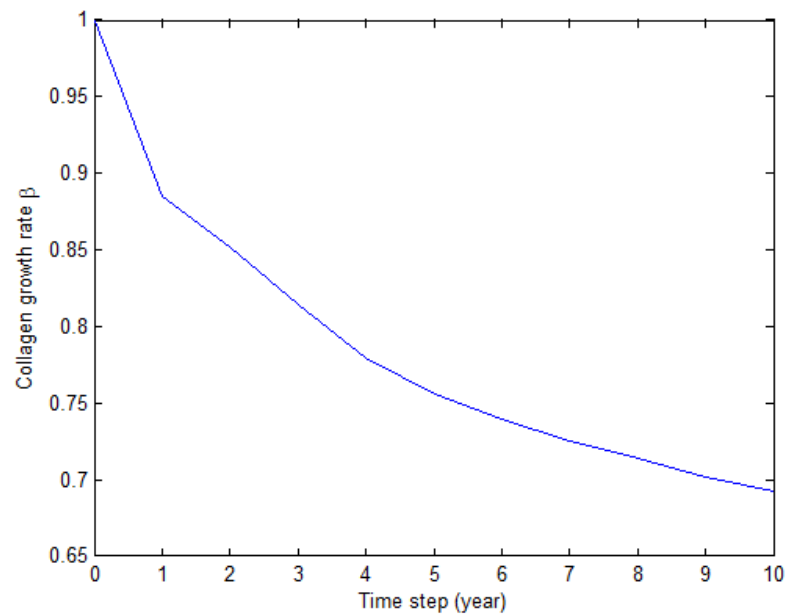


Figure 4.15: Influence of the uniform and non-uniform elastin degradation on aneurysm diameter (Case 1 vs Case 2).

than the original value under non-uniform elastin degradation condition. For Case 1 with uniform elastin degradation, parameter  $k_2$  in the adventitia increases because current stresses are lower than the homeostatic level. For Case 2 with non-uniform elastin degradation, current stress in the adventitia goes beyond its value at homeostasis with the diameter expansion and no elastin degradation in the adventitia. The portion of elastin in the adventitia is still bearing the loads which controls the mechanical equilibrium in response to the  $k_2$  remodelling. For Case 2, the remodelling behaviours in the media and adventitia layers are similar as  $k_2$  in both layers are remodelled lower than the initial values. However,  $k_2$  values in the adventitia are remodelled to almost zero at  $t = 10$  years, while the average value of  $k_2$  in the media is reduced to half of the initial value at the last time step. This implies the stresses in the adventitia increase more than those in the media during G&R. A larger scale of  $k_2$  remodelling is due to a greater stress deviation within. For the media layer, the amount of  $k_2$  reduction is greater at the inner point than the outer point in correlation with greater stress deviation towards the inner surface of the arterial wall. Figure 4.18 demonstrates the result of the growth of normalised collagen mass density in Case 2 elastin degradation. The collagen constituents are growing in both the media and adventitia layers because of the increasing stresses within. However, collagen growth in the adventitia layer is much more evident than those in the media layer. The normalised mass density of collagen in the adventitia  $m_C^A$  proliferates to more than 200 times the initial value 1 at the last time step, while the



(a)



(b)

Figure 4.16: Under non-uniform elastin degradation (Case 2): (a) Normalised oxygen concentration  $\overline{C_w}$  at each times step during aneurysm growth and thrombus propagation; (b) Collagen growth rate  $\beta$  changes over time.

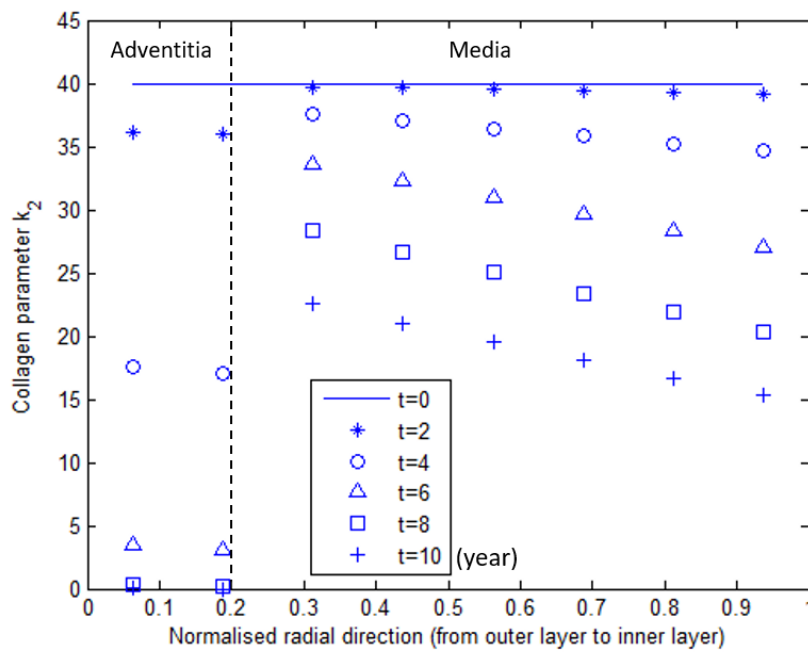


Figure 4.17: Collagen parameter  $k_2$  along the wall thickness changes during G&R with non-uniform elastin degradation in each time step (Case 2).

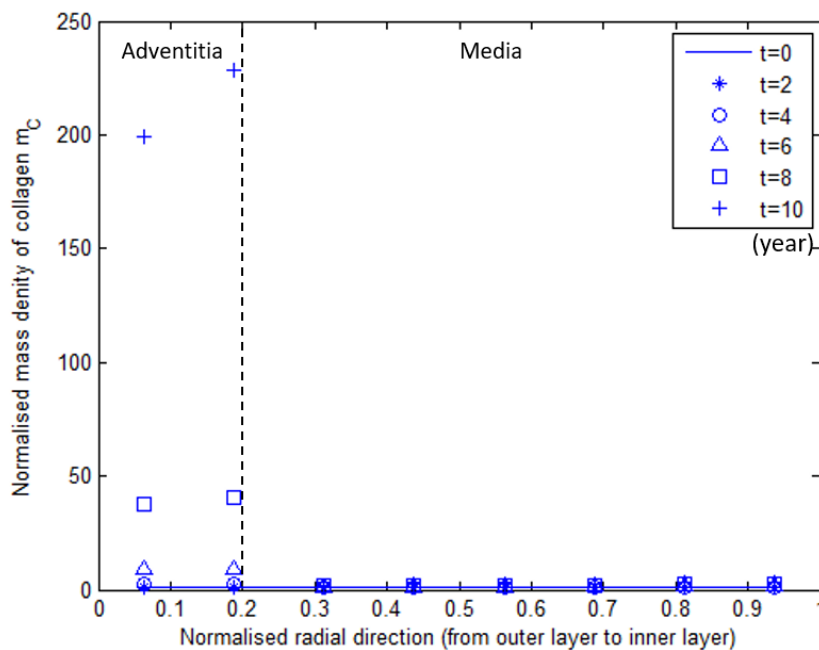


Figure 4.18: Normalised mass density of collagen along the wall thickness changes during G&R with non-uniform elastin degradation in each time step (Case 2).

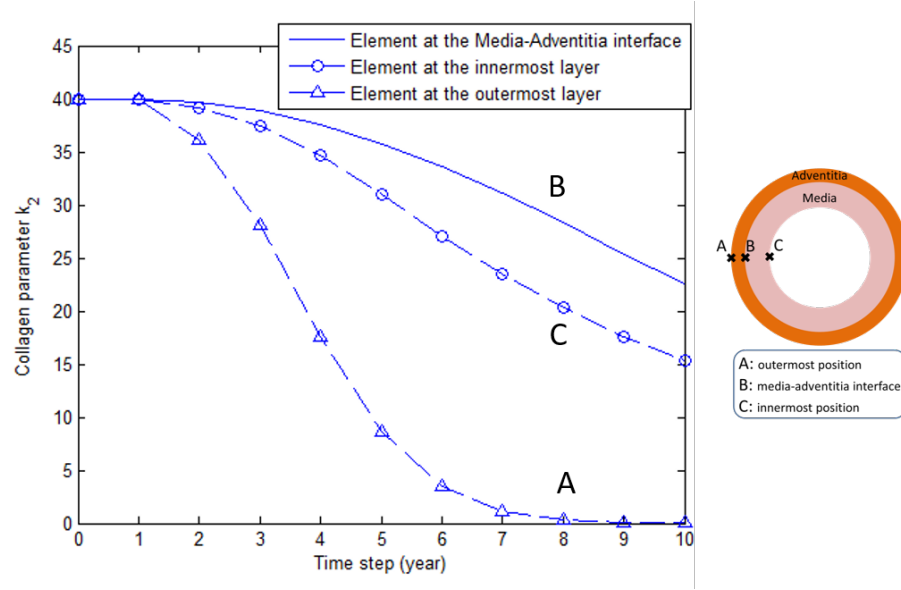


Figure 4.19: Comparison of the  $k_2$  evolution between the elements at the innermost layer, outermost layer, and the media-adventitia interface (Case 2).

maximum growth of  $m_C^M$  in the media is approximately 3 times. It can be foreseen from the  $k_2$  remodelling in Figure 4.17 that the stress deviation is greater in the adventitia. As a result, the collagen growth is more stable in the media compared to the growth in the adventitia.

Figures 4.19, 4.20, and 4.21 depict and emphasise the continual change over time of the transmural variation of  $k_2$  remodelling, collagen mass density growth and stress deviation respectively. The innermost layer, the media-adventitia interface and the outermost layer are included and compared to examine the G&R behaviour through the wall thickness. The dominant term (stress deviation) for the G&R is shown in Figure 4.21. Note that the deviation in the outermost layer is almost constantly increasing during aneurysm enlargement. In Figure 4.19, the difference of  $k_2$  between the innermost layer and the interface becomes constant from  $t = 6$  years as the stress deviation of the two layers narrows in Figure 4.21. At the outermost layer, the  $k_2$  remodelling is slowing down as of  $t = 6$  years as  $k_2$  is already downgraded to almost zero.

In Figure 4.20, for the Case 2 elastin degradation, the normalised collagen growth is up to 3.1 in the innermost layer and 2.4 at the interface. While for the Case 1 elastin degradation in Figure 4.12, the normalised collagen growth is up to 5.5 in

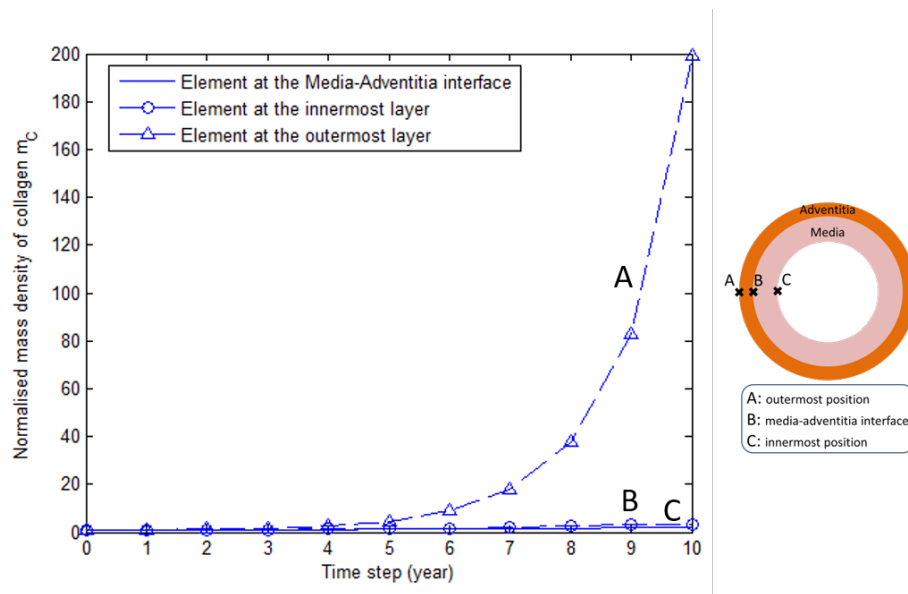


Figure 4.20: Comparison of the growth of normalised mass density of collagen between the elements at the innermost layer, outermost layer, and the media-adventitia interface (Case 2).

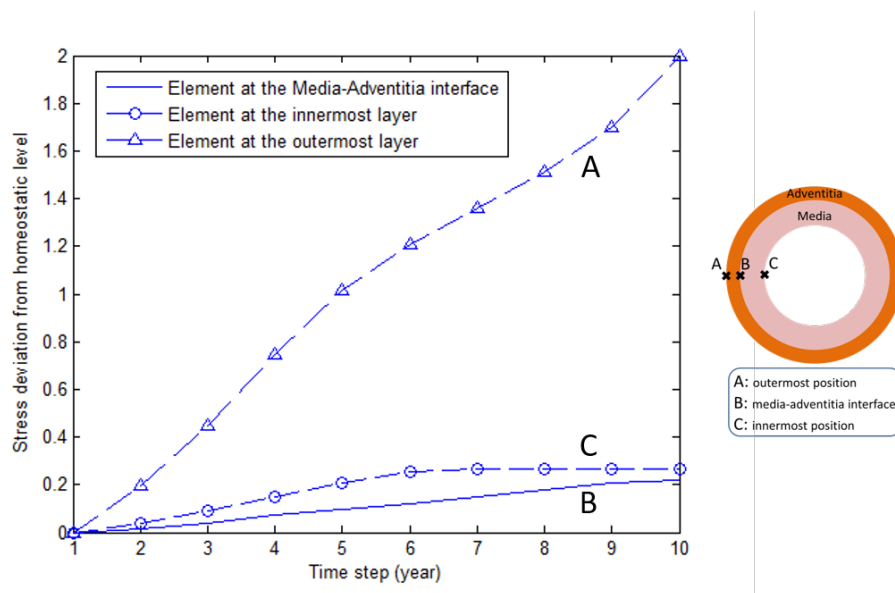


Figure 4.21: Circumferential stress deviation  $(\sigma(t) - \sigma_h)/\sigma_h$  at each time step and the comparison between the innermost layer, outermost layer, and the media-adventitia interface (Case 2).

the innermost layer and 3.4 at the interface. The difference of the collagen growth between the two cases is in response to the different elastin degradation in the adventitia layer. For the outermost layer (basically the adventitia layer) in Figure 4.20, the collagen growth is continuously accumulating to 200 times the initial value at  $t = 10$  years due to significant stress increase. The major load bearer is gradually transferred from the media to the adventitia for Case 2 elastin degradation. As for the Case 1 uniform elastin degradation, the adventitia is an even weaker structure than the media, resulting in the adhesion of the two layers restricting the adventitia from further expansion, thus the stress inside the adventitia is lower than the homeostatic level. Too much elastin loss in the adventitia layer softens the structure and fails to support the media layer. However, based on physiological observations, the adventitia should act as a "jacket" to restrain the radial expansion of the artery. In addition, the majority of elastin constituents reside in the media layer. Therefore, less or no elastin loss in the adventitia layer is a more reasonable simulation assumption for modelling the G&R of aneurysm structure.

## 4.6 DISCUSSION

This chapter presents a simple 1D SGT example to link the mechanical stress and oxygen level to the G&R of vascular collagen constituent. During the aneurysm progression, the load bearer is transferred from the elastin to collagen fibres due to the loss of elastin and the higher strain state. The remodelling of the collagen parameter  $k_2$  is right-shifting the stress-strain relationship, yielding the decrease of stresses inside the wall under the same pressure. Meanwhile, the mass of collagen is growing to prevent further enlargement. If  $k_2$  stays constant without remodelling, the diameter will expand less but with higher stresses inside the wall. In the proposed computational model, the stress is the primary indicator to aneurysm G&R process. Although the 1D model is relatively simple, it provides a basic chemo-mechano-biological scheme on how to model the mechanical and chemical environments of the arterial wall and the link to aneurysm evolution. Further clinical data and phenomenological information are desired for the improvement of the mechanical-mediated standard for the simulation of aneurysms. This framework initiates the setup of a model to be implemented in clinical cases and enables the interaction between *in silico*, *in vivo*, and *in vitro* models.

The key aspect of the SGT framework is linking the oxygen concentration to the

synthesis of collagen. The decline in collagen growth rate  $\beta$  is defined by equation (4.7), whereby the oxygen concentration is downregulated by the propagation of the thrombus layer. A faster decrease in  $\beta$  could possibly slow down the increase in collagen. The growth of collagen constituents retains the model from further radial expansion. If there is no new collagen deposition ( $\beta = 0$ ), the thrombus layer propagates more and creates a possible hypoxic environment. On the other hand, if the collagen mass density keeps growing without restriction ( $\beta = 1$ ), the corresponding synthesis of cells could also lead in hypoxia by excessive cell respiration. This indicates the critical consideration of the oxygen transport and its further influence on cell functionality. Fibroblasts require a minimum amount of oxygen in order to function. Thus, under the anoxic condition, the balance between the fibre deposition, cells respiration and local oxygen level is essential to maintain the health and strength of arterial wall. The SGT model utilises the growth rate  $\beta$  corresponding to the oxygen concentration to imply the functionality of fibroblasts for stimulating the growth of collagen. Although the extreme condition ( $\overline{C_w} = 0$ ) is not shown here, we demonstrate the potential of modelling the possible deleterious effects of thrombus on aneurysm evolution.

It is also important to point out the limitations of this conceptual 1D G&R. Firstly, the oxygen consumption rate inside the wall stays constant, which may not be true as the cell proliferation and turnover rate are not considered. Oxygen within the arterial wall is mainly consumed by the SMCs in the media and fibroblasts in the adventitia. As the aneurysm evolves, the concentration of SMCs and fibroblasts varies over time. Thus, the adaptive response of cellular components to the descending oxygen level is the correlation between the oxygen consumption rate and the cell concentration. This correlation requires further definitions and experimental data to enhance our physiological understanding. Holland (2012) proposed a hypothetical mathematical model to represent the oxygen consumption rate to be a function of average oxygen tension, and the normalised mass density of elastin and collagen. This method could be implemented in the SGT framework, but the focus here is to include the influence of oxygen level to aneurysm progression.

Also, the thrombus formation is simply defined by the radial expansion of the artery and the fixed lumen diameter. The assumption made here resembles the experimental observation (Weiss et al. (1986); Nesbitt et al. (2009); Bowker (2010)) that the formation of a thrombus is intrinsically associated with local wall shear stress

(WSS). The greater diameter of aneurysm leads to lower WSS resulting in a faster thrombus deposition rate. The difference in the proposed SGT is that the flow dynamics is not disturbed with a fixed lumen diameter and a geometrical specification is applied to develop the thrombus. The oxygen transport modelling in the SGT provides a hypothetical stabilising result to recover the WSS back to the normal condition of a healthy artery. Although this formulation displays the dynamic progression of thrombus during aneurysm growth, its oversimplification cannot demonstrate the biocomplexity for the deposition of a blood clot. In the oxygen transport model developed by Holland (2012), thrombus growth velocity  $V_{th}$  is linked to local WSS:

$$V_{th} = f\left(\frac{1}{WSS}\right) \quad (4.10)$$

With a lower WSS due to the enlargement of aneurysm, the thrombus layer accumulates faster. As the lumen diameter is recovered by the thrombus progression, the propagation velocity reduces with greater WSS values. This could be potentially applied in the SGT model to compete with thrombus formation hypothesis in the future.

In Appendix C, a stability analysis of the stress-mediated G&R process is conducted on a single-layered tube model. Results of this analysis indicate that the radial stretch and the  $k_2$  remodelling are not able to stabilise under the G&R based on the total stress presented in this chapter, however, they are able to stabilise under the G&R based on the collagen fibre stress. This is due to the significant increase of stress in elastin during the dilation of the model. In this chapter, the total stress G&R is applied on the two-layered tube model consisting of different material parameters in each layer. The stabilisation of stress deviation and  $k_2$  remodelling in the media of Case 2 is due to the adherence of the two-layered structure and the non-uniform elastin degradation to restrict its radial enlargement. While in the adventitia of Case 2 and both layers of Case 1 demonstrate an unstabilised condition of  $k_2$  remodelling. This is in agreement with the stability analysis in the appendix.

To summarise, the purpose of  $k_2$  remodelling is to reduce the stresses on the collagen, while the collagen growth is to support the strength of the structure and prevent excessive enlargement of the aneurysm. The stabilisation of the diameter not only avoids further radial expansion, but also retains a steady oxygen level within the vessel wall for a settled thrombus thickness. The focus of the approach presented here is to study the interactions between the mechanical and chemical responses to the cell and tissue levels by this 1D SGT framework. Although the G&R

method is relatively simple, it provides a novel multi-scale and multi-physics computational framework to couple the mechanobiology and the influence of chemical transport within a diseased artery. A more comprehensive G&R method requires further physiological data which can be implemented in this framework when it is available.

## 4.7 CONCLUSION: THE BENCHMARK OF THE 1D MODEL

An extra thought of the proposed SGT model compared to previous aneurysm evolution models is linking the average oxygen tension within the wall to the growth rate of collagen fibres. The oxygen level is disturbed by the presence of a thrombus layer which is commonly present in AAAs (Harter et al., 1982) and also speculated to have the same effect on IAs (Lasheras (2007); Humphrey and Taylor (2008)). Therefore, it is crucial to model the propagation of the thrombus layer and how the fibroblasts and arterial structure respond to oxygen deficiency during the progression of the aneurysm. This SGT framework provides a very basic and general computational tool to simulate the connection between the thrombus propagation, the oxygen level, and the growth of collagen. Furthermore, it considers the transmural variation in a thick-walled model where the G&R of collagen constituents in different layers and positions through the wall thickness are taken into account.

The example of the SGT model illustrated here is implemented with a stress-mediated G&R method which can be replaced and computed with other G&R methods for further improvement. The dominant term of this stress-mediated G&R method is the stress deviation which influences both the remodelling of  $k_2$  and the growth of collagen mass density. For the diffusion modelling, the decreasing oxygen level decelerates the growth rate of collagen, represented as the functionality of fibroblasts. This is a simple illustrative case for the cell functionality in the SGT framework. It still requires more physiological definitions on the connection between the fibroblasts, the cellular respiration rates, and the turnover of collagen to be implemented in the SGT.

Although, the variables within the 1D model are based on previous computational research, it still demands further improvements to be applied on a patient-specific aneurysm model. The mechanical and chemical stimuli merit better representations in order to correspond to spatial variation in genuine aneurysm geome-

tries. Nevertheless, this novel chemo-mechano-biological model is a step further towards modelling a realistic aneurysm development time frame, from its initiation and evolution, to the possibility on bursting.



## APPLICATION ON 2D SGT FUSIFORM MODEL

---

This chapter introduces an axisymmetric fusiform aneurysm model implemented in the SGT framework to investigate the spatial variation in both axial and radial directions. For the idealised fusiform model, the axisymmetric characteristic is initiated by the dimensional variation of elastin degradation in axial direction from the tube-like healthy artery. Moreover, due to the geometrical influence of the axisymmetric deformation, the thickness of thrombus deposition varies along the axial position resulting in the non-uniform oxygen concentration through the length of the model. To link the influence of spatially distributed oxygen level to collagen synthesis, an element-based projection between the vascular mechanical modelling and transport modelling is developed. Therefore the localisation of mechanical and chemical stimuli in relation to the G&R of individual element is achieved.

---

**Objective:** the objective of this chapter is to extend the application of the proposed G&R framework on an idealised aneurysm geometry to investigate the spatial variation of the G&R responses. Due to the difference in radial enlargement and oxygen distribution, the localisation of mechanical and chemical stimuli in relation to the G&R process can be observed.

### 5.1 2D SGT FUSIFORM ANEURYSM

This section introduces the geometrical setup of the fusiform model and how to project the concentration data from transport modelling on the structural mesh of

the aneurysm.

### 5.1.1 Axisymmetric elastin degradation (Fusiform aneurysm)

The SGT framework utilises a mathematical formulation to simulate the elastin degradation in response to time. The 1D tube model in the last chapter demonstrates the modelling behaviour of the SGT in a uniform response along the axial direction. However, from clinical observations, although the shape of an aneurysm seems arbitrary, it is generally in a fusiform or a localised destruction (?). The 1D model disregards the variation through the length of the model. Therefore, in order to illustrate the spatial degradation of the aneurysm structure, we apply a simple axisymmetric degradation function (5.1) according to Watton et al. (2004) on the cylindrical model. A rate of elastin degradation is presented to describe the variation in axial direction over time:

$$m_E(x_1, t) = 1 - \left( \left( 1 - (c_{min})^{\frac{t}{T}} \right) e^{-m_1 \left( \frac{L_1 - 2x_1}{L_1} \right)^2} \right) \quad (5.1)$$

where  $x_1$  denotes the axial position of the model from 0 to  $L_1$ , which is the axial length of the model;  $t$  indicates the time step with in total time  $T$ ;  $c_{min}$  is the minimum concentration of elastin at  $t = T$ . Note that  $m_1$  controls the degree of localisation of the degradation of elastin in the axial direction: increasing the value of  $m_1$  renders the degradation more localised to the centre point of the model; decreasing the value of  $m_1$  means that the degradation behaves more uniformly through the axial length of the model. If  $m_1 = 0$ , it yields a uniform degradation throughout the axial domain as introduced by the 1D model in Chapter 4. In addition, the transmural difference through the wall thickness is also included in the fusiform model. As mentioned in Section 4.5.2, the loss of elastin mainly occurs in the media layer. Given different minimum values of the normalised mass density of elastin in the media and adventitia layers, the portion of elastin degradation varies in layers over time. Two minimum values  $c_{min}^M$  and  $c_{min}^A$  follow the definition in equation (4.9) to represent the minimum elastin concentration in the media and adventitia respectively. For the fusiform aneurysm model, the minimum values of elastin only happen at the pivot of the model and exponentially increase towards the two ends to reach the initial value of 1.

Figure 5.1 shows an illustrative example of an axisymmetric fusiform aneurysm

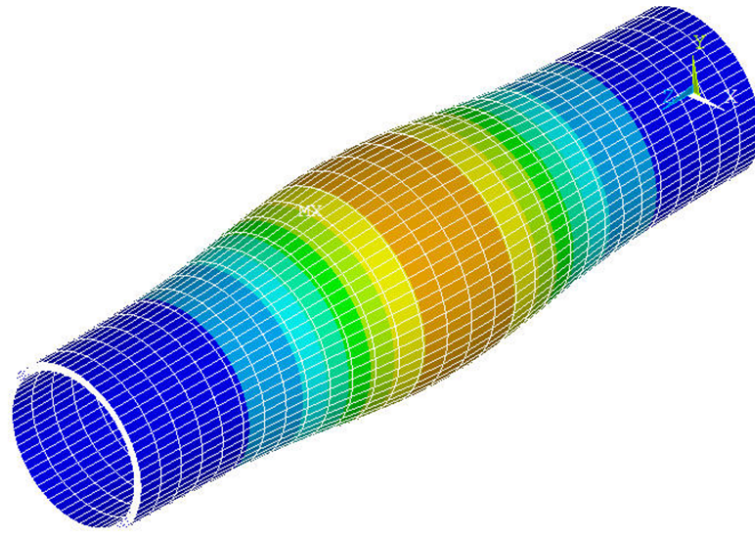


Figure 5.1: Illustration of the axisymmetric fusiform aneurysm on the tube model (different colours indicate different levels of radial deformation).

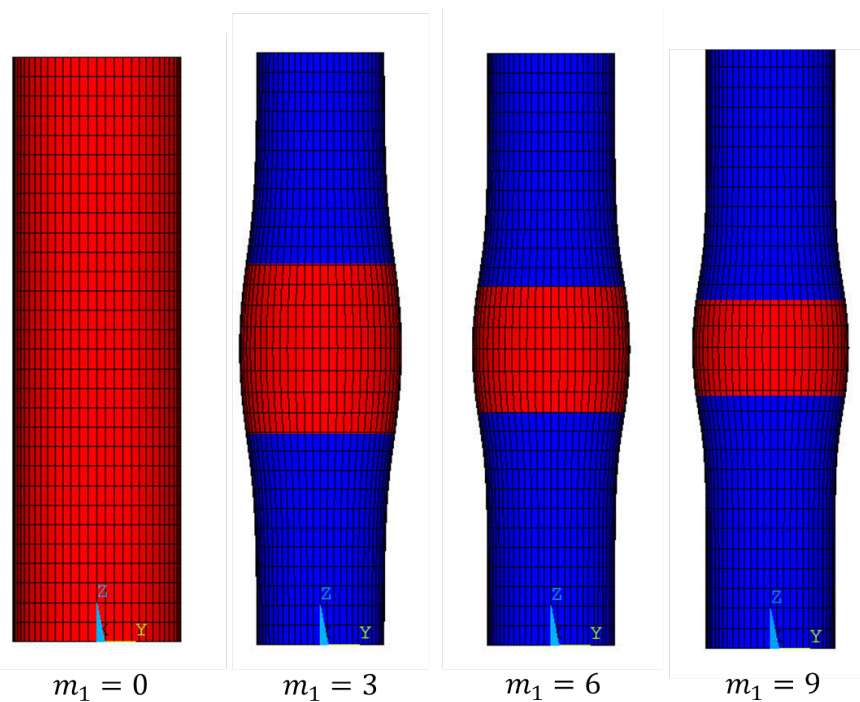


Figure 5.2: Illustrative models with different degree of the localisation in elastin degradation ( $m_1$ ): red colour indicates the radial deformation is more than 15% of the original diameter; blue colour indicates the deformation is less than 15%.

model. Due to the primary loss of elastin in the central region, the maximum deformation happens at the same location, while the other two ends remain in their initial positions. Therefore, the deformed geometry is symmetric with respect to the centre section and the corresponding mechanical responses within the arterial wall change according to the position. In Figure 5.2, the influence of different values of the localised parameter  $m_1$  on the shape of the fusiform model is illustrated: the red part in the model indicates that the radial deformation at that point is more than 15% of the original diameter; the blue part indicates the deformation is less than 15% of the original diameter. It can be seen that when  $m_1 = 0$  the enlargement of the model is even, while with the increase of the  $m_1$  value, the red part is more concentrated towards the central point.

Note that the G&R hypothesis introduced in Section 4.2 is also implemented in the fusiform model to test the effect of the spatial variation during aneurysm progression. Results will be shown in Section 5.2, in which the boundary condition and constitutive parameters are based on Table 4.1, while the elastin degradation in equation (5.1) is applied for non-uniform deformation along the axial position. The focus is to demonstrate how the SGT model adjusts and reacts to non-uniform mechanical responses. A longer time frame is applied here ( $t = 15$  years) with more time steps of G&R to investigate the modelling behaviour of the fusiform model, especially for the significant variation in its axial direction. Therefore, with more applications of different scenarios on G&R, this SGT framework can be modified for modelling the spatially distributed mechanical responses with a more complex geometry.

### 5.1.2 Mesh projection between solid model and transport model

In Chapter 4, the collagen growth rate  $\beta$  is associated with the average oxygen concentration and uniformly distributed in the 1D model. However, for the fusiform model, the local oxygen level differentiates not only through the radial direction but also along the axial direction. This is due to the non-uniform deformation resulting in different thickness of thrombus propagation along the length of the model. A thicker thrombus layer blocks more oxygen transport through the arterial wall. Thus, it can be conceived that the lowest local oxygen level is taken place at the peak of the deformed geometry.

For the 1D model, we assume the collagen growth rate is at the same pace

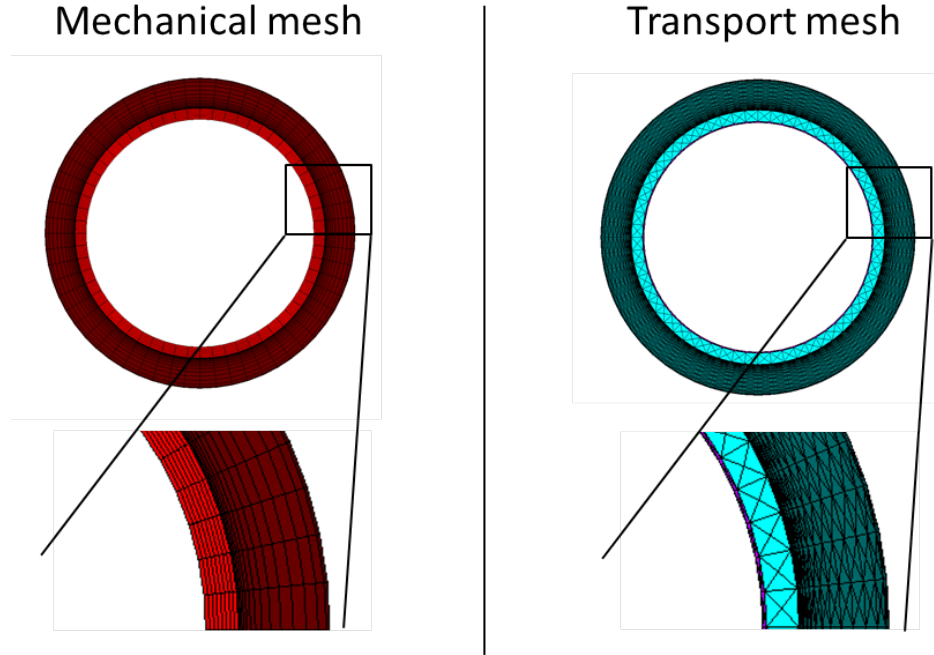


Figure 5.3: Meshes for the mechanical model and transport model of the arterial wall.

throughout the domain as the oxygen level is in a general response along the axial direction. However, for the fusiform model, the oxygen concentration is spatially distributed due to various thicknesses of thrombus layer. Fibroblasts sense the variation of oxygen level within the space, thus the collagen synthesis shall regulate differently according to the position inside the arterial wall in relation to the localised oxygen deficiency. A mathematical representation is derived to interpret the influence of local oxygen level on local collagen growth. Equation (5.2) is modified from equation (4.6) which links the growth rate to average oxygen concentration in the 1D model:

$$\beta^i(t) = \beta_0^i + (\beta_{min}^i - \beta_0^i) \left( \frac{(C_w^i(t)) - (C_w^i)_0}{(C_w^i)_{min} - (C_w^i)_0} \right) \quad (5.2)$$

where  $i$  denotes the mesh number of the mechanical model;  $C_w^i(t)$  is the oxygen tension within the corresponding position of the  $i$ th element of the mechanical model in time  $t$ ;  $(C_w^i)_0$  is the initial oxygen concentration of the  $i$ th element;  $(C_w^i)_{min}$  is the minimal required oxygen level of the  $i$ th element. Thus, the growth rate is spatially and transmurally different in response to the current and local oxygen level within the arterial wall.

The SGT framework is fully integrated in the ANSYS software, whereby the solid

structure and the oxygen transport are simulated separately with different modelling packages. The main issue when linking the corresponding oxygen level to the collagen growth rate at individual positions in the arterial wall is the projection of the oxygen concentration on mechanical meshes. For the 1D G&R model, we only need one value from the transport modelling which is the average oxygen concentration in each time step. However, for the fusiform aneurysm model, oxygen concentrations throughout the arterial wall are exported and associated with the growth rate  $\beta$  in each element. As presented in Chapter 2 and Chapter 3, the mechanical model and transport model of the arterial wall are simulated with different element types in ANSYS APDL. For the arterial mechanical model, the mesh element is SOLID185 (3D 8-node Hexahedron) with a self-defined ordering on mesh number; for the oxygen transport modelling, the mesh element is SOLID240 (3D 10-node tetrahedral diffusion solid) with an unstructured mesh in ANSYS APDL. SOLID240 only has one degree of freedom in concentration and cannot interplay or translate the data to SOLID185 which only has degrees of freedom in the nodal  $x, y, z$  directions. In addition, the mesh type and numbers in the mechanical model and the oxygen diffusion model are different to each other as shown in Figure 5.3, thus the concentration data in the transport model cannot be directly transferred to the mechanical model. Therefore, we need to develop a systematic process to map the concentration on each SOLID185 element during the aneurysm G&R.

To be able to translate the information from transport to solid, we begin with the output of the oxygen transport results. In the post-processing of the oxygen diffusion model, the results are exported by naming the user-defined paths from the outer surface to the inner surface of vascular wall. The oxygen data inside the thrombus layer is ignored as we only require the oxygen level within the wall for G&R. Each path is defined by multiple nodes through the thickness of the arterial wall and the corresponding nodes are located according to the nodal positions from the inner surface to the outer surface of mechanical mesh. As there are 8 elements along the radial direction in the mechanical model, 9 nodes along one path are defined from the inner surface to the outer surface. As there are 30 mechanical elements in the axial direction and 60 elements in the circumferential direction, 31 paths on one axial plane and a total number of 1860 paths are given. The 9 nodal concentration data on one path are projected on the radial positions of the mechanical nodes. The nodal solutions of concentration in the transport model are then exported for the mechanical model.

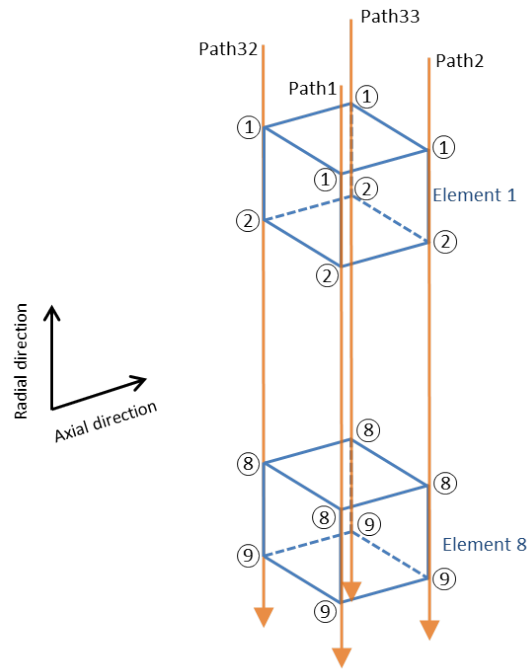


Figure 5.4: Definition of nodes and paths along the radial direction.

Note that the G&R method is an element-based algorithm to update the material parameters within. Therefore, for remodelling purposes, an element-based concentration is needed for updating the collagen growth rate  $\beta$  in equation (5.2). For the 3D mechanical model, one element is a brick element formed by 8 nodes whereby every 2 nodes are on one path from the transport model. Therefore, to find all the nodal concentrations in the relevant 8 nodes of one brick element, it needs to identify the associated path number and the corresponding two nodes as illustrated in Figure 5.4:

Element 1:	Element 8:
Path 1: node 1 & 2	Path 1: node 8 & 9
Path 2: node 1 & 2	Path 2: node 8 & 9
Path 32: node 1 & 2	Path 32: node 8 & 9
Path 33: node 1 & 2	Path 33: node 8 & 9

Path 1 and Path 2 are on the same axial plane, whilst Path 32 and Path 33 are on the other axial plane. All 4 paths collect the corresponding two nodes to form the brick element. Thus, the 4 paths and the 2 nodes on each path provide 8 nodal concentrations in one element. The average value of the 8 nodal concentrations is

taken to represent the concentration for the mechanical element. In addition, the element number sequence formed by the designated nodes for the path in the transport modelling is identical to the element order of the mechanical model. Therefore the element-based concentration can be directly transferred for the element mapping between mechanical and transport models in the SGT framework. A simultaneous update of the element-based growth rate  $\beta$  according to the element-based oxygen concentration is developed. Consequently, the growth rate is not linked to the average oxygen concentration as in the 1D model but to the individual oxygen level in each element. Therefore the collagen growth rate varies along the axial and radial position due to the corresponding oxygen concentration.

For the fusiform model, the thickness of thrombus varies along the axial direction due to the axisymmetric elastin degradation resulting in the spatial difference of oxygen concentration and subsequently the growth rate  $\beta$ . It can be expected that the oxygen level is diminished the most at the centre with the thickest thrombus, while at the two ends of the model, the oxygen level is less disturbed because of the extremely thin layer of thrombus. Subsequent influence of the non-uniform thrombus layer to the collagen growth will be demonstrated in the results section. As existing aneurysm models focus on the mechanical stimuli to the G&R of arterial constituents, the proposed SGT framework includes the oxygen transport with the localised effect during aneurysm evolution. The oxygen concentration modelling renders an example of molecular transport through the aneurysm domain and addresses its influence on collagen adaptation when there is disturbance from the homeostatic condition.

## 5.2 RESULTS

The parameters for the fusiform aneurysm model are based on Table 4.1 from the 1D model and required additional setup in Table 5.1, which gives the minimum elastin concentration in the media and the adventitia, the degree of the localisation on elastin degradation, and the minimum requirement of the oxygen concentration in an element-based approach. The non-uniform elastin degradation within the arterial wall is applied to the cylindrical model based on the assumption stated in Section 4.5.2 that the major elastin loss happens in the media layer. However, in order to amplify the scale of the diameter change within the central region and to decrease the excessive collagen growth in the adventitia as shown in Case 2 1D model,

<i>Parameter</i>	<i>Symbol</i>	<i>Value</i>
Minimum normalised mass density of elastin in media	$c_{min}^M$	0.1
Minimum normalised mass density of elastin in adventitia	$c_{min}^A$	0.25
Degree of localisation on elastin degradation	$m_1$	3
Minimum requirement of oxygen level in each element	$(C_w^i)_{min}$	$0.1(C_w^i)_0$

Table 5.1: Parameters used for modelling the evolution of fusiform aneurysm.

we also apply an axisymmetric elastin loss in the adventitia layer for the fusiform aneurysm. Figure 5.5 shows the prescribed elastin concentration within the media layer every 5 years; Figure 5.6 shows the prescribed elastin concentration within the adventitia layer every 5 years. In both layers, the central point of the model loses more elastin as described by equation (5.1) and the variation through the axial direction is illustrated in these figures. The difference in elastin concentration at the axial positions increases during aneurysm progression, especially between the central region and the two ends. As to be expected, the largest radial deformation of the model happens at the lowest elastin concentration during aneurysm progression. Figure 5.7 focuses on the central region of the fusiform model with the cross-section along the axial direction at  $t = 15$  years. The arterial wall (the blue part in the figure) undergoes an axisymmetric radial deformation from the central line of the model, while the thrombus layer (the purple part in the figure) is deposited between the inner surface of the wall and the lumen diameter. Consequently, the thickness of the thrombus layer is thickest at the centre and decreases towards the two ends. Thus the oxygen distribution within the arterial wall could be spatially influenced by the non-uniform thickness of thrombus formation. Figure 5.8 shows the diameter changes over time at the centre of the model where the major dilation happens. The diameter keeps increasing during the G&R process while the other two ends almost stay in their original positions.

Figure 5.9 shows that the oxygen concentration varies along the axial and radial direction due to the presence of the thrombus layer. The thicker the thrombus layer within the model, the lower the oxygen concentration is. As a result, the least oxygen level in the three different layers in Figure 5.9 always occurs at the peak deformation,

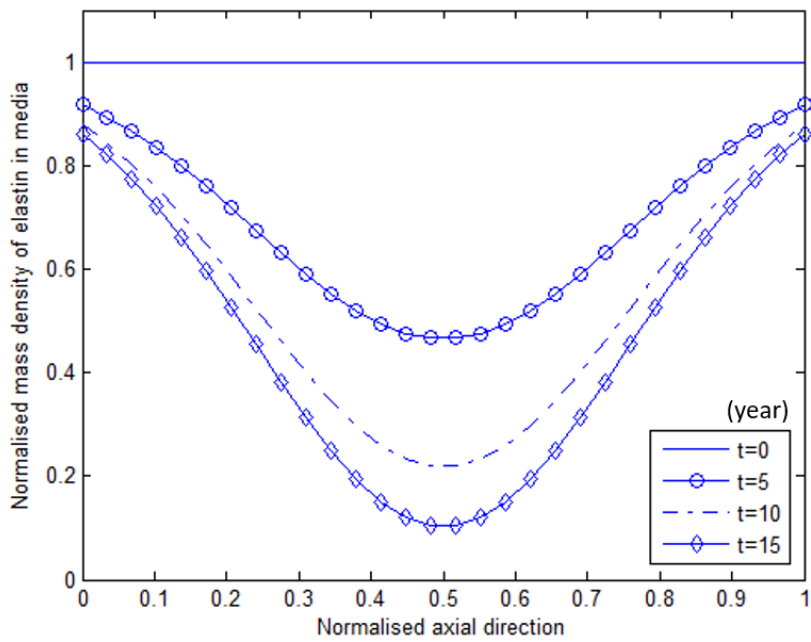


Figure 5.5: Axisymmetric elastin degradation in the media layer.

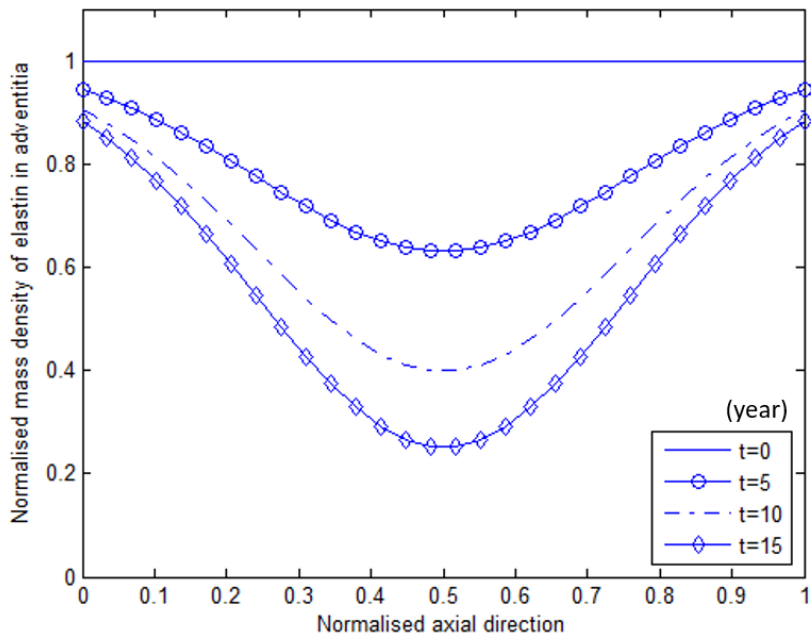


Figure 5.6: Axisymmetric elastin degradation in the adventitia layer.

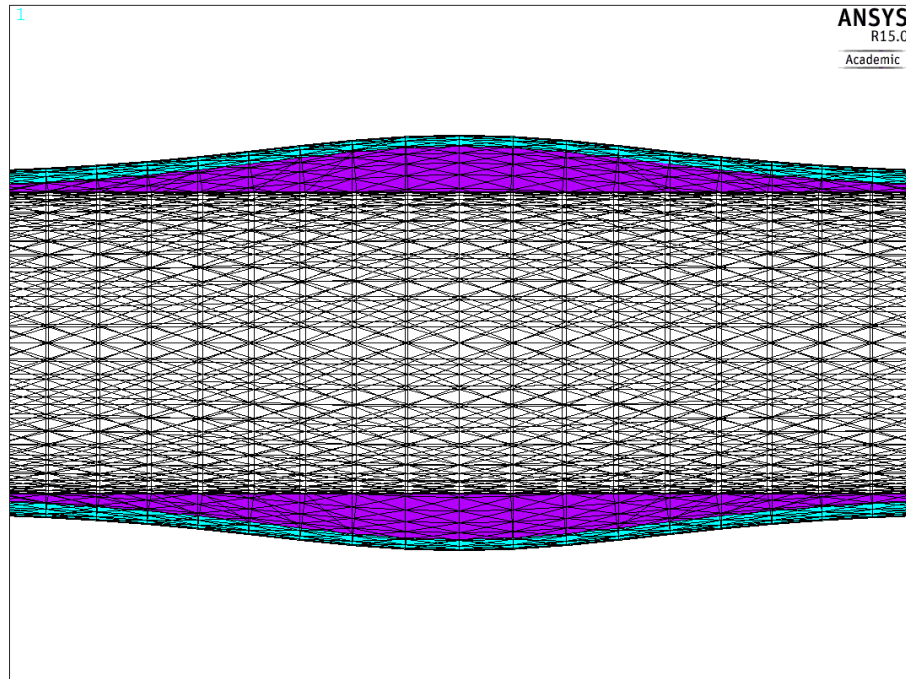


Figure 5.7: Axial cross-section of the fusiform model and the thrombus layer within.

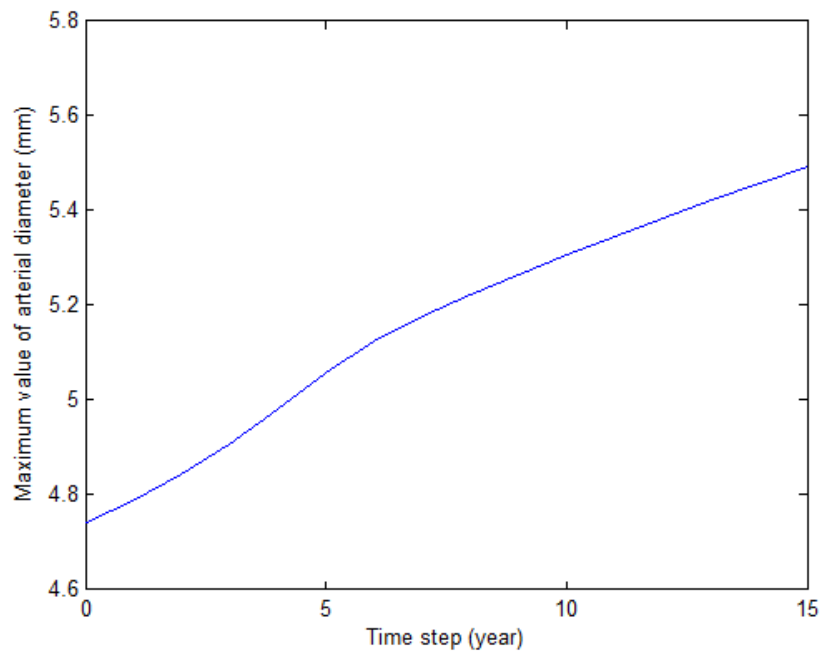


Figure 5.8: Maximum diameter of the fusiform aneurysm at each time step.

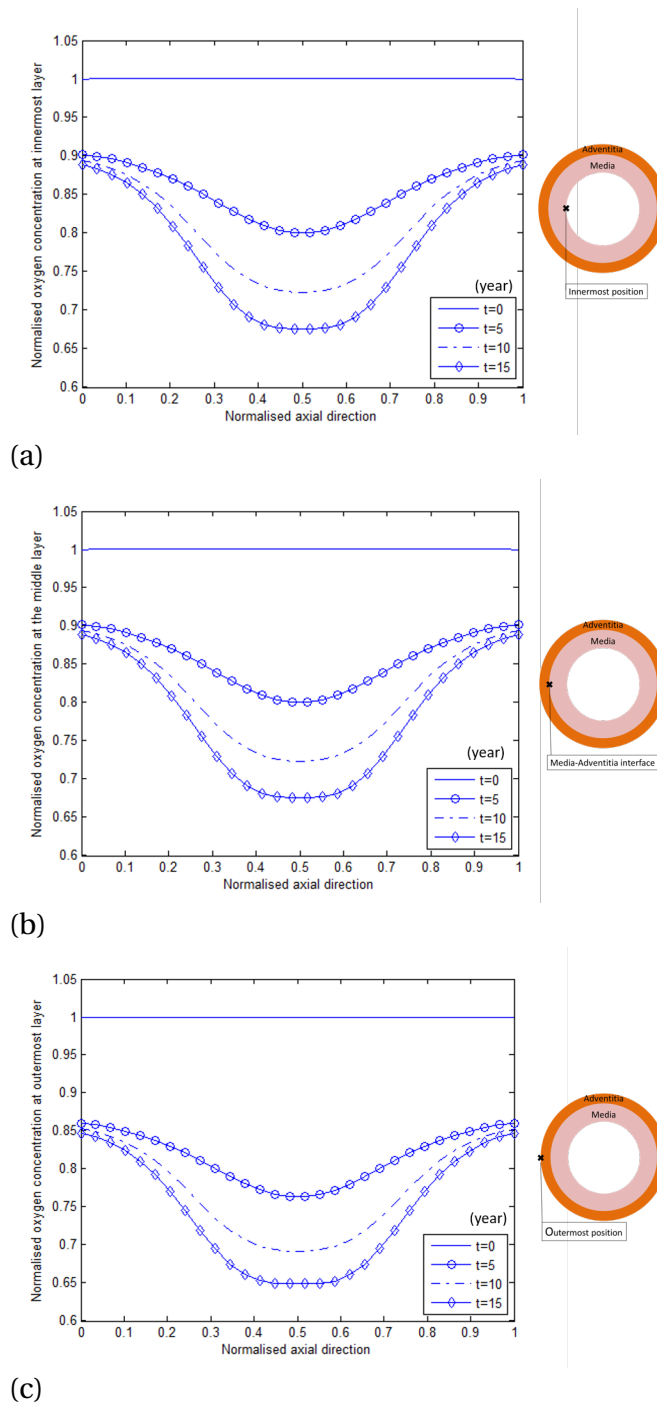


Figure 5.9: Oxygen concentration in different layers along the axial direction during the aneurysm progression: (a) innermost layer; (b) middle layer; (c) outermost layer.

which is the centre of the model. Furthermore, it can be seen that the outermost position is with the lowest oxygen level in every time step compared to the innermost and middle positions. Thus, the corresponding collagen growth rate  $\beta$  is lower at the adventitia layer, especially at the central region of the model. In Figure 5.10, the transmural variation of the growth rate  $\beta$  at the central region of the model is demonstrated at different time steps. Due to the fact that oxygen concentration is transmurally and spatially different, as shown in Figure 5.9, the growth rate associated with the local oxygen level in equation (5.2) is non-uniform within the arterial wall. The overall tendency is that the oxygen level is higher at the inner surface and gradually decreases towards the outer surface which reflects on the growth rate of  $\beta$  in Figure 5.10. With the higher oxygen level at the inner surface the growth rate is greater, while with the lower oxygen level at the outer surface the growth rate is lesser. When comparing different time steps during the aneurysm progression, all the growth rates through the radial direction are reduced proportionally from previous time step in correspondence with the thrombus propagation. The growth rate is highly dependent on the local oxygen level in its position within the wall. Therefore, the collagen synthesis is not only controlled by the element-based stress deviation but also the element-based oxygen concentration. This is an improvement from the 1D model which assumes a uniform collagen growth rate throughout the whole model. The fusiform model demonstrates the geometrical influence on oxygen transport and accounts for the spatial variation of the mechanical and chemical responses into the G&R process.

Figures 5.11, 5.12, and 5.13 show the  $k_2$  remodelling process over time in 3 different radial positions: innermost, outermost and media-adventitia interface layers respectively, through the wall thickness. The innermost layer can be the representation of media layer for the general response, while the outermost layer can be the representation of the adventitia layer. The interface layer shows the transitional relation between the two load-bearing layers. The  $k_2$  remodelling is dominated by the deviation of circumferential stresses as demonstrated in Chapter 4.

In Figure 5.11, for the media layer, the decrease of  $k_2$  at the central region indicates the major increase of stresses is located in the middle of axial position during the development of the fusiform aneurysm. At  $t = 15$  years,  $k_2$  at the centre is decreased to almost 10% of the original value, which reflects the fact that the normalised elastin density is degraded to 0.1 by that point. The stresses around the two

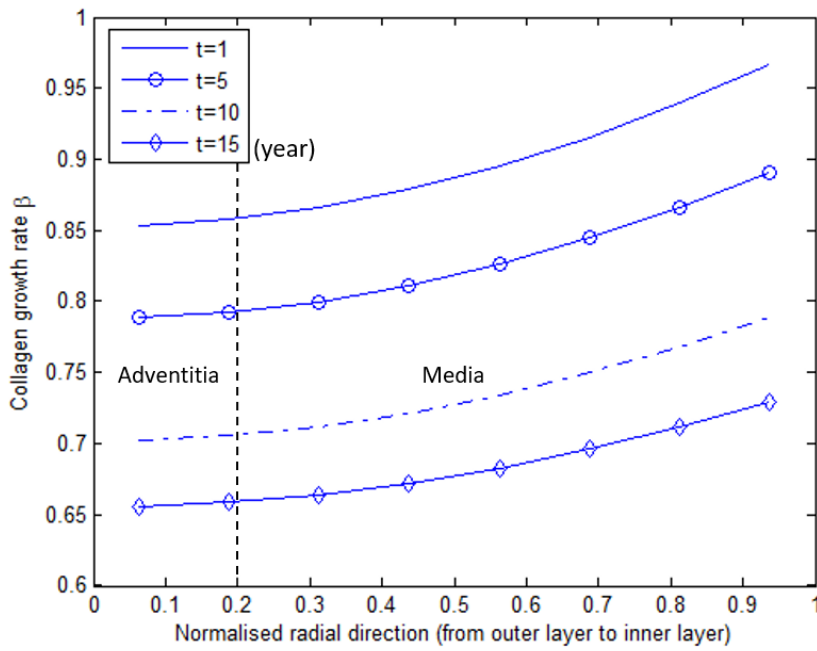


Figure 5.10: Collagen growth rate  $\beta$  along the wall thickness over time at the centre of the fusiform model.

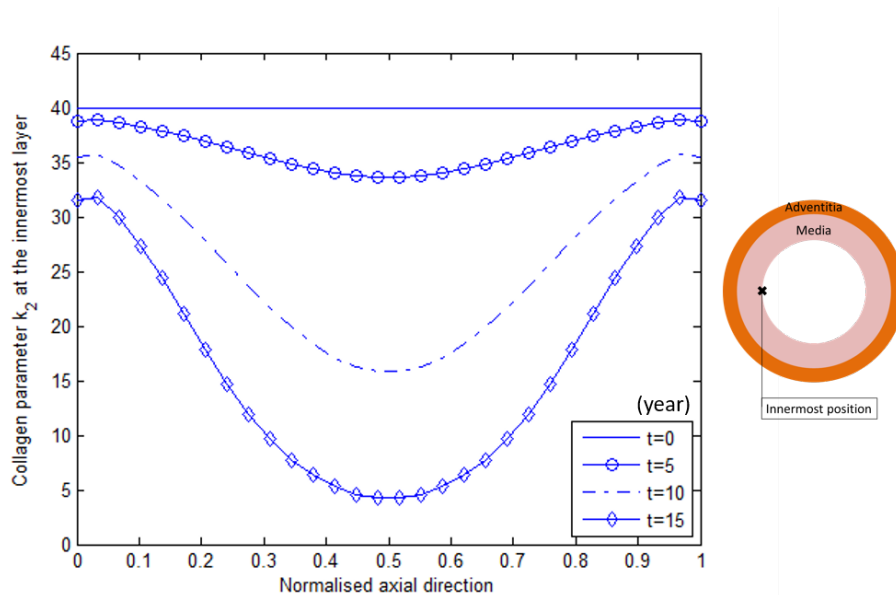


Figure 5.11:  $k_2$  remodelling at the innermost layer over time of the fusiform model.

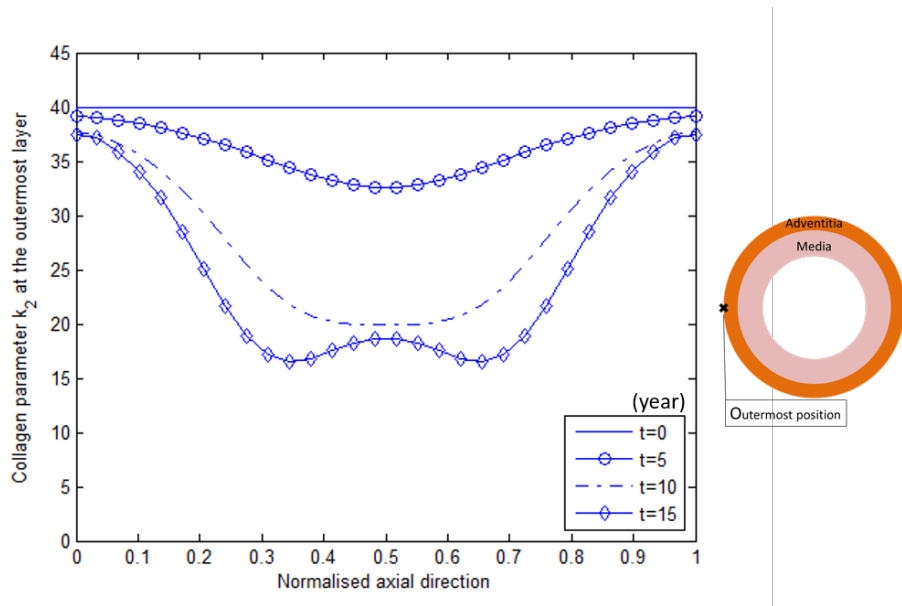


Figure 5.12:  $k_2$  remodelling at the outermost layer over time of the fusiform model.

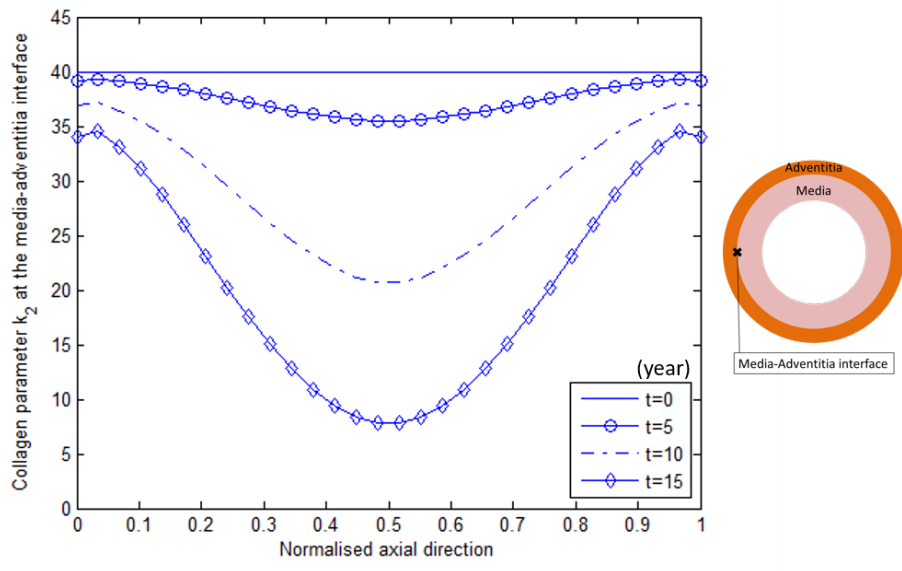


Figure 5.13:  $k_2$  remodelling at the media-adventitia interface over time of the fusiform model.

ends are relatively stable due to the very few elastin losses there, resulting in the smaller reduction in  $k_2$ . Consequently, the difference of the  $k_2$  value between the central point and the two ends is increasing over time as more elastin losses concentrate towards the centre. Overall, the  $k_2$  remodelling behaviour of the innermost layer is generally similar to the medial elastin degradation shown in Figure 5.5.

In Figure 5.12, for the adventitia layer, the decrease of  $k_2$  generally arises at the central region, which is also demonstrated at the media layer in Figure 5.11. However, the reducing amounts of  $k_2$  parameters in the adventitia layer are much less than those in the media layer. The least value of  $k_2$  is around 16 at  $t = 15$  years in the adventitia layer, whilst the least value of  $k_2$  in the media layer is around 4. This is due to the stress deviations in the adventitia layer are less than the deviations in the media layer, which implies that the medial stresses increase more than the homeostatic level during the evolution of aneurysm. The adventitia layer requires less collagen remodelling to reduce the stress deviation. Moreover, a significant event happens in the central region of the model at  $t = 15$  years: the least value of  $k_2$  is no longer in the centre but the two surrounding points. Additionally, the  $k_2$  parameters in the centre at  $t = 10$  and  $t = 15$  years have a minor difference which suggests that the stress deviation is stabilising. The stresses in the central elements are decreased during the G&R whereby the surrounding regions still undergo inadequate G&R to reduce the higher stresses. The maximum stress deviation is at the surrounding two points of the centre leading to the continual decrease of  $k_2$  in those regions. Overall, the general reducing response of  $k_2$  enhances the enlargement of the aneurysm, while the stabilisation of  $k_2$  remodelling in the middle point may arrest its own radial expansion from the surrounding area.

In Figure 5.13, the  $k_2$  remodelling at the media-adventitia interface is shown, where the integrated response is identical to the innermost layer in Figure 5.11, but with less reduction in  $k_2$ . The stress deviation increases towards the central point and the least value of  $k_2$  is around 7, which implies that the stress deviation at the interface is less than the deviation in the innermost layer. The transition between the media and adventitia layers shown here demonstrates the transmural variation of the fusiform model. Consequently, non-uniform collagen remodelling through the radial and axial directions in response to the localised elastin destruction is demonstrated here. Overall, the axisymmetric elastin degradation forces the  $k_2$  remodelling are concentrated in the central region.

Figures 5.14, 5.15, and 5.16 show the normalised mass density of collagen over time in 3 different radial positions: innermost, outermost and media-adventitia interface layers respectively, through the wall thickness. In Figure 5.14, as to be expected, the collagen fibres at the innermost layer are growing significantly in the central region during the aneurysm progression. The peak value of  $m_C$  is around 13 at  $t = 15$  years at the centre, while  $m_C$  at the two ends remains approximately 1. The collagen growth is regulated by the stress deviation and the growth rate  $\beta$  which is associated with the local oxygen concentration. Different from the 1D model, the growth rate is spatially different due to the fact that the oxygen level is influenced by the axisymmetric thrombus layer formation. If the growth rate is a uniform value based on the average oxygen level in each G&R iteration, the collagen growth would increase more at the central region. Additionally, the collagen growth from  $t = 10$  to  $t = 15$  increases massively in the innermost layer compared to the outermost layer and the interface shown in Figure 5.15 and Figure 5.16. The higher stress deviation and the higher local oxygen level in the innermost layer lead to greater growth of collagen mass density. Although fibroblasts synthesis is not directly demonstrated in the SGT model, the increase of collagen mass refers to an active fibroblasts functionality within the arterial tissue which may consume more oxygen resulting in the extreme hypoxic condition. The potential of including the influence of cell respiration rate will be introduced in the discussion section.

In Figure 5.15, the amount of collagen growth in the outermost layer is much less than the amount in the innermost layer. The difference between the outermost and innermost layer in  $m_c$  is even greater than in  $k_2$ . It can be assumed that both the growth rate and the stress deviation are lower in the outermost layer. With the lower oxygen level close to the adventitia layer, the lower growth rate  $\beta$  goes towards the outermost layer at the same time step. This demonstrates a great transmural difference here from the 1D model which assumes the collagen growth rate is uniformly distributed through the whole model.

The modelling characteristic shown by  $k_2$  remodelling is also shown here as the peak value of  $m_c$  arises in the surrounding points of the centre. Note that at the central point, the difference of the  $m_c$  in  $t = 10$  and  $t = 15$  is very small which indicates that collagen synthesis stabilises at the central point. The stresses are reduced from a higher level to the homeostatic level, while the growth rate is downgraded to 0.65, which corresponds to the current normalised oxygen level 0.65 at the central

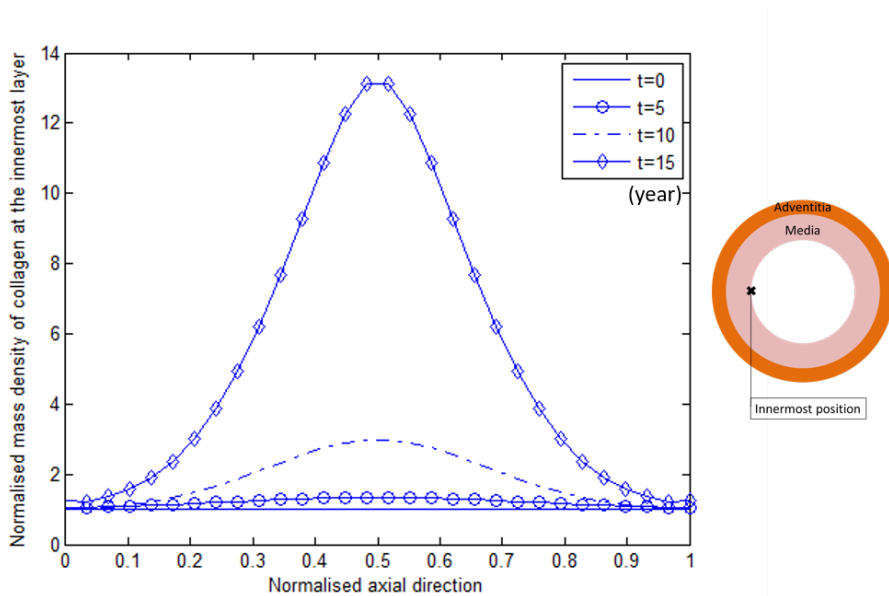


Figure 5.14: Normalised collagen mass density at the innermost layer over time of the fusiform model.

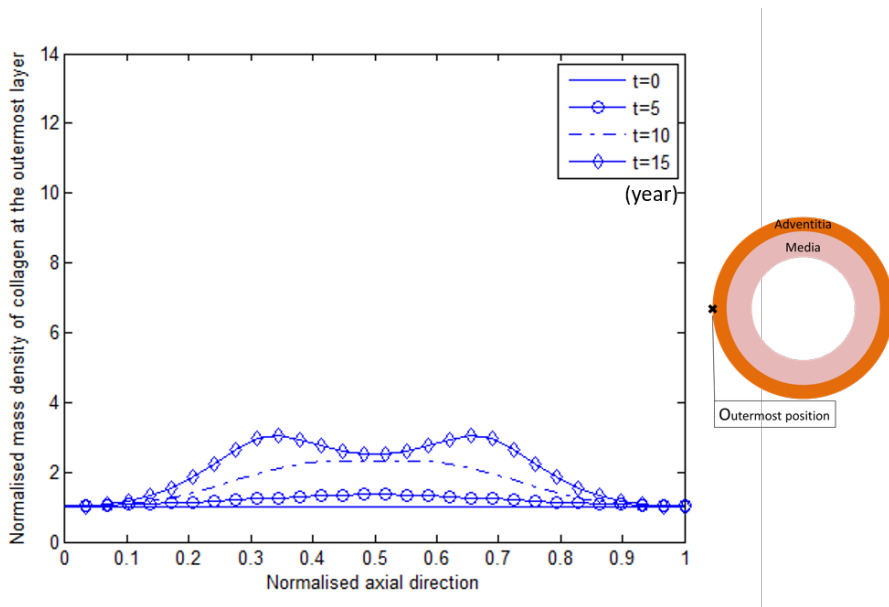


Figure 5.15: Normalised collagen mass density at the outermost layer over time of the fusiform model.

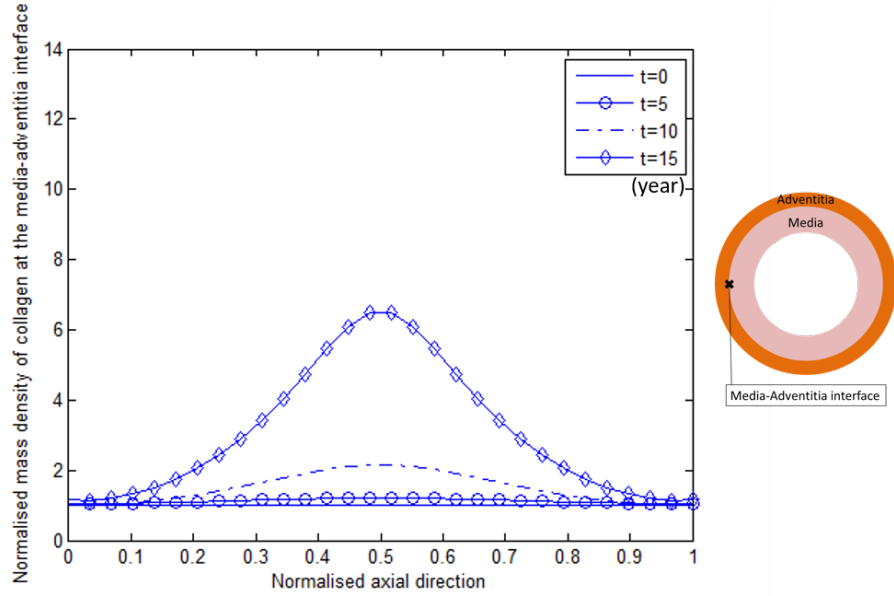


Figure 5.16: Normalised collagen mass density at the media-adventitia interface over time of the fusiform model.

point at  $t = 15$  years shown in Figure 5.10. The outer layer retains its functionality as a protective sheath to the media layer as the mechanical response within the layer is reaching a new homeostasis, especially within the central region. The reduced amount of elastin degradation and collagen G&R in the adventitia layer inhibit the radial expansion of the fusiform model.

Figure 5.16 shows the transitional interface of the normalised collagen mass density between the media and adventitia layer. It displays a similar trend of collagen growth in the innermost layer, but the overall values of  $m_c$  are approximately half the values in the innermost layer. The difference between the innermost layer and the interface is greater in  $m_c$  than in  $k_2$ , because for the collagen growth modelling, there is an additional term  $\beta$  linking to the transmural different oxygen concentration. Note if we compare the updating curve between the  $k_2$  and  $m_c$ , it is evident that the increase in  $m_c$  is more centralised than  $k_2$  reduces during the G&R. This is due to the multiplication by the growth rate and the stress deviation when modelling the collagen growth. Both terms are axisymmetric and centralised towards the centre. Additionally, this centralising characteristic is even more obvious in the innermost layer with greater axial variation in oxygen level and stress deviation between the centre and the two ends.

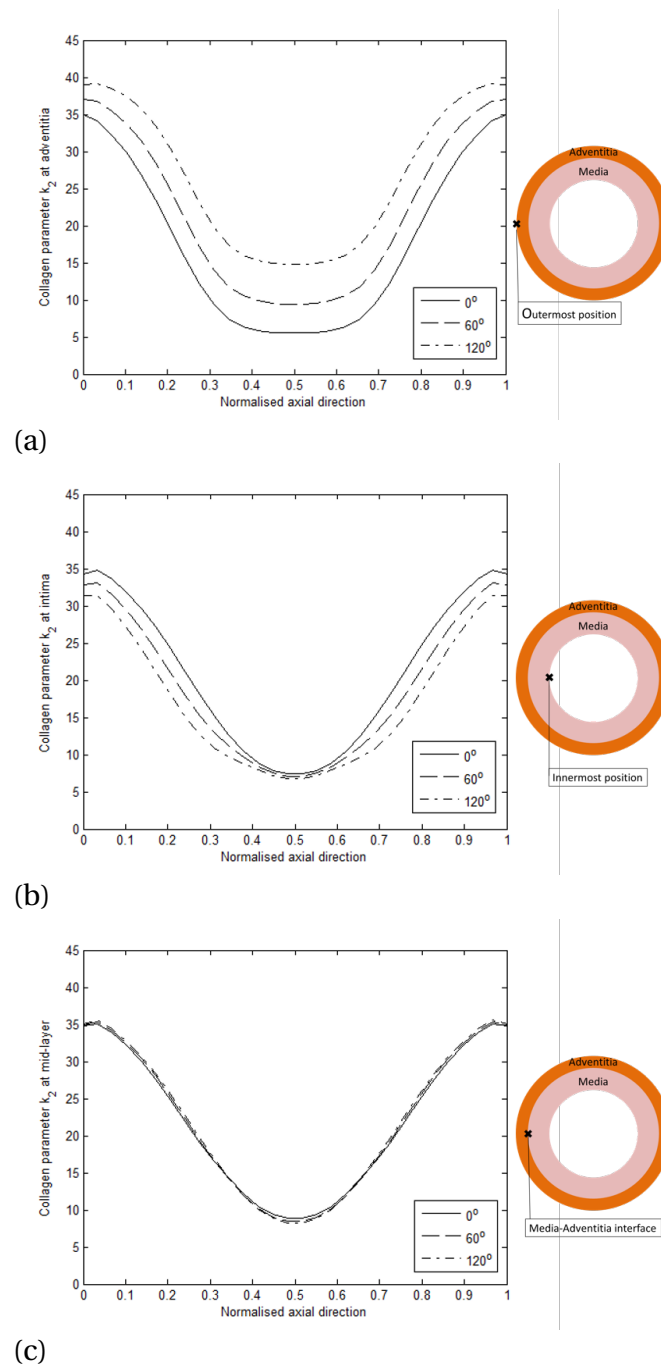


Figure 5.17: Influence of the opening angle on the  $k_2$  remodelling in different layers: (a) outermost layer (b) innermost layer (c) middle layer.

Results shown above are according to a 60 degree opening angle when constructing the tube model of an artery. Here, we recall the opening angle method and investigate its influence to the G&R on the fusiform model, especially to the stress responses on  $k_2$  remodelling. The influence of opening angle is shown in Figure 5.17 with three different opening angles ( $0^\circ$ ,  $60^\circ$ ,  $120^\circ$ ) in three different radial positions (innermost, middle, outermost layer) at the time step  $t = 10$  years. If there is no opening angle,  $k_2$  is reduced more in the outermost layer but less in the innermost layer compared to the other two opening angles. The  $k_2$  remodelling behaviour for a  $0^\circ$  opening angle indicates the stress deviation is significantly increasing in the outer (adventitia) layer. If the opening angle is  $120^\circ$ ,  $k_2$  is reduced more in the innermost layer but less in the outermost layer compared to the other two opening angles. The stress deviation in the adventitia for a  $120^\circ$  opening angle is relatively low among the three opening angles. If the opening angle is  $60^\circ$ , the  $k_2$  remodelling is approximately the average of the two other cases. Therefore, for the adventitia layer, a greater stress deviation is given by a smaller opening angle resulting in a greater reduction in  $k_2$ ; for the media layer, the remodelling behaviour is opposite to the adventitia layer given that the greater stress deviation is given by a larger opening angle. For the middle layer of the arterial wall, the stress deviation is not affected by the opening angle as it is located at the neutral line. Note that the influence of the opening angle is more significant in the outer layer than the inner layer which implies the opening angle has great influence on the protecting sheath (adventitia) to prevent/enhance further enlargement.

### 5.3 DISCUSSION OF FUSIFORM MODEL

This fusiform model demonstrates an axisymmetric G&R behaviour of the SGT framework. The collagen synthesis corresponds to individual position, localised mechanical response and chemical influence (oxygen concentration) within the arterial wall.

With regard to the implementation of G&R approach, the main technical issue is the communication between the vascular solid model and the oxygen transport within. The projection between the mechanical model and transport model renders a methodology for the interaction of chemical signal and collagen synthesis. An interpolation scheme between two meshes is coupled in the SGT framework. The transmural and spatial variation of chemical level is taken into account to sim-

ulate the G&R in each element within the mechanical model of the artery. Moreover, the advantage of this projection is recording the mechanical and chemical responses in every corresponding element of the vascular structure during the evolution of aneurysm. For the fusiform model presented here, the stress and oxygen data in each element are exported and ready for further development on G&R. Oxygen transport is used as the example for chemical influence on aneurysm progression. Other enzyme or chemical substances related to vascular biology, i.e. lipoproteins (intermediate-density lipoprotein (IDL) (Shoji et al., 1998); low-density lipoprotein (LDL) (Witztum and Steinberg, 1991), (Kenjereš and de Loor, 2014)) and TGF $\beta$  (Lindahl et al., 2002), are deemed to have impact on the cellular signal pathway (Aparício et al., 2016) and can also be implemented in the SGT with a defined mathematical application.

The element-based G&R in the SGT framework confers a one way connection to link the oxygen transport to regulate the collagen synthesis. However, the oxygen conformance (Rissanen et al., 2006) is not included, a definition of the cellular respiratory rate is in response to the falling oxygen availability. The cell respiration is determined by the metabolic activity within the arterial tissue. If the oxygen tension is lower than a critical value (Schumacker et al., 1993), the artery would adapt the hypoxic environment by reducing the metabolic activity and energy demand to increase the resistance to the low oxygen supply. Thus, the bio-complexity of aneurysm evolution may not be directly triggered in one way, but possibly in a two-way interaction between oxygen consumption rate and collagen adaptation, which could be applied in the SGT in a later case with validated experimental data. Consequently, the multiscale modelling involving the cell and tissue level would have a more explicit description of the interaction between the vascular constituents and cells embedded in the vascular structure.

The fusiform aneurysm model emphasises the variation of elastin degradation in the arterial wall domain and shows a non-uniform modelling behaviour along the radial and axial positions. Note that the results draw an attention to the central point in the adventitia layer where it restores the balance with the stabilising collagen parameters  $k_2$  and  $m_c$  before the surrounding areas. This provides a potential thought on the indication of possible localised weak points in the aneurysms based on the evolving parameters. If the model is able to differentiate the stabilised and unstabilised points within the aneurysm structure, it could assist with the monitor-

ing process and make clinical decision whether to have necessary intervention or not. In the case of the proposed fusiform model, the collagen G&R arrests the enlargement at the central point, but the surrounding points are still expanding. The localised and dimensional effect demonstrated with this specific model provides a general instruction for the potential functionality on analysing and targeting the possible location on rupturing. Although this still needs further improvement to describe the complex biological system, the preliminary results demonstrate a computational tool to investigate the spatial changes of mechanical response within the wall during aneurysm progression. Overall, this fusiform model demonstrates the spatial variation of G&R in the whole domain, which has the potential to model the heterogeneity of physiological responses in a more complex geometry.

## 5.4 CONCLUSION

In this chapter, we have described and investigated a 2D model representing the arterial structure for the description of aneurysm evolution. The mechanical and chemical environments are simulated and their effects to aneurysm evolution are examined in a localised manner. Although there are limitations, it still shows the advantages of individual components of the computational framework to improve the current basis of modelling the G&R of the aneurysm wall. Two important factors, stress deviation and oxygen concentration in relation to the mechanical stimuli and chemical stimuli, are incorporated to collagen adaptation. Moreover, the spatial variation of oxygen availability is simulated in both radial and axial directions of the fusiform model. The collagen growth rate  $\beta$  in each element is influenced by the corresponding position of local oxygen level. Therefore, this fusiform aneurysm model provides a conceptual idea of the heterogeneous modelling of the G&R within a vascular wall according to its local mechanical and chemical environments.



## APPLICATION ON 3D FSGT PATIENT-SPECIFIC ANEURYSM

---

This chapter integrates methodologies from previous chapters and applies the FSGT workflow to patient-specific intracranial aneurysm geometry. Furthermore, the collagen growth and remodelling is sophisticated: collagen remodelling acts to maintain fibre stress towards a homeostatic value; collagen growth is linked to stretches experienced by fibroblasts, where the fibroblasts continually remodel their attachment to the extracellular matrix to maintain a preferred stretch relative to the loaded geometry. A thrombus is generated on the geometry and the impact of oxygen concentration with/without thrombus on collagen growth and remodelling is illustrated.

---

**Objective:** the objective of this chapter is to build the first chemo-mechano-biological aneurysm model with the application of patient-specific geometry.

### 6.1 3D FSGT FRAMEWORK

This section introduces the integrated FSGT computational framework and its application on a clinical intracranial saccular aneurysm. The clinical IA model was provided by our collaborator, Professor Anne Robertson, in the University of Pittsburgh. This specific case was part of a study (Robertson et al., 2015) that investigates the collagen fibre architecture from tissue samples of a group of clinical IAs. The analysis of these clinical aneurysms were approved by the institutional review

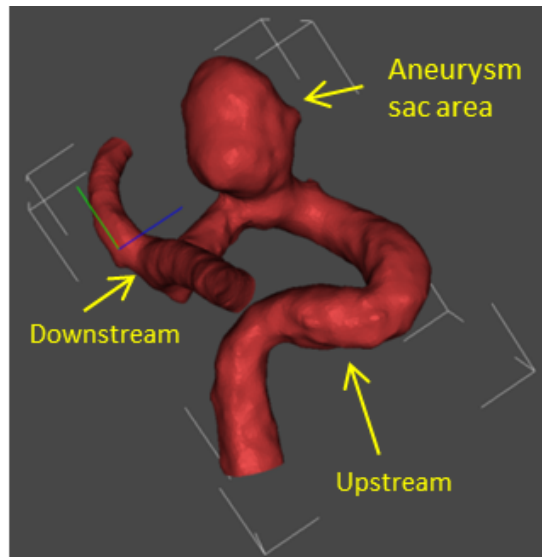


Figure 6.1: Geometry of intracranial saccular aneurysm.

boards (IRB) along with patient consent at both the Allegheny General Hospital and the University of Pittsburgh. The IA case demonstrated here is from a 27 year old male, whose aneurysm was found incidentally and had no signs of drug use, hypertension or diabetes. The 3D geometry of the aneurysm was built from computed tomography (CT) images and converted to a Stereolithography (STL) mesh file as a membrane model which is composed of the aneurysm sac, the parent vessel, and the upstream and downstream connecting regions as shown in Figure 6.1. The simulation workflow of the FSGT application begins with the structural analysis of the clinical aneurysm geometry. In previous chapters, the aneurysm model is established in a simple cylindrical tube to represent a hypothetical healthy artery. However, the simple geometry of the tube model cannot reflect the physiological distribution of haemodynamics and thus the blood flow simulation is not included in previous modelling framework. Therefore, the significant point of the FSGT framework is the coupling of solid, fluid, and transport simulations based on a realistic aneurysm domain.

### 6.1.1 Overview of the FSGT

This novel mechanistic model of arterial/aneurysm tissue mechanobiology is formed by the coupling of SGT framework presented in previous chapters and blood flow simulation. It is to identify and quantify the influence of mechanical and chem-

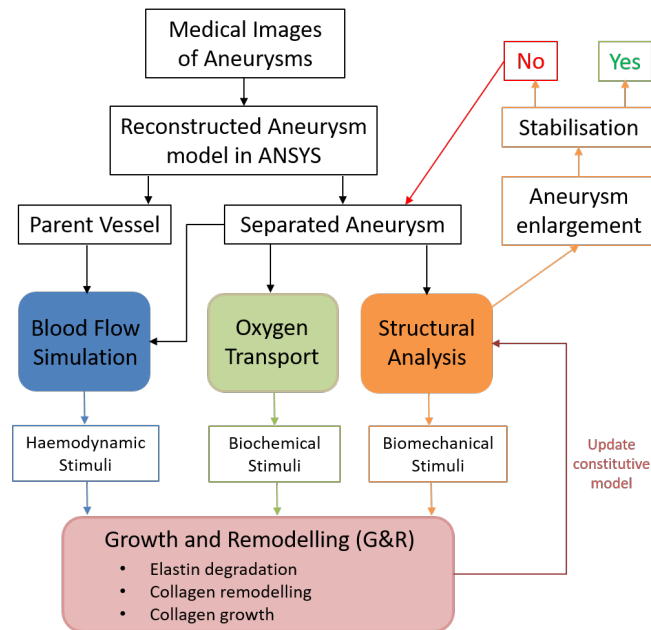


Figure 6.2: Workflow of the 3D FSGT framework: this simulation loop includes three primary simulations: (1) Structural analysis of the arterial wall; (2) Computational Fluid Dynamics (CFD); (3) Oxygen transport modelling. Results from the mechanical, CFD and transport simulations provide inputs to the G&R algorithms, which update the constitutive model of the aneurysm wall.

ical stimuli to the G&R of a patient-specific aneurysm. The mechanical stimuli are the disturbance of physiological forces from homeostatic levels arising from the flow (wall shear stress) and the mechanics of the wall, e.g. Cauchy stress. The chemical stimuli arise from the concentration distribution of biomolecules inside the arterial wall; these influence the degradation of the wall and/or the adaptive response of the cells that remodel the tissue. Figure 6.2 gives a general idea of the interaction between solid, fluid, diffusion and growth of aneurysm evolution modelled by the novel FSGT framework. The 3D clinical aneurysm model is built from the medical image shown in Figure 6.1 and separated into two parts: aneurysm sac and healthy parent vessel. The structural analysis and the transport model are focused on the aneurysm sac, while the fluid simulation includes both the parent vessel and the aneurysm sac to yield a realistic blood flow within the sac. Results from these simulations provide the mechanical and chemical stimuli for the G&R approach. The code and scripts for the FSGT framework can be found in Appendix D.

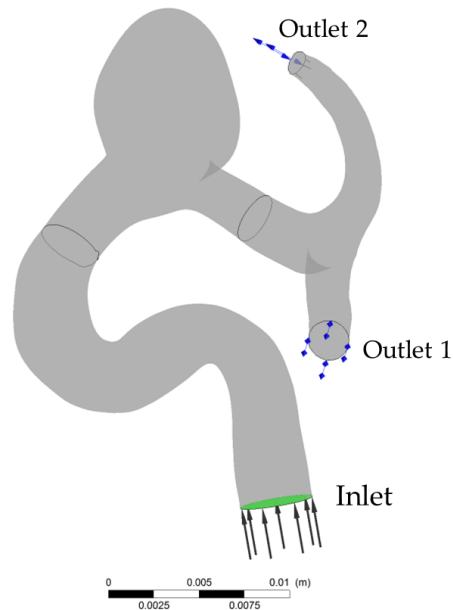


Figure 6.3: Boundary conditions of human intracranial aneurysm: (1) inlet: the flow rate is  $4.38 \times 10^{-6} (m/s)$ ; (2) outlet 1: the pressure is 22.5 mmHg; (3) outlet 2: the pressure is 22.5 mmHg.

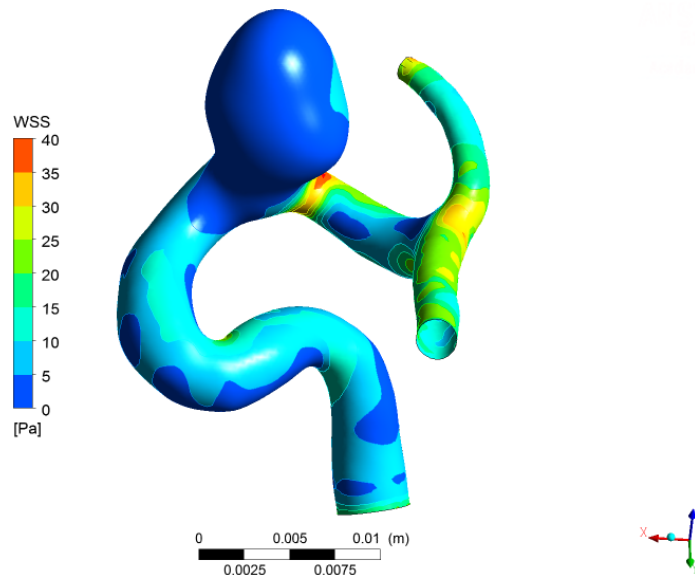


Figure 6.4: CFD simulation of the 3D IA: WSS distribution.

### 6.1.2 Blood flow simulation

In this section, we briefly introduce the blood flow simulation to be integrated in our computational framework. Inner surface of the aneurysm is imported in the meshing suit ANSYS ICEM which automatically generates an unstructured tetrahedral mesh for the fluid domain. After meshing, the boundary conditions are applied (Figure 6.3) and the flow domain is solved by ANSYS CFX. The solver is based on incompressible Navier-Stokes equations using a finite volume formulation (Ferziger and Peric, 2012). The blood flow is assumed incompressible Newtonian with a no-slip condition at the arterial wall as the geometry is regarded as a rigid wall. Blood properties are with constant density  $\rho = 1,069\text{kgm}^{-3}$  and constant viscosity  $\eta = 0.0035\text{Pa}\cdot\text{s}$  throughout the flow domain (Oshima et al. (2001); Chatziprodromou et al. (2007)). We follow the study of Watton et al. (2009a) which solves a steady flow of systolic pressure within a cerebral aneurysm geometry for the purpose of connecting the corresponding WSS (Wall Shear Stress) to elastin degradation. The steady flow of the proposed aneurysm model is simulated based on the boundary conditions shown in Figure 6.3: the flow rate at the inlet is  $4.38 \times 10^{-6}(\text{m}/\text{s})$ , and a constant pressure 22.5 mmHg for both outlets is given (Reymond et al., 2009). Figure 6.4 shows the simulation result of WSS data for the aneurysm geometry. Note that the WSS around the aneurysm dome is significantly lower compared to the healthy parent vessel. The flow-side mechanical influence will be coupled with the SGT framework from the 1D model to form the FSGT framework for the 3D aneurysm model.

### 6.1.3 Structural analysis

The wall structure of the 3D aneurysm is simulated as a thick-walled model. A uniform thickness of arterial wall (0.2 mm) is given to the aneurysm geometry. On this complex 3D geometry, we model the wall, as a single-layered, fibre-reinforced composite. Although with the simplicity of only one single layer of wall, the transmural difference of mechanical responses across the wall is still considered in the 3D model. Furthermore, in order to reduce the computational time and focus on the mechanical simulation around the aneurysm sac, we make two cuts from the original aneurysm geometry as shown in Figure 6.5. Implementation of the single layer model in ANSYS mechanics basically follows the constitutive description in Chapter 2 and the parameters for the SEF are specified in Table 6.1. We assume that

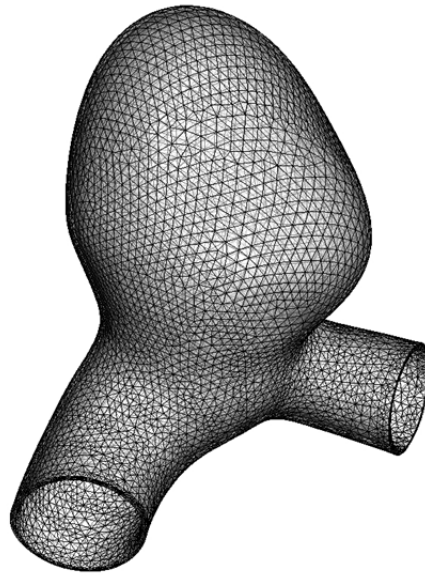


Figure 6.5: The localised region and meshes of the 3D aneurysm model for structural analysis.

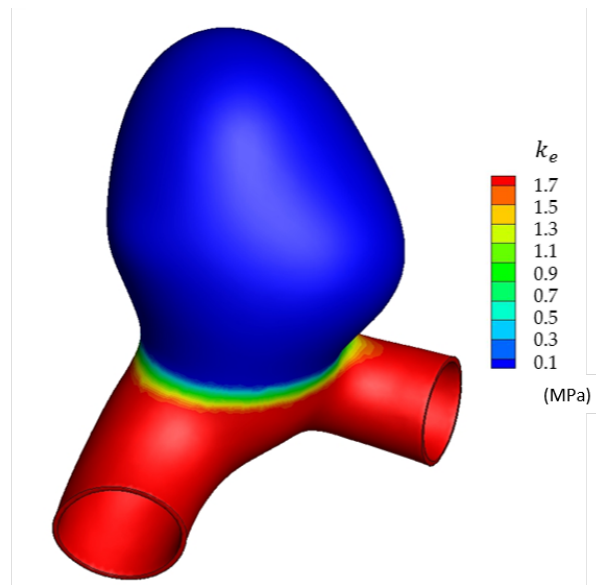


Figure 6.6: Distribution of constitutive modulus on the extracted aneurysm model: (1) Aneurysm:  $k_e = 0.1$ (MPa),  $k_1 = 1$ (MPa); (2) Parent vessel:  $k_e = 1$ (MPa),  $k_1 = 1$ (MPa); (3) Aneurysm neck: linear interpolation between the aneurysm region and parent vessel.

the mechanical response of the parent artery is dominated by elastin whereas the aneurysm sac is modelled as collagenous.

<i>Parameter</i>	<i>Value</i>
<b>Elastin modulus</b>	
$k_e$ (aneurysm)	0.1 (MPa)
$k_e$ (parent vessel)	1 (MPa)
<b>Collagen parameters</b>	
$k_1$ (aneurysm)	1 (MPa)
$k_1$ (parent vessel)	1 (MPa)
$k_2$ (aneurysm)	40
$k_2$ (parent vessel)	40

Table 6.1: Material parameters for the 3D aneurysm model.

Note that the aneurysm region and the parent healthy vessel are given different elastin modulus with a transition area at the neck of aneurysm as shown in Figure 6.6. Differentiated by the neck region, the aneurysm part has weaker elastin modulus (0.1MPa), while the parent vessel has stronger elastin modulus (1MPa) as the healthy state. The collagen modulus in both parts is identical (1 MPa). The whole domain of the extracted aneurysm model is meshed with element type: SOLID187 (3D 10-Node Tetrahedral Structural Solid) as shown in Figure 6.5. This element type (SOLID187) is also suitable for modelling incompressible hyperelastic materials as we use SOLID185 for 1D model. More importantly, SOLID187 element has quadratic displacement behaviour and is well suited to model irregular geometry. For boundary conditions, a systolic blood pressure of 125(mmHg) is applied to the inner surface of the aneurysm, while the two openings shown in Figure 6.5 are fixed to maintain the position of the parent vessel. The initial stress distribution of the current configuration ( $t = 0$ ) is defined as the homeostatic distribution to initiate the subsequent simulation on aneurysm evolution.

### 6.1.3.1 Fibre orientation

This section briefly introduces the individual implementation of collagen fibre orientation in each element for the patient-specific geometry. For the 1D mode, fibre orientation is simply assigned with a constant angle in the global coordinate due to its geometrical simplicity. However, for the 3D aneurysm model with a complex geometrical shape, the orientation of fibres cannot be represented by only one uniform angle to model the physiological structure. Therefore, we need to define a computa-

tional algorithm to characterise the fibre orientation in each corresponding position of elements.

Ma et al. (2004) considered the relation between the aneurysm shape and the rupture potential, in which various indices (i.e. maximum diameter, surface area, principal curvature, and convexity ratio) were developed to characterise the arbitrary 3D geometry of aneurysm. A later work by Ma et al. (2007) postulated that the collagen fibres are orientated to the direction of the local wall stress which is highly affected by the surface curvature of a membrane structure. It is assumed that a stiff fibre aligns to the direction of principal stress, and the direction of principal stress coincides with the direction of principal curvature. Motivated by the above studies, we utilise the index of principal curvature in order to define the distinctive feature of direction on each element according to its geometrical position. The methodology on determining the principal curvature on the surface is described in Ma et al. (2004).

Figure 6.7 illustrates an example of the definition of principal curvature. At a random node  $p$  on the surface, a local orthogonal coordinate is established with a unit normal vector  $n$ , and two unit vectors  $(u, v)$  on the tangent plane. The unit normal vector  $n$  is the approximation by the weighted average of unit normal vectors in the surrounding elements connecting to the node  $p$ . A second order bivariate polynomial  $f(u, v)$  in the local coordinate is to represent and fit in a quadratic surface patch connecting by node  $p$  and its adjoining nodes:

$$f(u, v) = au^2 + buv + cv^2 \quad (6.1)$$

and the shape matrix (Gauss-Weingarten map) to define a type of curvature for the surface patch is

$$A = \begin{pmatrix} 2a & 2b \\ 2b & 2c \end{pmatrix} \quad (6.2)$$

The two eigenvalues and two eigenvectors of matrix  $A$  are denoted as the principal curvatures and principal directions at node  $p$  respectively. Note that the two planes of principal curvatures are always perpendicular.

Based on this approach, an on-line resource developed in MATLAB function (Shabat, 2016) for the calculation of curvature on the triangle mesh is utilised for the numerical implementation of fibre orientation into the structural model of FSGT framework. The two principal directions are then defined as the orientations for

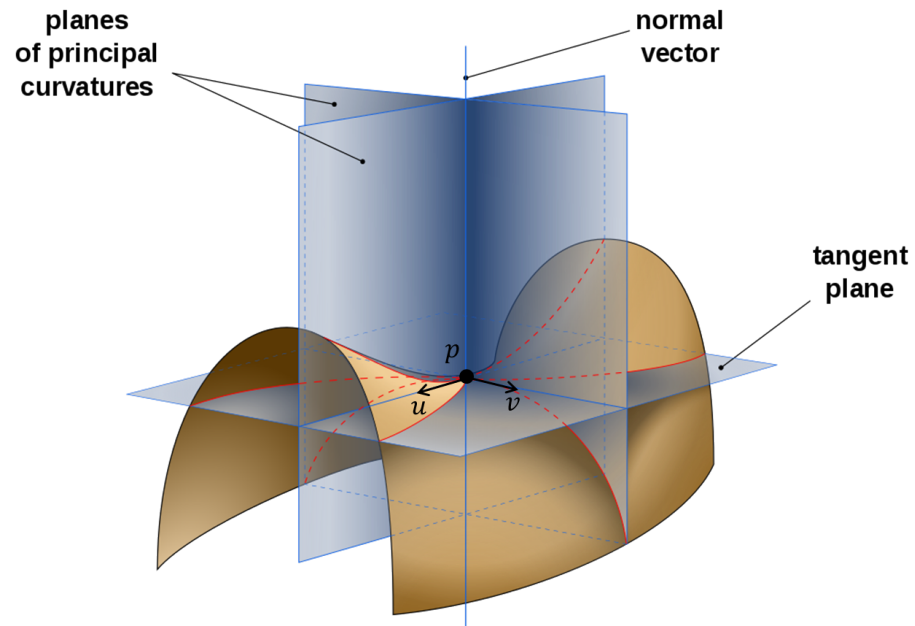


Figure 6.7: Saddle surface with normal planes in directions of principal curvatures (adapted from [https://commons.wikimedia.org/wiki/File:Minimal\\_surface\\_curvature\\_planes-en.svg](https://commons.wikimedia.org/wiki/File:Minimal_surface_curvature_planes-en.svg)).

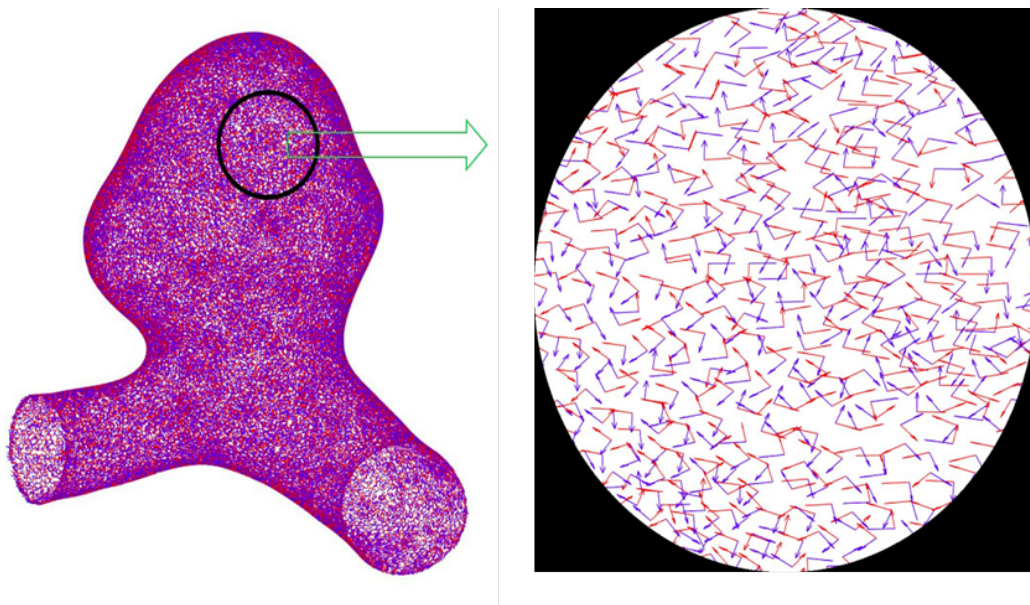


Figure 6.8: Distribution of principal curvatures on the surface of aneurysm geometry: red vectors indicate the 1st principal curvature and blue vectors indicate the 2nd principal curvature.

the two families of fibres in each element. Figure 6.8 illustrates the vectors of principal curvatures on the surface of patient-specific aneurysm. Note that this analysis of principal curvature can only be applied on the inner and outer surfaces of aneurysm geometry. Fibre orientations within the elements across the wall thickness are interpolated by the two boundary surfaces based on the distance. This approach is conducted by the software TECPLOT360 for an in-built inverse-distance interpolation using a distance based weighting. Therefore, these principal vectors are then implemented in the ANSYS structural model as demonstrated in Section 2.4 to represent the fibre orientation in individual elements of the patient-specific aneurysm.

### 6.1.4 Collagen adaption

Collagen fabric adapts via remodelling (organisational changes) and growth (mass changes). Here we introduce a novel method to utilise the growth and remodelling approach of Watton et al. (2004) with an in-built ANSYS constitutive model. The model simulates collagen fibres remodelling towards a homeostatic value of stress as aneurysm enlarges and mass changes are explicitly linked to cell stretches; the stretches of which are defined relative to the current configuration. This is the first application of Watton et al. (2004) to an anatomical aneurysm geometry. The computational codes for modelling collagen adaption can be found in Appendix D listing 3.

#### 6.1.4.1 Collagen remodelling

Watton et al. (2004) simulate collagen remodelling by evolving the reference configurations that fibres are recruited to bear load such that in the loaded configuration the fibre stretch remodels towards a constant value, denoted the attachment stretch  $\lambda_{AT}^C$ . Furthermore, it is assumed that the energy stored in a fibre is a function of the stretch that it experiences; this implies that the fibre Cauchy stress  $\sigma_j^C(\lambda_j^C)$  will remodel to a homeostatic value, i.e.  $\sigma_{jH}^C = \sigma_j^C(\lambda_{AT}^C)$ . Whilst ANSYS does not model distinct reference configurations of elastin and collagen, we can have an equivalent remodelling framework to remodel the collagen fibre stress towards a homeostatic value. In fact, this can be achieved by remodelling material parameters in the collagen fibre strain energy function, i.e.

$$\frac{\delta k_1}{\delta t} = -\alpha \frac{\sigma_j^C - \sigma_{jH}^C}{\sigma_{jH}^C} \quad (6.3)$$

to remodel the fibre Cauchy stress. Note that, the total collagen stress is weighted by the mass-density of the fibre distributions  $\sigma^C = m_j^C \sigma_j^C$ .

The collagen fibre stress is not generated by ANSYS. However,  $I_j$  can be post-computed from the strain matrix and then the fibre stresses calculated with explicit equations for stress derived from the collagen strain energy function. The calculation of collagen fibre stress can be found in equation (C.3) of Appendix C. Note that the remodelling of  $k_2$  presented in previous chapters is modified by the remodelling of  $k_1$  here; this is found to be numerically more stable as the stress is less sensitive to changes in  $k_1$ . The code for the remodelling function is attached in Appendix D listing 4.

#### 6.1.4.2 Collagen growth

We follow Watton et al. (2011) and link growth/atrophy of collagen to stretch based stimuli of fibroblasts. We assume fibroblasts align along the collagen directions and attempt to maintain a homeostatic attachment stretch to the extra-cellular matrix; here we assume  $\lambda_{AT}^F = 1.05$ . An initial fibroblast recruitment stretch field is computed in the initial loaded configuration, i.e.

$$\lambda_{R_j}^F(\mathbf{X}, t = 0) = \frac{\sqrt{I_j(\mathbf{X}, t = 0)}}{\lambda_{AT}^F} \quad (6.4)$$

for the two families of collagen fibres in the  $I_4$  and  $I_6$  directions. As an aneurysm enlarges, the fibroblast stretches at time  $t$  are given by

$$\lambda_j^F(\mathbf{X}, t) = \frac{\sqrt{I_j(\mathbf{X}, t)}}{\lambda_{R_j}^F(\mathbf{X}, t)} \quad (6.5)$$

and the fibroblast recruitment stretch field remodels to maintain fibroblast stretches in the loaded configuration towards their homeostatic values, i.e.

$$\frac{d\lambda_{R_j}^F(\mathbf{X}, t)}{dt} = \alpha_F \frac{\lambda_j^F(\mathbf{X}, t) - \lambda_{AT}^F}{\lambda_{AT}^F} \quad (6.6)$$

The code for the remodelling function is attached in Appendix D listing 5. We then evolve the mass density of the fibre collagen families  $m_j^C$

$$\frac{dm_j^C(\mathbf{X}, t)}{dt} = \beta_F m_j^C(\mathbf{X}, t) \frac{\lambda_j^F(\mathbf{X}, t) - \lambda_{AT}^F}{\lambda_{AT}^F} \quad (6.7)$$

The code for the growth function is attached in Appendix D listing 6.

### 6.1.5 Elastin degradation link to low WSS

To implement this computational framework to clinical aneurysms, the distribution of elastin degradation could be improved depending on the position and environmental effect. Many experimental works (Shimizu et al. (2006); Zeng et al. (2010); Hennig et al. (2011)) present and compare the CFD simulation of a patient-specific aneurysm and its evolution in real time domain. Also, the majority of aneurysm models consider the blood flow conditions such as wall shear stress (WSS) or oscillatory shear index (OSI) to have a great influence on elastin degradation (Sho et al. (2004); Meng et al. (2014)). Major focus is on investigating the WSS effect on aneurysm growth and rupture, and whether higher or lower WSS has a greater impact on the change of aneurysm structure. In the SGT model, the deletion of elastin is prescribed and disregards the physiological change in flow. The prescribed elastin degradation triggers the aneurysm inception, however, it is suggested that the following elastin degradation within the aneurysm wall is significantly affected by the flow condition (Sho et al., 2004). Based on the above studies, a phenomenological method has been proposed by Watton et al. (2009a) to describe the relation between the local WSS and the degree of elastin loss at the inner surface of the arterial wall:

$$\frac{\partial m_E}{\partial t} = -F_D D_{max} m_E \quad (6.8)$$

where  $D_{max}$  is the maximum rate of degradation per year, e.g.  $D_{max} = 0.75$  indicates 75% loss of elastin per year, and  $F_D \in [0, 1]$  is a spatially-dependent normalised function of the WSS to be linked to elastin degradation. Furthermore, we follow the mathematical definition linking the  $F_D$  parameter to low WSS proposed by Watton et al. (2011): when the WSS (systolic) is greater than a critical value,  $\tau_{crit}$ , no elastin degradation occurs ( $F_D = 0$ ). Lower WSS would encourage the loss of elastin in the arterial wall. We suppose there is a lower bound of WSS:  $\tau_X$ , which gives the maximum elastin degradation ( $F_D = 1$ ). In the range between the two WSS values:  $\tau_X < \tau < \tau_{crit}$ , we use a simple quadratic functional form to interpolate the degree of elastin degradation, i.e.

$$F_D(\tau, t) = \begin{cases} 0, & \tau \geq \tau_{crit} \\ \left( \frac{\tau_{crit} - \tau}{\tau_{crit} - \tau_X} \right)^2, & \tau_X < \tau < \tau_{crit} \\ 1, & \tau \leq \tau_X \end{cases} \quad (6.9)$$

For the values of  $\tau_{crit}$  and  $\tau_X$ , Shojima et al. (2004) observed that the average WSS (systolic) in the aneurysm region ( $1.64 \pm 1.16$  Pa) is evidently lower than in the

healthy region ( $3.64 \pm 1.25$  Pa). Based on this study, Watton et al. (2011) hypothesised that the  $\tau_{crit} = 2$  (Pa) for maintaining the structure of vessel wall and  $\tau_X = 0.5$  (Pa) for leading to the maximum loss of elastin. However, for our 3D aneurysm model, we assume a greater value of  $\tau_{crit}$ : ( $\tau_{crit} = 4$  Pa) to increase the areas affected by the WSS in order to grow the aneurysm.

Additionally, for the one-layered aneurysm model, we assume the elastin degradation is uniform through the wall thickness for each WSS point. This is achieved by the interpolation of TECPLOT360. Therefore, the loss of elastin is not only happening at the inner surface of vessel wall but spreading throughout the 3D domain. Furthermore, the elastin degradation is restricted above the neck of the aneurysm and concentrated in the aneurysm dome, while the elastin mass density within the parent vessel remains constant.

## 6.2 3D PATIENT-SPECIFIC ANEURYSM WITH ELASTIN DEGRADATION LINKED TO WSS

This section shows the illustrative result of how the flow condition affects the elastin degradation of the 3D aneurysm model based on the approach stated in Section 6.1.5. More importantly, to demonstrate the implementation of the fluid simulation into the SGT framework built in Chapter 4 and 5. Here we focus on the influence of blood flow and the change of elastin distribution, the G&R of collagen is turned off during the simulation process. The physiological time domain for the aneurysm evolution is simulated for 10 years ( $t = 0 \sim 10$  years).

### 6.2.1 Evolution of WSS and $m_E$

Figure 6.9 shows the results from CFD simulation with WSS data at  $t = 0, 5, 10$  years. It can be seen that the enlargement of the aneurysm is insignificant, thus the distributions of WSS in each time step are almost identical. Following the hypothesis of linking flow to elastin degradation in Section 6.1.5, the contour map of WSS data in Figure 6.9 is in the range of 0 to 4 (Pa). Inside the aneurysm dome, where the WSS is greater than 4 Pa (red regions), the degradation parameter  $F_D$  is equal to 0 and this renders no elastin degradation; where the WSS is smaller than 0.5 Pa (deep blue regions),  $F_D$  is equal to 1 and this renders a maximum degradation  $D_{max}$ . Other colours indicate different level of elastin degradation with the quadratic interpola-

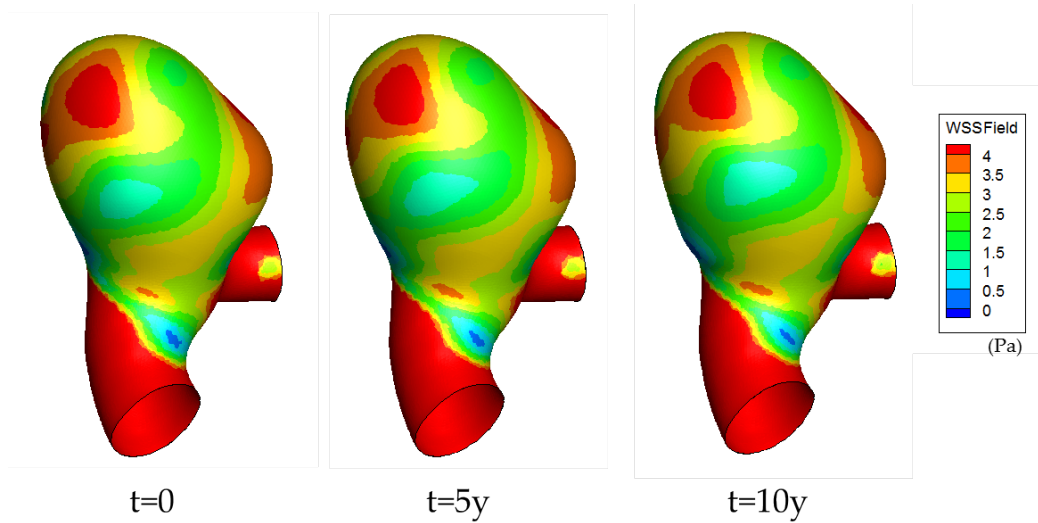


Figure 6.9: Spatial evolution of WSS at the inner surface of the aneurysm geometry at  $t = 0, 5, 10$  years, where the WSS contour range is restricted between 0 to 4 (MPa) for the indication of elastin degradation.

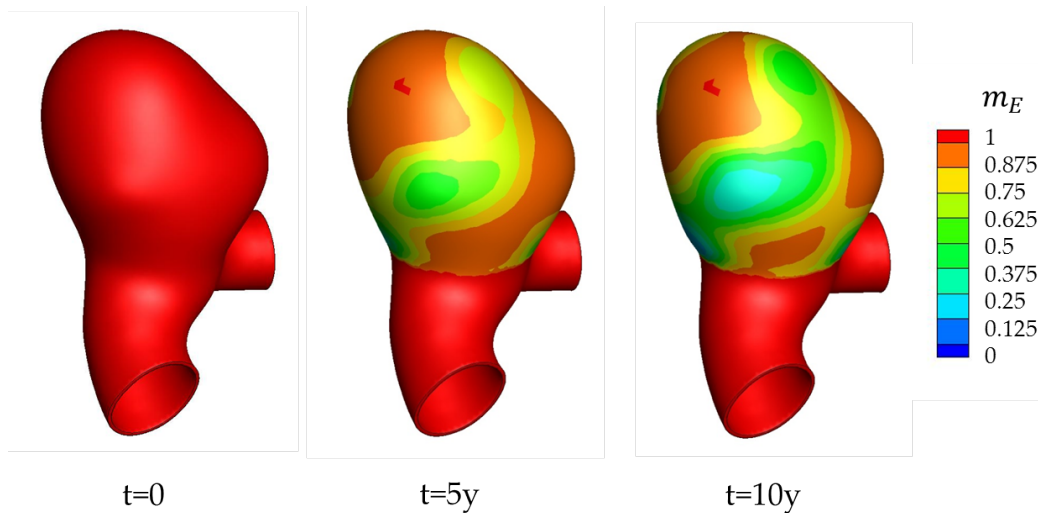


Figure 6.10: Spatial evolution of normalised mass density of elastin  $m_E$  in the aneurysm geometry at  $t = 0, 5, 10$  years. The degradation region of elastin is linked to WSS and restricted in the aneurysm sac above the neck of the aneurysm.

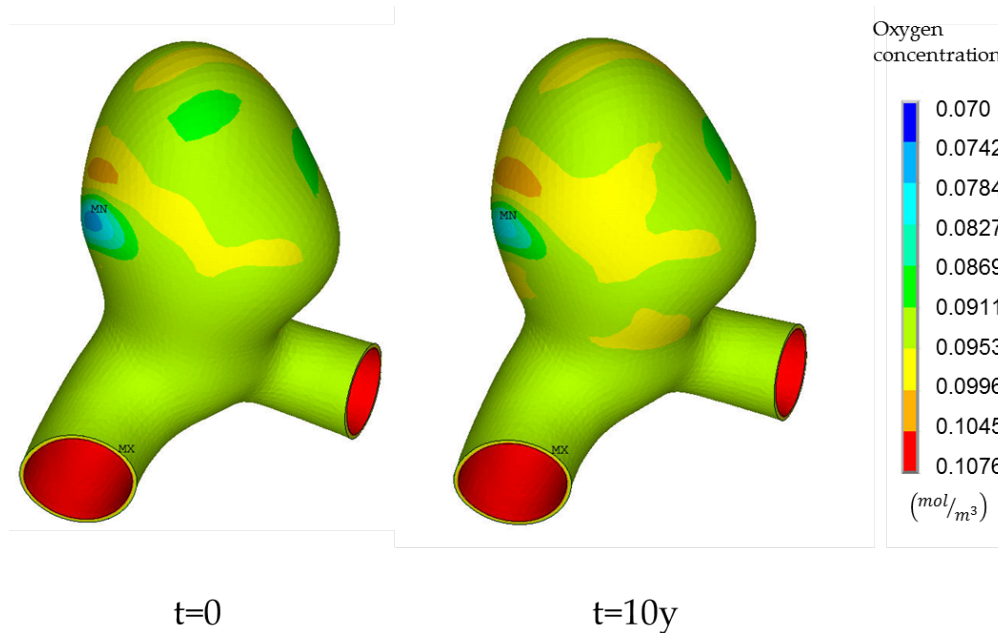


Figure 6.11: Comparison of oxygen concentration at the outer surface of the aneurysm at  $t = 0, 10$  years (Boundary conditions: fixed oxygen concentration at the inner surface ( $0.1076 \text{ mol/m}^3$ ); oxygen diffusivity in the wall ( $0.9 \times 10^{-9} \text{ m}^2/\text{s}$ ); oxygen consumption rate in the wall ( $1 \times 10^{-3} \text{ mol/m}^2/\text{s}$ ).

tion from equation (6.9). As a result, the corresponding normalised mass density of elastin  $m_E$  in the aneurysm geometry is depicted in Figure 6.10. In the duration of aneurysm evolution,  $m_E$  in the aneurysm dome reduces due to the WSS influence. We can observe that the pattern of elastin degradation is consistent with the distribution of WSS, e.g. the lowest  $m_E$  value corresponds to the location of lowest WSS data in Figure 6.9.

## 6.2.2 Evolution of oxygen concentration

In this FSGT example, a simple oxygen transport model is also included in the simulation workflow. However, the thrombus layer is not modelled and the oxygen concentration is not linked to the growth rate of collagen. This FSGT model only demonstrates the transport modelling as one of the individual process which has the potential to be linked to the G&R for further development. In the 3D model, boundary conditions and oxygen transport properties (diffusivity and consumption term) of the wall are based on Table 4.1 from the 1D model in Chapter 4, but the thrombus layer is excluded. Figure 6.11 shows the oxygen concentration at the outer

surface of the aneurysm at the initial time step  $t = 0$  and the last time step  $t = 10$ , in which only a slight alteration of oxygen level is observed. As the oxygen distribution at  $t = 0$  is the homeostatic values, concentration at  $t = 10$  is not disturbed without the presence of thrombus thus no further impact on collagen synthesis. In the next section, the thrombus layer is modelled on the geometry and the impact of oxygen transport to the growth of collagen is illustrated.

### 6.3 TWO COMPARATIVE CASES WITH TRANSPORT MODELLING ON/OFF

This section presents two scenarios of the proposed FSGT framework. The main difference is the on/off of the oxygen transport modelling linked to the collagen growth. The purpose of comparing these two cases is to investigate the influence of oxygen concentration to the growth of patient-specific aneurysm with the presence of thrombus. The two comparative cases are:

- Case 1: FSGT, collagen growth not linked to oxygen concentration
- Case 2: FSGT, collagen growth linked to oxygen concentration

#### 6.3.1 Model setup

This section introduces the 3D FSGT modelling with two specific configurations to emphasise the effect of oxygen transport.

A thrombus layer is created within the aneurysm sac in order to alter the distribution of oxygen within the wall. A degradation of elastin and collagen is prescribed within this region. The tissue can adapt by collagen remodelling and depositing new collagen mass (growth).

##### ***Sphere restriction***

Secondary aneurysm blebs are often observed on an aneurysm sac (Brisman et al. (2006); Lasheras (2007)) and for the case of interest it appears that localised enlargement is occurring at the side of the aneurysm. We aim to investigate growth and remodelling in this region driven by a localised degradation. The degradation of elastin and collagen is restricted within a spherical region of influence ( Figure 6.12).

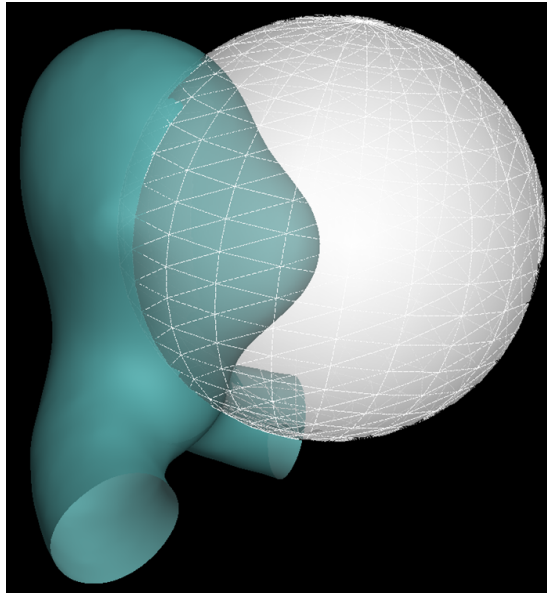


Figure 6.12: A spherical coordinate is placed at the aneurysm bulb to restrict the degradation of elastin and collagen within this region.

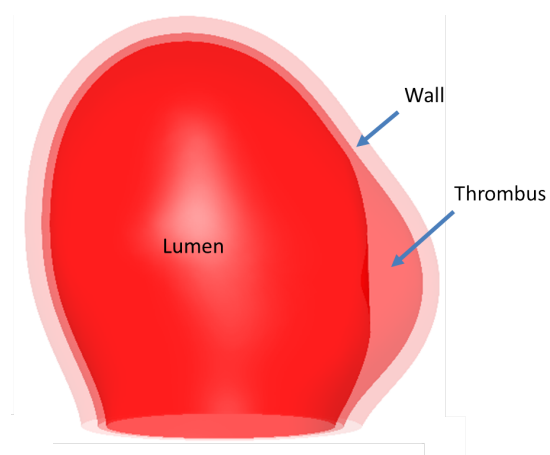


Figure 6.13: A thrombus layer is created at the bulb of aneurysm: the thrombus layer is created within the region of the spherical coordinate that the thickness of thrombus is thicker towards the centre of the sphere, while a uniform thickness is given around the aneurysm sac outside the sphere and the parent vessel remains free of thrombus formation.

The prescribed degradation function is defined as

$$\text{for } |\mathbf{r}_c - E_n(\mathbf{X}, t)| \leq r \quad \text{deg}(\mathbf{X}, t) = \left( \frac{|\mathbf{r}_c - E_n(\mathbf{X}, t)|}{r} \right)^4. \quad (6.10)$$

$$\text{for } |\mathbf{r}_c - E_n(\mathbf{X}, t)| > r \quad \text{deg}(\mathbf{X}, t) = 0 \quad (6.11)$$

where  $\text{deg}$  denotes the degradation intensity;  $r_c = (-2, 4, 4)$  is the centre of the secondary bleb formation on the side of aneurysm;  $r$  indicates the radius of the sphere;  $E_n(\mathbf{X}, t)$  is the coordinates of an element centroid. Therefore, the maximum  $\text{deg}$  is around the centre of the sphere, while  $\text{deg}$  is zero at the intersections of aneurysm and sphere. The mass density of elatin and collagen regulated by the degradation function can be defined as

$$m^i(\mathbf{X}, t) = (1 - \text{deg}(\mathbf{X}, t)(1 - D_{max})^t), \quad i = E, C. \quad (6.12)$$

where  $E, C$  denote elastin and collagen, respectively, and  $D_{max}$  denotes the maximum degradation per year, which is set to be 0.2 in this case. Other parameters regarding to structural analysis are based on previous chapters.

### **Thrombus creation**

A thrombus is created within the aneurysm sac. This is achieved by calculating the normal vectors of the aneurysm surface (loaded geometry at  $t = 0$ ) and projecting the surface inwards throughout the domain in the direction of the normals and by a specified thrombus thickness  $T_H$ ,

$$T_H = R_T(\mathbf{X}, t) \cdot T_H^{max} + T_H^{uni}. \quad (6.13)$$

where

$$\text{for } |\mathbf{r}_c - E_n(\mathbf{X}, t)| \leq r \quad R_T(\mathbf{X}, t) = \left( \frac{|\mathbf{r}_c - E_n(\mathbf{X}, t)|}{r} \right)^4. \quad (6.14)$$

$$\text{for } |\mathbf{r}_c - E_n(\mathbf{X}, t)| > r \quad R_T(\mathbf{X}, t) = 0 \quad (6.15)$$

$T_H^{max}$  is the maximum thrombus thickness (which is set to be 2 (mm) in this case);  $T_H^{uni}$  is a uniform thickness outside the spherical region, which is set to be 0.2(mm). The result of thrombus formation generated by this method is illustrated in Figure 6.13. The code for the thrombus formation can be found in Appendix D listing 2.

### 6.3.2 Results of the two comparative cases

Modelling results of the two cases are presented in the following contents. The major difference between these two cases is the coupling with transport modelling. For Case 1, collagen growth parameter  $\beta$  is a constant value; For Case 2, collagen growth parameter  $\beta$  is influenced by the local oxygen concentration. The prescribed elastin and collagen degradation is applied in both cases with the same degradation intensity. Comparisons between the two cases in the geometric deformation, the remodelling of  $k_1$ , the collagen growth, and the effective stiffness are illustrated.

#### 6.3.2.1 Comparison of geometric changes

Figure 6.14 compare the change of geometry in both cases at their final states, and the original unpressurised geometry as the indicator for the level of aneurysm enlargement. It shows clearly that enlargement of Case 2 is greater than that of Case 1 in the spherical region, while other positions of the aneurysm sac are difficult to be differentiated between these two cases. As the degradation region is localised in both cases, it is obvious that there is no dilation happening outside the sphere. The further enlargement of Case 2 is due to the variation in growth parameter  $\beta$  resulting in the less compensation from collagen growth. The thrombus layer detains the oxygen transport through the wall such that low oxygen is associated with low value of  $\beta$  in collagen proliferation.

#### 6.3.2.2 Elastin and collagen degradation

The degradation of elastin and collagen is prescribed in both cases. According to the destructive function in equation (6.12), the mass densities of elastin and collagen of Case 1 and Case 2 at their final state are illustrated and compared with the initial value at  $T=0$ . It is of note that the initial value of the mass density of elastin  $m_E$  is different between the aneurysm sac and the parent artery, and there is a transition area at the aneurysm neck. The elastin mass density of the aneurysm sac at  $T=0$  is denoted as  $m_E(t=0) = 0.05$  to represent the degenerative structure of the developed aneurysm sac, while the collagen mass density of the aneurysm sac at  $T=0$  remains 1 ( $m_C(t=0) = 1$ ) for the representation of normalised collagen growth during the evolution.

Figure 6.15(a) shows the mass density of elastin  $m_E$  between the two cases and the initial state. The range of the contour map of  $m_E$  in Case 1 and Case 2 is limited

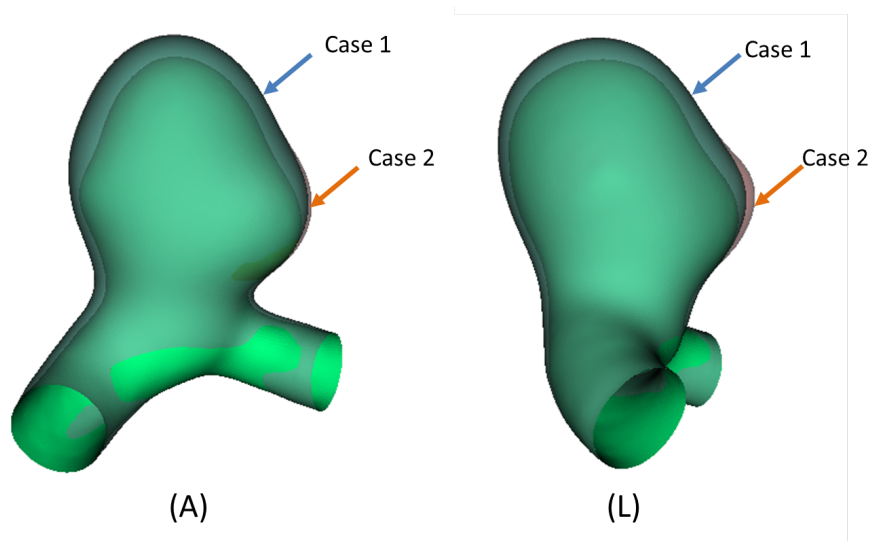


Figure 6.14: Comparison of aneurysm enlargements between Case 1 and Case 2 from the anterior view (A) and lateral view (L): it shows that the enlargement of Case 2 is slightly bigger than that of Case 1 at the aneurysm bulb. The most inner geometry is the unpressurised original geometry.

from 0 to 0.05 which is the initial value at  $T=0$ . There is no  $m_E$  change in the parent vessel and also the variation of  $m_E$  between the parent vessel and aneurysm sac is significant, so the parent artery is in blank colour for separation. In both cases, the  $m_E$  values decrease corresponding to position within the spherical coordinate and the lowest value is at the centre of the sphere. Although the degradation rate is the same in both cases, it is obvious that the distribution of elastin is much lower in Case 1 than in Case 2. Reason for this situation is that Case 1 ended up at time step 40 for stabilisation, while Case 2 stopped at time step 16. The termination of Case 2 simulation is due to the highly distorted elements in the structural analysis.

Figure 6.15(b) shows the mass density of collagen between the two cases and the initial state. Here the degradation of collagen is denoted as  $m_{C1}$  to be separated from the growth of collagen. The initial mass density of collagen is 1 throughout the whole geometry. Comparing Case 1 and Case 2, it also shows similar pattern from the elastin degradation such that the distribution of  $m_{C1}$  is lower in Case 1 in the prescribed region with longer simulation loops.

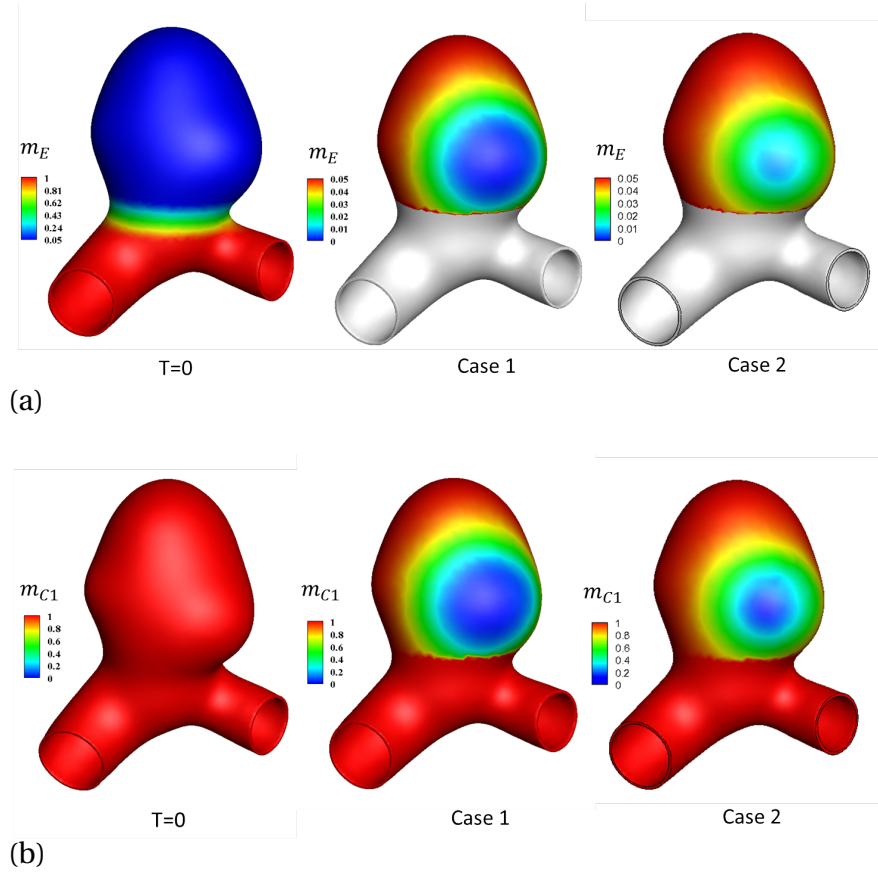


Figure 6.15: Degradation of elastin and collagen: (a) Mass density of elastin at  $T=0$ , the ending state of Case 1 and Case 2 of the aneurysm model; (b) Mass density of collagen  $m_{C1}$  at  $T=0$ , the ending state of Case 1 and Case 2 of the aneurysm model.

### 6.3.2.3 Collagen Remodelling

Collagen remodelling is the adaptive response stimulated by the change of mechanical environment in order to restore the homeostatic state. The remodelling process is a protective action to prevent the potential risk of aneurysm rupture. According to Section 6.1.4.1, in response to the increased stress,  $k_1$  remodelling will be initiated to reduce the stress back to homeostatic level. Given that the remodelling is dependent on the stress deviation, the distribution of Cauchy stress at the homeostasis ( $T=0$ ) and its difference with the two cases are illustrated with the two families of fibres:  $I_4$  in Figure 6.16;  $I_6$  in Figure 6.17.

Figure 6.16 presents the  $k_1$  distribution of the first collagen family  $I_4$  for Case 1 (B) and Case 2 (C). The homeostatic state of Cauchy stress for  $I_4$  is shown in Fig-

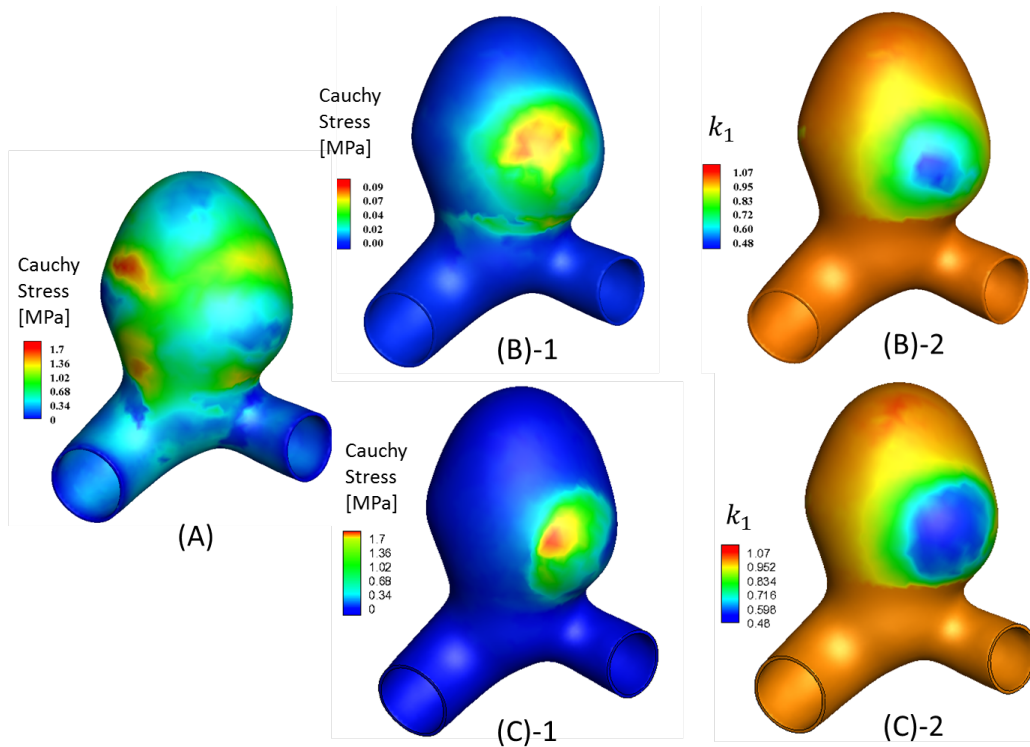


Figure 6.16: Remodelling of first family of collagen fibres  $I_4$ : (A) Cauchy stress at  $T=0$  (Homeostasis). (B)-1 illustrates the difference of Cauchy stress between  $T=0$  and Case 1; (B)-2 is the  $k_1$  remodelling of Case 1. (C)-1 illustrates the difference of Cauchy stress between  $T=0$  and Case 2; (C)-2 is the  $k_1$  remodelling of Case 2.

ure 6.16(A). For Case 1, the overall deviation of Cauchy stress is very low ( $< 0.09$  MPa), which indicates that the stress of the aneurysm sac is successfully down-graded to the homeostatic level. For Case 2, the stress deviation is higher around the restricted region, especially at the centre of the sphere that reaches the maximum value of 1.7 (MPa). Based on the remodelling equation (6.3), higher stress deviation would lead to significant reduction of  $k_1$ . However, the distributions of the stress deviation and the  $k_1$  of the two cases are not perfectly matched ((B)-1 to (B)-2 and (C)-1 to (C)-2). The reason behind this is that the stress deviation of (B)-1 and (C)-1 is the comparison between the final and initial state, while the  $k_1$  remodelling is a cumulating consequence through the G&R process. The common point of the two cases is that the localised phenomenon of  $k_1$  decreasing is concentrated towards the centre of the prescribed region limited by the sphere.

For the second collagen family, Figure 6.17 shows a very similar pattern with the result of the first family collagen in Figure 6.16 such that the stress deviation

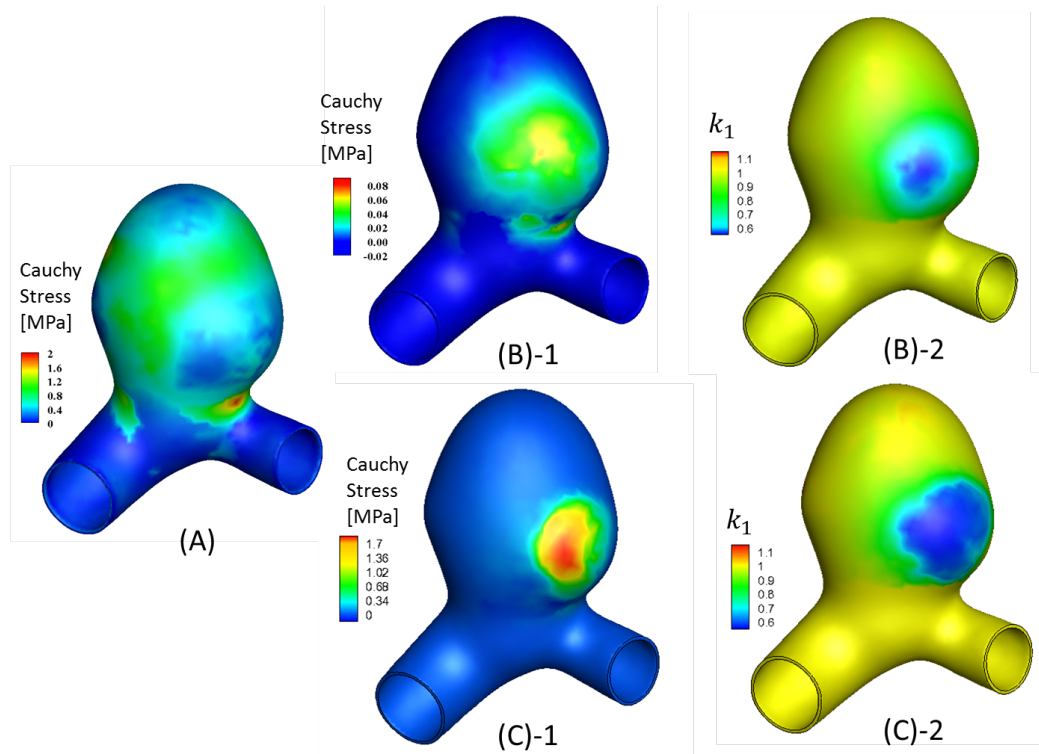


Figure 6.17: Remodelling of first family of collagen fibres  $I_6$ : (A) Cauchy stress at  $T=0$  (Homeostasis). (B)-1 illustrates the difference of Cauchy stress between  $T=0$  and Case 1; (B)-2 is the  $k_1$  remodelling of Case 1. (C)-1 illustrates the difference of Cauchy stress between  $T=0$  and Case 2; (C)-2 is the  $k_1$  remodelling of Case 2.

of Case 1 is very low ( $<0.08$  MPa), while the deviation of Case 2 remains high close to the centre of the sphere (1.7 MPa). The slower collagen growth rate  $\beta$  in Case 2 results in the less compensation of collagen from the loss of elastin. As a result, the aneurysm model of Case 1 is with a stronger structure to bear more loads than Case 2. Moreover, this high stress deviation of Case 2 promotes the  $k_1$  remodelling with a larger low  $k_1$  region compared to Case 1. Even though the computational iteration of Case 2 is terminated much earlier than Case 1, the decline of  $k_1$  of Case 2 is way more faster than that of Case 1 due to the turning on of the oxygen transport.

#### 6.3.2.4 Collagen Growth

In the proposed FSGT framework, the collagen growth is associated with the fibroblast stretch and the local oxygen concentration. The remodelling of the recruitment stretch of fibroblasts regulates the proliferation of collagen fibres, while the local oxygen level has an impact on the collagen growth rate. Here, the collagen growth

of Case 1 is only associated with the fibroblast stretch disregarding the thrombus effect on oxygen availability, while the collagen growth of Case 2 is dependent on both the influences from the fibroblast stretch and the oxygen transport.

Figure 6.18 shows the fibroblast stretch of Case 1 and Case 2 at the final state with the two families collagen  $I_4$  in (A) and  $I_6$  in (B). For both cases, greater stretches are concentrated towards the centre of the sphere with a maximum value at that spot. To compare the stretch level between these two cases, fibroblast stretch in Case 1 (maximum: 1.069) is lower than in Case 2 (maximum: 1.25/1.3). This indicates that stretches in Case 1 are remodelled to the attachment stretch ( $\lambda_{AT}^F = 1.05$ ) more successfully without the interference of thrombus on oxygen availability. Figure 6.19 shows the distribution of oxygen at the outer surface in (A) and the corresponding growth parameter  $\beta$  in (B) for Case 2. The oxygen concentration around the aneurysm sac is altered by the presence of thrombus layer, while the parent vessel remains oxygen homeostasis. It can be observed that the oxygen concentration at the aneurysm bulb is very low (very close to zero) with the maximum thickness of thrombus layer at the spherical centre. Therefore the corresponding growth parameter  $\beta$  is close to zero around the aneurysm bulb.

Figure 6.20 illustrates the collagen growth of Case 1 and Case 2 with the two families collagen  $I_4$  in (A) and  $I_6$  in (B). Here the growth of collagen is denoted as  $m_{C2}$  to be differentiated from the degradation of collagen  $m_{C1}$ . In Case 1, the collagen growth is only associated with the change of fibroblast stretch, so the distribution of  $m_{C2}$  is directly corresponding to Figure 6.18(A). Consequently, greater stretch would lead to greater collagen growth. The growth of the mass density of collagen  $m_{C2}$  in Case 1 is significant (maximum value: 273 for  $I_4$ ; maximum value: 423 for  $I_6$ ). In Case 2, the collagen growth is controlled by the fibroblast stretch in Figure 6.18(B) and the growth parameter in Figure 6.19(B). Although the stretches in Case 2 are greater than Case 1 around the aneurysm bulb, the collagen growth of Case 2 is insignificant (maximum value: 4.5) compared to that of Case 1 due to the low oxygen level at that region. It is of note that the collagen growth of Case 2 is concentrated around the side of the aneurysm bulb instead of the centre. This is due to the compromise between the stretch-mediated growth function and the corresponding growth parameter, however, the increase of the collagen mass density is still much lower than that of Case 1.

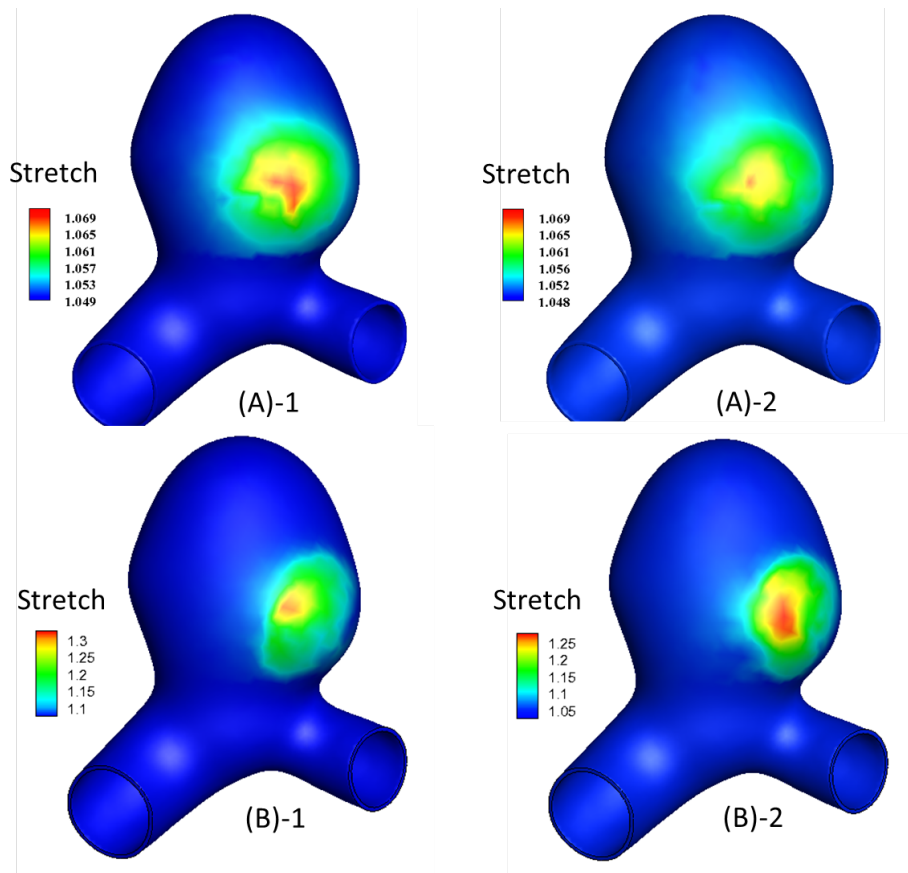


Figure 6.18: Stretches of fibroblasts in the direction of collagen family  $I_4$  and  $I_6$  in Case 1 and Case 2: (A) shows the stretch of Case 1 in the direction of  $I_4$  (A)-1 and  $I_6$  (A)-2; (B) shows the stretch of Case 2 in the direction of  $I_4$  (B)-1 and  $I_6$  (B)-2.

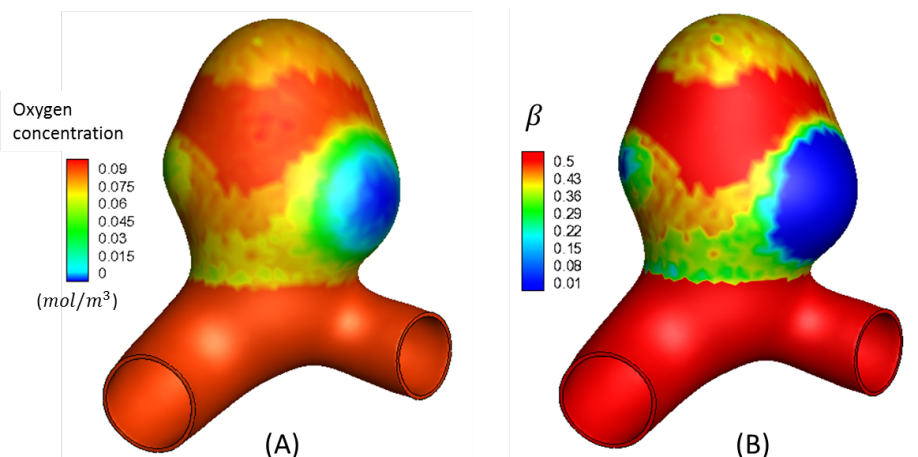


Figure 6.19: Oxygen distribution (A) and corresponding growth parameter  $\beta$  (B) for Case 2 at the final state: oxygen concentration is very low around the aneurysm bulb resulting in the low growth parameter  $\beta$  at the same region.

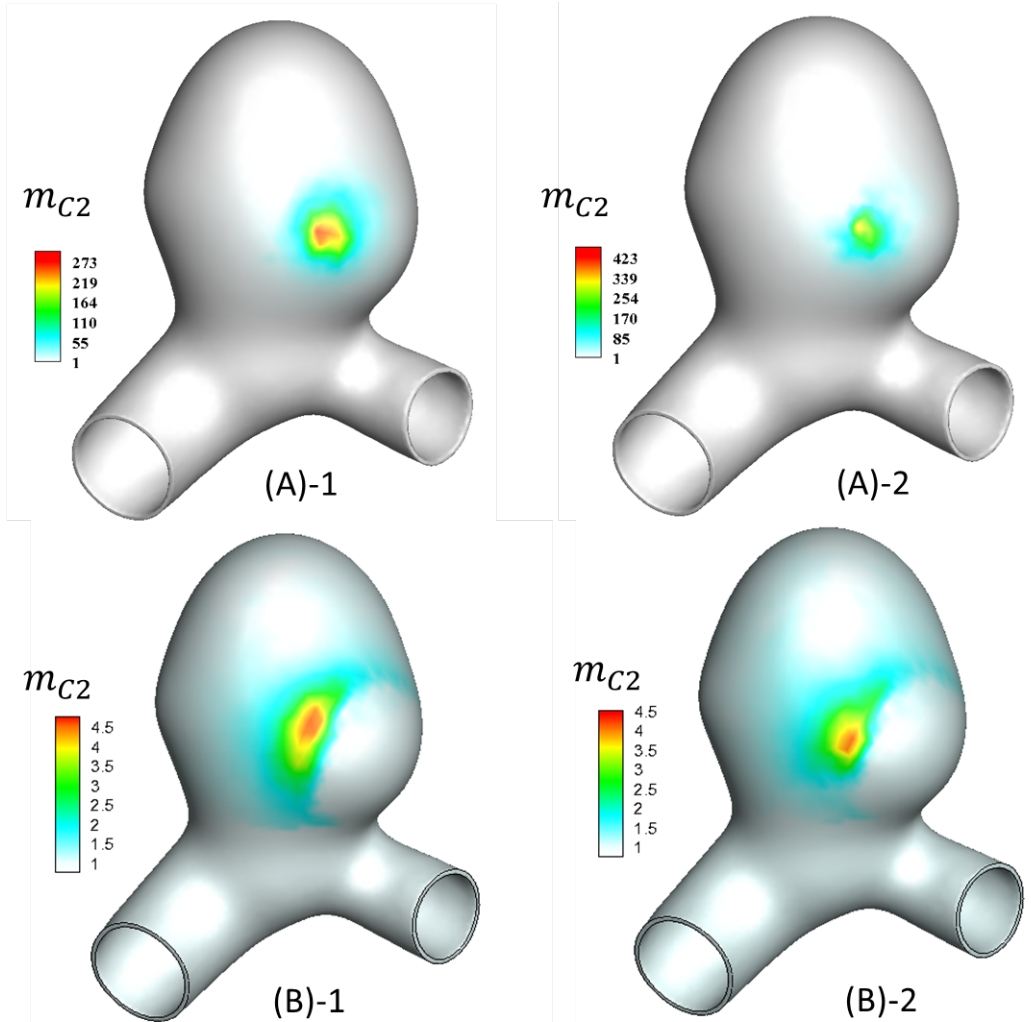


Figure 6.20: Corresponding mass density of collagen fibres  $m_{C2}$  mediated from Figure 6.18: (A) shows  $m_{C2}$  of Case 1 with first collagen family  $I_4$  in (A)-1 and second collagen family  $I_6$  in (A)-2; (B) shows  $m_{C2}$  of Case 2 with first collagen family  $I_4$  in (B)-1 and second collagen family  $I_6$  in (B)-2. For Case 1,  $m_{C2}$  growth is only linked to the fibroblast stretch shown in Figure 6.18(A) so the  $m_{C2}$  growth is at the corresponding position of greater stretch, however, for Case 2,  $m_{C2}$  growth is linked to both the fibroblast stretch (Figure 6.18(B)) and the varied growth parameter  $\beta$  (Figure 6.19(B)) so the  $m_{C2}$  is greater around the side of aneurysm bulb with the balance between stretch and  $\beta$ .

### 6.3.2.5 Collective Variation from Collagen Degradation and Growth

This section introduces the collective results for the variation of collagen mass density and a potential index (effective stiffness) to investigate the strength of the aneurysm structure.

Figure 6.21 shows the collective collagen mass density for Case 1 in (A) and Case 2 in (B) with the two families of collagen. The collective mass density of collagen  $m_C$  is the combination of the collagen degradation  $m_{C1}$  in Figure 6.15(B) and the collagen growth  $m_{C2}$  in Figure 6.20 for the overall collagen response after the G&R. The collective mass density of collagen can be formulated as

$$m_C = m_{C1} \times m_{C2} \quad (6.16)$$

In Case 1, for the first collagen family  $I_4$ , the collagen distribution has the highest value ( $\sim 1.6$ ) and the lowest value ( $\sim 0.5$ ) within the aneurysm bulb which implies both the positive growth and the negative decay happened in this restricted region. While for the second collagen family  $I_6$ , the collagen density is generally low ( $< 0.5$ ) in the aneurysm bulb with a slightly higher collagen density surrounded ( $\sim 1.12$ ). In Case 2, both of the two collagen families demonstrate a large region of low collagen concentration ( $< 0.5$ ) around the aneurysm bulb. This is due to the low collagen growth in Figure 6.20(B). Note that a positive growth of collagen is around the side of the aneurysm bulb for the first collagen family in Case 2, while the positive growth for the second collagen family is close to the dome of the aneurysm sac.

As we have obtained the results of the evolution of the mass density of collagen and the stress-like collagen parameter  $k_1$  through the aneurysm progression, these data can be applied to determine the strength of the aneurysm model as an indicator to evaluate the risk of final rupture. The effective stiffness is defined as the production of collagen mass density and collagen parameter  $k_1$  in equation (6.17), which can be used to represent the mechanical behaviour of the collagen fibres.

$$\text{Effective stiffness} = k_1 \times m_C \quad (6.17)$$

Figure 6.22 illustrates the effective stiffness of collagen fibres in Case 1 in (A) and Case 2 in (B) with the two collagen families. The blank colour in the contour map depicts the homeostatic value ( $\equiv 1$ ) of the stiffness as the initial value of the collagen mass density and the  $k_1$  are all equal to 1. Low effective stiffness denotes a weak structure of the aneurysm.

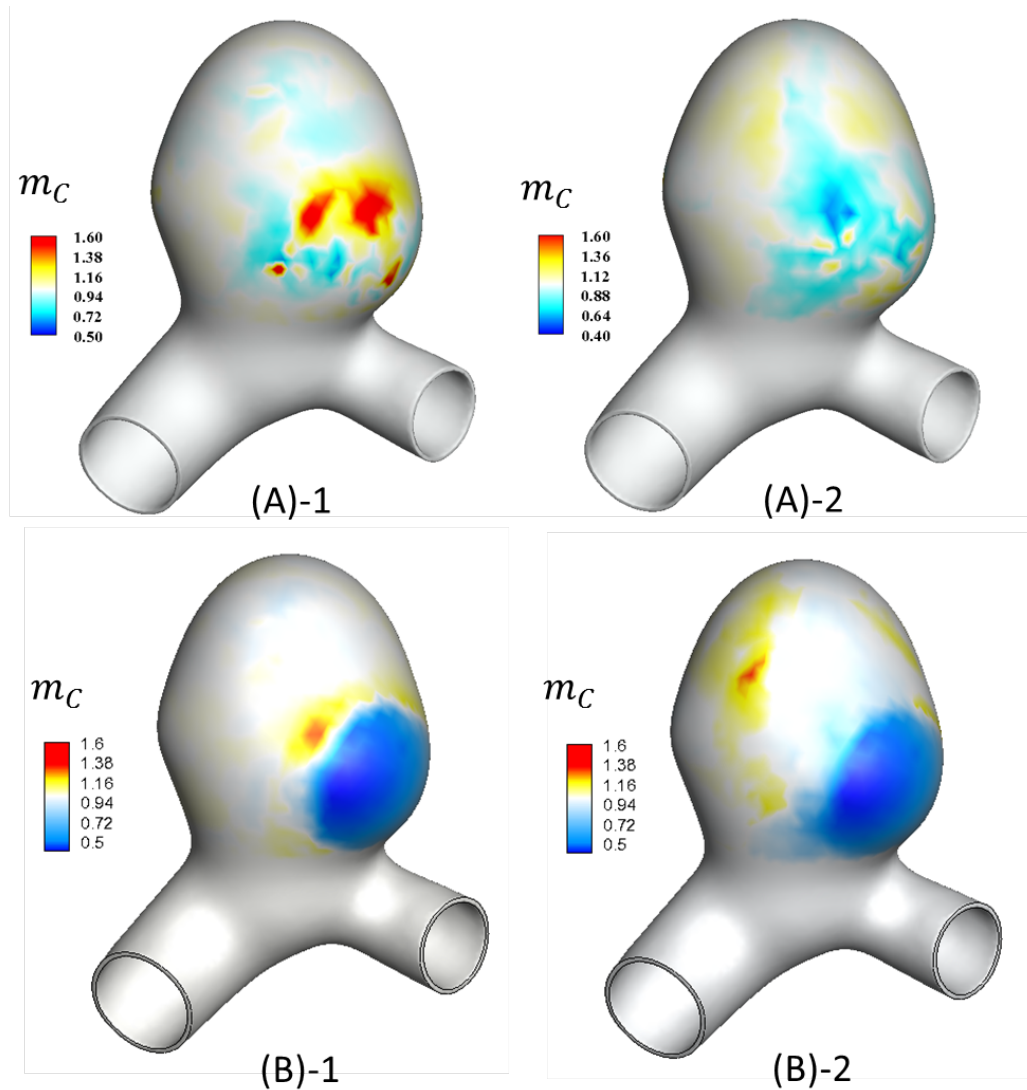


Figure 6.21: Collective mass density of collagen fibres  $m_C$ : (A) shows  $m_C$  of Case 1 with first collagen family  $I_4$  in (A)-1 and second collagen family  $I_6$  in (A)-2; (B) shows  $m_C$  of Case 2 with first collagen family  $I_4$  in (B)-1 and second collagen family  $I_6$  in (B)-2. For Case 1, collagen growth is concentrated at the region with greater stretches to compensate the loss of elastin and collagen; while for Case 2, due to the link with the influence of oxygen transport, collagen growth around the aneurysm bulb is low compared to Case 1.

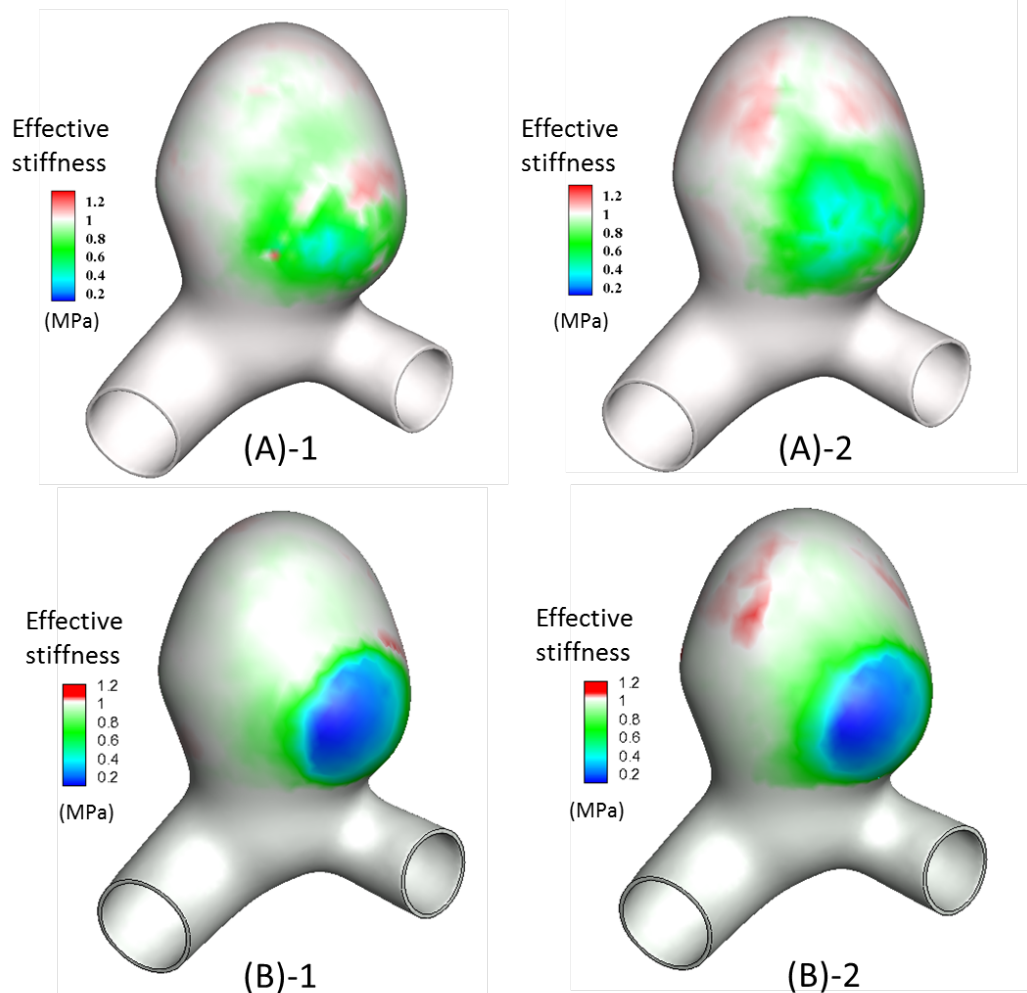


Figure 6.22: Effective stiffness of collagen fibres: (A) shows the effective stiffness of Case 1 with first collagen family  $I_4$  in (A)-1 and second collagen family  $I_6$  in (A)-2; (B) shows the effective stiffness of Case 2 with first collagen family  $I_4$  in (B)-1 and second collagen family  $I_6$  in (B)-2. The effective stiffness of Case 1 is greater than that of Case 2 around the aneurysm bulb, which supports the simulation result that Case 2 is not stabilised and the simulation process is terminated at time step 16 while Case 1 is stabilised towards the end of simulation.

In Case 2, relatively low values of the effective stiffness ( $\leq 0.2$ ) are presented in a large region of the aneurysm bulb for both collagen families. This result is predictable as the  $k_1$  values and the collagen mass densities are much lower in Case 2 than those in Case 1 in the region restricted by the sphere. For Case 1, without the disturbance of oxygen level, the effective stiffness is ranged from 0.4 to 0.8 in the prescribed degradation region which is much higher than the general stiffness in Case 2. As a result, the structure of Case 1 is much stronger than that of Case 2 based on the performance of effective stiffness.

## 6.4 DISCUSSION

The G&R approach for the patient-specific case is updated according to the stability analysis in Appendix C for collagen remodelling, and Watton et al. (2004) for collagen growth function represented by fibroblasts. This modification improves the drawbacks of the 1D model in which the stress homeostasis is not able to restore, and also has a physiological interpretation of the cell/tissue interaction that the increase or decrease in the concentration of collagen fibres represents the regulation by fibroblasts.

This 3D clinical aneurysm model demonstrates a spatial G&R behaviour based on its geometrical shape, mechanical response, and flow condition. Although the arterial layer is relatively simple with only one single layer, the implementation of fibre orientation in principal direction and flow-based elastin degradation improves the limitation from previous SGT model. The structural analysis in the FSGT workflow provides an approach to determine the local fibre orientation in each element according to its principal curvature. Although in this aneurysm example the fibre orientation of each element remains its initial orientation through the evolution, it is of note that if the geometrical change of aneurysm is significant, the principal curvature would be altered and the fibre orientation would need to be updated. During the aneurysm evolution, the elastin is almost deleted and the main-load bearer is transferred to collagen fibres. Therefore, for the simulation of clinical aneurysms, it is important to accurately model the mechanical structure of collagen fibres. This FSGT framework utilises a potential computational method to present the fibre orientation on arbitrary aneurysm geometry. Another important aspect of the FSGT is the blood flow simulation and its influence on elastin degradation. In Section 6.1.5, the elastin degradation is stimulated by low WSS, however there is still discussion on

other flow indices such as OSI (generated by pulsatile blood flow) which may also play a crucial role for the elastin loss (Xiang et al. (2011); Lu et al. (2011)). Different indices of flow conditions could be implemented in the FSGT framework for further investigation.

The two comparative cases provide a practical application of the sophisticated FSGT framework on the clinical aneurysm geometry. Illustrative figures on the 3D aneurysm geometry give a better visualisation than the 1D and 2D models. Although the influence of blood flow is not included in the comparison, Section 6.2 has demonstrated the pathway to link WSS to elastin degradation. On the other hand, the prescribed degradation of elastin and collagen mimics the development of a secondary aneurysm on the aneurysm bulb. Consequently, the G&R of collagen fibres is concentrated within that restricted region.

The enlargement of the secondary aneurysm is more significant with the transport modelling turning on. In response to the increased stress induced by the enlargement, the remodelling of  $k_1$  is aiming to restore the homeostatic stress. The Cauchy stress in Case 1 is successfully downgraded back to its homeostasis, while the Cauchy stress in Case 2 remains in a higher level resulting in the termination of the simulation. Even there is a larger region with lower  $k_1$  values in Case 2, the remodelling process is not able to achieve the task. The collagen growth is mediated by the stretch of fibroblasts, which would continually remodel their attachment to the ECM in the altered configuration. In Case 1, the collagen growth is in consistent with the distribution of fibroblast stretch such that greater stretch presents greater collagen proliferation. However, in Case 2 with the disturbance of thrombus in oxygen availability, there is no growing of collagen towards the centre of the aneurysm bulb even there is greater stretches compared to Case 1. The collagen growth parameter  $\beta$  has a profound impact on the stretch-mediated growth function as it is acting as an additional rate. Lower value of  $\beta$  in the aneurysm bulb leads to lower increase in collagen. It shows a more considerable variation between the two cases with the result of collective mass density of collagen. The collagen distribution in the prescribed region in Case 2 is downgraded from the initial value 1 to below 0.5, while in Case 1, it is relatively stable, even with a positive growing of the first collagen family. Histological studies on aneurysms have proved that the collagen concentration is very low in ruptured aneurysms (Gaetani et al. (1998); Vanrossomme et al. (2015)). The stability of aneurysm relies on the competition between aneurysm re-

pair and degeneration to reach a dynamic balanced condition (Etminan and Rinkel, 2016), in this thesis, it is denoted by the homeostasis of the fibroblast stretch and the fibre Cauchy stress. The result of Case 1 is in agreement with the above statement. The collagen G&R in Case 1 demonstrates the evolution process searching for a new stable condition of the aneurysm according to the original configuration. On the other hand, Case 2 shows a high possibility of rupture risk with the thrombus formation which is often presented in aneurysms. Moreover, many experimental studies have revealed that softer aneurysm wall has higher risk of rupture than the stiffer one (Sanchez et al. (2013); Brunel et al. (2017)). The effective stiffness presented in this chapter is able to quantify the stiffness of the aneurysm wall and also locate the corresponding position with the risk of rupture.

## 6.5 CONCLUSION

This chapter presents a sophisticated FSGT framework which is the first model to investigate the chemo-mechano-biology on a patient-specific aneurysm geometry. The comparative result suggests that the thrombus is crucial for the stability of the aneurysm. An index is introduced in this research to identify the stiffness of the aneurysm wall for the evaluation of rupture risk.

## CONCLUSIONS AND CONSIDERATIONS FOR FUTURE DEVELOPMENT

---

The main focus of this research is to establish an *in silico* framework to investigate, numerically quantify, and test important chemo-mechano-biological hypotheses to model the evolution of aneurysms. The methodology is based on two important notions:

1. Determination of mechanical homeostasis through the arterial wall and its hypothetical role in aneurysm evolution;
2. Influence of oxygen concentration on collagen growth in a thrombosed aneurysm.

### 7.1 SUMMARIES OF THE STUDY

Chapter 2 introduces the mechanical structure of an artery based on Holzapfel et al. (2000) and its implementation in the ANSYS software for numerical modelling. The hollow cylindrical model is demonstrated as the example to simulate the mechanical stress responses across the wall thickness. The physiological stress condition is fulfilled by including the residual stresses within the arterial wall, which utilises the opening angle method in the ANSYS model. The purpose of modelling the homeo-

static stress inside the wall is the basis of the hypothetical G&R approach in order to simulate the micro-structural change in relation to the change of wall stress during aneurysm evolution, which is presented in Chapter 4.

Chapter 3 presents the oxygen transport modelling with its implementation in ANSYS. The model is still a simple tube shape to simulate the steady state oxygen diffusion through a thrombosed artery. We investigate the influence of thrombus thickness, oxygen diffusivity, and oxygen consumption rate in the wall on the oxygen concentration through the two-layered model. Based on the finding (Steinbrech et al., 1999) that the collagen synthesis is associated with oxygen levels, we use a simple mathematical equation to quantify the influence of oxygen on collagen growth in order to incorporate the chemical transport effect in the chemo-mechano-biological framework by using oxygen as the example.

In Chapter 4, the SGT model is presented to combine the important concepts in Chapter 2 and Chapter 3, and their links to aneurysm G&R on the tube model. The elastin degradation is prescribed along the axial direction thus this is a 1D model with only transmural variation through the wall thickness. The chemo-mechano-biological interaction is illustrated by the element-based stress-driven G&R and oxygen-affected collagen growth rate. The results show the transmural G&R behaviour which takes into account the mechanical responses of local positions in different layers of this thick-walled model. This provides more details of the heterogeneity inside the arterial wall which is a great improvement from previous membrane models. However, the influence of blood flow conditions is not included in the SGT framework for the 1D model due to insignificant alteration in the flow domain.

Chapter 5 extends the SGT framework on an idealised fusiform aneurysm by inducing an axisymmetric elastin degradation to examine the modelling behaviour in a 2D domain. The mechanical stress responses and oxygen concentrations are spatially distributed in both the radial and axial direction due to the axisymmetric enlargement and thrombus propagation. An improvement from the 1D model is the projection of local oxygen level on corresponding mechanical elements. Therefore the localisation of mechanical and chemical stimuli in relation to the G&R of individual elements is achieved in the ANSYS model.

Chapter 6 presents the sophisticated FSGT framework on the anatomical

aneurysm geometry. The structural analysis is updated by a potential approach to characterise the collagen fibre orientation according to the arbitrary surface curvature of the aneurysm. The degradation of elastin is associated with the physiological change of EC morphology controlled by the blood flow condition. Collagen adaptation is deemed to play a key role for reaching a dynamic balanced condition in aneurysm progression. The growth of collagen is represented by the fibroblast stretch, while the remodelling of collagen parameter is governed by the fibre stress. The oxygen availability to the aneurysm wall regulates the growth rate of collagen. Results of this 3D model illustrate the evolution of geometric changes, mass density of elastin and collagen, collagen parameter, and stiffness of the aneurysm structure.

This FSGT framework is fully integrated in the ANSYS software to validate the vascular structural analysis, blood flow simulation, chemical transport in the wall, and the interplay among them. The important aspect of this framework is that we consider the local chemical environment within the wall and its influence on the aneurysm evolution, while most research focused on the mechanical perspectives. Once there is a feedback mechanism connected with available experimental data, this FSGT framework provides a platform for the interaction between *in vivo*, *in vitro*, and *in silico* models, which can inform us of valuable information on the chemo-mechano-biology of vascular wall.

## 7.2 LIMITATIONS OF THE PROPOSED FSGT FRAMEWORK

It is vital to reflect the limitations of the proposed FSGT framework for future adjustments.

- **Blood flow is simulated in a steady state**

The blood flow condition in the FSGT framework is simulated as the systolic flow to describe the relation between the local WSS and the degree of elastin loss at the inner surface of the arterial wall. This assumption of the WSS-induced elastin degradation is based on the study of Watton et al. (2009a). However, the blood flow is not a steady flow and the WSS changes with pulsatile nature of the flow. Watton et al. (2011) compared the spatial distribution of WSS for the steady and pulsatile flow. Although the result indicates that the WSS distribution of the steady flow is qualitatively similar to the mean value

from pulsatile flow, the cyclic distension of the ECs is governed by the pulsatility of the flow acting on the wall (Qiu et al., 2000). Furthermore, a more comprehensive representation of physiological influence is essential for the modelling purpose.

- **Lack of clinical validations for the G&R hypothesis**

As mentioned in Chapter 1 for the limitation of the existing FSG model, it is difficult to track the mechanical and chemical changes within the aneurysm wall. Parameters used for this framework are mostly obtained from conceptual mathematical models and *in vitro* experimental observations on arterial tissues. Therefore, the exact function for the aneurysm growth is not genuinely understood. However, this FSGT framework provides a computational platform that can be modified and updated according to different methodologies for the interpretation of underlying mechanisms.

- **Definition of homeostasis in 3D model**

In the 3D case of patient-specific aneurysm, the evolution process is initiated from the current aneurysm geometry, which is denoted as the homeostatic state for the remodelling. This implies the stabilisation of aneurysm is aiming to restore the diseased state as it is the original configuration. Ideally, the homeostasis of the artery is defined in the healthy state prior to aneurysm formation, yet it is not applicable for the 3D case. However, the key issue should be the definition of homeostasis whether it can represent the criterion for the adaptive response during aneurysm evolution.

- **Simple diffusion model**

Oxygen transport in the FSGT framework is simulated in a diffusion-only formulation. The cell respiration rate is assumed to be constant regardless of the local cellular composition of the wall layer. However, growth/atrophy of ECM constituents and migration of vascular cells during aneurysm evolution would alter the consumption of oxygen. Moreover, the influence of possible convective flux of oxygen through the thrombus is evident when the thickness of thrombus is thicker (Holland, 2012). As a result, an evaluation of diffusion, convection, and respiration rate of an organised thrombosed aneurysm structure is needed.

- **Thrombus is not mechanically contributed**

The thrombus layer generated in this research is not considered the mechanical contribution to the overall aneurysm structure. Some studies (Wilson et al. (2013); Virag et al. (2015)) indicate that the thrombus is not only biological active but also acting as a cushion to hold the enlargement of aneurysm. However, the adherence of the thrombus to the arterial wall is an important factor for the transport of mechanical forces (Bowker, 2010). Nonetheless, the mechanical behaviour of the thrombus should be included in the structural analysis of the FSGT framework.

## 7.3 POTENTIAL IMPROVEMENTS TO THE COMPUTATIONAL FRAMEWORK

### 7.3.1 Multiscale modelling on EC morphology

The proposed computational framework compiles the basic modelling approach to quantify the mechanical and chemical stimuli in relation to a hypothetical G&R method for modelling the microstructure evolution in aneurysms. However, a comprehensive *in silico* modelling framework of aneurysms would expand to the multi-scale level: cellular, tissue, and organ scales, to explore the underlying mechanisms that affect the development of aneurysms, and subsequently to stabilise or rupture (Ho et al., 2011).

In the consideration of multiscale modelling, the FSGT model has associated the fibroblast stretch to the synthesis of collagen for the representation of cell/tissue interaction. For the potential development of the FSGT, which includes the modelling of the flow domain within the aneurysm, this framework can be enriched with an explicit representation of endothelial morphology and be associated with the permeability of the oxygen transport modelling. The competing influences of both cyclic stretch (CS) and WSS will be included to guide ECs shape and alignment (Sinha et al. (2016); Pakravan et al. (2016)). The goal is to model the morphology of ECs subject to competing WSS and CS stimuli and predict EC distribution on a patient-specific aneurysm. The morphology of ECs determines the permeability of an EC monolayer which would have further impact on aneurysm evolution. Therefore, the diffusivity parameter of the inner surface of the arterial wall in transport modelling would not

be a constant but determined by the flow condition.

Once a better definition of ECs alignment is defined by the mechanical factors in the ANSYS model, larger molecules such as LDL can be modelled to have broader application of the FSGT, especially the endothelial permeability is deemed to have great impact on the transport of this type of large molecule to the arterial wall. Moreover, the development of a mathematical expression for the functionality of transmural cells (SMCs; fibroblasts) embedded in the vascular layers is needed and moreover their interactions with the ECM. This is to specifically characterise the mechanical and chemical influence on the functionality of SMCs and fibroblasts, and cellular mechanics which control the adaptation of elastin and collagen microstructures within the arterial wall. However, this improvement cannot solely rely on computational models but also needs the assistance from available *in vitro* experiments which can provide guidance on linking cell functionality to the local environments and boundary conditions by culturing cells. In return, *in silico* models can provide detailed corresponding mechanical and chemical responses to characterise and quantify the change which can be compared against the control group of healthy arteries. Therefore, the cycle of the interaction between the experimental data and computational estimates can be continuously developed and updated.

### 7.3.2 Volumetric change

In the presented FSGT model, we assume non-volume changing (isochoric) during the aneurysm progression, while there is mass density changing of the elastin and collagen constituents. However, as highlighted in the review article (Humphrey and Holzapfel, 2012), it is important to address the characteristic of thick-walled and volumetric adaptation for modelling aneurysm evolution. Therefore, the FSGT framework can be improved under the basis of thick-walled solid model by implementing the volumetric change to form an advanced and comprehensive FS<sup>V</sup>GT computational model.

Based on the studies of Schmid et al. (2012) and Eriksson et al. (2014), a novel formulation was proposed to simulate the volumetric changes as a consequence of local change in mass of constituents. Mass changes could result in the alteration of either the density or the volume. Different types of mass growth were shown in this study:

- Constant individual density (CID): individual density is constant and the individual volume changes;
- Adaptive individual density (AID): individual density is adaptive and the individual volume is constant.

In the FSGT model, we basically follow the AID approach in which the volume of individual element is constant regardless of the change of mass density. The changes of the normalised mass densities  $m_E$  and  $m_C$  determined by the G&R method directly indicate the mass change of elastin and collagen constituents in each element without volumetric adaptation. On the other hand, to implement the CID approach for volumetric change in the ANSYS model, the mass densities in each element needs to remain constant, thus the G&R of the normalised mass densities  $m_E$  and  $m_C$  correspond to the ratio of volumetric change instead of the mass change. The change of the normalised mass density would be transferred to the volumetric change in each element of the ANSYS model. Numerical results from Eriksson et al. (2014) showed that when modelling the elastin degradation, it is suitable to apply the AID approach to avoid the volumetric reduction resulting in the decrease of arterial radius, while for modelling the collagen growth, it is suitable to apply the CID approach for volumetric adaptation. However, these numerical examples assumed an isotropic volumetric change, and this has been recently extended to anisotropic volumetric growth by Grytsan et al. (2017).

### 7.3.3 Reconstruction of healthy artery

The 1D and 2D SGT models provide insights into how to link G&R to transport processes, while the 3D FSGT model presents the physiological influence on subsequent aneurysm evolution. Therefore, it is of great interest to connect these important concepts by modelling the aneurysm from its 'hypothetical' healthy state.

On the basis of the same clinical IA geometry presented in Section 6.1, Mandalzi (2016) reconstructed a healthy membrane cylinder to replace the aneurysm region and applied the FSG framework to model the vascular mechanobiology with a prescribed elastin degradation on the target position of aneurysm. Figure 7.1 illustrates the reconstruction procedure of the hypothetical healthy artery connected to the upstream and downstream parent vessels in the original aneurysm geometry. Following this reconstruction algorithm, the thick-walled model presented in Chap-

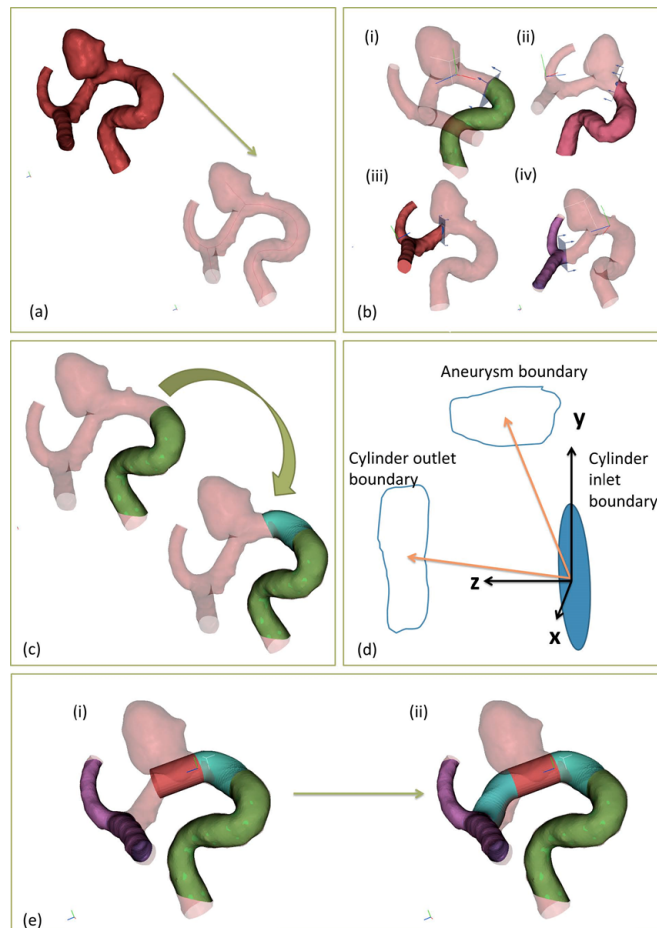


Figure 7.1: Reconstruction of the hypothetical healthy artery from the geometry of patient-specific IA (adapted from (Mandaltzi, 2016)): (a) skeleton of geometrical file of clinical aneurysm; (b) the geometry is clipped to define boundaries of the (i) upstream parent vessel; (ii) aneurysm connecting inlet; (iii) aneurysm connecting outlet; (iv) downstream parent vessel; (c) Smooth surface is created at the aneurysm connecting inlet to connect the upstream parent vessel with the reconstructed healthy cylinder; (d) a transformation of Cartesian coordinate which converts the  $z$ -direction from the inlet boundary to the outlet boundary, while  $y$ -direction is pointing to the aneurysm boundary; (e) replace the aneurysm with the reconstructed cylinder and create the smooth surface to connect the downstream parent vessel.

ter 2 could be the replacement of the healthy state artery, which includes the residual stresses within the arterial wall for physiological representation of stress distribution. Therefore the FSGT model will be fully integrated with the assumptions from the 1D, 2D, and 3D models presented in this thesis, which take into account the transmural variation through the wall thickness and the flow-induced elastin degradation.

## 7.4 CONCLUDING REMARKS

An updated FSGT framework is presented to investigate, quantify and elucidate the influence of mechanical and chemical stimuli on the cell functionality and the remodelling of arterial tissue. This generates a substantial multiscale and multiphysics simulation for modelling aneurysm evolution, involving the cell functionality and the constitutive synchronisation. In other words, the synthesis and adaptation of the cells (fibroblast and ECs) are represented numerically in order to regulate the constitutive structure (elastin and collagen) inside the aneurysm tissue. Although this seems to be overambitious and requires further biological study, the coupling between this modelling framework and potential experimental data could guide and enhance our current understanding to explore the etiology of aneurysm disease.



## REFERENCES

---

- ADOLPH, R., VORP, D. A., STEED, D. L., WEBSTER, M. W., KAMENEVA, M. V., AND WATKINS, S. C. Cellular content and permeability of intraluminal thrombus in abdominal aortic aneurysm. *Journal of Vascular Surgery*, 25(5):916–926, 1997.
- AKKAS, N. Aneurysms as a biomechanical instability problem. In *Biomechanical Transport Processes*, pages 303–311. Springer, 1990.
- AKPEK, S., ARAT, A., MORSI, H., KLUCZNICK, R. P., STROTHER, C. M., AND MAWAD, M. E. Self-expandable stent-assisted coiling of wide-necked intracranial aneurysms: a single-center experience. *American Journal of Neuroradiology*, 26(5):1223–1231, 2005.
- ALIMOHAMMADI, M., PICHARDO-ALMARZA, C., AGU, O., AND DÍAZ-ZUCCARINI, V. Development of a patient-specific multi-scale model to understand atherosclerosis and calcification locations: comparison with in vivo data in an aortic dissection. *Frontiers in physiology*, 7:238, 2016.
- ALIMOHAMMADI, M., PICHARDO-ALMARZA, C., AGU, O., AND DÍAZ-ZUCCARINI, V. A multiscale modelling approach to understand atherosclerosis formation: A patient-specific case study in the aortic bifurcation. *Proceedings of the Institution of Mechanical Engineers, Part H: Journal of Engineering in Medicine*, 231(5):378–390, 2017.
- ALSHEKHEE, A., MEHTA, S., EDGELL, R. C., VORA, N., FEEN, E., MOHAMMADI, A., KALE, S. P., AND CRUZ-FLORES, S. Hospital mortality and complications of electively clipped or coiled unruptured intracranial aneurysm. *Stroke*, 41(7):1471–1476, 2010.
- APARICIO, P., MANDALTSI, A., BOAMAH, J., CHEN, H., SELIMOVIC, A., BRATBY, M., UBEROI, R., VENTIKOS, Y., AND WATTON, P. Modelling the influence of endothelial heterogeneity on the progression of arterial disease: application to abdominal aortic aneurysm evolution. *International journal for numerical methods in biomedical engineering*, 30(5):563–586, 2014.
- APARÍCIO, P., THOMPSON, M. S., AND WATTON, P. N. A novel chemo-mechano-biological model of arterial tissue growth and remodelling. *Journal of biomechanics*, 49(12):2321–2330, 2016.
- AVRIL, S., BADEL, P., GABR, M., SUTTON, M. A., AND LESSNER, S. M. Biomechanics of porcine renal arteries and role of axial stretch. *Journal of biomechanical engineering*, 135(8):081007, 2013.
- BACK, L. H. Theoretical investigation of mass transport to arterial walls in various blood flow regions-ii. oxygen transport and its relationship to lipoprotein accumulation. *Mathematical Biosciences*, 27(3-4):263–285, 1975.
- BACK, L. H. Analysis of oxygen transport in the avascular region of arteries. *Mathematical Biosciences*, 31(3-4):285–306, 1976.
- BAEK, S., RAJAGOPAL, K., AND HUMPHREY, J. A theoretical model of enlarging intracranial fusiform aneurysms. *Journal of biomechanical engineering*, 128(1):142–149, 2006.
- BAEK, S., VALENTIN, A., AND HUMPHREY, J. Biochemomechanics of cerebral vasospasm and its resolution: ii. constitutive relations and model simulations. *Annals of biomedical engineering*, 35(9):1498, 2007.
- BARRON, J. T., KOPP, S. J., TOW, J., AND PARRILLO, J. E. Substrate-dependent alteration in o<sub>2</sub> consumption and energy metabolism in vascular smooth muscle. *American Journal of Physiology-Heart and Circulatory Physiology*, 270(6):H1869–H1877, 1996.
- BIRD, R. B., STEWART, W. E., LIGHTFOOT, E. N., AND KLINGENBERG, D. J. *Introductory transport phenomena*. Wiley Global Education, 2015.

- BJORK, J. W., SAFONOV, A. M., AND TRANQUILLO, R. T. Oxygen transport in bioreactors for engineered vascular tissues. In *Computational Modeling in Tissue Engineering*, pages 287–306. Springer, 2012.
- BOWKER, T. J. *A computational model for thrombus prediction*. PhD thesis, Oxford University, 2010.
- BRISMAN, J. L., SONG, J. K., AND NEWELL, D. W. Cerebral aneurysms. *New England Journal of Medicine*, 355(9):928–939, 2006.
- BRUNEL, H., AMBARD, D., DUFOUR, H., ROCHE, P., COSTALAT, V., AND JOURDAN, F. Relationship between cerebral aneurysm wall stiffness and rupture risk. *Computer methods in biomechanics and biomedical engineering*, 20(sup1):33–34, 2017.
- BUERK, D. G. AND GOLDSTICK, T. K. Arterial wall oxygen consumption rate varies spatially. *American Journal of Physiology-Heart and Circulatory Physiology*, 243(6):H948–H958, 1982.
- CANHAM, C. D. Different responses to gaps among shade-tolerant tree species. *Ecology*, 70(3):548–550, 1989.
- CARANCI, F., BRIGANTI, F., CIRILLO, L., LEONARDI, M., AND MUTO, M. Epidemiology and genetics of intracranial aneurysms. *European journal of radiology*, 82(10):1598–1605, 2013.
- CARDAMONE, L., VALENTIN, A., EBERTH, J., AND HUMPHREY, J. Origin of axial prestretch and residual stress in arteries. *Biomechanics and modeling in mechanobiology*, 8(6):431–446, 2009.
- CHATZIPRODROMOU, I., TRICOLI, A., POULIKAKOS, D., AND VENTIKOS, Y. Haemodynamics and wall remodelling of a growing cerebral aneurysm: a computational model. *Journal of biomechanics*, 40(2):412–426, 2007.
- CHIEN, S. Mechanotransduction and endothelial cell homeostasis: the wisdom of the cell. *American Journal of Physiology-Heart and Circulatory Physiology*, 292(3):H1209–H1224, 2007.
- CHIU, J.-J. AND CHIEN, S. Effects of disturbed flow on vascular endothelium: pathophysiological basis and clinical perspectives. *Physiological reviews*, 91(1):327–387, 2011.
- CHUONG, C.-J. AND FUNG, Y.-C. Residual stress in arteries. In *Frontiers in biomechanics*, pages 117–129. Springer, 1986.
- COPPOLA, G. AND CARO, C. Oxygen mass transfer in a model three-dimensional artery. *Journal of The Royal Society Interface*, 5(26):1067–1075, 2008.
- CRAWFORD, D. W., COLE, M. A., AND BACK, L. H. Evidence for the blood oxygen boundary layer po<sub>2</sub> gradient ( $\Delta p_{O_2}$ ) as a significant determinant of intimal (pw) and lowest medial po<sub>2</sub> (p<sub>delta n</sub>) in the vivo dog femoral artery. *Advances in experimental medicine and biology*, 159:197, 1983.
- CRAWFORD, D. AND BLANKENHORN, D. Arterial wall oxygenation, oxyradicals, and atherosclerosis. *Atherosclerosis*, 89(2-3):97–108, 1991.
- CUMMINS, P. M., VON OFFENBERG SWEENEY, N., KILLEEN, M. T., BIRNEY, Y. A., REDMOND, E. M., AND CAHILL, P. A. Cyclic strain-mediated matrix metalloproteinase regulation within the vascular endothelium: a force to be reckoned with. *American Journal of Physiology-Heart and Circulatory Physiology*, 292(1):H28–H42, 2007.
- CUNNINGHAM, K. S. AND GOTLIEB, A. I. The role of shear stress in the pathogenesis of atherosclerosis. *Laboratory investigation*, 85(1):9, 2005.
- DE ROOIJ, N. K., LINN, F. H., VAN DER PLAS, J. A., ALGRA, A., AND RINKEL, G. J. Incidence of subarachnoid haemorrhage: a systematic review with emphasis on region, age, gender and time trends. *Journal of Neurology, Neurosurgery & Psychiatry*, 2007.
- DI TOMASO, G., PICHARDO-ALMARZA, C., AGU, O., AND DÍAZ-ZUCCARINI, V. A multiscale and patient-specific computational framework of atherosclerosis formation and progression: a case study in the aorta and peripheral arteries. *Procedia Computer Science*, 51:1118–1127, 2015.
- DIAMOND, S. L. Engineering design of optimal strategies for blood clot dissolution. *Annual review of biomedical engineering*, 1(1):427–461, 1999.
- DÍAZ-ZUCCARINI, V., DI TOMASO, G., AGU, O., AND PICHARDO-ALMARZA, C. Towards personalised management of atherosclerosis via computational models in vascular clinics: technology based on patient-specific simulation approach. *Healthcare technology letters*, 1(1):13–18, 2014.
- ERIKSSON, T., WATTON, P., LUO, X., AND VENTIKOS, Y. Modelling volumetric growth in a thick walled fibre reinforced artery. *Journal of the Mechanics and Physics of Solids*, 73:134–150, 2014.

- EROSCHENKO, V. P. AND DI FIORE, M. S. *DiFiore's atlas of histology with functional correlations*. Lippincott Williams & Wilkins, 2013.
- ETMINAN, N., DREIER, R., BUCHHOLZ, B. A., BESEOGLU, K., BRUCKNER, P., MATZENAUER, C., TORNER, J. C., BROWN, R. D., STEIGER, H.-J., HÄNGGI, D., ET AL. Age of collagen in intracranial saccular aneurysms. *Stroke*, 45(6):1757–1763, 2014.
- ETMINAN, N. AND RINKEL, G. J. Unruptured intracranial aneurysms: development, rupture and preventive management. *Nature Reviews Neurology*, 12(12):699, 2016.
- FERZIGER, J. H. AND PERIC, M. *Computational methods for fluid dynamics*. Springer Science & Business Media, 2012.
- FINLAY, H. M., WHITTAKER, P., AND CANHAM, P. B. Collagen organization in the branching region of human brain arteries. *Stroke*, 29(8):1595–1601, 1998.
- FORSTING, M. AND WANKE, I. Intracranial vascular malformations and aneurysms: From diagnostic work-up to endovascular therapy. *Springer*, 2008.
- FRÖSEN, J., PIIPPO, A., PAETAU, A., KANGASNIEMI, M., NIEMELÄ, M., HERNESNIEMI, J., AND JÄÄSKELÄINEN, J. Remodeling of saccular cerebral artery aneurysm wall is associated with rupture. *Stroke*, 35(10):2287–2293, 2004.
- FUNG, Y. What principle governs the stress distribution in living organs. *Biomechanics in China, Japan, and USA*, pages 1–13, 1983.
- FUNG, Y. What are the residual stresses doing in our blood vessels? *Annals of biomedical engineering*, 19(3):237–249, 1991.
- FUNG, Y. AND CHUONG, C. Three-dimensional stress distribution in arteries. In *ASME*, volume 105, pages 268–274, 1983.
- FUNG, Y. AND LIU, S. Strain distribution in small blood vessels with zero-stress state taken into consideration. *American Journal of Physiology-Heart and Circulatory Physiology*, 262(2):H544–H552, 1992.
- GAETANI, P., TARTARA, F., GRAZIOLI, V., TANCIONI, F., INFUSO, L., AND Y BAENA, R. R. Collagen cross-linkage, elastolytic and collagenolytic activities in cerebral aneurysms: a preliminary investigation. *Life sciences*, 63(4):285–292, 1998.
- GASSER, T. C., OGDEN, R. W., AND HOLZAPFEL, G. A. Hyperelastic modelling of arterial layers with distributed collagen fibre orientations. *Journal of the royal society interface*, 3(6):15–35, 2006.
- GLEASON JR, R. L. AND HUMPHREY, J. D. A 2d constrained mixture model for arterial adaptations to large changes in flow, pressure and axial stretch. *Mathematical Medicine and Biology*, 22(4):347–369, 2005.
- GOODMAN, M. E., LUO, X., AND HILL, N. A mathematical model on the feedback between wall shear stress and intimal hyperplasia. *International Journal of Applied Mechanics*, 8(07):1640011, 2016.
- GREVING, J. P., RINKEL, G. J., BUSKENS, E., AND ALGRA, A. Cost-effectiveness of preventive treatment of intracranial aneurysms new data and uncertainties. *Neurology*, 73(4):258–265, 2009.
- GRYTSAN, A., ERIKSSON, T. S., WATTON, P. N., AND GASSER, T. C. Growth description for vessel wall adaptation: a thick-walled mixture model of abdominal aortic aneurysm evolution. *Materials*, 10(9):994, 2017.
- GRYTSAN, A., WATTON, P. N., AND HOLZAPFEL, G. A. A thick-walled fluid–solid-growth model of abdominal aortic aneurysm evolution: Application to a patient-specific geometry. *Journal of biomechanical engineering*, 137(3):031008, 2015.
- GUO, X., LU, X., AND KASSAB, G. S. Transmural strain distribution in the blood vessel wall. *American Journal of Physiology-Heart and Circulatory Physiology*, 288(2):H881–H886, 2005.
- GUYTON, J. R. AND KLEMP, K. F. The lipid-rich core region of human atherosclerotic fibrous plaques. prevalence of small lipid droplets and vesicles by electron microscopy. *The American journal of pathology*, 134(3):705, 1989.
- HAGA, J. H., LI, Y.-S. J., AND CHIEN, S. Molecular basis of the effects of mechanical stretch on vascular smooth muscle cells. *Journal of biomechanics*, 40(5):947–960, 2007.
- HAN, H. AND FUNG, Y. Residual strains in porcine and canine trachea. *Journal of biomechanics*, 24(5):307311–309315, 1991.
- HARRISON, D., GRIENDLING, K. K., LANDMESSER, U., HORNIG, B., AND DREXLER, H. Role of oxidative stress in atherosclerosis. *The American journal of cardiology*, 91(3):7–11, 2003.

- HARTER, L. P., GROSS, B. H., CALLEN, P. W., AND BARTH, R. A. Ultrasonic evaluation of abdominal aortic thrombus. *Journal of Ultrasound in Medicine*, 1(8):315–318, 1982.
- HASLACH, H. W. AND HUMPHREY, J. D. Dynamics of biological soft tissue and rubber: internally pressurized spherical membranes surrounded by a fluid. *International Journal of Non-Linear Mechanics*, 39(3):399–420, 2004.
- HAYKOWSKY, M., FINDLAY, J., AND IGNASZEWSKI, A. Aneurysmal subarachnoid hemorrhage associated with weight training: three case reports., 1996.
- HE, C. M. AND ROACH, M. R. The composition and mechanical properties of abdominal aortic aneurysms. *Journal of vascular surgery*, 20(1):6–13, 1994.
- HENNIG, T., MOGENSEN, C., KIRSCH, J., POHL, U., AND GLOE, T. Shear stress induces the release of an endothelial elastase: role in integrin  $\alpha\beta 3$ -mediated fgf-2 release. *Journal of vascular research*, 48(6):453–464, 2011.
- HIMBURG, H. A., GRZYBOWSKI, D. M., HAZEL, A. L., LAMACK, J. A., LI, X.-M., AND FRIEDMAN, M. H. Spatial comparison between wall shear stress measures and porcine arterial endothelial permeability. *American Journal of Physiology-Heart and Circulatory Physiology*, 286(5):H1916–H1922, 2004.
- HO, H., SURESH, V., KANG, W., COOLING, M. T., WATTON, P. N., AND HUNTER, P. J. Multiscale modeling of intracranial aneurysms: cell signaling, hemodynamics, and remodeling. *IEEE Transactions on Biomedical Engineering*, 58(10):2974–2977, 2011.
- HOFFMAN, B. D., GRASHOFF, C., AND SCHWARTZ, M. A. Dynamic molecular processes mediate cellular mechanotransduction. *Nature*, 475(7356):316–323, 2011.
- HOLLAND, E. C. *Computational modelling of transport phenomena in cerebral aneurysms*. PhD thesis, University of Oxford, 2012.
- HOLZAPFEL, A. G. Nonlinear solid mechanics ii. 2000.
- HOLZAPFEL, G. A. Determination of material models for arterial walls from uniaxial extension tests and histological structure. *Journal of theoretical biology*, 238(2):290–302, 2006.
- HOLZAPFEL, G. A. AND GASSER, T. C. Computational stress-deformation analysis of arterial walls including high-pressure response. *International journal of cardiology*, 116(1):78–85, 2007.
- HOLZAPFEL, G. A., GASSER, T. C., AND OGDEN, R. W. A new constitutive framework for arterial wall mechanics and a comparative study of material models. *Journal of elasticity and the physical science of solids*, 61(1-3):1–48, 2000.
- HOLZAPFEL, G. A., GASSER, T. C., AND OGDEN, R. W. Comparison of a multi-layer structural model for arterial walls with a fung-type model, and issues of material stability. *Journal of biomechanical engineering*, 126(2):264–275, 2004.
- HOLZAPFEL, G. A., SOMMER, G., GASSER, C. T., AND REGITNIG, P. Determination of layer-specific mechanical properties of human coronary arteries with nonatherosclerotic intimal thickening and related constitutive modeling. *American Journal of Physiology-Heart and Circulatory Physiology*, 289(5):H2048–H2058, 2005.
- HSU, E., LIU, A., DOWNS, J., RIGAMONTI, D., AND HUMPHREY, J. A triplane video-based experimental system for studying axisymmetrically inflated biomembranes. *IEEE Transactions on Biomedical Engineering*, 42(5):442–450, 1995.
- HUMPHREY, J. D. Vascular mechanics, mechanobiology, and remodeling. *Journal of mechanics in medicine and biology*, 9(02):243–257, 2009.
- HUMPHREY, J. D., SCHWARTZ, M. A., TELLIDES, G., AND MILEWICZ, D. M. Role of mechanotransduction in vascular biology. *Circulation research*, 116(8):1448–1461, 2015.
- HUMPHREY, J. Vascular adaptation and mechanical homeostasis at tissue, cellular, and sub-cellular levels. *Cell biochemistry and biophysics*, 50(2):53–78, 2008.
- HUMPHREY, J. AND HOLZAPFEL, G. A. Mechanics, mechanobiology, and modeling of human abdominal aorta and aneurysms. *Journal of biomechanics*, 45(5):805–814, 2012.
- HUMPHREY, J. AND KYRIACOU, S. The use of laplace's equation in aneurysm mechanics. *Neurological research*, 18(3):204–208, 1996.
- HUMPHREY, J. AND NA, S. Elastodynamics and arterial wall stress. *Annals of biomedical engineering*, 30(4):509–523, 2002.

- HUMPHREY, J. AND RAJAGOPAL, K. A constrained mixture model for growth and remodeling of soft tissues. *Mathematical models and methods in applied sciences*, 12(03):407–430, 2002.
- HUMPHREY, J. AND TAYLOR, C. Intracranial and abdominal aortic aneurysms: similarities, differences, and need for a new class of computational models. *Annu. Rev. Biomed. Eng.*, 10:221–246, 2008.
- INAGAWA, T. AND HIRANO, A. Autopsy study of unruptured incidental intracranial aneurysms. *Surgical neurology*, 34(6):361–365, 1990.
- IRACE, C., CORTESE, C., FIASCHI, E., CARALLO, C., FARINARO, E., AND GNASSO, A. Wall shear stress is associated with intima-media thickness and carotid atherosclerosis in subjects at low coronary heart disease risk. *Stroke*, 35(2):464–468, 2004.
- ISAKSEN, J. G., BAZILEVS, Y., KVAMSDAL, T., ZHANG, Y., KASPERSEN, J. H., WATERLOO, K., ROMNER, B., AND INGEBRIGTSEN, T. Determination of wall tension in cerebral artery aneurysms by numerical simulation. *Stroke*, 39(12):3172–3178, 2008.
- KAAZEMPUR-MOFRAD, M. AND ETHIER, C. Mass transport in an anatomically realistic human right coronary artery. *Annals of biomedical engineering*, 29(2):121–127, 2001.
- KAAZEMPUR-MOFRAD, M., WADA, S., MYERS, J., AND ETHIER, C. Mass transport and fluid flow in stenotic arteries: axisymmetric and asymmetric models. *International Journal of Heat and Mass Transfer*, 48(21):4510–4517, 2005.
- KANETO, H., KATAKAMI, N., MATSUHISA, M., AND MATSUOKA, T.-A. Role of reactive oxygen species in the progression of type 2 diabetes and atherosclerosis. *Mediators of inflammation*, 2010, 2010.
- KARŠAJ, I. AND HUMPHREY, J. D. A multilayered wall model of arterial growth and remodeling. *Mechanics of materials*, 44:110–119, 2012.
- KASSAM, A., HOROWITZ, M., CHANG, Y.-F., AND PETERS, D. Altered arterial homeostasis and cerebral aneurysms: A review of the literature and justification for a search of molecular biomarkers. *Neurosurgery*, 54(5):1199–1212, 2004.
- KEEDY, A. An overview of intracranial aneurysms. *McGill Journal of Medicine: MJM*, 9(2):141, 2006.
- KENJEREŠ, S. AND DE LOOR, A. Modelling and simulation of low-density lipoprotein transport through multi-layered wall of an anatomically realistic carotid artery bifurcation. *Journal of The Royal Society Interface*, 11(91):20130941, 2014.
- KIRK, J., EFFERSØE, P., AND CHIANG, S. The rate of respiration and glycolysis by human and dog aortic tissue. *Journal of gerontology*, 9(1):10–35, 1954.
- KOJDA, G. AND HARRISON, D. Interactions between no and reactive oxygen species: pathophysiological importance in atherosclerosis, hypertension, diabetes and heart failure. *Cardiovascular research*, 43(3):652–671, 1999.
- KONDO, S., HASHIMOTO, N., KIKUCHI, H., HAZAMA, F., NAGATA, I., AND KATAOKA, H. Apoptosis of medial smooth muscle cells in the development of saccular cerebral aneurysms in rats. *Stroke*, 29(1):181–189, 1998.
- KRINGS, T., MANDELL, D. M., KIEHL, T.-R., GEIBPRASERT, S., TYMIANSKI, M., ALVAREZ, H., HANS, F.-J., ET AL. Intracranial aneurysms: from vessel wall pathology to therapeutic approach. *Nature Reviews Neurology*, 7(10):547–559, 2011.
- KRISANDA, J. M. AND PAUL, R. J. Energetics of isometric contraction in porcine carotid artery. *American Journal of Physiology-Cell Physiology*, 246(5):C510–C519, 1984.
- LAMBRECHTS, D., SCHROOTEN, J., VAN DE PUTTE, T., AND VAN OOSTERWYCK, H. Computational modeling of mass transport and its relation to cell behavior in tissue engineering constructs. In *Computational Modeling in Tissue Engineering*, pages 85–105. Springer, 2012.
- LANGILLE, B. L. AND ADAMSON, S. L. Relationship between blood flow direction and endothelial cell orientation at arterial branch sites in rabbits and mice. *Circulation Research*, 48(4):481–488, 1981.
- LASHERAS, J. C. The biomechanics of arterial aneurysms. *Annu. Rev. Fluid Mech.*, 39:293–319, 2007.
- LEE, R. T., YAMAMOTO, C., FENG, Y., POTTER-PERIGO, S., BRIGGS, W. H., LANDSCHULZ, K. T., TURI, T. G., THOMPSON, J. F., LIBBY, P., AND WIGHT, T. N. Mechanical strain induces specific changes in the synthesis and organization of proteoglycans by vascular smooth muscle cells. *Journal of biological chemistry*, 276(17):13847–13851, 2001.

- LI, C. AND XU, Q. Mechanical stress-initiated signal transduction in vascular smooth muscle cells in vitro and in vivo. *Cellular signalling*, 19(5):881–891, 2007.
- LINDAHL, G. E., CHAMBERS, R. C., PAKRIVOPOULOU, J., DAWSON, S. J., JACOBSEN, M. C., BISHOP, J. E., AND LAURENT, G. J. Activation of fibroblast procollagen  $\alpha 1$  (i) transcription by mechanical strain is transforming growth factor- $\beta$ -dependent and involves increased binding of ccaat-binding factor (cbf/nf-y) at the proximal promoter. *Journal of Biological Chemistry*, 277(8): 6153–6161, 2002.
- LIU, C., ESKIN, S., AND HELLUMS, J. The oxygen permeability of cultured endothelial cell monolayers. In *Oxygen Transport to Tissue XV*, pages 723–730. Springer, 1994.
- LIU, S. AND FUNG, Y. Zero-stress states of arteries. *Journal of biomechanical engineering*, 110(1):82–84, 1988.
- LU, G., HUANG, L., ZHANG, X., WANG, S., HONG, Y., HU, Z., AND GENG, D. Influence of hemodynamic factors on rupture of intracranial aneurysms: patient-specific 3d mirror aneurysms model computational fluid dynamics simulation. *American Journal of Neuroradiology*, 32(7):1255–1261, 2011.
- MA, B., HARBAUGH, R. E., AND RAGHAVAN, M. L. Three-dimensional geometrical characterization of cerebral aneurysms. *Annals of biomedical engineering*, 32(2):264–273, 2004.
- MA, B., LU, J., HARBAUGH, R. E., AND RAGHAVAN, M. L. Nonlinear anisotropic stress analysis of anatomically realistic cerebral aneurysms. *Journal of biomechanical engineering*, 129(1):88–96, 2007.
- MA, P., LI, X., AND KU, D. N. Convective mass transfer at the carotid bifurcation. *Journal of biomechanics*, 30(6):565–571, 1997.
- MALEK, A. M., ALPER, S. L., AND IZUMO, S. Hemodynamic shear stress and its role in atherosclerosis. *Jama*, 282(21):2035–2042, 1999.
- MANDALTSI, A. *Modelling the mechanobiological evolution of aneurysms: An integrative in vivo, in vitro and in silico approach*. PhD thesis, University of Oxford, 2016.
- MARINO, M., PONTRELLI, G., VAIRO, G., AND WRIGGERS, P. Coupling microscale transport and tissue mechanics: modeling strategies for arterial multiphysics. In *Modeling of microscale transport in biological processes*, pages 77–112. Elsevier, 2017a.
- MARINO, M., PONTRELLI, G., VAIRO, G., AND WRIGGERS, P. A chemo-mechano-biological formulation for the effects of biochemical alterations on arterial mechanics: the role of molecular transport and multiscale tissue remodelling. *Journal of The Royal Society Interface*, 14(136):20170615, 2017b.
- MENG, H., TUTINO, V., XIANG, J., AND SIDDIQUI, A. High wss or low wss? complex interactions of hemodynamics with intracranial aneurysm initiation, growth, and rupture: toward a unifying hypothesis. *American Journal of Neuroradiology*, 35(7):1254–1262, 2014.
- MENG, H., METAXA, E., GAO, L., LIAW, N., NATARAJAN, S. K., SWARTZ, D. D., SIDDIQUI, A. H., KOLEGA, J., AND MOCCO, J. Progressive aneurysm development following hemodynamic insult. *Journal of neurosurgery*, 114(4):1095–1103, 2011.
- MITCHELL, P. AND JAKUBOWSKI, J. Estimate of the maximum time interval between formation of cerebral aneurysm and rupture. *Journal of Neurology, Neurosurgery & Psychiatry*, 69(6):760–767, 2000.
- MONSON, K. L., GOLDSMITH, W., BARBARO, N. M., AND MANLEY, G. T. Axial mechanical properties of fresh human cerebral blood vessels. *Journal of biomechanical engineering*, 125(2):288–294, 2003.
- MOORE, J. AND ETHIER, C. Oxygen mass transfer calculations in large arteries. 1997.
- MOORE, S., DAVID, T., CHASE, J., ARNOLD, J., AND FINK, J. 3d models of blood flow in the cerebral vasculature. *Journal of biomechanics*, 39(8):1454–1463, 2006.
- MURRAY, J. On the molecular mechanism of facilitated oxygen diffusion by haemoglobin and myoglobin. *Proceedings of the Royal Society of London B: Biological Sciences*, 178(1050):95–110, 1971.
- NEREM, R. M. Hemodynamics and the vascular endothelium. *TRANSACTIONS-AMERICAN SOCIETY OF MECHANICAL ENGINEERS JOURNAL OF BIOMECHANICAL ENGINEERING*, 115: 510–510, 1993.
- NESBITT, W. S., WESTEIN, E., TOVAR-LOPEZ, F. J., TOLOUEI, E., MITCHELL, A., FU, J., CARBERRY, J., FOURAS, A., AND JACKSON, S. P. A shear gradient-dependent platelet aggregation mechanism drives

- thrombus formation. *Nature medicine*, 15(6):665–673, 2009.
- OSHIMA, M., TORII, R., KOBAYASHI, T., TANIGUCHI, N., AND TAKAGI, K. Finite element simulation of blood flow in the cerebral artery. *Computer methods in applied mechanics and engineering*, 191(6):661–671, 2001.
- PAKRAVAN, H., SAIDI, M., AND FIROOZABADI, B. A mechanical model for morphological response of endothelial cells under combined wall shear stress and cyclic stretch loadings. *Biomechanics and modeling in mechanobiology*, 15(5):1229–1243, 2016.
- PANDIT, A., LU, X., WANG, C., AND KASSAB, G. S. Biaxial elastic material properties of porcine coronary media and adventitia. *American Journal of Physiology-Heart and Circulatory Physiology*, 288(6):H2581–H2587, 2005.
- PARK, H.-K., HOROWITZ, M., JUNGREIS, C., GENEVRO, J., KOEBBE, C., LEVY, E., AND KASSAM, A. Periprocedural morbidity and mortality associated with endovascular treatment of intracranial aneurysms. *American Journal of Neuroradiology*, 26(3):506–514, 2005.
- PIEROT, L. Flow diverter stents in the treatment of intracranial aneurysms: Where are we? *Journal of Neuroradiology*, 38(1):40–46, 2011.
- PIETILÄ, K. AND JAAKKOLA, O. Effect of hypoxia on the synthesis of glycosaminoglycans and collagen by rabbit aortic smooth muscle cells in culture. *Atherosclerosis*, 50(2):183–190, 1984.
- PITTMAN, R. N. AND DULING, B. R. Oxygen sensitivity of vascular smooth muscle: I. in vitro studies. *Microvascular research*, 6(2):202–211, 1973.
- PONTRELLI, G. AND DE MONTE, F. Mass diffusion through two-layer porous media: an application to the drug-eluting stent. *International Journal of Heat and Mass Transfer*, 50(17-18):3658–3669, 2007.
- QIU, Y., TARBELL, J. M., ET AL. Numerical simulation of pulsatile flow in a compliant curved tube model of a coronary artery. *TRANSACTIONS-AMERICAN SOCIETY OF MECHANICAL ENGINEERS JOURNAL OF BIOMECHANICAL ENGINEERING*, 122(1):77–85, 2000.
- RAPPITSCH, G. AND PERKTOLD, K. Pulsatile albumin transport in large arteries: a numerical simulation study. *TRANSACTIONS-AMERICAN SOCIETY OF MECHANICAL ENGINEERS JOURNAL OF BIOMECHANICAL ENGINEERING*, 118:511–519, 1996.
- RAPPITSCH, G., PERKTOLD, K., AND PERNKOPF, E. Numerical modelling of shear-dependent mass transfer in large arteries. *International Journal for Numerical Methods in Fluids*, 25(7):847–857, 1997.
- RAY, J. B., ARAB, S., DENG, Y., LIU, P., PENN, L., COURTMAN, D. W., AND WARD, M. E. Oxygen regulation of arterial smooth muscle cell proliferation and survival. *American Journal of Physiology-Heart and Circulatory Physiology*, 294(2):H839–H852, 2008.
- REYMOND, P., MERENDA, F., PERREN, F., RUFENACHT, D., AND STERGIOPULOS, N. Validation of a one-dimensional model of the systemic arterial tree. *American Journal of Physiology-Heart and Circulatory Physiology*, 297(1):H208–H222, 2009.
- RISSANEN, E., TRANBERG, H. K., AND NIKINMAA, M. Oxygen availability regulates metabolism and gene expression in trout hepatocyte cultures. *American Journal of Physiology-Regulatory, Integrative and Comparative Physiology*, 291(5):R1507–R1515, 2006.
- ROBERTSON, A. M., DUAN, X., AZIZ, K. M., HILL, M. R., WATKINS, S. C., AND CEBRAL, J. R. Diversity in the strength and structure of unruptured cerebral aneurysms. *Annals of biomedical engineering*, 43(7):1502–1515, 2015.
- ROBERTSON, A. M. AND WATTON, P. N. Mechanobiology of the arterial wall. *Modeling of transport in biological media*. Elsevier, New York, pages 275–347, 2013.
- RODRIGUEZ-FEO, J., SLUIJTER, J., DE KLEIJN, D., AND PASTERKAMP, G. Modulation of collagen turnover in cardiovascular disease. *Current pharmaceutical design*, 11(19):2501–2514, 2005.
- ROWE, A. J., FINLAY, H. M., AND CANHAM, P. B. Collagen biomechanics in cerebral arteries and bifurcations assessed by polarizing microscopy. *Journal of vascular research*, 40(4):406–415, 2003.
- RYAN, J. AND HUMPHREY, J. Finite element based predictions of preferred material symmetries in saccular aneurysms. *Annals of biomedical engineering*, 27(5):641–647, 1999.
- SANCHEZ, M., AMBARD, D., COSTALAT, V., MENDEZ, S., JOURDAN, F., AND NICOU, F. Biomechanical assessment of the individual risk of rupture of

- cerebral aneurysms: a proof of concept. *Annals of biomedical engineering*, 41(1):28–40, 2013.
- SCHIEVINK, W. I. Intracranial aneurysms. *New England Journal of Medicine*, 336(1):28–40, 1997.
- SCHMID, H., PAULI, L., PAULUS, A., KUHL, E., AND ITSKOV, M. Consistent formulation of the growth process at the kinematic and constitutive level for soft tissues composed of multiple constituents. *Computer methods in biomechanics and biomedical engineering*, 15(5):547–561, 2012.
- SCHMID, H., WATTON, P., MAURER, M., WIMMER, J., WINKLER, P., WANG, Y., RÖHRLE, O., AND ITSKOV, M. Impact of transmural heterogeneities on arterial adaptation. *Biomechanics and modeling in mechanobiology*, 9(3):295–315, 2010.
- SCHMID, H., GRYSAN, A., POSHTAN, E., WATTON, P. N., AND ITSKOV, M. Influence of differing material properties in media and adventitia on arterial adaptation-application to aneurysm formation and rupture. *Computer methods in biomechanics and biomedical engineering*, 16(1):33–53, 2013.
- SCHNEIDERMAN, G. AND GOLDSTICK, T. K. Significance of luminal plasma layer resistance in arterial wall oxygen supply. *Atherosclerosis*, 31(1):11–20, 1978.
- SCHNEIDERMAN, G., MOCKROS, L. F., AND GOLDSTICK, T. K. Effect of pulsatility on oxygen transport to the human arterial wall. *Journal of biomechanics*, 15(11):849–858, 1982.
- SCHUMACKER, P. T., CHANDEL, N., AND AGUSTI, A. Oxygen conformance of cellular respiration in hepatocytes. *American Journal of Physiology-Lung Cellular and Molecular Physiology*, 265(4):L395–L402, 1993.
- SELIMOVIC, A., VENTIKOS, Y., AND WATTON, P. N. Modelling the evolution of cerebral aneurysms: Biomechanics, mechanobiology and multiscale modelling. *Procedia IUTAM*, 10:396–409, 2014.
- SESHAIYER, P., HSU, F., SHAH, A., KYRIACOU, S., AND HUMPHREY, J. Multiaxial mechanical behavior of human saccular aneurysms. *Computer Methods in Biomechanics and Biomedical Engineering*, 4(3):281–289, 2001.
- SHABAT, I. B. Computes curvature and curvature derivative tensors in each vertex of a triangle meshes. <https://uk.mathworks.com/matlabcentral/fileexchange/47134-curvature-estimationl-on-triangle-mesh>, 2016.
- SHADWICK, R. E. Mechanical design in arteries. *Journal of Experimental Biology*, 202(23):3305–3313, 1999.
- SHAH, A. AND HUMPHREY, J. Finite strain elastodynamics of intracranial saccular aneurysms. *Journal of biomechanics*, 32(6):593–599, 1999.
- SHIMIZU, K., MITCHELL, R. N., AND LIBBY, P. Inflammation and cellular immune responses in abdominal aortic aneurysms. *Arteriosclerosis, thrombosis, and vascular biology*, 26(5):987–994, 2006.
- SHO, E., SHO, M., HOSHINA, K., KIMURA, H., NAKAHASHI, T. K., AND DALMAN, R. L. Hemodynamic forces regulate mural macrophage infiltration in experimental aortic aneurysms. *Experimental and molecular pathology*, 76(2):108–116, 2004.
- SHOJI, T., NISHIZAWA, Y., KAWAGISHI, T., KAWASAKI, K., TANIWAKI, H., TABATA, T., INOUE, T., AND MORII, H. Intermediate-density lipoprotein as an independent risk factor for aortic atherosclerosis in hemodialysis patients. *Journal of the American Society of Nephrology*, 9(7):1277–1284, 1998.
- SHOJIMA, M., OSHIMA, M., TAKAGI, K., TORII, R., HAYAKAWA, M., KATADA, K., MORITA, A., AND KIRINO, T. Magnitude and role of wall shear stress on cerebral aneurysm. *Stroke*, 35(11):2500–2505, 2004.
- SINHA, R., LE GAC, S., VERDONSCHOT, N., VAN DEN BERG, A., KOOPMAN, B., AND ROUWKEMA, J. Endothelial cell alignment as a result of anisotropic strain and flow induced shear stress combinations. *Scientific reports*, 6:29510, 2016.
- SOKOLIS, D. P., KRITHARIS, E. P., GIAGINI, A. T., LAMPROPOULOS, K. M., PAPADODIMA, S. A., AND ILIOPOULOS, D. C. Biomechanical response of ascending thoracic aortic aneurysms: association with structural remodelling. *Computer methods in biomechanics and biomedical engineering*, 15(3):231–248, 2012.
- SOMMER, G. Mechanical properties of healthy and diseased human arteries. *TU Graz*, 2008.
- STEINBRECH, D. S., LONGAKER, M. T., MEHRARA, B. J., SAADEH, P. B., CHIN, G. S., GERRETS, R. P., CHAU, D. C., ROWE, N. M., AND GITTES, G. K. Fibroblast response to hypoxia: the relationship between angiogenesis and matrix regulation. *Journal of surgical Research*, 84(2):127–133, 1999.

- SUN, N., LEUNG, J., WOOD, N., HUGHES, A., THOM, S., CHESHIRE, N., AND XU, X. Computational analysis of oxygen transport in a patient-specific model of abdominal aortic aneurysm with intraluminal thrombus. *The British journal of radiology*, 82(special\_issue\_1):S18–S23, 2009.
- SUN, N., WOOD, N. B., HUGHES, A. D., THOM, S. A., AND XU, X. Y. Influence of pulsatile flow on ldl transport in the arterial wall. *Annals of biomedical engineering*, 35(10):1782–1790, 2007.
- TABER, L. A. AND HUMPHREY, J. D. Stress-modulated growth, residual stress, and vascular heterogeneity. *Journal of biomechanical engineering*, 123(6):528–535, 2001.
- TADA, S. Numerical study of oxygen transport in a carotid bifurcation. *Physics in medicine and biology*, 55(14):3993, 2010.
- TADA, S. AND TARBELL, J. M. Oxygen mass transport in a compliant carotid bifurcation model. *Annals of biomedical engineering*, 34(9):1389–1399, 2006.
- TARBELL, J. Bioengineering studies of the endothelial transport barrier. *BMES Bull*, 17:35–39, 1993.
- TARBELL, J. M. Mass transport in arteries and the localization of atherosclerosis. *Annual review of biomedical engineering*, 5(1):79–118, 2003.
- TARBELL, J. M. AND QUI, Y. Arterial wall mass transport: the possible role of blood phase resistance in the localization of arterial disease. *The Biomedical Engineering Handbook, 2nd ed., edited by JD Bronzino*. New York: CRC, pages 100–1, 2000.
- TATESHIMA, S., TANISHITA, K., OMURA, H., VILLABLANCA, J., AND VINUELA, F. Intra-aneurysmal hemodynamics during the growth of an unruptured aneurysm: in vitro study using longitudinal ct angiogram database. *American journal of neuro-radiology*, 28(4):622–627, 2007.
- TEDGUI, A. AND LEVER, M. Filtration through damaged and undamaged rabbit thoracic aorta. *American Journal of Physiology-Heart and Circulatory Physiology*, 247(5):H784–H791, 1984.
- TRAUB, O. AND BERK, B. C. Laminar shear stress. *Arteriosclerosis, thrombosis, and vascular biology*, 18(5):677–685, 1998.
- UEDA, A., SHIMOMURA, M., IKEDA, M., YAMAGUCHI, R., AND TANISHITA, K. Effect of glycocalyx on shear-dependent albumin uptake in endothelial cells. *American Journal of Physiology-Heart and Circulatory Physiology*, 287(5):H2287–H2294, 2004.
- VAISHNAV, R. N. AND VOSSOUGH, J. Residual stress and strain in aortic segments. *Journal of biomechanics*, 20(3):235239–237, 1987.
- VALENTÍN, A. AND HUMPHREY, J. Parameter sensitivity study of a constrained mixture model of arterial growth and remodeling. *Journal of biomechanical engineering*, 131(10):101006, 2009.
- VAN ROOIJ, W. AND SLUZEWSKI, M. Procedural morbidity and mortality of elective coil treatment of unruptured intracranial aneurysms. *American Journal of Neuroradiology*, 27(8):1678–1680, 2006.
- VANROSSOMME, A., EKER, O., THIRAN, J.-P., COURBEBAISSE, G., AND BOUDJELTIA, K. Z. Intracranial aneurysms: Wall motion analysis for prediction of rupture. *American Journal of Neuroradiology*, 36(10):1796–1802, 2015.
- VIRAG, L., WILSON, J. S., HUMPHREY, J. D., AND KARŠAJ, I. A computational model of biochemomechanical effects of intraluminal thrombus on the enlargement of abdominal aortic aneurysms. *Annals of biomedical engineering*, 43(12):2852–2867, 2015.
- VIRAG, L., WILSON, J. S., HUMPHREY, J. D., AND KARŠAJ, I. A computational model of biochemomechanical effects of intraluminal thrombus and roles of risk factors in the evolution of abdominal aortic aneurysms. 2018.
- VORP, D., WANG, D., WEBSTER, M., AND FEDERSPIEL, W. Effect of intraluminal thrombus thickness and bulge diameter on the oxygen diffusion in abdominal aortic aneurysm. *Journal of biomechanical engineering*, 120(5):579–583, 1998.
- VORP, D. A., FEDERSPIEL, W. J., AND WEBSTER, M. W. Does laminated intraluminal thrombus within abdominal aortic aneurysm cause anoxia of the aortic wall? *Journal of vascular surgery*, 23(3):540–541, 1996.
- VORP, D. A., LEE, P. C., WANG, D. H., MAKAROUN, M. S., NEMOTO, E. M., OGAWA, S., AND WEBSTER, M. W. Association of intraluminal thrombus in abdominal aortic aneurysm with local hypoxia and wall weakening. *Journal of Vascular Surgery*, 34(2):291–299, 2001.

- WADA, S. AND KARINO, T. Theoretical study on flow-dependent concentration polarization of low density lipoproteins at the luminal surface of a straight artery. *Biorheology*, 36(3):207–223, 1999.
- WANG, J. H.-C. AND THAMPATTY, B. P. An introductory review of cell mechanobiology. *Biomechanics and modeling in mechanobiology*, 5(1):1–16, 2006.
- WATTON, P. AND VENTIKOS, Y. Modelling evolution of saccular cerebral aneurysms. *The Journal of Strain Analysis for Engineering Design*, 44(5):375–389, 2009.
- WATTON, P. N., RABERGER, N. B., HOLZAPFEL, G. A., AND VENTIKOS, Y. Coupling the hemodynamic environment to the evolution of cerebral aneurysms: computational framework and numerical examples. *Journal of biomechanical engineering*, 131(10):101003, 2009a.
- WATTON, P. N., VENTIKOS, Y., AND HOLZAPFEL, G. A. Modelling the growth and stabilization of cerebral aneurysms. *Mathematical medicine and biology: a journal of the IMA*, 26(2):133–164, 2009b.
- WATTON, P. AND HILL, N. Evolving mechanical properties of a model of abdominal aortic aneurysm. *Biomechanics and modeling in mechanobiology*, 8(1):25–42, 2009.
- WATTON, P., HILL, N., AND HEIL, M. A mathematical model for the growth of the abdominal aortic aneurysm. *Biomechanics and modeling in mechanobiology*, 3(2):98–113, 2004.
- WATTON, P., SELIMOVIC, A., RABERGER, N., HUANG, P., HOLZAPFEL, G., AND VENTIKOS, Y. Modelling evolution and the evolving mechanical environment of saccular cerebral aneurysms. *Biomechanics and modeling in mechanobiology*, 10(1):109–132, 2011.
- WEISS, H. J., TURITTO, V. T., AND BAUMGARTNER, H. R. Role of shear rate and platelets in promoting fibrin formation on rabbit subendothelium. studies utilizing patients with quantitative and qualitative platelet defects. *Journal of Clinical Investigation*, 78(4):1072, 1986.
- WHEREAT, A. F. Oxygen consumption of normal and atherosclerotic intima. *Circulation research*, 9(3):571–575, 1961.
- WIEBERS, D. O., OF UNRUPTURED INTRACRANIAL ANEURYSMS INVESTIGATORS, I. S., ET AL. Unruptured intracranial aneurysms: natural history, clinical outcome, and risks of surgical and endovascular treatment. *The Lancet*, 362(9378):103–110, 2003.
- WILSON, J. S., VIRAG, L., DI ACHILLE, P., KARŠAJ, I., AND HUMPHREY, J. D. Biochemomechanics of intraluminal thrombus in abdominal aortic aneurysms. *Journal of biomechanical engineering*, 135(2):021011, 2013.
- WITZTUM, J. L. AND STEINBERG, D. Role of oxidized low density lipoprotein in atherogenesis. *Journal of Clinical Investigation*, 88(6):1785, 1991.
- WOLF, Y. G., THOMAS, W. S., BRENNAN, F. J., GOFF, W. G., SISE, M. J., AND BERNSTEIN, E. F. Computed tomography scanning findings associated with rapid expansion of abdominal aortic aneurysms. *Journal of vascular surgery*, 20(4):529–538, 1994.
- WONG, G. K., KWAN, M. C., NG, R. Y., SIMON, C., AND POON, W. Flow diverters for treatment of intracranial aneurysms: current status and ongoing clinical trials. *Journal of Clinical Neuroscience*, 18(6):737–740, 2011.
- XIANG, J., NATARAJAN, S. K., TREMMEL, M., MA, D., MOCCO, J., HOPKINS, L. N., SIDDIQUI, A. H., LEVY, E. I., AND MENG, H. Hemodynamic–morphologic discriminants for intracranial aneurysm rupture. *Stroke*, 42(1):144–152, 2011.
- ZENG, Z., KALLMES, D. F., DURKA, M. J., DING, Y., LEWIS, D., KADIRVEL, R., AND ROBERTSON, A. M. Sensitivity of cfd based hemodynamic results in rabbit aneurysm models to idealizations in surrounding vasculature. *Journal of biomechanical engineering*, 132(9):091009, 2010.
- ZHANG, J., SCHMIDT, J., RYSCHICH, E., SCHUMACHER, H., AND ALLENBERG, J. Increased apoptosis and decreased density of medial smooth muscle cells in human abdominal aortic aneurysms. *Chinese medical journal*, 116(10):1549–1552, 2003.



## RADIAL INFLATION OF A CYLINDRICAL MEMBRANE MODEL

---

Following the definition for the mechanical response in a thick-walled cylindrical model, here we provide a simplified geometry to show the characteristic of mechanical response of constituents in the artery under physiological loading. The artery is subjected to the internal pressure  $p$ , axial stretch  $\lambda_z$ . The governing equation of the radial inflation of an incompressible cylindrical membrane subject to a constant axial stretch of  $\lambda_z$  can be written as

$$p = \frac{H_j}{R_0 \lambda_z} \left( \frac{\partial w_j}{\partial E} \right) = \frac{H_j}{R_0 \lambda_z} \frac{\partial \lambda_\theta}{\partial E} \left( \frac{\partial w_j}{\partial \lambda_\theta} \right) = \frac{H_j}{R_0 \lambda_z \lambda_\theta} \left( \frac{\partial w_j}{\partial I_1} \frac{\partial I_1}{\partial \lambda_\theta} + \frac{\partial w_j}{\partial I_4} \frac{\partial I_4}{\partial \lambda_\theta} \right), j = \{M, A\} \quad (\text{A.1})$$

where  $w_j$  is the strain energy function and  $H_j$  is the wall thickness of each layer,  $j = \{M, A\}$  for media and adventitia;  $\lambda_\theta$  is the circumferential stretch with undeformed radius  $R_0$ ; radial stretch is implied by assuming incompressibility of the membrane. The Green-Lagrange strain  $E$  is related to the stretch  $\lambda_\theta$  as follows:  $E = \frac{(\lambda_\theta)^2 - 1}{2}$ . Deformation invariants  $I_1$  and  $I_4$  are associated with the stretches and pitches  $\alpha_j$  of collagen structure:

$$I_1 = \lambda_\theta^2 + \lambda_z^2 + \frac{1}{\lambda_\theta^2 \lambda_z^2}, \quad (\text{A.2})$$

$$I_4^j = \lambda_z^2 \sin^2 \alpha_j + \lambda_\theta^2 \cos^2 \alpha_j, \quad j = M, A \quad (\text{A.3})$$

The strain energy function follows the definition in section 2.3 characterised the distribution of elastin and collagen.

$$w^M = \frac{k_e^M}{2}(I_1 - 3) + \frac{k_1^M}{2k_2^M} \left\{ \exp \left[ k_2^M (I_4^M - 1)^2 \right] - 1 \right\}, \quad \text{in media} \quad (\text{A.4})$$

$$w^A = \frac{k_e^A}{2}(I_1 - 3) + \frac{k_1^A}{2k_2^A} \left\{ \exp \left[ k_2^A (I_4^A - 1)^2 \right] - 1 \right\}, \quad \text{in adventitia} \quad (\text{A.5})$$

Thus, we can obtain the equilibrium from (A.1) to determine the stretch  $\lambda_\theta$  corresponding to the pressure  $p$ :

$$p = \frac{1}{R_0 \lambda_z} \left\{ (H_M k_e^M + H_A k_e^A) \left( 1 - \frac{1}{\lambda_z^2 \lambda_\theta^4} \right) + \sum_{j=M,A} 2H_j k_1^j (I_4^j - 1) \exp \left[ k_2^j (I_4^j - 1)^2 \right] \cos^2 \alpha_j \right\} \quad (\text{A.6})$$

## DEFINE THE NUMBER OF NODES AND ELEMENTS

---

Here, we demonstrate how to arrange the order of nodes and elements in the artery mesh. First, we begin with the coordinate of reference configuration to have a sense of the geometry. In Figure B.1,  $\varphi'$  is the reference angle;  $\varphi$  is the opening angle, where  $\varphi + \varphi' = 2\pi$ . Given the curvature  $\kappa$  for the reference sector, the reference radius  $R$  at the middle plane of the vessel is equal to  $1/\kappa$ . The nodal position  $r_p$  inside the thickness of the vessel is from  $t_{ref}$  to 0 which it is defined from the outer layer to inner layer ( $t_{ref}$  is the wall thickness of the vessel). The coordinate of each point at the initial position is defined as below:

$$\begin{aligned} X &= \left[ \left( R - \frac{t_{ref}}{2} \right) + r_p \right] \cos(\theta) \\ Y &= \left[ \left( R - \frac{t_{ref}}{2} \right) + r_p \right] \sin(\theta) \end{aligned} \quad (B.1)$$

$$Z = 0 \sim L_{ref}$$

where  $L_{ref}$  is the axial length of the vessel;  $\theta$  is the angle for each node and the range is from  $\left(\pi - \frac{\varphi'}{2}\right)$  to  $\left(\pi + \frac{\varphi'}{2}\right)$ .

The number of nodes will be setting up by the order of the 3D mesh and the elements will be defined in terms of their grid location allows for easy correspondence between elements and nodes via local coordinate schemes. Next, we label

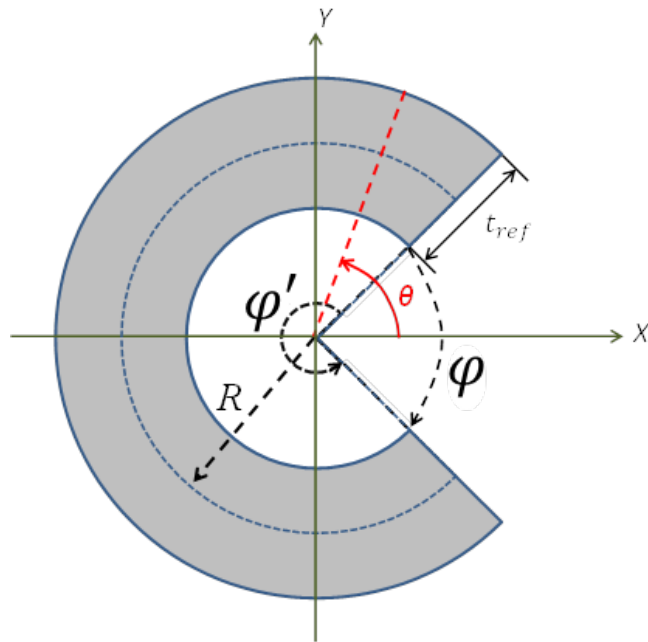


Figure B.1: Reference configuration with an opening angle  $\varphi$

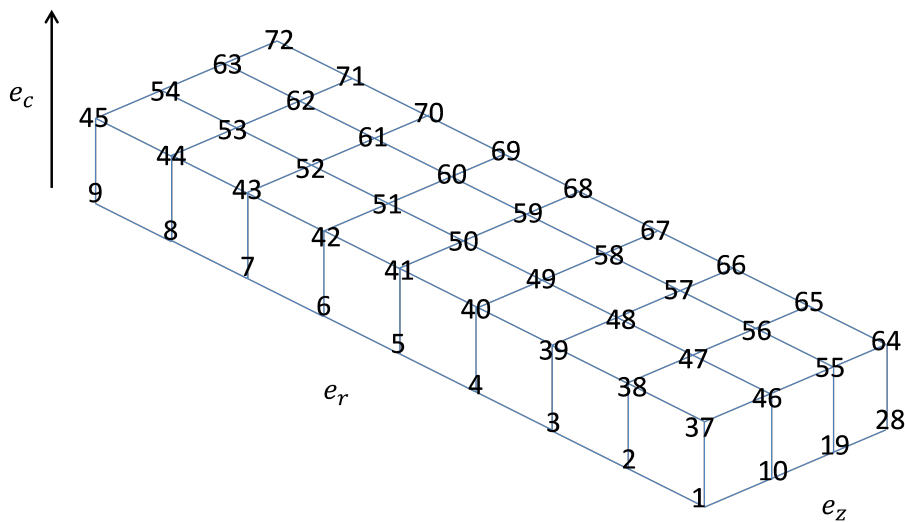


Figure B.2: Labelling of nodes of one layer in a 3-D domain with  $e_r = 8, e_z = 3$

the elements with mathematical expression. Given parameters  $e_r$ ,  $e_c$ ,  $e_z$  are the element numbers of radial, circumferential and axial directions, so the total number of elements of the vessel is  $e_r e_c e_z$ .

The number of element can be expressed as (B.2) based on the order of grid location.

$$\tilde{E}(m, n, s) = m + e_r(s - 1) + e_r e_z(n - 1) \quad (\text{B.2})$$

where  $m = 1 \sim e_r$ ;  $n = 1 \sim e_c$ ;  $s = 1 \sim e_z$ . The first node of element can be written as

$$\tilde{G}(1, \tilde{E}(m, n, s)) = \tilde{E}(m, n, s) + (s - 1) + (n - 1)(e_r + e_z + 1) \quad (\text{B.3})$$

For the rest of nodes of the element, they can be defined from the first node

$$\begin{aligned} \tilde{G}(2, \tilde{E}(m, n, s)) &= \tilde{G}(1, \tilde{E}(m, n, s)) + (e_r + 1) \\ \tilde{G}(3, \tilde{E}(m, n, s)) &= \tilde{G}(1, \tilde{E}(m, n, s)) + (e_r + 1) + (e_r + 1)(e_z + 1) \\ \tilde{G}(4, \tilde{E}(m, n, s)) &= \tilde{G}(1, \tilde{E}(m, n, s)) + (e_r + 1)(e_z + 1) \\ \tilde{G}(5, \tilde{E}(m, n, s)) &= \tilde{G}(1, \tilde{E}(m, n, s)) + 1 \\ \tilde{G}(6, \tilde{E}(m, n, s)) &= \tilde{G}(2, \tilde{E}(m, n, s)) + 1 \\ \tilde{G}(7, \tilde{E}(m, n, s)) &= \tilde{G}(3, \tilde{E}(m, n, s)) + 1 \\ \tilde{G}(8, \tilde{E}(m, n, s)) &= \tilde{G}(4, \tilde{E}(m, n, s)) + 1 \end{aligned} \quad (\text{B.4})$$

Expressions in (B.4) can be expanded as (B.5) in the form of element number.

$$\begin{aligned} \tilde{G}(1, \tilde{E}(m, n, s)) &= \tilde{E}(m, n, s) + (s - 1) + (n - 1)(e_r + e_z + 1) \\ \tilde{G}(2, \tilde{E}(m, n, s)) &= \tilde{E}(m, n, s) + (s + e_r) + (n - 1)(e_r + e_z + 1) \\ \tilde{G}(3, \tilde{E}(m, n, s)) &= \tilde{E}(m, n, s) + (s + e_r) + (n)(e_r + e_z + 1) + e_r e_z \\ \tilde{G}(4, \tilde{E}(m, n, s)) &= \tilde{E}(m, n, s) + (s - 1) + (n)(e_r + e_z + 1) + e_r e_z \end{aligned} \quad (\text{B.5})$$

Or a more detailed representation based on the number of the element along every direction. An illustrative example is shown in Figure B.2.

$$\begin{aligned} \tilde{G}(1, \tilde{E}(m, n, s)) &= m + (n - 1)(e_r + 1)(e_z + 1) + (s - 1)(e_r + 1) \\ \tilde{G}(2, \tilde{E}(m, n, s)) &= m + (n - 1)(e_r + 1)(e_z + 1) + (s)(e_r + 1) \\ \tilde{G}(3, \tilde{E}(m, n, s)) &= m + (n)(e_r + 1)(e_z + 1) + (s)(e_r + 1) \\ \tilde{G}(4, \tilde{E}(m, n, s)) &= m + (n)(e_r + 1)(e_z + 1) + (s - 1)(e_r + 1) \\ \tilde{G}(5, \tilde{E}(m, n, s)) &= \tilde{G}(1, \tilde{E}(m, n, s)) + 1 \\ \tilde{G}(6, \tilde{E}(m, n, s)) &= \tilde{G}(2, \tilde{E}(m, n, s)) + 1 \\ \tilde{G}(7, \tilde{E}(m, n, s)) &= \tilde{G}(3, \tilde{E}(m, n, s)) + 1 \\ \tilde{G}(8, \tilde{E}(m, n, s)) &= \tilde{G}(4, \tilde{E}(m, n, s)) + 1 \end{aligned} \quad (\text{B.6})$$

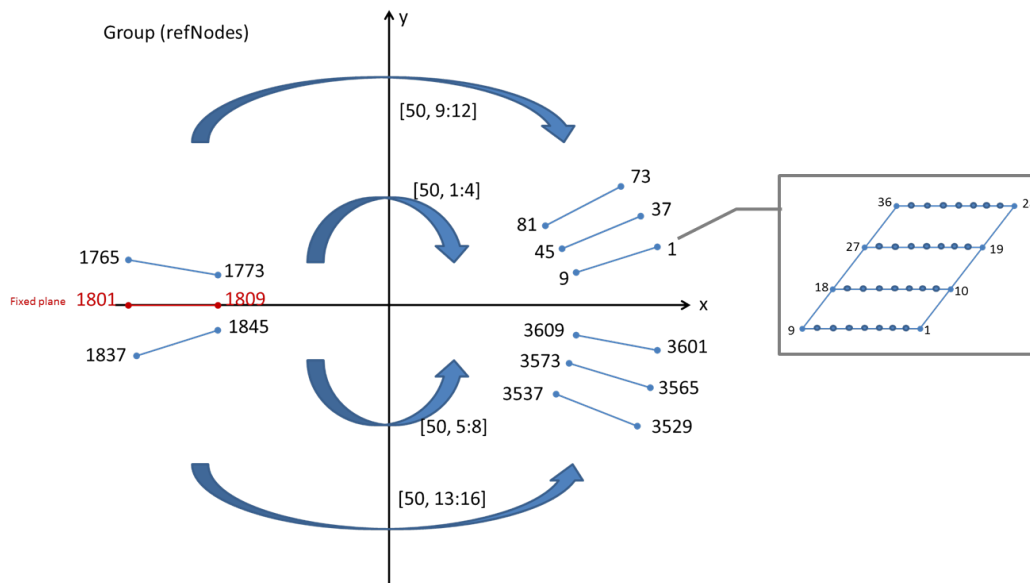


Figure B.3: Group the reference nodes (elR=8, elC=100, elZ=3)

**Groups of nodes:** Forming groups of nodes in order to apply displacements in an easier manner; implies a specific ordering of the nodes. Following the numbering of reference nodes, two groups of the inner circle and outer circle are assigned in order to move the nodes to form a closed circle. From the fixed plane on the left hand side (1801-1809) in Figure B.3, the nodes are moving group by group to the specific position to include residual stresses in the arterial wall. Two planes (1-9) and (3601-3609) shown in Figure B.3 will be converged to seal the interface.

Figure B.3 shows that how the MATLAB scripts number the inner and outer nodes with a given mesh: elR=8, elC=100, elZ=3. One longitudinal slice includes 36 nodes and with 4 nodes for each inner and outer side. There is a fixed plane at the left (1801-1809) and separates the upper and lower sector. In the matrix of reference nodes which is a 50x16 matrix, the first 8 columns are at the inner diameter, column 1 to 4 are at upper sector and column 5 to 8 are the at lower sector. For the outer diameter, column 9 to 12 are at upper sector and column 13 to 16 are at lower sector. Starting from the fixed plane, a group of nodes of the upper and lower sector (1765, 1773; 1837, 1845) moves towards the target position. Following the displacement of the first group, the next group (1729, 1737; 1873, 1881) then moves towards its target position. It takes 50 steps to close the opening cylindrical tube group by group, because there are 50 nodes along both upper and lower sectors. The last group is (1, 9; 3601, 3609) to seal the opening sector.



## MATHEMATICAL STABILITY OF THE G&R FRAMEWORK

---

Following the stress mediated G&R method presented in Chapter 4, this section demonstrates and compares different arterial G&R approaches in order to investigate whether the mechanical response of the aneurysm wall will stabilise or not to achieve a new homeostatic level. The focus is on remodelling the collagen parameter  $k_2$  by using a simple 1D single-layered model to show the influence of different G&R to the overall arterial response during aneurysm progression. The comparison of different G&R approaches lays on two parts: (1) the influence of  $k_2$  remodelled according to the total stress or the collagen fibre stress on the stress-mediated G&R; (2) the influence of different SEF forms on the mechanical response of aneurysm wall during G&R. Material parameters of this 1D arterial model follow the parameters of the media layer used in Chapter 4. The normalised mass density of elastin  $m_E$  is downgraded to 0.7 at the first time step to force the radius enlargement of the 1D model and initiate the G&R process.

In Chapter 4, the G&R method is mediated by the deviation of the total stress between its current and homeostatic levels. This is based on the approach proposed by Baek et al. (2006) that the collagen turnover rate appears to be modulated by the overall stress. However, the total stress includes the stress within the elastin and collagen which would continuously increase over the continuing enlargement of

arterial radius and thus it is not able to restore its homeostatic value. As a result, the value of  $k_2$  would keep decreasing and the mass density of collagen  $m_C$  would keep increasing without stabilisation due to the amplifying stress deviation through G&R. Therefore, instead of remodelling based on the total stress, the G&R approach tested here is based on the deviation of collagen fibre stress between current and homeostatic levels in order to exclude the effect of elastin stress. We recall the SEF terms presented in Chapter 4 that the mechanical responses of collagen fibres are associated with the  $k_2$  parameter. If  $k_2$  is downgraded, the collagen stress would be reduced to achieve the mechanical equilibrium. The advantage of the collagen fibre stress G&R is that it restores the homeostatic value of stress in collagen and deletes the influence of continuously increasing stress in elastin of the total stress mediated G&R, which assists the system to reach a new stabilised condition through the G&R.

Figure C.1 compares two different stress G&R approaches on the 1D model. The blue lines are remodelled based on the total stress, while the red lines are remodelled based on the collagen fibre stress. Results show that the circumferential stretch and collagen parameter  $k_2$  both stabilise under the G&R approach mediated by collagen fibre stress, while the stretch under the G&R mediated by total stress keeps increasing even that  $k_2$  is very close to zero. We then look into the mechanical stress response of the arterial model: for collagen fibre stress G&R, both the collagen stress and the total stress are stabilised towards the end of time such that the whole system reaches a balanced condition; however, for total stress G&R, both collagen stress and total stress are not stabilising, they either keep decreasing or increasing due to the significant increase of stress in elastin. Even though the stress in collagen is downgraded lower than the homeostatic level, the total stress deviation is still increasing, resulting in the unstabilising  $k_2$  remodelling. If the computational model is for modelling a stabilising aneurysm wall, the collagen stress G&R is apparently more suitable and reasonable for simulation purpose as the overall response goes to a new steady state. However, although the collagen fibre stress G&R reaches the stabilised state more efficiently, the expansion of stretch is very limited which is not able to model the stabilisation of larger aneurysms.

On the other hand, the main issue of the total stress G&R is that the total stress cannot be remodelled to the homeostatic value. The increasing deviation in total stress leads to the unstabilised state of  $k_2$  remodelling and mechanical responses. Therefore, if the total stress can be downgraded through the total stress G&R, the

1D model can potentially reach a new steady state. One way to balance the total stress is to reduce the collagen stress in each time step as the elastin stress keeps increasing during aneurysm enlargement. This can be achieved by modifying the SEF term for modelling the mechanical response of the arterial model.

We recall the SEF for arterial structure presented in Chapter 4 which follows the HGO SEF proposed by Holzapfel et al. (2000):

$$w = m_E \frac{k_e}{2} (I_1 - 3) + m_C \frac{k_1}{2k_2} \left\{ \exp \left[ k_2 (I_4 - 1)^2 \right] - 1 \right\} \quad (\text{C.1})$$

The elastin stress  $\sigma_E$  and the collagen fibre stress  $\sigma_C$  can be derived as the differential of the SEF against the circumferential stretch ( $\lambda$ ) of the simple 1D model:

$$\sigma_E = \lambda k_E \left( \lambda - \frac{1}{\lambda^3} \right) \quad (\text{C.2})$$

$$\sigma_C = \lambda \frac{k_1}{2k_2} \exp \left[ k_2 (\lambda^2 - 1)^2 \right] 2k_2 (\lambda^2 - 1) 2\lambda \quad (\text{C.3})$$

the two  $k_2$  parameters outside the exponential term of  $\sigma_C$  will cancel out each other.

For the G&R process,  $k_2$  is a time-dependent variable and keeps decreasing to downgrade the stress in collagen fibres to restore the stress balance. For the HGO SEF,  $k_2$  remodelling only influences the exponential term of the collagen fibre stress and right-shifting the stress-strain curve of the 1D model. In order to reduce the unstabilised increase of stress in the G&R mediated by the total stress, we accelerate and amplify the degrading process of the collagen fibre stress to investigate if the total stress can be downgraded in a sufficient way. A modified version of the HGO model keeps the initial parameters of the HGO model but takes into account the influence of the dynamic variable  $k_2$  outside the exponential term of the collagen stress:

$$w^* = m_E \frac{k_e}{2} (I_1 - 3) + m_C k_1^* \left\{ \exp \left[ k_2 (I_4 - 1)^2 \right] - 1 \right\} \quad (\text{C.4})$$

where

$$k_1^* = \frac{k_1}{2k_2(t=0)} \quad (\text{C.5})$$

and the collagen fibre stress can be represented as

$$\sigma_C^* = \lambda k_1^* \exp \left[ k_2 (\lambda^2 - 1)^2 \right] 2k_2 (\lambda^2 - 1) 2\lambda \quad (\text{C.6})$$

The updated  $k_1^*$  is associated with the original  $k_2$  value at  $t = 0$ , thus  $k_1^*$  is a constant value through G&R. Therefore,  $w = w^*$  and  $\sigma_C = \sigma_C^*$  only at  $t = 0$ , but would

have differentiation through the G&R with the  $k_2$  variable effect. We illustrate the comparison between the HGO SEF and the modified SEF under total stress G&R in Figure C.2. Result shows that with this modified approach, although the decrease of collagen stress drops faster than the HGO model, the total stress is still increasing significantly and not able to restore its homeostatic level. Thus the modified SEF fails on the purpose for downgrading the total stress due to greater circumferential enlargements for achieving the mechanical equilibrium in each time step. The circumferential stretch of the modified SEF is magnified almost twice the stretch of the HGO SEF to the end of time. Moreover, the enlargement of the 1D model is not stabilising and the G&R process is terminated when  $k_2 = 0$  which means zero stress in collagen fibres. This case may not be applied as the collagen fibres are assumed to compensate the loss of elastin and provide mechanical support to the aneurysm wall. However, this modified SEF shows a potential way to increase the size of aneurysm, as in Chapter 4 and 5 the enlargements of aneurysms are limited under the total stress G&R for HGO SEF.

Additionally, we compare the results of the two SEFs under collagen stress G&R in Figure C.3. Not surprisingly, the mechanical responses of the two SEFs are stabilised to the end of time, while the modified SEF stabilises slightly faster than the HGO SEF. The  $k_2$  variable effect assists the decrease of collagen stress in a more efficient way such that  $k_2$  of the modified SEF reaches a steady value which is higher than the steady  $k_2$  value of the HGO SEF at the end of the G&R. Although the radius expansion of the 1D model under collagen fibre stress G&R is still restricted, the modified SEF shows a potential approach to accelerate the stabilisation of the system without changing the growth parameters.

In order to understand how the decreases of  $k_2$  values affect the mechanical responses of the SEFs more specifically, Figure C.4 is generated to show the  $k_2$  influence on the stress and stretch curves compared with the two SEFs. The  $k_2$  values are downgraded gradually from 40 to 5 and the stress-stretch curves of both SEFs are right-shifted to allow further enlargement under the same loading condition. It can be observed that the modified SEF right-shifts the stress-strain curve more than the HGO SEF which could accelerate the G&R process to restore the homeostatic stress.

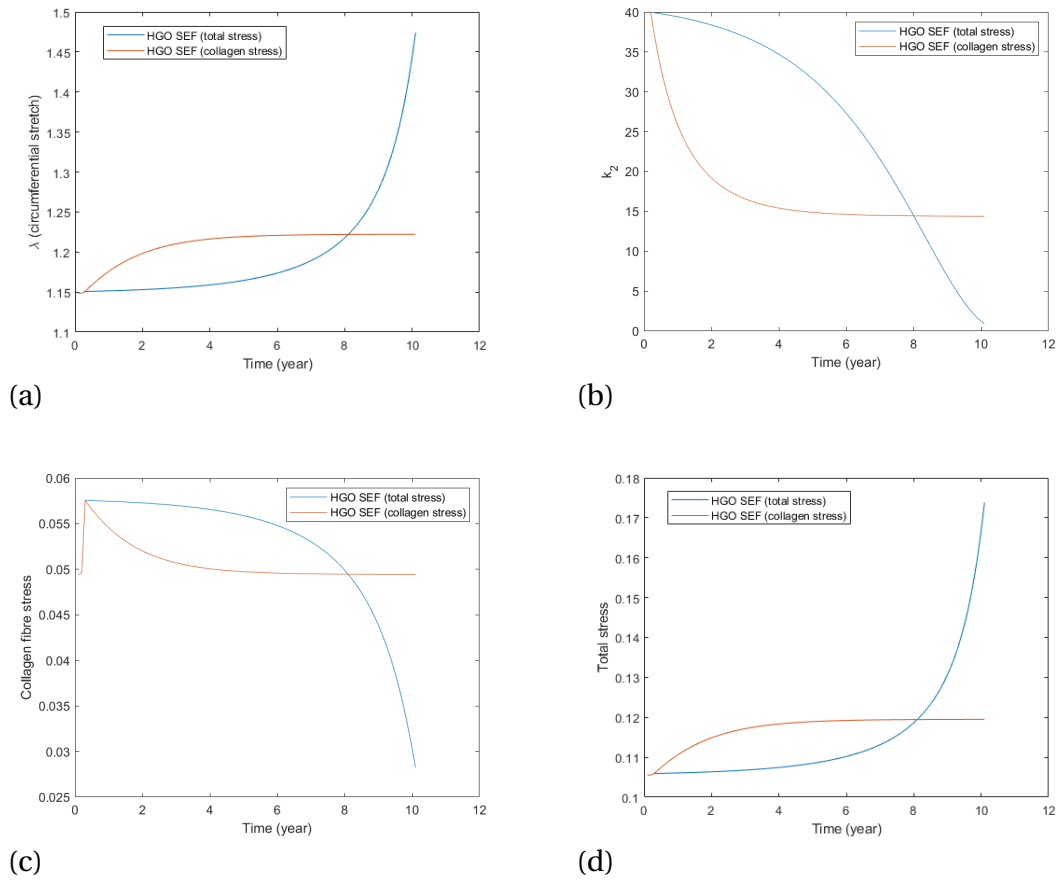


Figure C.1: Comparison of different stress-mediated G&R approaches: (a) circumferential stretches under different stress G&R: it shows that if remodelled based on the total stress, the tube model expands slowly at the beginning but stretches significantly over time without stabilisation; If remodelled based on the collagen stress, the stretch goes larger at the beginning compared to the total stress remodeling but stabilises towards the end of time. (b) collagen parameter  $k_2$  evolves through G&R: if remodelled based on the collagen stress,  $k_2$  is downgraded in an exponential curve to a stabilised value ( $\sim 15$ ) where the collagen stress is restored to its homeostatic level; If remodelled based on the total stress, the degradation of  $k_2$  increases over time, and when  $k_2$  is very close to zero the total stress deviation is still significant as shown in (d). (c) collagen fibre stress through the G&R: if remodelled based on the collagen stress, the collagen fibre stress is downgraded in an exponential curve towards the homeostatic collagen stress. If remodelled based on the total stress, the collagen stress remains at higher values at the beginning but drops rapidly at the half time period and goes even lower than the homeostatic total stress corresponding to the point of maximum stretch in (a). (d) total stress through the G&R: if remodelled based on the collagen stress, the total stress is also stabilised towards the end of time; however, if remodelled based on the total stress, the total stress is unstabilised and keeps increasing.

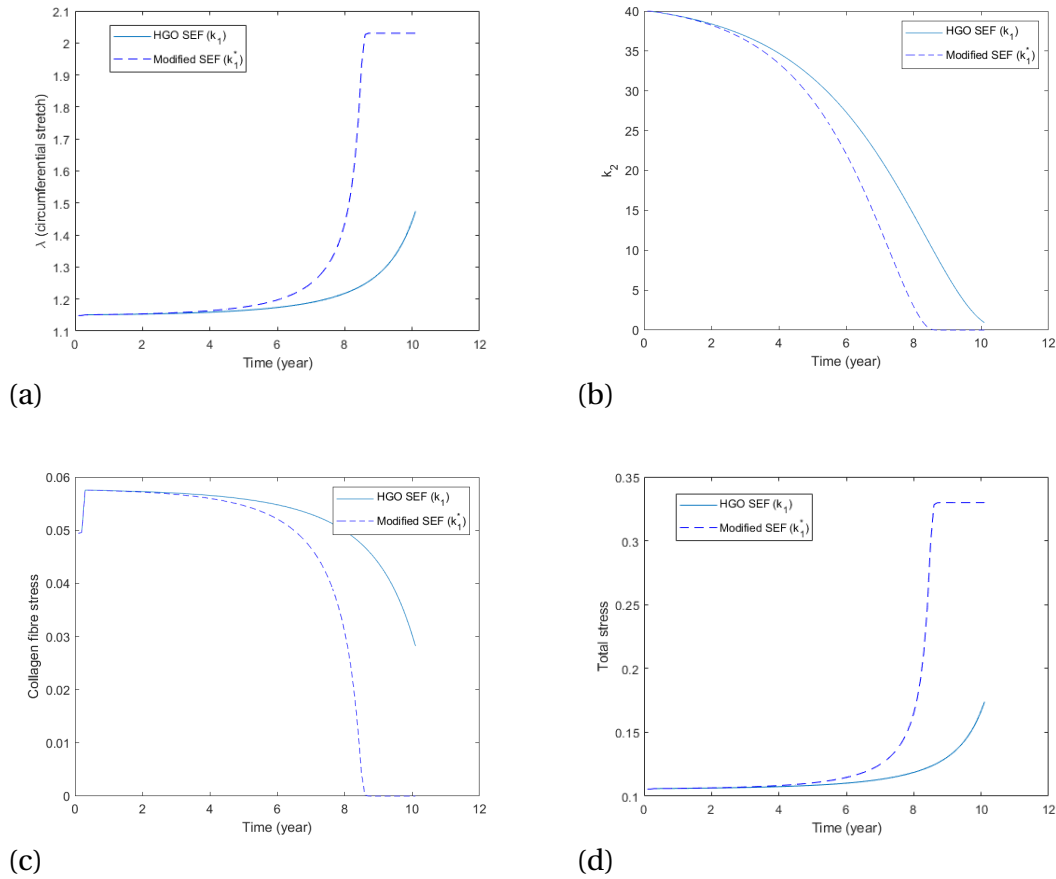


Figure C.2: Comparison of different SEFs on G&R (remodelled based on total stress): (a) circumferential stretches under different SEFs: the stretches of the two SEFs increase rapidly close to the end of time, while the modified SEF increases faster than the HGO SEF and stops enlarging at the point where  $k_2$  is remodelled to zero shown in (b). (b) collagen parameter  $k_2$  evolves through G&R: both  $k_2$  values of the two SEFs are downgraded rapidly towards the end of time, while the  $k_2$  of the modified SEF is remodelled to zero around 8th year so that the G&R is terminated at that time point. (c) collagen fibre stress through the G&R: the collagen stresses of the two SEFs are downgraded rapidly to even lower than the homeostatic value due to the amplifying deviation in total stress, while the collagen stress of the modified SEF is reduced faster and remodelled to zero corresponding to  $k_2 = 0$  in (b). (d) total stress through the G&R: both total stresses in two different SEFs increase continuously without stabilisation towards the end of time. The total stress of the modified SEF increases to a higher level than the HGO SEF through the G&R, while this trend is identical to the enlargement of circumferential stretch shown in (a).

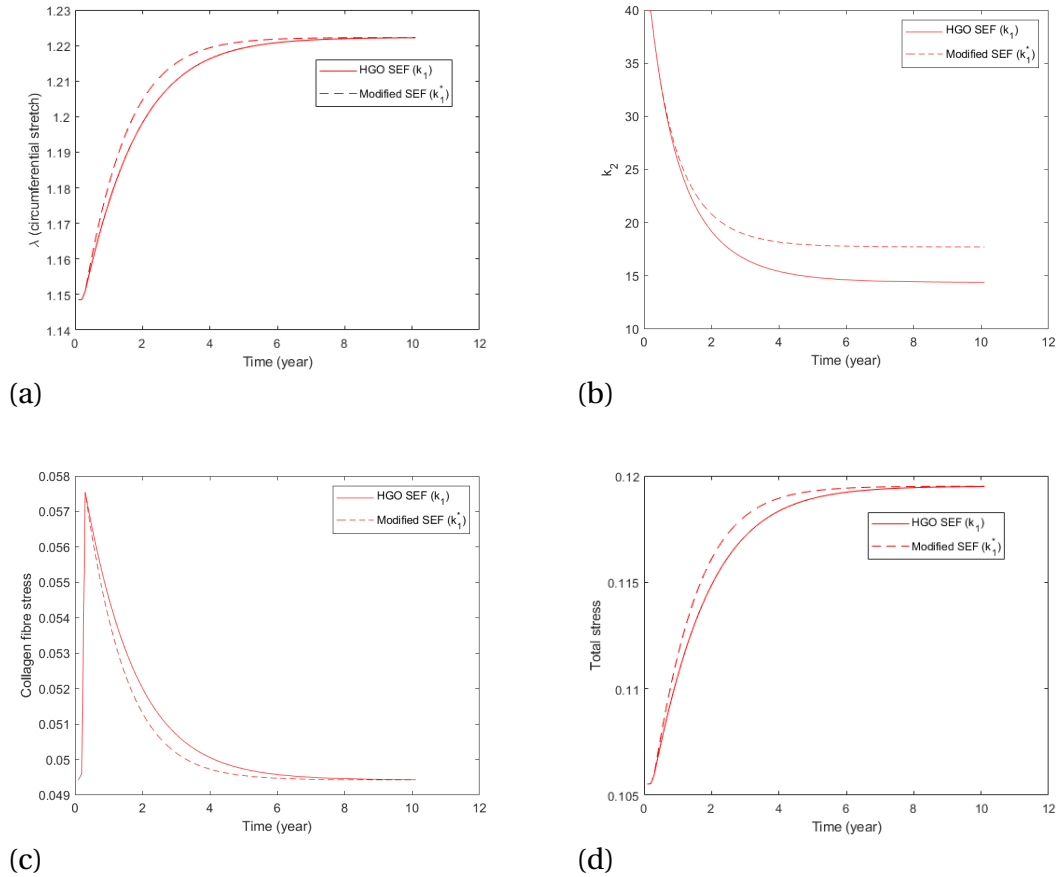


Figure C.3: Comparison of different SEFs on G&R (remodelled based on collagen fibre stress): (a) circumferential stretches under different SEFs: the stretch of the modified SEF increases faster than the stretch of the HGO SEF, while both are stabilised close to  $\lambda = 1.22$ . (b) collagen parameter  $k_2$  evolves through G&R: both  $k_2$  values of the modified and HGO SEFs are downgraded rapidly at the beginning of the G&R process and stabilised towards the end of time, while the  $k_2$  of the modified SEF stabilises to a constant value which is slightly greater than the stabilised  $k_2$  value of HGO. (c) collagen fibre stress through the G&R: both collagen stresses in two different SEFs restore the homeostatic stress through the G&R process, while the collagen fibre stress of the modified SEF returns to its homeostatic value faster than the HGO SEF. (d) total stress through the G&R: both total stresses in two different SEFs increase continuously and stabilise towards the end of time. The total stress of the modified SEF is slightly greater than the HGO SEF through the G&R, while this trend can also be seen in the circumferential stretch shown in (a).

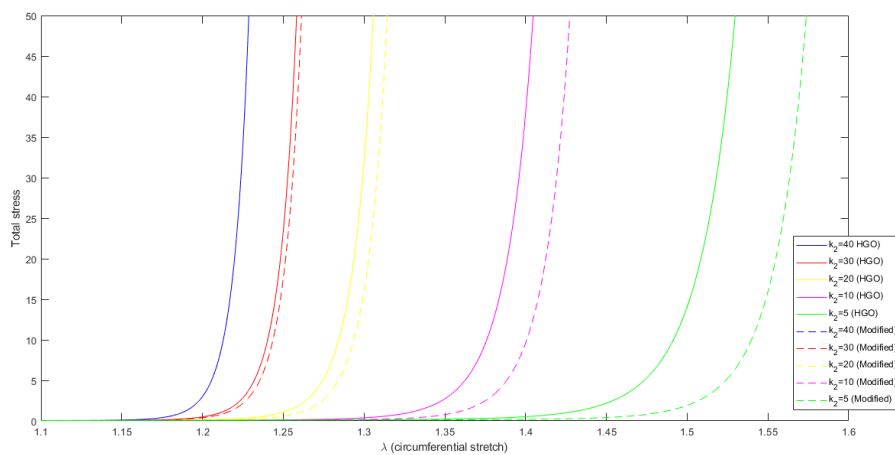


Figure C.4: Stress against stretch curves of the two different SEF forms right-shift with decreased  $k_2$  values: these curves indicate that the modified SEF bears less loads under the same stretch compared to the HGO SEF, while the modified SEF has larger deformations under the same stress. The modified SEF allows greater enlargement of the wall under the same mechanical loads which has the potential to solve the issue of small enlargements shown in Chapter 5. On the other hand, the modified SEF right-shifts the stress-strain curve to a larger degree than the HGO SEF which could accelerate the G&R process to restore the homeostatic stress. In addition, with lower value of  $k_2$ , the difference between the HGO and modified SEFs increases.



## MODELLING CODES AND SCRIPTS

---

This appendix shows the main scripts to run the demonstrated FSGT computational framework in this thesis. These modelling codes can be modified to simulate different aneurysm geometries and investigate various G&R hypotheses.

Listing D.1: FSGT (central command script)

```
#!/usr/bin/perl
use strict;
use warnings;
use File::Copy; # The File::Copy module exports two functions, copy and move
use File::Find; # The File::Find module exports to find the file
use File::Copy qw(move);
#Initialise variables...(if variables are not set to their types/defined
    »something funny happens in the while loop)
my $nfiles = 0;
my $FSGTtype = 1;
my $pulsatile = 0;
open(MYDATA, "./controlparameters.dat") or
die("Error: cannot open file 'controlparameters.dat'\n");
my $theline;
my $number = 0;
while( $theline = <MYDATA> )
{
```

```

$number++;
$files = &strip_comment($theline)  if ($number==1);
$FSGTtype = &strip_comment($theline)  if ($number==2);
$spulsatile = &strip_comment($theline)  if ($number==3);
}
close MYDATA;
#-----print the simulation information-----
my $step = $files;
print "Run for $step steps.";
print "\n";
print "\n";
if ($FSGTtype==0)
{print "Batch Simulation = Solid Only\n";}
if ($FSGTtype==1)
{print "Batch Simulation = FSG\n";}
if ($FSGTtype==2)
{print "Batch Simulation = FSGT\n";}
print "\n";
print "\n";
#####
#                Solid Simulation                #
#####
#-----copy source to solid documents-----
chdir "./solid";
find(\&wanted, "../source_solid");
#-----copy all .m files and .inp files into the target file-----
sub wanted{
if (-f $File::Find::name){
if ($File::Find::name =~ /\..m$/){
copy("$File::Find::name","../solid")||warn "could not copy files :$!";
}
if ($File::Find::name =~ /\..inp$/){
copy("$File::Find::name","../solid")||warn "could not copy files :$!";
}
}
# unlink $File::Find::name ;
}
}

#--- Run ansys to get the mesh centroid information
print "Ansys mesh generating and output the 'centroid' information files \n";
print "\n";
print "\n";

```

```

# output the 'element_centroid.dat' file
print "Run ANSYS to get the mesh information. \n";
print "\n";
print "\n";
system("ansys150 -b -i run_mesh.inp -o ansys.out");
sleep 10;
#-----deal with the element_centroid.dat---transform to tecplot format
»-----
print "generating the tecplot_format centroid coordinates\n";
print "\n";
print "\n";
# input 'element_centroid.dat' file
# output 'centroid_tecplot.dat' file
copy("../curvature/centroid_tecplot_format.m", "../solid") || warn "could not
    »copy files :$!" ;
system('matlab -nosplash -nodesktop -minimize -logfile matlablog.log -nojvm
    »-wait -r centroid_tecplot_format');
sleep 10;

#-----interpolate the principal curvature direction to centroids-----

print "interpolate the principal curvature direction to centroid\n";
print "\n";
print "\n";

# input 'centroid_tecplot.dat' 'firstPrincipalCurvatureVector.dat' '
    »secondPrincipalCurvatureVector.dat'
# output 'centroid_first_curvature_vector.dat' '
    »centroid_second_curvature_vector.dat'
copy("../curvature/firstPrincipalCurvatureVector.dat", "../solid") || warn "could
    » not copy files :$!" ;
copy("../curvature/secondPrincipalCurvatureVector.dat", "../solid") || warn "
    »could not copy files :$!" ;
copy("../curvature/curvature_vector_interplation.mcr", "../solid") || warn "could
    » not copy files :$!" ;
system ( "tecplot -b -p curvature_vector_interplation.mcr");

#-----normlize the vector to unit vector-----
print "normalize the principal curvature direction on centroid\n";
print "\n";
print "\n";
# input 'centroid_first_curvature_vector.dat' '
    »centroid_second_curvature_vector.dat'

```

```

# output 'normalized centroid_first_curvature_vector_temp.dat' 'normalized
  »centroid_second_curvature_vector_temp.dat'
system('matlab -nosplash -nodesktop -minimize -logfile matlablog.log -nojvm
  »-wait -r normlize_centriod_prinCurvaDir');
sleep 10;

#####
#                               Start loop                               #
#####
#----- define the loop for different time step-----
for my $i (1 ..$step) {
print "Run for number $i step. \n";
print "\n";
print "\n";
my $step_file = $i;
my $file1 = 'step_file.txt';
open(my $f1, ">", $file1) or die; # > in writing style
print $f1 "$step_file" ;
close($f1);
#---- Matlab to generate input file for ANSYS-----
#----deal with the different state of the value of K2 and C----
print "produce the changed k,c values file\n";
print "\n";
print "\n";
copy("../controlparameters.dat", "../solid") || warn "could not copy files :$!" ;
if ($FSGTtype==0)
{print "Batch Simulation = Solid Only\n";
system ("matlab -nosplash -nodesktop -minimize -logfile matlablog.log -nojvm
  » -wait -r growth");
sleep 10;}
else{
if ($pulsatile ==1)
# input 'element_centroid.dat' 'centroid_cfd_pulsatile.dat' 'cauchy_stress1/2.
  »dat'
# output 'c_k_value.dat'
{system ("matlab -nosplash -nodesktop -minimize -logfile matlablog.log -nojvm
  » -wait -r growth");
sleep 10;}
else
# input 'element_centroid.dat' 'centroid_WSS_WSSG.dat' 'cauchy_stress1/2.dat'
# output 'c_k_value.dat'
{system ("matlab -nosplash -nodesktop -minimize -logfile matlablog.log -nojvm
  » -wait -r growth");}

```

```

sleep 10;}}

print "produce the matHGO.inp\n";
print "\n";
print "\n";
# input 'normalizeCentiod_first_prinCurvaDir_temp.dat' 'element_centroid.dat'
# input 'normalizeCentiod_second_prinCurvaDir_temp.dat' 'c_k_value.dat'
# output 'matHGO.inp'

system ('matlab -nosplash -nodesktop -minimize -logfile matlablog.log -nojvm
  »-wait -r write_HGO');
sleep 10;

#matHGO.inp ---record the k2,c value of each element
my $matHGO='./matHGO.inp';
my $matHGOTemp='./matHGO'. $step_file.'.inp';
rename($matHGO,$matHGOTemp)
or warn "Rename $matHGO to $matHGOTemp failed: $!\n";
# rename the c k value
my $ck='./c_k_value.dat';
my $ck_update='./c_k_value'. $step_file.'.dat';
rename($ck, $ck_update)
or warn "Rename $ck to $ck_update failed: $!\n";
#---run ANSYS to do the structural analysis with time-difference material
print "step $i begin\n";
print "\n";

#--- Matlab to generate input file for ANSYS-----
print "generating input file for ansys output deformed geometry\n";
print "\n";
system ('matlab -nojvm -r output_deformed');
sleep 10;
#---output the run file-----
print "Run matlab to write the run file. \n";
print "\n";
print "\n";
# input 'run1.inp'
# output 'run(n).inp'
system ('matlab -nojvm -r write_run_file');
sleep 10;
my $file3= 'run'. $step_file.'.inp';
unlink ('run.inp');
rename($file3, 'run.inp')

```

```

or warn "Rename $file3 to run.inp failed: $!\n";

#-----go on the remodelling-----

# input 'run.inp' 'output_deformed.inp'
# output 'nlist(n).txt' 'deformcoordiner(n),txt' 'strain_element(n).dat'
print "Run ANSYS to do the structural analysis and output the stress and
      »deformation. \n";
print "\n";
system("ansys150 -b -i run.inp -o ansys.out");
my $db_file = 'structural_model'.'$step_file'.'.db';
while (1) {
last if -e $db_file;
}

#-----change the output stress file format, extract the element number and
      » SI stress-----
my $strain_element='./strain_element'.'$step_file'.'.dat';
my $strain_element_temp='./strain_element.dat';
unlink("$strain_element");
rename("$strain_element","$strain_element_temp")
or warn "Rename $strain_element to $strain_element_temp failed: $!\n";

print "Run matlab to extract the average strain on each element. \n";
print "\n";
# input 'strain_element.dat'
# output 'element_averageStrain_Matix.dat'
system('matlab -nosplash -nodesktop -minimize -logfile matlablog.log -nojvm
      »-wait -r modify_standard_element_strain');
sleep 10;

my $element_averagestrain_file = 'element_averageStrain_Matix.dat';
while (1) {
last if -e $element_averagestrain_file;
}

#-----on the basis of different step to deal with the stress file and output
      » the averageStress of each element-----
print "Run matlab to calculate the cauchy stress for each collagen fiber
      »families. \n";
print "\n";
# input 'element_averageStrain_Matix.dat'
# output 'stretch_cauchy_stress.dat'

```

```

system( 'matlab -nosplash -nodesktop -minimize -logfile matlablog.log -nojvm
  »-wait -r I4_cauchystress_calculation' );
sleep 10;

#-----on the basis of different step to deal with the strain file and output
  » the averageStrain of each element-----
if( $step_file==1){
my $stretch_cauchy_stress='stretch_cauchy_stress.dat';
my $stretch_cauchy_stress_temp='stretch_cauchy_stress1.dat';
rename($stretch_cauchy_stress,$stretch_cauchy_stress_temp)
or warn "Rename $stretch_cauchy_stress to $stretch_cauchy_stress_temp failed:
  »$!\n";
}
if( $step_file==2){
my $stretch_cauchy_stress='stretch_cauchy_stress.dat';
my $stretch_cauchy_stress_temp='stretch_cauchy_stress2.dat';
rename($stretch_cauchy_stress,$stretch_cauchy_stress_temp)
or warn "Rename $stretch_cauchy_stress to $stretch_cauchy_stress_temp failed:
  »$!\n";
}
if( $step_file >2){
my $stretch_cauchy_stress='stretch_cauchy_stress.dat';
my $stretch_cauchy_stress_temp='stretch_cauchy_stress2.dat';
unlink( "$stretch_cauchy_stress_temp");
sleep 5;
rename($stretch_cauchy_stress,$stretch_cauchy_stress_temp)
or warn "Rename $stretch_cauchy_stress to $stretch_cauchy_stress_temp failed:
  »$!\n";
}

#-----rename element_averageStrain_Matix(n) file-----
my $element_averageStrain_Matix='element_averageStrain_Matix.dat';
my $element_averageStrain_Matix_temp='element_averageStrain_Matix'. $step_file.
  »'.dat';
rename($element_averageStrain_Matix,$element_averageStrain_Matix_temp)
or warn "Rename $element_averageStrain_Matix to
  »$element_averageStrain_Matix_temp failed: $!\n";

#-----plot c k1 k2 distribution on solid model
# input 'mesh_connectivity.dat' 'deformcoordiner_full.dat' 'step_file.txt'
  »'c_k_value(i).dat'
# output 'centroid_c_k.dat' 'deformed_element.dat'

```

```

copy("../source_solid/mesh_connectivity.dat", "../solid") || warn "could not copy
  » files :$!" ;
system('matlab -nosplash -nodesktop -minimize -logfile matlablog.log -nojvm
  »-wait -r element_c_k');
sleep 10;
# input 'centroid_c_k.dat' 'deformed_element'
# output 'solid_c_k.dat'
copy("../source_solid/c_k_interpolation.mcr", "../solid") || warn "could not copy
  » files :$!" ;
system ("tecplot -b -p c_k_interpolation.mcr");
# rename the c k value
my $solid_c_k='../solid_c_k.dat';
my $solid_c_k_update='../solid_c_k'.$step_file.'.dat';
rename($solid_c_k, $solid_c_k_update)
or warn "Rename $solid_c_k to $solid_c_k_update failed: $!\n";
#----- run matlab to produce deformed geometry coordinates
  »-----
print "Run matlab to produce deformed geometry coordinates. \n";
print "\n";
system('matlab -nosplash -nodesktop -minimize -logfile matlablog.log -nojvm
  »-wait -r build_new_stl');
sleep 10;

#####
#                               fluid simulation                               #
#####
#----- output the deformed aneurysm innersurface stl file
  »-----

if ($FSGTtype>0)
{
if ($step_file==1||($step_file-1)%5 == 0)
{ print "Run matlab to produce py file. \n";
print "\n";
system('matlab -nosplash -nodesktop -minimize -logfile matlablog.log -nojvm
  »-wait -r write_stl_py_file_local');
print "\n" ;
print "generate STL file\n";
print "\n" ;
my $file5 = 'geomagic_stl'.$step_file.'.py'
or die "Can't find the file!";
unlink('stl.py');
rename($file5, 'stl.py');
system('Studio stl.py');

```

```

}
}

my $file6= 'file.rst'
or die "Can't find the file!";
my $file7= 'structural_model'.$step_file.'.rst'
or die "Can't find the file!";
rename($file6,$file7);

if($step_file==1){
my $file4= 'run.inp';
sleep 3;
rename($file4,'run1.inp')
or warn "Rename $file4 to run1.inp failed: $!\n";
}
print "\n";
#----- Execute fluid perl script-----
if ($step_file==1||($step_file-1)%20 == 0)
{
    if ($FSGTtype==1)
    {chdir "..";
system ("perl fluid.pl");
chdir "./fluid";
my $base_path = 'AR_tec'.$step_file.'.dat';
while (1) {
last if -e $base_path;
sleep 10;}
chdir "../solid";}
if ($FSGTtype==2)
{
chdir "..";
system ("perl fluid.pl");
system ("perl transport.pl");
chdir "./solid";}
}
}

#####
#                               End of Loop                               #
#####

sub strip_comment
{
# /* Get The Parameter Passed To The Function */
$theline = shift;

```

```

# /* Search For The First Occurance Of ! */
my $where = index($theline , "!");

# /* If We Find No Comment, Return The Entire Line Passed To us */
if ($where eq -1) {
return $theline;
}

# /* Get The Part Of The String Up To, And Including The Colon */
my $goodpart = substr($theline , 0, $where);

# /* Remove The Colon */
chop($goodpart);

# /* Return Only The Portion Of The String Before The Colon */
return $goodpart;
}

```

Listing D.2: Thrombus formation

```

%Morphing Aneurysm
%Coordinates of Sphere of influence for morphing
xmorph=-3.8;
ymorph= 2.5;
zmorph= 3.5;
%Radius of Sphere of Influence
rmorph=3.5;
%Max distance to morph
dmorph = 1.5;
%Min distance to morph
dmorph_min = 0.2;
%Polynomial exponet for morphing
polyexp = 1;
%Wall thickness
wthick = 0.4;
%Potential for variable wall thickness – wall to aneurysm
%NB Max morphing distance occurs at points at centre of sphere of influence
%Points on radius of sphere of influence don't move
%Points outside sphere of influence Fixed

```

```

load ( 'points.dat' )
load ( 'connect.dat' )

lp=length(points);
lc=length(connect);

count=0;
for i=1:lp
for j=1:3
count=count+1;
x(count) = points(i,3*(j-1)+1);
y(count) = points(i,3*(j-1)+2);
z(count) = points(i,3*(j-1)+3);
end
end

v(:,1) = x;
v(:,2) = y;
v(:,3) = z;
lx=length(x);

c(:,1) = connect(:,2)+1;
c(:,2) = connect(:,3)+1;
c(:,3) = connect(:,4)+1;

col = z';

% Find all edges in mesh, note internal edges are repeated
E = sort ([c(:,1) c(:,2); c(:,2) c(:,3); c(:,3) c(:,1)]')');
% determine uniqueness of edges
[u,m,n] = unique(E, 'rows');
% determine counts for each unique edge
counts = accumarray(n(:), 1);
% extract edges that only occurred once
O = u(counts==1,:);
%plot3 ([v(O(:,1),1) v(O(:,2),1)]', [v(O(:,1),2) v(O(:,2),2)]', [v(O(:,1),3) v(O(
    »(:,2),3)]', '- ')

%CREATE THE EXTRA CONNECTIVITY MATRIX
lengthO=length(O);
for i=1:lengthO
tria=O(i,1);
trib=O(i,2);

```

```

tric=O(i,1)+lx;
trid=O(i,2)+lx;
%Triangles connectivity abc, acd
Endcon(2*i-1,1)=3;
Endcon(2*i-1,2)=tria-1;
Endcon(2*i-1,3)=trib-1;
Endcon(2*i-1,4)=trid-1;
Endcon(2*i,1)=3;
Endcon(2*i,2)=tria-1;
Endcon(2*i,3)=tric-1;
Endcon(2*i,4)=trid-1;
end

lpmat = lx*linspace(1,1,lc)';
connect2(:,1) = connect(:,1);
connect2(:,2) = connect(:,2)+lpmat;
connect2(:,3) = connect(:,3)+lpmat;
connect2(:,4) = connect(:,4)+lpmat;

connect3=[connect;connect2;Endcon];

%Calculation of unit normals
%Unit normals for elements
for i=1:lc
%Create two vectors in each element (consistent on orientation)
vec1(1)= x(c(i,3))-x(c(i,2));
vec1(2)= y(c(i,3))-y(c(i,2));
vec1(3)= z(c(i,3))-z(c(i,2));

vec2(1)= x(c(i,1))-x(c(i,2));
vec2(2)= y(c(i,1))-y(c(i,2));
vec2(3)= z(c(i,1))-z(c(i,2));

%compute the cross product
crossvec = cross(vec1,vec2);
normcrossvec = (crossvec(:,1)^2+crossvec(:,2)^2+crossvec(:,2)^2)^0.5;
scrossvec = crossvec/normcrossvec;
normvec(i,:) = scrossvec;
end

%UNIT normals for vertices
for i=1:lx
store=[];

```

```
for j=1:lc
if c(j,1) == i
store(end+1) = j;
end
if c(j,2) == i
store(end+1) = j;
end
if c(j,3) == i
store(end+1) = j;
end
end
lstore=length(store);
vertvex(i,1)= 0;
vertvex(i,2)= 0;
vertvex(i,3)= 0;
for k=1:lstore
for s=1:3
vertvex(i,s) = vertvex(i,s)+normvec(store(k),s);
end
end
avertvex(i,:)=vertvex(i,:)/lstore;
end

%Associate a unit vector with each vertice
%Case 1 – Morph in z direction
if option ==1
for i =1:lx
vecmorph(i,1) = 0;
vecmorph(i,2) = 0;
vecmorph(i,3) = 1;
end
else
%Case 2 – Morph in normal direction
for i=1:lx
mag = (avertvex(i,1)^2+avertvex(i,2)^2+avertvex(i,3)^2)^0.5;
vecmorph(i,:) = avertvex(i,:)/mag;
end
end

%Calculate distance of all points from centre of Sphere of Influence
for i = 1:lx
dist(i) = (((x(i)-xmorph)^2)+ ((y(i)-ymorph)^2) + ((z(i)-zmorph)^2))^0.5;
end
```

```

%Morph Points by element number
%Loop through elements
%calculate the
%Morph Points
%Condition if points within sphere of influence they can be moved
thrombuspoints = [];
for i=1:lx
    if (dist(i)<rmorph & z(i)>0 )
        thrombuspoints(end+1)=i;
        local_dist = (rmorph-dist(i))/rmorph;
        local_dist_fn = local_dist^1.5;
        local_dist_ang = local_dist_fn*pi/2; %angle 0 to pi/2
        %           move = dmorph_min+(dmorph-dmorph_min)*((rmorph-dist(i))/rmorph)^
            »polyexp;
        move = dmorph_min+(dmorph-dmorph_min)*sin(local_dist_ang);

        %           if (move>dmorph*0.75)
        %           move = dmorph*0.75
        %           end

mv(i,1) = v(i,1)-move*vecmorph(i,1);
mv(i,2) = v(i,2)-move*vecmorph(i,2);
mv(i,3) = v(i,3)-move*vecmorph(i,3);
    else
        move = dmorph_min;
        mv(i,1) = v(i,1)-move*vecmorph(i,1);
        mv(i,2) = v(i,2)-move*vecmorph(i,2);
        mv(i,3) = v(i,3)-move*vecmorph(i,3);
    end
end

%Create the external surface from initial surface
for i=1:lx
    exv(i,1) = v(i,1)+wthick*vecmorph(i,1);
    exv(i,2) = v(i,2)+wthick*vecmorph(i,2);
    exv(i,3) = v(i,3)+wthick*vecmorph(i,3);
end

figure
%inner wall layer
patch_handle1 = patch('Faces',c,'Vertices',v,'EdgeColor','none','Edgealpha'
    » ,1,'FaceColor','red','FaceAlpha',.25,'facelighting','phong')

```

```

hold on
%thrombus/EC inner layer
patch_handle2 = patch('Faces',c,'Vertices',mv,'EdgeColor','none','Edgealpha'
    » ,1,'FaceColor','red','FaceAlpha',.5,'facelighting','phong')
hold on
%outer wall
patch_handle3 = patch('Faces',c,'Vertices',exv,'EdgeColor','none','Edgealpha'
    » ,1,'FaceColor','red','FaceAlpha',.1,'facelighting','phong')
daspect([1 1 1]);
set(patch_handle1,'AmbientStrength',0.8,'DiffuseStrength',0.5,'
    »SpecularStrength',0.75);
set(patch_handle2,'AmbientStrength',0.8,'DiffuseStrength',0.5,'
    »SpecularStrength',0.5);
set(patch_handle3,'AmbientStrength',0.8,'DiffuseStrength',0.5,'
    »SpecularStrength',0.5);
light('Position',[1 1 1]);
view(45,45);
axis equal

figure
%thrombus/EC inner layer
patch_handle4 = patch('Faces',c,'Vertices',mv,'EdgeColor','none','Edgealpha'
    » ,1,'FaceColor','red','FaceAlpha',.5,'facelighting','phong')
hold on
set(patch_handle4,'AmbientStrength',0.8,'DiffuseStrength',0.5,'
    »SpecularStrength',0.5);
light('Position',[1 1 1]);
view(45,45);
axis equal

%Write out as a vtk file
%reshape matrix
%Outer
for i=1:lp
    startline1=3*i;
    ox(i,1)= exv(startline1-2,1);
    ox(i,2)= exv(startline1-2,2);
    ox(i,3)= exv(startline1-2,3);
    ox(i,4)= exv(startline1-1,1);
    ox(i,5)= exv(startline1-1,2);
    ox(i,6)= exv(startline1-1,3);
    ox(i,7)= exv(startline1,1);
    ox(i,8)= exv(startline1,2);

```

```

ox(i,9)= exv(startline1,3);
end
wox=ox';

%thrombus
for i=1:lp
startline1=3*i;
ux(i,1)= mv(startline1-2,1);
ux(i,2)= mv(startline1-2,2);
ux(i,3)= mv(startline1-2,3);
ux(i,4)= mv(startline1-1,1);
ux(i,5)= mv(startline1-1,2);
ux(i,6)= mv(startline1-1,3);
ux(i,7)= mv(startline1,1);
ux(i,8)= mv(startline1,2);
ux(i,9)= mv(startline1,3);
end
wux=ux';
wconnect=connect';

% open a file for writing
fid = fopen('innerwall.vtk', 'w');
% print a header line
fprintf(fid, '# vtk DataFile Version 3.0\n');
fprintf(fid, 'vtk output\n');
fprintf(fid, 'ASCII\n');
fprintf(fid, 'DATASET POLYDATA\n');
fprintf(fid, 'POINTS %i float\n',lx);
% two values appear on each row of the file
fprintf(fid, '%f %f %f %f %f %f %f %f %f\n', wux);
fprintf(fid, '\n');
fprintf(fid, 'POLYGONS %i %i\n', lc, 4*lc);
fprintf(fid, '%i %i %i %i\n', wconnect);
fprintf(fid, '\n');
fprintf(fid, 'CELL_DATA %i\n',lc);
fprintf(fid, 'POINT_DATA %i\n',lx);
fclose(fid);

% open a file for writing
osurf = fopen('outerwall.vtk', 'w');
% print a header line
fprintf(osurf, '# vtk DataFile Version 3.0\n');
fprintf(osurf, 'vtk output\n');

```

```

fprintf(osurf, 'ASCII\n');
fprintf(osurf, 'DATASET POLYDATA\n');
fprintf(osurf, 'POINTS %i float\n',lx);
% two values appear on each row of the file
fprintf(osurf, '%f %f %f %f %f %f %f %f %f\n', wox);
fprintf(osurf, '\n');
fprintf(osurf, 'POLYGONS %i %i\n', lc, 4*lc);
fprintf(osurf, '%i %i %i %i\n', wconnect);
fprintf(osurf, '\n');
fprintf(osurf, 'CELL_DATA %i\n',lc);
fprintf(osurf, 'POINT_DATA %i\n',lx);
fclose(osurf);

%Create a final of the thrombus
%Create an stl comprised of both surfaces
%Write out as a vtk file
wux=ox';
wvux=ux';
combinedw=[wux wox];
wconnect3=connect3';
lc3=length(wconnect3);

% open a file for writing
fid = fopen('combinedwall.vtk', 'w');
% print a header line
fprintf(fid, '# vtk DataFile Version 3.0\n');
fprintf(fid, 'vtk output\n');
fprintf(fid, 'ASCII\n');
fprintf(fid, 'DATASET POLYDATA\n');
fprintf(fid, 'POINTS %i float\n',2*lx);
fprintf(fid, '%f %f %f %f %f %f %f %f %f\n', combinedw);
fprintf(fid, '\n');
fprintf(fid, 'POLYGONS %i %i\n', lc3, 4*lc3);
fprintf(fid, '%i %i %i %i\n', wconnect3);
fprintf(fid, '\n');
fprintf(fid, 'CELL_DATA %i\n',lc3);
fprintf(fid, 'POINT_DATA %i\n',2*lx);
fclose(fid);

%combinedthrombus
combinedw2=[points' wux];
% open a file for writing
fid = fopen('combinedthrombus.vtk', 'w');

```

```

% print a header line
fprintf(fid, '# vtk DataFile Version 3.0\n');
fprintf(fid, 'vtk output\n');
fprintf(fid, 'ASCII\n');
fprintf(fid, 'DATASET POLYDATA\n');
fprintf(fid, 'POINTS %i float\n', 2*lx);
fprintf(fid, '%f %f %f %f %f %f %f %f %f\n', combinedw2);
fprintf(fid, '\n');
fprintf(fid, 'POLYGONS %i %i\n', lc3, 4*lc3);
fprintf(fid, '%i %i %i %i\n', wconnect3);
fprintf(fid, '\n');
fprintf(fid, 'CELL_DATA %i\n', lc3);
fprintf(fid, 'POINT_DATA %i\n', 2*lx);
fclose(fid);

```

Listing D.3: Growth and Remodelling

```

%% main functions of this script
% Specify time zones:
% step 1; Material parameters for initial structural analysis ANSYS
% step2; Fibroblast Recruitment Stretch Field
% step >2 Degradation, Growth & Remodelling
% divide the region to 3 parts: aneurysm, transitional region, parent vessel
% 1. considering the collagen mass density
% 2. Elastin degrades with high AR (from step 3)
% 3. collagen degrades with high AR (from step 3)
% 4. collagen mass density regulated by fibroblasts stretch deviation (from
    »step 3)
% 5. collagen remodels (k2) with cauchy fibre stress deviation (from step 4)
%% Define modelling paramters here
%Geometric parameters for specification of z-regions for G&R spatial control:
top    = 1; % top limitation of transitional region
bottom = -1; % bottom limitation of transitional region
tmb    = top-bottom;

% This is cap for stress-based remodelling function of k1
max_stress_diff_growth_fn = 0.5; %remodelling rate levels off is deviation
    »exceeds 50% of original stress

%Elastin degradation

```

```

prescribedegradation = 0; %if 1 prescribed, else link to flow.
deg_flow_t0 = 1;
prescribe_el_deg_rate = 0.8;
prescribe_col_deg_rate = 0.8;

%Region of Degradation
localised = 1;% if prescribed and 1, localise to a specific region of sac.
%Coordinates and radius of Sphere of influence for degradation
sphere_x = -2; sphere_y = 4; sphere_z = 4; sphere_r = 8;
%Polynomial exponet for spatial degradation
polyexp = 4;

%ELASTIN
% elastin mass density
mE_p = 1;          %Parent artery
mE_a = 1;          %aneurysm sac
%Neo-Hookean shear modulus
k_p = 4;           %Parent artery (MPa)
k_a = 4;           %aneurysm sac (MPa)
%Effective shear modulus for ANSYS (Neo-Hookean)
c_p = k_p*mE_p;    %Parent artery (MPa)
c_a = k_a*mE_a;    %aneurysm sac (MPa)

%COLLAGEN
% collagen mass density
mC_p = 1; %parent artery
mC_a = 1; %aneurysm sac
%collagen mass density mC1 for degradtion
mC1_I4=1; mC1_I6=1; %
%collagen mass density mC2 for growth
mC2_I4=1; mC2_I6=1; %
%collagen mass density mC
mC_I4=mC1_I4*mC2_I4;%
mC_I6=mC1_I6*mC2_I6;

%k1 value
k1_a = 0;%MPa
k1_a_I4 = k1_a; k1_a_I6 = k1_a; %MPa on aneurysm
k1_p = 0; %MPa parent_vessel
k1_p_I4 = k1_p; k1_p_I6 = k1_p; %MPa on aneurysm
%Collagen k2
k2_a=0.01;
k2_a_I4 = k2_a; k2_a_I6 = k2_a; %k2 value of a01/a02 collagen families on

```

```

    »aneurysm
k2_p    = 0.01; %k2 value of a01/a02 collagen families on parent vessel

%k1 values for ANSYS
k1_mC_a_I4= mC1_I4*mC2_I4*k1_a_I4; %k1 in the ANSYS (I4)
k1_mC_a_I6= mC1_I6*mC2_I6*k1_a_I6; %k1 in the ANSYS (I6)

%Flow metric to drive degradation
flowmetricdeg = 1;% %1=OSI, 2=AR, 3=LowWSS, 4 = HighWSS, 5= transWSS

%Thresholds for pulsatile flow stimuli to degrade constituents
%OSI
OSI_crit = 0.075;
OSI_max  = 0.1;
%AR metric
AR_crit  = 0.5;
AR_max   = 0.75;
%trans_WSS
transWSS_crit =4;
transWSS_max  = 8;
%Low mean WSS
Low_WSS_crit = 2;
Low_WSS_max  = 1;
%High mean WSS
High_WSS_crit = 4;
High_WSS_max  = 6;

if flowmetricdeg==1
flow_metric_crit = OSI_crit;
flow_metric_max  = OSI_max;
elseif flowmetricdeg ==2
flow_metric_crit = AR_crit;
flow_metric_max  = AR_max;
elseif flowmetricdeg ==3
flow_metric_crit = transWSS_crit;
flow_metric_max  = transWSS_max;
end

%Degradation parameters
%at most 10% of the existing elastinous constituents are degraded per year
max_elastin_degradation = 0.5;
%maximum amount of the existing collagenous constituents are degraded per year
max_collagen_degradation = 0.5;

```



```

%parent artery
elseif (z(i)<bottom)
fprintf(fid, '%f      %f      %f      %f      %f      %f      %f      %f      %f      %f\n'
    »f      %f      %f      %f      %f      %f      %f      %f      %f      %f
    »      %f      %f      %f\n' ,...
c_p,mC_p*k1_p,k2_p,mC_p*k1_p,k2_p,...
mE_p,mC_p,mC_p,...
0,0,0,0,...
mC1_I4,mC1_I6,mC2_I4,mC2_I6, k1_p, k1_p);
%transition region
elseif (z(i)>=bottom&&z(i)<top)
zinterp = (z(i)-bottom)/tmb;
%Elastin
mE_t(i)    = mE_p+((mE_a-mE_p)*zinterp);
c_t(i)     = k_p*mE_t(i);
%Collagen (mcp and mca are equal)
if mC_p~=mC_a
mC_t(i) = mC_p+(mC_a-mC_p)*zinterp;
else
mC_t(i) = mC_p;
end
%interpolation of k1
k1_I4_t(i) = k1_p+(zinterp*(k1_a_I4-k1_p));
k1_I6_t(i) = k1_p+(zinterp*(k1_a_I6-k1_p));
%stiffness parameter for collagen – product of density*k1
k1_mC_I4_t(i) = mC_t(i)*k1_I4_t(i);
k1_mC_I6_t(i) = mC_t(i)*k1_I6_t(i);
%interpolation of k2
k2_I4_t(i) = k2_p+(zinterp*(k2_a_I4-k2_p));
k2_I6_t(i) = k2_p+(zinterp*(k2_a_I6-k2_p));

fprintf(fid, '%f      %f      %f      %f      %f      %f      %f      %f      %f      %f\n'
    »f      %f      %f      %f      %f      %f      %f      %f      %f      %f
    »      %f      %f      %f\n' ,...
c_t(i),mC_t(i)*k1_I4_t(i),k2_I4_t(i),mC_t(i)*k1_I6_t(i),k2_I6_t(i),...
mE_t(i),mC_t(i),mC_t(i),...
0,0,0,0,...
mC1_I4,mC1_I6,mC2_I4,mC2_I6, k1_I4_t(i), k1_I6_t(i));
end
end
end

%% the Time 2

```



```

%Collagen Mass mC
mC_I4_t(i) = mC1_I4_t(i)* mC2_I4_t(i);
mC_I6_t(i) = mC1_I6_t(i)* mC2_I6_t(i);
%ANSYS k1*mC1*mC2
k1_mC_I4_t(i)=k1_I4_t(i)*mC_I4_t(i);    k1_mC_I6_t(i)=k1_I6_t(i)*mC_I6_t(i);
%Output
fprintf(fid, '%f      %f      %f      %f      %f      %f      %f      %f      %f      %f\n',
    »f      %f      %f      %f      %f      %f      %f      %f      %f      %f\n',
    »      %f      %f      %f\n', ...
c_t(i), k1_mC_I4_t(i), k2_I4_t(i), k1_mC_I6_t(i), k2_I6_t(i), mE_t(i), mC_I4_t(i),
    »mC_I6_t(i), ...
lambda_F_AT, lambda_F_AT, lambda_F_Rc_I4(i), lambda_F_Rc_I6(i), mC1_I4_t(i),
    »mC1_I6_t(i), mC2_I4_t(i), mC2_I6_t(i), ...
k1_I4_t(i), k1_I6_t(i));
end
end
end

%% the Time 3.....n

if step_number>2
% IMPORT DATA
% read the c, k1, k2, mE, mC value from last step
filename=[ 'c_k_value' ,int2str(step_number-1), '.dat' ];
c_k_last_step=load(filename);
c_last_step = c_k_last_step(:,1);
k1_last_step_I4 = c_k_last_step(:,17);    k2_last_step_I4 = c_k_last_step(:,3)
    »;
k1_last_step_I6 = c_k_last_step(:,18);    k2_last_step_I6 = c_k_last_step(:,5)
    »;
mE_last_step = c_k_last_step(:,6);
mC1_I4_last_step = c_k_last_step(:,13);
mC1_I6_last_step = c_k_last_step(:,14);
mC2_I4_last_step = c_k_last_step(:,15);
mC2_I6_last_step = c_k_last_step(:,16);
% recruitment stretch of fibroblasts from the last step
lambda_F_Rc_I4_last = c_k_last_step(:,11);
lambda_F_Rc_I6_last = c_k_last_step(:,12);
% load the stretch and cauchy stress result
cauchy_stress1=load('./stretch_cauchy_stress1.dat');
cauchy_stress2=load('./stretch_cauchy_stress2.dat');
% stretch in the direction of collagen fibres
stretch_I4=cauchy_stress2(:,1);

```

```

stretch_I6=cauchy_stress2(:,2);
% stretch on fibroblast
lambda_F_I4=stretch_I4./lambda_F_Rc_I4_last;
lambda_F_I6=stretch_I6./lambda_F_Rc_I6_last;

% load the CFD result
if prescribedegradation==0
if (deg_flow_t0 == 1)
centroid_cfd=importdata(' ../ source_solid/centroid_cfd_pulsatile_t0.dat ');
else
centroid_cfd=importdata(' centroid_cfd_pulsatile.dat ');
end
% OSI = centroid_cfd.data(:,5);
% AR = centroid_cfd.data(:,6);
% meanWSS = centroid_cfd.data(:,8);
% transWSS = centroid_cfd.data(:,9);
if flowmetricdeg==1 %OSI
var_flow_metric_deg = centroid_cfd.data(:,5);
elseif flowmetricdeg ==2 %AR
var_flow_metric_deg = centroid_cfd.data(:,6);
elseif flowmetricdeg ==3 %transWSS
var_flow_metric_deg = centroid_cfd.data(:,9);
end

end

for i=1:row
% aneurysm region, highest elastin degradation, collagen remodelling
if z(i)>=top

%ALL GROWTH AND REMODELLING IS CONTROLLED HERE and FUNCTIONS at end.

if (prescribedegradation==1)
if (localised==1)
localdegfactor=spatialdeg(x(i),y(i),z(i),sphere_x,sphere_y,sphere_z,sphere_r,
»polyexp);
else
localdegfactor=1;
end
el_deg_rate = 1 + (prescribe_el_deg_rate-1)*localdegfactor;
col_deg_rate = 1 + (prescribe_col_deg_rate-1)*localdegfactor;
%elastin degradation
mE_t(i) = mE_last_step(i)* el_deg_rate;

```

```

%collagen degrades
mC1_I4_t(i) = mC1_I4_last_step(i)* col_deg_rate;
mC1_I6_t(i) = mC1_I6_last_step(i)* col_deg_rate;
else

%Linking Growth and remodelling with pulsatile flow metric in this region (see
» Function)
[mE_deg_i,mCdeg_i]=degradation(var_flow_metric_deg(i),flow_metric_crit ,
»flow_metric_max );
%elastin degradation with pulsatile flow metric
mE_t(i) = mE_last_step(i)*(1-mE_deg_i*max_elastin_degradation);
%collagen degrades with pulsatile flow metric
mC1_I4_t(i) = mC1_I4_last_step(i)*(1-mCdeg_i*max_collagen_degradation);
mC1_I6_t(i) = mC1_I6_last_step(i)*(1-mCdeg_i*max_collagen_degradation);
end
c_t(i) = k_a*mE_t(i);

%fibroblast recruitment stretch remodels
lambda_F_Rc_I4_t(i) = Fibroblast_Remodelling(lambda_F_I4(i),lambda_F_AT,
»alpha_F,lambda_F_Rc_I4_last(i));
lambda_F_Rc_I6_t(i) = Fibroblast_Remodelling(lambda_F_I6(i),lambda_F_AT,
»alpha_F,lambda_F_Rc_I6_last(i));
% collagen growth mediated by fibroblasts
mC2_I4_t(i) = Fibroblast_Growth(lambda_F_I4(i),lambda_F_AT,beta_F,
»mC2_I4_last_step(i));
mC2_I6_t(i) = Fibroblast_Growth(lambda_F_I6(i),lambda_F_AT,beta_F,
»mC2_I6_last_step(i));
%collagen remodelling - k1
k1_I4_t(i) = rem_k1_CS(cauchy_stress2(i,3),cauchy_stress1(i,3),
»collagen_remodelling_rate,k1_last_step_I4(i),max_stress_diff_growth_fn);
k1_I6_t(i) = rem_k1_CS(cauchy_stress2(i,4),cauchy_stress1(i,4),
»collagen_remodelling_rate,k1_last_step_I6(i),max_stress_diff_growth_fn);
%collagen remodelling - k2 (no remodelling)
k2_I4_t(i) = k2_a_I4;
k2_I6_t(i) = k2_a_I6;

%%%%%%%%%%%%%%%%%%%%%%%%%%%%%%%%%%%%%%%%%%%%%%%%%%%%%%%%%%%%%%%%%%%%%%%%
% END OF G&R IN ANEURYSM SAC
%%%%%%%%%%%%%%%%%%%%%%%%%%%%%%%%%%%%%%%%%%%%%%%%%%%%%%%%%%%%%%%%%%%%%%%%

% Update Total Collagen Mass Density mC
mC_I4_t(i) = mC1_I4_t(i)* mC2_I4_t(i);
mC_I6_t(i) = mC1_I6_t(i)* mC2_I6_t(i);

```

```

%Update k1 stiffness parameter for ANSYS
k1_mC_I4_t(i) = k1_I4_t(i)*mC_I4_t(i);
k1_mC_I6_t(i) = k1_I6_t(i)*mC_I6_t(i);

% parent vessel region
elseif z(i)<bottom
%elastin
mE_t(i) = mE_p;    c_t(i) = k_p;
%collagen mC1
mC1_I4_t(i) = mC_p;    mC1_I6_t(i) = mC_p;
%Collagen Growth mC2
mC2_I4_t(i) = mC2_I4;    mC2_I6_t(i) = mC2_I6;
%Collagen Mass mC
mC_I4_t(i) = mC1_I4_t(i)* mC2_I4_t(i);    mC_I6_t(i) = mC1_I6_t(i)* mC2_I6_t(
    »i);
%k1
k1_I4_t(i) = k1_p;    k1_I6_t(i) = k1_p;
%ANSYS k1 *mC1*mC2
k1_mC_I4_t(i)=k1_I4_t(i)*mC1_I4_t(i)*mC2_I4_t(i);    k1_mC_I6_t(i)=k1_I6_t(i)*
    »mC1_I6_t(i)*mC2_I6_t(i);
%k2
k2_I4_t(i) = k2_p;    k2_I6_t(i) = k2_p;

%Prescribe Fibroblast recruitment stretches to maintain homeostatic fibroblast
    » stretch in this region
lambda_F_Rc_I4_t(i) =stretch_I4(i)/lambda_F_AT;
lambda_F_Rc_I6_t(i) =stretch_I6(i)/lambda_F_AT;

% transitional region
elseif z(i)>=bottom && z(i)<top
zinterp = (z(i)-bottom)/tmb;
%elastin
mE_t(i) = mE_p+((mE_a-mE_p)*zinterp);
c_t(i) = k_p*mE_t(i);
%collagen mC1
mC1_I4_t(i) = mC_p+((mC_a-mC_p)*zinterp);    mC1_I6_t(i) = mC_p+((mC_a-mC_p)*
    »zinterp);
%Collagen Growth mC2
mC2_I4_t(i) = mC2_I4;    mC2_I6_t(i) = mC2_I6;
%Collagen Mass mC
mC_I4_t(i) = mC1_I4_t(i)* mC2_I4_t(i);    mC_I6_t(i) = mC1_I6_t(i)* mC2_I6_t(
    »i);
%k1

```

```

k1_I4_t(i) = k1_p+((k1_a_I4-k1_p)*zinterp);    k1_I6_t(i) = k1_p+((k1_a_I6-
    »k1_p)*zinterp);
%ANSYS k1*mC1*mC2
k1_mC_I4_t(i)=k1_I4_t(i)*mC_I4_t(i);    k1_mC_I6_t(i)=k1_I6_t(i)*mC_I6_t(i);
%k2
k2_I4_t(i) = k2_p+(k2_a_I4-k2_p)*zinterp;    k2_I6_t(i) = k2_p+(k2_a_I6-k2_p)*
    »zinterp;

%Prescribe Fibroblast recruitment stretches to maintain homeostatic fibroblast
    » stretch in this region
lambda_F_Rc_I4_t(i) =stretch_I4(i)/lambda_F_AT;
lambda_F_Rc_I6_t(i) =stretch_I6(i)/lambda_F_AT;

end
%Output
fprintf(fid, '%f    %f    %f    %f    %f    %f    %f    %f    %f
    »f    %f    %f    %f    %f    %f    %f    %f
    »    %f    %f    %f\n', ...
c_t(i), mC_I4_t(i)*k1_I4_t(i), k2_I4_t(i), mC_I6_t(i)*k1_I6_t(i), k2_I6_t(i), mE_t(
    »i), mC_I4_t(i), mC_I6_t(i), ...
lambda_F_I4(i), lambda_F_I6(i), lambda_F_Rc_I4_t(i), lambda_F_Rc_I6_t(i), mC1_I4_t
    »(i), mC1_I6_t(i), mC2_I4_t(i), mC2_I6_t(i), ...
k1_I4_t(i), k1_I6_t(i));
end
fclose(fid);
close all

end

```

Listing D.4:  $k_1$  remodelling

```

function [k1_t]=rem_k1_CS(cst, cshom, rate, k1_last_step,
    »max_stress_diff_growth_fn)

if cst>0
dev=(cst-cshom)/cshom;
if dev<=max_stress_diff_growth_fn
diff = dev;
elseif dev >max_stress_diff_growth_fn
diff = max_stress_diff_growth_fn;
else

```

```
diff = 0;  
end  
k1_t = k1_last_step - (rate * diff * k1_last_step);  
if k1_t < 0.001  
k1_t = 0.001;  
end  
else  
k1_t = k1_last_step;  
end  
end
```

#### Listing D.5: Fibroblast Remodelling

```
%Fibroblast Recruitment Stretch Remodels  
function [rec] = Fibroblast_Remodelling(stretch, att_stretch, rate, var_last_step  
    »)  
rec = var_last_step + (var_last_step * rate * (stretch - att_stretch) / att_stretch);  
if rec < 0.1  
rec = 0.1;  
end  
end
```

#### Listing D.6: Fibroblast Growth

```
%Fibroblast Remodelling and Growth Functions  
function [mCt] = Fibroblast_Growth(stretch, att_stretch, rate, var_last_step)  
  
mCt = var_last_step + (var_last_step * rate * (stretch - att_stretch) / att_stretch);  
if mCt < 0.01  
mCt = 0.01;  
end  
end
```